DISSERTATION / DOCTORAL THESIS

Titel der Dissertation /Title of the Doctoral Thesis

„Excited State Simulations in the Presence of Laser Fields using Linear Vibronic Coupling Potentials“

verfasst von / submitted by

Moritz Heindl, BSc MSc

angestrebter akademischer Grad / in partial fulfilment of the requirements for the degree of

Doktor der Naturwissenschaften (Dr. rer. nat.)

Wien, 2022 / Vienna 2022

Studienkennzahl lt. Studienblatt / degree programme code as it appears on the student record sheet:	A 796 605 419
Dissertationsgebiet lt. Studienblatt / field of study as it appears on the student record sheet:	Chemie
Betreut von / Supervisor:	Univ.-Prof. Dr. Dr. h.c. Leticia González
Mitbetreut von / Co-Supervisor:	

CONTENTS

ABSTRACT

At the very core of fundamental processes that shape life on our planet, lies the interplay of light with matter. For an experimental investigation of such inherently quantum interactions an extremely high time resolution is needed, necessitating the use of ultrashort laser pulses. A complementary route is the direct simulation of the quantum dynamics in the manifold of electronic states, necessitating inclusion of the laser pulses for compatibility to experimental results.

Different layers of approximation exist for quantum simulations, ranging from exact propagation and multi-configurational time-dependent Hartree (MCTDH) to approximations in the form of a mixed quantum-classical description, where the lion's share of the quantum nature of nuclei is forfeited, increasing computational speed. A popular of these mixed quantum-classical methods is fewest-switches surface hopping (SH), allowing for the efficient simulation of dynamics for molecules on the complete manifold of nuclear degrees of freedom. Since SH can not directly be linked to exact propagations, no unique way to overcome some of the deficiencies innate to SH is available, resulting in many different SH protocols of varying accuracy. If explicit laser fields are included in the simulations to mimic experimental setups or to modify the excited state dynamics, this uncertainty in accuracy is amplified due to additional interference terms that may arise.

In this work, the validity of SH in the presence of laser fields is put to the test by comparing different SH protocols and pulse lengths to reference MCTDH calculations. Such a comparison is enabled by the use of linear vibronic coupling (LVC) potentials for both types of simulations. A three-dimensional model of SO_2 and a ten-dimensional model of 2-thiocytosine are employed, providing systems that go far beyond the one-dimensional systems previously often used to validate SH. The reduction of the 33-dimensional 2-thiocytosine to only ten dimensions has been achieved by a previously devised automatic selection procedure. In both test systems, a qualitative description of the interaction with the laser field was achieved, with longer interaction times resulting in larger deviations from MCTDH results, especially for small systems. As for the SH protocols, no unique set of best performing protocols has been found.

The strength of SH paired with LVC potentials is demonstrated in the detailed investigation of a ruthenium photosensitizer equipped with a disulfide bridge at one of the ligands ($[\mathrm{Ru}(^{S-S}\mathrm{bpy})(\mathrm{bpy})_2]^{2+}$) employing 161-dimensional surfaces for all 78 considered electronic states. The fluctuations of electronic character throughout the simulation time show that S–S bond elongation occurs after the excited electron is located at the sulfurated ligand, resulting in a stabilization of low-energy triplet states. Finally, a pulse sequence is designed, capable of counteracting the S–S bond elongation and the accompanying energy lowering of the lowest energy triplet states, trapping the population for the duration of the pulse sequence.

In addition, this thesis features the on-the-fly and full-dimensional simulation of the excited state dynamics of pyrrole after excitation into a $\pi \rightarrow \pi^*$ state. The main deactivation channel is N–H bond dissociation, observed with a time scale of 64 ± 13 fs. The valence-Rydberg mixing in pyrrole is found to be at the heart of the peculiar shape of the potential energy surface along the dissociative coordinate.

ZUSAMMENFASSUNG

Die Interaktion von Licht mit Materie bildet die Grundlage fundamentaler Prozesse, die das Leben auf unserem Planeten ermöglicht haben. Zur experimentellen Untersuchung solcher Quantenprozesse wird eine extrem hohe Zeitauflösung benötigt, die nur mit ultrakurzen Laserpulsen erreicht werden kann. Ein ergänzender Zugang liegt in der Simulation dieser mit Quantendynamik in der Vielzahl an elektronischen Zuständen, wobei die vorhin erwähnten Pulse inkludiert werden müssen um eine Vergleichbarkeit zu experimentellen Ergebnissen zu gewährleisten.

Es existieren verschiedene Abstufungen von Quantendynamik, die von formell exakter Evolution der Welleneigenschaften über multi-configurational time-dependent Hartree (MCTDH) bis hin zu Näherungen in der Form einer Mischung aus Quanten- und klassischer Dynamik. In dieser wird der Großteil der Quanteneigenschaften der Atomkerne vernachlässigt, um die entsprechenden Rechnungen zu vereinfachen. Eine der bekanntesten dieser Methoden ist fewest-switches surface hopping (SH) mit welcher Systeme mit mehreren hundert Atomen simuliert werden können. Da SH nicht direkt von exakter Quantendynamik abgeleitet werden kann, gibt es kein klares Bild darüber wie manche der Unzulänglichkeiten dieser Methode überwunden werden können, weswegen eine Vielzahl an unterschiedlichen Modifikationen mit wechselnder Genauigkeit existieren. Wenn explizite Laserpulse in der Simulation inkludiert werden um entweder experimentelle Gegebenheiten widerzuspiegelen oder aber die Dynamik in angeregten Zuständen zu verändern, werden die Ungewissheiten in Bezug auf die vielen unterschiedlichen Modifikationen und deren Auswirkungen auf die Genauigkeit potenziert.

In dieser Arbeit wird die Anwendbarkeit von SH in der Anwesenheit von Laserpulsen auf die Probe gestellt indem unterschiedliche Modifikationen von SH mit unterschiedlichen Pulslängen mit Referenz-MCTDH Rechnungen verglichen werden. Diese Vergleiche werden durch die Verwendung von linear vibronic coupling (LVC) Potenzialen für beide Simulationsmethoden ermöglicht Ein drei-dimensionales Modell für $\mathrm{SO_2}$ und ein zehn-dimensionales Modell für 2-Thiocytosin werden dafür zu Rate gezogen. Damit werden weitaus größere Systeme verwendet als die sonst üblichen ein-dimensionalen Systeme, die für solche Vergleiche zu Rate gezogen werden. Die Reduktion des eigentlich 33-dimensionalen 2-Thiocytosins zu einem zehn-modigen System wurde durch ein vorher konzipiertes automatisches Auswahlverfahren realisiert. In beiden Testsystemen wurde eine qualitative Übereinstimmung für die Interaktion mit den Laserpulsen beobachtet, wobei längere Laserpulse zu größeren Abweichungen geführt haben, insbesondere für kleine Systeme. In Bezug auf die getesteten Modifikationen wurde kein optimales Set an Modifikationen gefunden.

Die Stärke von SH in Kombination mit LVC Potenzialen wird anhand der detailierten Untersuchung eines Ruthenium Photosensibilisators, der eine Disulfidbrücke an einem der Liganden besitzt ($[\mathrm{Ru}(^{S-S}\mathrm{bpy})(\mathrm{bpy})_2]^{2+}$), aufgezeigt, wobei 161-dimensionale Oberflächen für alle 78 verwendeten elektronischen Zustände verwendet werden. Eine genaue Beobachtung der Änderungen des elektronischen Charakters entlang der Simulation zeigt, dass die S–S Bindung verlängert wird sobald das angeregte Elektron am entsprechenden Liganden lokalisiert ist. Im Zuge dessen, kommt es auch zu einer Stabilisierung von niedrig-energetischen Triplett Zuständen. Schlussendlich wird eine Pulssequenz entworfen, die diese S–S Bindungsver-

längerung und die dazugehörigen Stabilisierungen in der Energie unterbindet und die angeregte Population in einem endlosen Kreislauf gefangen hält solange die Pulssequenz anhält.

Zusätzlich wurde in dieser Arbeit die voll-dimensionale Simulation der Dynamik der angeregten Zustände von Pyrrol nach Anregung eines $\pi \rightarrow \pi^*$ Zustandes unternommen. Der Hauptrelaxationsweg in diesem Molekül ist N–H Bindungsbruch der in einer Zeitskala von 64 ± 13 fs beobachtet wird. Das Mischen von Rydberg- und Valenzorbitalen wurde als das entscheidende Kriterium für die sonderbare Form der Potentialenergieoberfläche entlang der dissoziativen Koordinate identifiziert.

UV	ultraviolet
TDSE	time-dependent Schrödinger equation
TISE	time-independent Schrödinger equation
BOA	Born-Oppenheimer approximation
NAC	non-adiabatic coupling
HF	Hartree-Fock
SCF	self-consistent field
CASSCF	complete active space self-consistent field
CI	configuration interaction
MCSCF	multi-configurational self-consistent field
CASSCF	complete active space self-consistent field
SA	state-average
CASPT2	complete active space perturbation theory of second order
MRCI	multi-reference configuration interaction
MRCIS	multi-reference configuration interaction using only singlet excitations
MRCISD	multi-reference configuration interaction using singlet and doublet excitations
DFT	density functional theory
KS	Kohn-Sham
TDDFT	time-dependent density functional theory
LVC	linear vibronic coupling
SOC	spin-orbit coupling
MCTDH	multi-configurational time-dependent Hartree
SH	surface hopping
SPF	single particle function
DOF	degrees of freedom
AFSSH	augmented fewest-switches surface hopping
EDC	energy-based decoherence correction
XMS	extended multi state
SA	state-averaging
ISC	intersystem crossing
MCH	molecular coulomb Hamiltonian
FWHM	full width at half maximum
bpy	2,2’-bipyridine
CT	charge-transfer
EW	excitation window

1

INTRODUCTION

1.1 EXCITED STATE DYNAMICS AND WHERE TO FIND THEM

Throughout the history of humankind and all its emergent cultures, a special place has been reserved for the sun as a bringer of life, promoting the light-matter interaction to one of the main driving forces for our existence. This belief and the sun's influence on the evolution of life is nowadays understood in the form of photon absorption processes that activate chemical reaction pathways inaccessible by other means. Such photochemical reactions are found at the heart of natural processes like photosynthesis or the formation of skin cancer,[1] demonstrating the immense power embodied in light itself. Attempts to harness this power beyond simply illuminating a dark hut have resulted in technologies as ambitious as solar cells[2] or photodynamic therapy that selectively attacks cancer cells.[3] The shared root for all these phenomena is the initial absorption of light in the visible or ultraviolet (UV) range of light, resulting in the excitation of one or multiple electrons to form a so-called electronic excited state. Such an electronic excited state represents a volatile situation for any molecule, due to the excess energy provided by the absorbed photon and the existence of the lower-energy initial state to which the molecule could return to. Because of the changed arrangement of the electrons after excitation, different nuclear movements are enabled, resulting in a motion of the excited molecule. As numerous different distributions of electrons exist, many electronically excited states do exist at once, making transitions between them a real possibility when the excited molecule is moving. The subsequent evolution of the so-coupled electronic-nuclear motion then results in the plethora of different photochemical phenomena that aim at arriving at a more favorable combination of nuclear and electronic arrangements than in the initially unstable excited state. An alternative pathway for the deactivation (i.e. the dissipation of the excess energy) of the excited molecule is the possibility to emit a photon itself in a spontaneous fashion. Such radiative deactivation processes are always competing with non-radiative channels but are most often found to be slower than the electronic-nuclear motion.

To design or understand specific photochemical applications, a two-fold approach is needed: on the one hand, the absorptive properties need to be measured and probably fine-tuned; On the other hand, detailed insight into the consecutive excited state dynamics is needed. In an experimental setup, the first of these aspects can be controlled quite easily since the measurement of the absorption of light is a rather straightforward procedure. An approach like this, however, is faces additional challenges when investigating the subsequent excited state dynamics that can occur in the time spans as short as a few hundred femtoseconds, including many electronic states and a variety of nuclear motions.[4] Here, experimental setups are pushed to their limit to provide the needed resolution in time although huge progress has been made throughout the last decades.[5] An additional issue arising is the fact that the underlying dynamics cannot be measured directly but only specific observables, necessitating a final step of mapping specific changes in observables to specific dynamical features. An assignment based on observed changes always carries the possibility that some important mechanism remains shrouded in the set of available observables. To obtain an accurate picture of the dynamics, a time resolution together of tens of femtoseconds and an almost complete set of measured properties is therefore desired. While such a task is beyond most experimental setups, theoretical simulations of dynamics are capable of providing exactly this insight, relying only on computational power and a mathematical foundation to describe atomic and molecular interactions for multiple excited states.

1.2 THE LADDER OF SIMULATION ACCURACY IN DYNAMICS

A theoretical framework for the simulation of excited state dynamics has been known since the Schrödinger equations have been postulated in 1926.[6] Solving those equations exactly for realistic molecular systems, however, has turned out to essentially be impossible, which is the reason why different levels of approximation are introduced for calculations of both static properties and the dynamical evolution of systems. This resulted in the establishment of a hierarchy of methods capable of simulating the molecular dynamics using more than a single electronic state:[7] At the very top of this list resides exact quantum propagation on a grid, where all nuclear quantum effects like nuclear interferences or tunneling are naturally included. This method finds some use in one-dimensional systems, collision reactions and other models in reduced dimensionality, allowing the simulation of only up to five degrees of freedom due to the increased computational effort required.[8]

To allow for the simulation of larger systems, approximations have to be introduced. In the case of the multi-configurational time-dependent Hartree method (MCTDH), this is realized by replacing the space-spanning grid on which the time-dependent Schrödinger equation is evaluated by a mobile grid, where the grid points will always be located at positions where the wave packet is evolving.[9] By doing so, the number of needed grid points can be drastically reduced, enabling the inclusion of more modes of movement for the investigated system. Paired with the attractive feature that MCTDH converges towards the exact solution if more and more grid points are used, this method sees considerable use in illuminating the blind spots encountered during experimental investigations.[10–13] The popularity of MCTDH led to a number of methods that are directly based upon MCTDH like Gaussian-based MCTDH[14], multi-configurational Gaussian (vMCG)[15] or the multi-layer framework for MCTDH[16] that allows for the simulation of a few hundred (but rather simple harmonic) degrees of freedom.[17] The limitations for the stated methods are: I) The reliance on precomputed electronic potential energy surfaces that have to be either calculated or approximated beforehand for all considered degrees of freedom and combinations thereof. A prominent choice to describe these surfaces is the vibronic coupling model that describes the influence of nuclear motion along a single or multiple modes on the electronic energy and all considered coupling elements based on a few reference calculations.[18,19] The general restriction to precomputed potentials in these methods has been lifted recently with the introduction of new methods that base the dynamics on on-the-fly evaluations coupled to a database.[20,21] II) All these methods come at a very high computational cost when many degrees of freedom are considered and a lot of grid points have to be employed to converge towards the exact solution.

The longing for a propagation method that shows a more favorable scaling heralded the advent of methods that simplify the nuclear propagation by treating it classically while the electronic wave function is still treated on a quantum level, terming these methods mixed quantum-classical. One of the most prominent of this class of methods is fewest-switches surface hopping (SH).[22,23] Here, the electronic wave function is used to determine a probability to switch the surface on which the classical propagation occurs in each time step, therefore allowing to simulate transitions – hops – between those. Since a classical trajectory cannot be delocalized in space or evolve on two surfaces at the same time – as a real wave packet would do – a set of independent trajectories is employed to recover this aspect of the quantum nature of nuclei. The strengths of SH are found in the extremely simple classical propagation, reducing the scaling with the system size to a trifle, the simple way of using it, and the inherent dependence on only local properties, therefore not needing any precomputed surfaces. All of these advantages are a direct consequence of the underlying schism between the electronic and nuclear treatment, as are the accompanying drawbacks of SH: Important nuclear quantum effects like tunneling or nuclear interference are neglected and often no direct connection to the exact propagation method can be established, therefore impeding the development of correction terms to the original formulation of SH.[24–26] Therefore, the all-permeating usage of SH for systems where no better reference dynamics is available without proper awareness of possible limitations or inadequate use of the many flavors and small modifications thereto is a rather delicate matter. Multiple small and larger scale investigations have therefore been conducted aiming at providing insight into the accuracy of SH validated against higher level methods or highlighting the differences between different treatments of the same physical effect.[27–35]

1.3 SIMULATION OF EXPLICIT LASER PULSES

More often than not, simulations of excited state dynamics use a so-called δ-pulse excitation where the ground state wave packet is projected onto a single or a set of excited states, without the need to include any explicit laser field to excite the system. However, there are at least two good reasons to include those fields explicitly in the simulation: First, since these simulations aim at either providing insight into experimental observations or should be usable to predict experimental outcomes, the conditions should match the experiment as close as possible. Interference terms due to the exciting laser field are neglected if this laser field is omitted from simulations. Second, explicit laser pulses allow for the control of the ensuing dynamics either via transient population transfer or the introduction of light-induced conical intersections via the dynamical Stark-effect.[36,37] The inherent power of such modifications to guide the excited state dynamics along a desired branch has been realized theoretically 35 years ago.[38,39] To harness the complete potential inherent in control pulses, optimal control theory was devised, capable of optimizing a laser pulse to maximize a target quantity or state.[40] In order to obtain this optimal pulse, the variational principle is used, requiring many iterations of forward and backwards propagations. A simpler route to increase a desired outcome of a given excited state dynamics has been proposed in the form of local control theory.[41] Here, a single dynamics run is needed and the laser adapted in each single time-step to maximise the target quantity for each current time step, therefore drastically reducing the computational work load.

Almost all of the discussed propagation methods have been extended to include the interaction with laser fields and a few examples of uses ranging from MCTDH to SH are found in the literature.[13,42–56] Although SH has been found to be adequate to obtain at least qualitative agreement with higher level propagation methods,[44,48,53,57] the additional complexity to the nuclear dynamics and interferences introduced by the coupling to the external field further puts a big strain on the accuracy. This decrease in accuracy has been observed to amount to qualitative deviations in some cases, showcasing a dependence on both the investigated system, the used laser pulses and the employed type of SH algorithm.[55,58,59] The consideration of laser pulses in SH simulations is therefore found to thicken the veil of mystery that surrounds SH when it comes to accuracy. One of the major reasons for this is the lack of comparisons between SH and higher-level propagation methods on systems beyond a single degree of freedom, that would give some indications on the expected error for realistically sized molecules. Such a limitation is especially crippling when considering the fact that SH opens up the possibility to investigate almost arbitrarily sized molecules that are far beyond the current capabilities of most other propagation methods.

1.4 AIMS OF THIS THESIS

When initially conceived, this thesis set out to demonstrate the capabilities of explicit laser pulses in combination with SH, focusing on a few molecules where strong laser fields should be used to open up additional deactivation pathways via light-induced conical intersections. As is often the case, such innocent ideas include unforeseen complications that here took the form of high computational costs and unstable electronic structure computations, rendering the investigation of the first studied molecule – pyrrole – in the presence of a laser pulse essentially impossible. At the same time, fortunate winds saw me working on a side project that included a side-by-side comparison of SH and MCTDH using the same sets of precomputed potentials in the form of a linear vibronic coupling model (LVC). Intrigued by the possibilities of such an approach, the thesis underwent a change in direction: instead of aiming for the full-dimensional on-the-fly application, it was then directed towards the very roots of the deviations between SH and MCTDH in the presence of laser fields. Therefore, the investigation of the validity of SH in combination with laser pulses lies at the very heart of this thesis and features a three- and a ten-dimensional test system, on which this comparison is conducted. The final part of the thesis is a full-scale theoretical investigation of a ruthenium photosensitizer that makes use of SH, the LVC model potentials employed, and the lessons learned from the investigation of the SH-laser interactions. This investigation sees a full characterization of the excited states and the respective dynamics after excitation as well as a way to control the subsequent excited state dynamics in a complex featuring 161 vibrational modes and 78 electronic states.

The remainder of the thesis adheres to the following structure: An overview of the theoretical foundations and the approximations that form the very basis of this work are introduced in Chapter 2. This is followed by a static and dynamical evaluation of the excited states of pyrrole and the respective dynamics on those states in Chapter 3. The high computational cost, made it impossible to run dynamics in the presence of a laser field, which is one of the reasons why the focus shifted towards calculations using the LVC model, lifting the computational burden. An iterative scheme benefiting from the strengths of both SH and MCTDH to reduce the size of any analytical Hamiltonian and to find appropriate SH protocols is presented in Chapter 4 together with the benchmark on various SH protocols in the presence of laser fields. Finally, Chapter 5 contains an in-depth photophysical analysis of the photosensitizer $[\mathrm{Ru}({}^{S-S}\mathrm{bpy})(\mathrm{bpy})_2]^{2+}$ culminating in the definition of pulse sequences capable of controlling its excited state dynamics.

2

THEORY

The present work revolves around the influence of laser pulses on single molecules, necessitating a description reaching beyond our everyday classical world and deep into the quantum nature of things. These quantum effects govern the interplay of electrons and protons which is found at the base of light-matter interaction, forming the basis for the emergence of sentient life on our planet. In the following, the various concepts needed and employed throughout this thesis will be introduced together with the respective nomenclature, showcasing that the current work is built at the fragile border between the classical and the quantum world.

The basics of a mathematical formulation for quantum mechanics is given in Section 2.1 in the form of the Schrödinger equation, the treatment of external fields and the Born-Oppenheimer approximation. This section will result in a split into the time-independent (TISE) and the time-dependent (TDSE) Schrödinger equation. The time-independent part will set the stage in the form of a manifold of different surfaces while the latter will determine how the coupled electronic-nuclear motion will occur on those. Approaches for solutions of the TISE are presented in Section 2.2 and in Section 2.3 for the TDSE.

2.1 THE FOUNDATIONS

2.1.1 *Schrödinger Equation*

The non-relativistic TDSE[6] can be found at the very heart of quantum mechanics, capable of treating the quantum nature of particles. Using atomic units, it can be written as

$$\hat{H}(\mathbf{r},\mathbf{R},t)|\Psi(\mathbf{r},\mathbf{R},t)\rangle = i\frac{\partial}{\partial t}|\Psi(\mathbf{r},\mathbf{R},t)\rangle \tag{1}$$

where $\hat{H}(\mathbf{r},\mathbf{R},t)$ acts on $|\Psi(\mathbf{r},\mathbf{R},t)\rangle$ and is the so-called *Hamilton operator* containing all interaction terms for all particles and with the surrounding environment. The Hamilton operator depends on the position of all considered particles – in the present case the position of electrons ($\mathbf{r}$) and nuclei ($\mathbf{R}$) – and the respective time, t. $|\Psi(\mathbf{r},\mathbf{R},t)\rangle$ is the *wave function* of the investigated system, which by itself is a complex function fulfilling the TDSE. Following normalization according to

$$\int_{-\infty}^{\infty} |\Psi(\mathbf{r},\mathbf{R},t)|^2 \mathrm{d}\tau = 1 \tag{2}$$

with $\mathrm{d}\tau$ being the integration along all particle coordinates, $|\Psi(\mathbf{r},\mathbf{R},t)|^2$ gives the probability density[60] and therefore information about the distribution of positions for all particles. In order to get an idea of the mathematical form of the mysterious quantity $\Psi(\mathbf{r},\mathbf{R},t)$, the following steps can be taken:[61] First, $\Psi(\mathbf{r},\mathbf{R},t)$ is split up according to

$$\Psi(\mathbf{r},\mathbf{R},t) = \Psi(\mathbf{r},\mathbf{R})\varphi(t) \tag{3}$$

into a time-independent ($\Psi(\mathbf{r},\mathbf{R})$) and a time-dependent ($\varphi(t)$) part based on the assumption that this is valid at least for some solutions of the TDSE equation. Inserting this separation into Equation 1, a separation of variables can be performed, resulting in

$$i\frac{\partial}{\partial t}\varphi(t) = E\varphi(t) \tag{4}$$

for the time-dependent part, with E being a constant, conveniently termed energy in foresight of things to come. From this, a general solution for the form of $\varphi(t)$ can be found in the form of

$$\varphi(t) = de^{-iEt} \tag{5}$$

where d is a constant. By inserting this formulation into Equation 3, two insights can be deduced:

First, calculating the probability density using the *ansatz* from Equation 4 shows that the time-dependent part cancels out, removing the time-dependence of any calculated property. This seemingly paradox turn of events where properties are found to be not depending on time within the TDSE is resolved by realizing that these solutions are true only for stationary states, hence explaining the time-independence. Movement of particles and evolution of properties in time is only observed in a superposition of two or more of such stationary states called a *wave packet*, giving rise to the following formulation for $\Psi(\mathbf{r}, \mathbf{R}, t)$

$$\Psi(\mathbf{r}, \mathbf{R}, t) = \sum_{k=1}^{\infty} c_k \Psi_k(\mathbf{r}, \mathbf{R}) d_k e^{-iE_k t} \tag{6}$$

with c_k being a coefficient, indicating how much each respective state is contributing to the overall wave function.

The second insight derives from inserting the split formulation of the total wave function into Equation 1. Assuming that the Hamilton operator is independent of time, multiplication with $\langle\varphi(t)|$ from the left yields the time-independent Schrödinger equation (TISE):

$$\hat{H}(\mathbf{r}, \mathbf{R})|\Psi(\mathbf{r}, \mathbf{R})\rangle = E|\Psi(\mathbf{r}, \mathbf{R})\rangle \tag{7}$$

allowing the evaluation of the respective energy for a given position of both electrons and nuclei.

Until now only the form of the wave function has been discussed extensively, relying on assumptions about the form of the Hamilton operator. The structure of the Hamilton operator is shown in the following to better understand in which cases this operator is explicitly time-dependent and in which cases the postulations that lead to the TISE are valid. The Hamilton operator considered in this thesis takes the following form for a system containing n electrons and N nuclei with a mass of m and a nuclear charge of Z:

$$\begin{aligned}\hat{H}(\mathbf{r}, \mathbf{R}, t) = &-\underbrace{\sum_{k}^{n} \frac{1}{2}\nabla_k^2}_{\hat{T}_r(\mathbf{r})} - \underbrace{\sum_{K}^{N} \frac{1}{2m_K}\nabla_K^2}_{\hat{T}_R(\mathbf{R})} + \underbrace{\sum_{k}^{n}\sum_{l>k}^{n} \frac{1}{|\mathbf{r}_k - \mathbf{r}_l|}}_{\hat{V}_{rr}(\mathbf{r})} + \underbrace{\sum_{K}^{N}\sum_{L>K}^{N} \frac{Z_K Z_L}{|\mathbf{R}_K - \mathbf{R}_L|}}_{\hat{V}_{RR}(\mathbf{R})} \\ &\underbrace{-\sum_{k}^{n}\sum_{K}^{N} \frac{Z_K}{|\mathbf{r}_k - \mathbf{R}_K|}}_{\hat{V}_{rR}(\mathbf{r}, \mathbf{R})} + \hat{V}_{ext}(\mathbf{r}, \mathbf{R}, t)\end{aligned} \tag{8}$$

It can be seen that the different contributions can be divided into kinetic energy terms of electrons ($\hat{T}_r(\mathbf{r})$) and nuclei ($\hat{T}_R(\mathbf{R})$) together with potential energy terms between all electrons ($\hat{V}_{rr}(\mathbf{r})$), all nuclei ($\hat{V}_{RR}(\mathbf{R})$), and all particles ($\hat{V}_{rR}(\mathbf{r}, \mathbf{R})$). All of these terms depend only on the respective coordinates and are therefore only implicitly time-dependent. The explicit time-dependence is due to the final term that includes any external interactions ($\hat{V}_{ext}(\mathbf{r}, \mathbf{R}, t)$) coming from outside the considered particles. $\hat{V}_{ext}(\mathbf{r}, \mathbf{R}, t)$ therefore contains all interaction terms with external electric fields, like laser pulses which are oscillating in time, hence introducing an explicit time-dependence to the total Hamilton operator. In the absence of any external field, $\hat{V}_{ext}(\mathbf{r}, \mathbf{R}, t)$ vanishes and $\hat{H}(\mathbf{r}, \mathbf{R}, t) = \hat{H}(\mathbf{r}, \mathbf{R})$, allowing the evaluation of the TISE.

The form $\hat{V}_{ext}(\mathbf{r}, \mathbf{R}, t)$ can take will be discussed in the following section before approximations to the TISE will be explored in Section 2.1.3.

2.1.2 *External Fields*

The $\hat{V}_{ext}(\mathbf{r}, \mathbf{R}, t)$ term in the Hamilton operator governs the interaction of the molecule with external fields. In theory, these could take many forms with the fields strong enough to influence the time evolution of a molecular system being either electric or magnetic fields. While the magnetic field can interact with the spins of the system, the resulting interaction is much weaker than the interaction with the electric field as long as the considered wavelength (λ) of the electromagnetic wave is sufficiently large. As this thesis focuses on absorption in the visible or ultraviolet region of light, electronic interactions and electronic transitions prevail, hence any magnetic effects will be neglected in the following.

In an exact description, both the electric field and all particles need to be treated on a quantum level. However, if sufficiently strong fields are used, the influence of the molecular wave function on the field is negligible, allowing for a classical description of the electric field where only the influence of the field on the quantum particles is considered. Even then, the interaction of an oscillating electric field – stretching infinitely into space – with the distribution of particles represented by $\Psi(\mathbf{r}, \mathbf{R}, t)$ is a rather delicate matter. Fortunately, the problem can be simplified straightforwardly by considering the fact, that the distribution of electrons and nuclei will be strongly correlated with both types of particles sticking close to each other. Therefore, the spatial extent of the probability distributions for both particles will be rather small compared to the employed λ values. This in turn means that the change of the electric field with the spatial coordinates is vanishing for the molecular system within a single time step. This reduces the multipole expansion of the various interaction terms with the electric field to a single contribution, namely the interaction with the dipole moments, coining the term *dipole approximation*:

$$\hat{V}_{ext}(\mathbf{r}, \mathbf{R}, t) \approx -\hat{\mu}(\mathbf{r}, \mathbf{R})\boldsymbol{\varepsilon}(t) \tag{9}$$

with $\hat{\mu}(\mathbf{r}, \mathbf{R})$ being the dipole operator yielding all dipole moments across all spatial coordinates when applied to a wave function. The electric field oscillating in time is given as $\boldsymbol{\varepsilon}(t)$ and can be written as

$$\boldsymbol{\varepsilon}(t) = \mathbf{p}\epsilon_0 \cos(\omega(t - t_0) + \eta)\; g(t, t_0) \tag{10}$$

Here, the spatial polarization of the field is contained in the vector $\mathbf{p}$ and the amplitude of the field amounts to ϵ_0. The field itself is defined by the frequency ω centered at a time t_0 and with a phase factor of η which will be set to zero throughout this thesis.

To limit the pulse in time, an envelope function $g(t, t_0)$ is multiplied to the electric field. In this work, either no envelope function ($g(t, t_0) = 1$) or Gaussian-shaped envelope functions defined by the full width at half maximum (t_{FWHM}) are used:

$$g(t, t_0) = \exp\left[-4\ln 2\left(\frac{t - t_0}{t_{\mathrm{FWHM}}}\right)^2\right] \tag{11}$$

Equipped with a formulation for $\hat{V}_{ext}(\mathbf{r}, \mathbf{R}, t)$, all terms of the Hamiltonian operator have been defined. Nevertheless, the task of actually solving any of the two Schrödinger equations for a number of particles remains nothing more than an Utopian ideal, out of reach without introducing further approximations.

2.1.3 *Born-Oppenheimer Approximation*

Driven by the inability to solve the Schrödinger equations for systems containing multiple particles, additional steps have been undertaken to simplify the problem at hand. With the time-dependence factored out from the TDSE to yield the TISE, the remaining crucial difficulty arises from the explicit coupling of nuclei and electrons, resulting in a intricate correlation between those particles. At the core of reducing the complexity of this issue lies a simple thought: Considering the differences in mass between nuclei and electrons, one obtains radically different scales of movement for both particles with electrons moving many orders of magnitude faster than even the lightest nuclei. Therefore, the electrons will respond almost instantaneously to any changes in **R** while nuclei experience the interaction with an averaged field of electrons. This allows for a separation of $\Psi(\mathbf{r}, \mathbf{R})$ into an electronic ($\Psi^{el}(\mathbf{r}; \mathbf{R})$) wave function, depending only parametrically on **R** (indicated via the preceding semicolon), and a nuclear ($\Psi^{nu}(\mathbf{R})$) wave function, forming one of the major steps in the *Born-Oppenheimer approximation* (BOA).[62]

$$\Psi(\mathbf{r}, \mathbf{R}) = \Psi^{el}(\mathbf{r}; \mathbf{R})\Psi^{nu}(\mathbf{R}) \tag{12}$$

Going one step further, the position of the nuclei can be assumed to be frozen in which case $\hat{T}_R(\mathbf{R})$ is rendered zero while $\hat{V}_{RR}(\mathbf{R})$ becomes constant. With this, an electronic Hamilton operator ($\hat{H}^{el}(\mathbf{r}; \mathbf{R})$) is obtained that only is applied to $\Psi^{el}(\mathbf{r}; \mathbf{R})$ and yields the electronic energy $E^{el}(\mathbf{R})$, forming the electronic Schrödinger equation:

$$\hat{H}^{el}(\mathbf{r}; \mathbf{R})|\Psi^{el}(\mathbf{r}; \mathbf{R})\rangle = E^{el}(\mathbf{R})|\Psi^{el}(\mathbf{r}; \mathbf{R})\rangle \tag{13}$$

The assumption of frozen nuclei and the respective parametrical dependence on **R** means that Equation 13 can be solved for all possible nuclear arrangements, spanning an electronic *potential energy surface* (PES) comprised of all the instantaneous energies arising from the electrons adapting to a given conformation of nuclei.

We can use the particular solutions provided by Equation 13 to gain more insight on the nature of the BOA. For this, we first expand $\Psi(\mathbf{r}, \mathbf{R})$ into a linear combination of states similar to Equation 6 just for a time-independent case and also perform the separation into nuclear and electronic wave functions introduced in the BOA:

$$\Psi(\mathbf{r}, \mathbf{R}) = \sum_{k=1}^{\infty} c_k \Psi_k^{el}(\mathbf{r}; \mathbf{R})\Psi_k^{nu}(\mathbf{R}) \tag{14}$$

Inserting this formulation into the TDSE (Equation 1), using a split of the total Hamilton Operator into $\hat{H}^{el}(\mathbf{r};\mathbf{R})$ and $\hat{T}_R(\mathbf{R})$, and projecting onto a single electronic state $\langle\Psi_a^{el}(\mathbf{r};\mathbf{R})|$ yields after some transformations:

$$\left(E_a^{el}(\mathbf{R}) + \hat{T}_R(\mathbf{R})\right)|\Psi_a^{nu}(\mathbf{R})\rangle + \sum_{k=1}^{\infty}\hat{T}_{ka}^{nac}(\mathbf{r},\mathbf{R})|\Psi_k^{nu}(\mathbf{R})\rangle = i\frac{\partial}{\partial t}|\Psi_a^{nu}(\mathbf{R})\rangle \tag{15}$$

where

$$\hat{T}_{ka}^{nac}(\mathbf{r},\mathbf{R}) = \sum_{K}^{N} -\frac{1}{2m_K}\left[\langle\Psi_k^{el}(\mathbf{r};\mathbf{R})|\nabla_K^2|\Psi_a^{el}(\mathbf{r};\mathbf{R})\rangle + \langle\Psi_k^{el}(\mathbf{r};\mathbf{R})|\nabla_K|\Psi_a^{el}(\mathbf{r};\mathbf{R})\rangle\nabla_K\right] \tag{16}$$

includes the correlation of the nuclear movement to the electronic wavefunctions via the two terms listed within the bracket in Equation 16, called *non-adiabatic couplings* (NACs). It is exactly these terms that are neglected in the BOA where the electronic states are treated to be completely independent of the nuclear movement. Therefore, the BOA is sufficiently applicable as long as the electronic states are not changing fast with changes of the nuclear arrangement; therefore, encountered states are termed *adiabatic* within the BOA. Setting $\hat{T}_{ka}^{nac}(\mathbf{r},\mathbf{R})$ to zero, Equation 15 simplifies to the TDSE for a single state, describing the nuclear evolution on a single electronic state:

$$\left(E_a^{el}(\mathbf{R}) + \hat{T}_R(\mathbf{R})\right)|\Psi_a^{nu}(\mathbf{R})\rangle = i\frac{\partial}{\partial t}|\Psi_a^{nu}(\mathbf{R})\rangle \tag{17}$$

However, in the manifold of electronic states, many situations arise, when this assumption does not hold, especially when electronic states come very close in energy and additional measures have to be considered to obtain a correct description at these points, going beyond the BOA. Methods capable of doing so and going beyond a simple adiabatic description are termed *non-adiabatic* and will be discussed in Section 2.3. Yet, since these methods rely on the availability of solutions for $E^{el}(\mathbf{R})$, the road for solutions to Equation 13 will be discussed in the upcoming section.

2.2 CALCULATING THE POTENTIAL ENERGY SURFACES

The previous section provided a separation of the TDSE via the BOA into two steps: the calculation of the electronic PESs for each state and a propagation of the nuclei on the so-calculated surfaces. Computation of $E^{el}(\mathbf{R})$ is still a quantum problem and the field of electronic structure methods reviewed in the upcoming section focuses on providing exactly these solutions following some approximations, limiting the applicability and respective accuracy. As these calculations would need to be repeated for every set of $\mathbf{R}$ to allow propagation on the PESs, a way of approximating these surfaces with only a handful of proper electronic structure calculations will be presented in Section 2.2.2.

2.2.1 *Electronic Structure Methods*

Tasked with solving the electronic Schrödinger equation, two terms need to be considered: $\hat{H}^{el}(\mathbf{r};\mathbf{R})$ and $\Psi^{el}(\mathbf{r};\mathbf{R})$. The former of these terms still contains the explicit electron-electron interaction in $\hat{V}_{rr}(\mathbf{r})$ found to be the root of evil for solving any of the Schrödinger equations. The latter demands a mathematical formulation for a many-particle wave function, including the indistinguishability of the electrons while retaining the antisymmetric nature of fermions. The Hartree-Fock[63] (HF) method uses a set of approximations to mold both terms into a more simplistic form, rendering the evaluation of the electronic Schrödinger equation possible. The first ingredient to HF consists in using a single Slater determinant[64] ($\Psi_{HF}(\mathbf{r})$) to approximate $\Psi^{el}(\mathbf{r};\mathbf{R})$, dropping the parametric dependence on **R** for brevity:

$$\Psi^{el}(\mathbf{r};\mathbf{R}) \approx \Psi_{HF}(\mathbf{r}) = \frac{1}{\sqrt{n!}} \begin{vmatrix} \phi_1(\mathbf{r}_1) & \phi_1(\mathbf{r}_2) & \cdots & \phi_1(\mathbf{r}_n) \\ \phi_2(\mathbf{r}_1) & \phi_2(\mathbf{r}_2) & \cdots & \phi_2(\mathbf{r}_n) \\ \vdots & \vdots & \ddots & \vdots \\ \phi_n(\mathbf{r}_1) & \phi_n(\mathbf{r}_2) & \cdots & \phi_n(\mathbf{r}_n) \end{vmatrix} \tag{18}$$

Here, $\mathbf{r}_k$ describes the spatial coordinates of the arbitrarily numbered electron number k while $\phi_k(\mathbf{r}_k)$ is the one-electron wave function for electron number k. Due to the use of a determinant, exchange of any two rows or columns reverses the overall sign of the wave function, hence adhering to the antisymmetric nature of the described system. The distribution of electrons into the different $\phi_k(\mathbf{r}_k)$ is known as an *electronic configuration*.

With this, the initial many-body problem is separated into finding the energetically most favored electronic configuration composed of single-electron wave functions. This can be achieved by using the variational principle, stating that any approximate wave function will always yield an equal or higher energy than the exact wave function. Hence, finding the energetically most favored single electron wave functions is a simple minimization problem. Within HF, this boils down to solving the following equation for each one-electron wave function:

$$\hat{f}_k(\mathbf{r}_k)|\phi(\mathbf{r}_k)\rangle = \epsilon_k|\phi(\mathbf{r}_k)\rangle \tag{19}$$

where $\hat{f}(\mathbf{r}_k)$ is the Fock-operator including $\hat{T}_r(\mathbf{r}_k)$, $\hat{V}_{rR}(\mathbf{r}_k)$, the interaction of electron k with all other electrons is taken into account in an average fashion, depending on all $\phi(\mathbf{r}_k)$. This interaction term results in an interdependence of all calculated single-electron wave functions, necessitating an iterative solution of Equation 19 for all electrons. As soon as the iterative solutions converge, a self-consistent solution is reached coining the name for such an approach: *self-consistent field* (SCF).

Each $\phi(\mathrm{r}_i)$ represents a *molecular orbital*, containing information of the distribution of the electron across the complete (molecular) system. Since no functional form for these molecular orbitals is known beforehand, each molecular orbital is commonly expressed as a linear combination of atomic orbitals $\chi_k(\mathbf{r})$, based on solutions obtained for the hydrogen atom for which the exact solutions can be obtained:

$$\phi(\mathrm{r}_i) = \sum_{k=1} c_{ik}(\mathbf{r}_i)\chi_k(\mathbf{r}_i) \tag{20}$$

Using this expression, the expansion coefficients $c_{ik}(\mathbf{r}_i)$ are then optimized via iteratively solving Equation 19. Due to the expansion of the n initial molecular orbitals into a larger set of atomic orbitals, more than n solutions will be found when solving the HF equations. Therefore, both occupied and unoccupied orbitals are calculated, a fact that will be important for methods that go beyond HF.

With this, the cornerstones of the HF method have been put into place, which represents the very foundation of most electronic structure methods. To understand where these other methods transcend their HF roots, the main shortcomings of the HF method will be recapped: First, the use of a limited expansion in atomic basis functions following Equation 20 limits the maximum accuracy that can be achieved. This use of limited *basis sets* will affect all used methods in a similar way, reducing the differences between methods to the upcoming points. Second, HF uses a single Slater determinant to approximate the complete electronic wave function although an infinite number of electronic configurations does exist. Truncating this manifold already to only the lowest energy term has been found to be a rather reasonable assumption for the ground state in a lot of molecules. Third, the replacement of the direct electron-electron interaction with the ensemble of interactions of a single electron with the average field of all the other electrons neglects the more explicit nature of electron-electron interaction. Fourth, the use of a single determinant allows only for the calculation of a single electronic state at a time and is therefore unsuited to provide the energies of multiple electronic states at a time. The first three of these shortcomings will result in an energy deviation between the total electronic energy calculated via HF and the exact electronic energy. In the following, the difference between any energy obtained via a variational method and the exact energy will be termed *correlation energy*.

A simple way to go beyond the HF method would simply be to not only keep one but also to include all electronic configurations in an approach termed *configuration interaction* (CI). The electronic wave function is then just written as

$$\Psi^{el}(\mathbf{r};\mathbf{R}) = c_{HF}\Psi_{HF}(\mathbf{r};\mathbf{R}) + \sum_{k}^{\#S} c_k \Psi_k^S(\mathbf{r};\mathbf{R}) + \sum_{k}^{\#D} c_k \Psi_k^D(\mathbf{r};\mathbf{R}) + \ldots \tag{21}$$

where the HF electronic configuration is taken as a basis for the construction of *excited* configurations where one, two or more electrons are promoted to formerly unoccupied orbitals, generating singly ($\Psi_k^S(\mathbf{r};\mathbf{R})$), doubly ($\Psi_k^D(\mathbf{r};\mathbf{R})$) or higher excited configurations. Here, $\#S$ is the number of all possible single excitations, promoting a single electron from an orbital a to an orbital k that has been formerly unoccupied, while $\#D$ is the number of all possible double excitations. Taking into account all possible configurations, each weighted by an expansion factor c_k that is optimized using the variational principle, a wave function description can be constructed going far beyond HF, called *full configuration interaction*. In the case of an infinitely large basis set, the electrons are distributed across all possible positions in space, remedying all the shortcomings of HF and yielding the exact wave function within the BOA. However, the number of possible electronic configurations increases extremely fast, rendering almost all calculations using this method computationally infeasible. A simple solution to this consists in truncating the expansion in Equation 21, including singly, doubly, etc. excited determinants, in methods termed CIS and CISD, respectively. These methods directly build upon the HF determinant and therefore more and more correlation energy is recovered the more terms are included in the expansion.

Complete active space self-consistent field

A different way of including more than a single Slater determinant is realized in the multi-configurational SCF method (MCSCF) where $\Psi^{el}(\mathbf{r};\mathbf{R})$ is expanded again in a basis of many electronic configurations:[65]

$$\Psi^{el}(\mathbf{r};\mathbf{R}) = \sum_{k} c_k \Psi_k^{SCF}(\mathbf{r};\mathbf{R}) \tag{22}$$

On a first glance, this approach seems almost identical with Equation 21 due to the fact that the real difference is hidden within $\Psi_k^{SCF}(\mathbf{r};\mathbf{R})$ which is not simply $\Psi_{HF}(\mathbf{r};\mathbf{R})$ with some orbital occupations being adjusted. Instead of using the HF orbitals as a basis, the respective orbitals shared in all Slater determinants are variationally optimized at the same time as the respective expansion coefficients c_k. While adjusting both sets of coefficients at the same time seems to be a good idea by providing more parameters to tune, it also does complicate Equation 21 greatly only to yield identical results in the limit of infinite basis functions. However, the beauty of this approach reemerges in realizing that the gained flexibility of the orbitals allows to obtain more accurate results for a limited number of electronic configurations than with original CI methods. A good use of the MCSCF methodology therefore benefits from a smart selection of which determinants to consider.

The most widespread use of a selection scheme for exactly this purpose is the *complete active space* SCF (CASSCF) method.[66] Here, the orbital space is divided into three parts: an inactive part of doubly occupied orbitals, the eponymous active space consisting of both occupied and unoccupied orbitals, and a final virtual part made up of always unoccupied orbitals. In CASSCF all possible determinants formed by exchanging positions of electrons within the active space are then considered in the sum of Equation 22. With this, an exact solution within the active orbital subspace is obtained, yielding results where the accuracy depends on the capability of this subspace to represent the most important interactions that are of interest. The selection of this subspace is therefore crucial in CASSCF, a fact complicated by the notion of "chemical intuition" that is often invoked when it comes to this task, leaving the user with not much more than some occult and mysterious advice. Automated selection tools for the active space orbitals have gained prominence throughout the last years[67] lending the user a hand in these matters.

The calculation of more than a single electronic state can easily be accomplished with CASSCF in a state-specific approach, yielding a different orbital basis for each electronic state. This complicates the calculation of properties between two states, which is the reason why in such cases a state-average approach (SA) is commonly chosen, where a shared set of orbitals is optimized for all states to yield the lowest average energy.

The downside of CASSCF is that the employed active spaces are commonly too small to obtain quantitative results, which is the reason why additional calculations can be employed on top of CASSCF calculations to retain some of the missing correlation energy. The two most prominent of those methods are the complete active space perturbation theory of second order (CASPT2) and multi-reference CI (MRCI). Both of these methods rely on expanding the accuracy of the underlying CASSCF calculation by including additional terms arising from the interaction of the inactive, active, and virtual subspaces with each other. In CASPT2, the interaction of all possible double excitations for all determinants between different subspaces is taken into account. In MRCI however, the CI formalism presented in Equation 21 is applied to all determinants created from CASSCF, yielding a huge number of new determinants which is the reason for truncating this expansion at either the only singles excitations or the singles and double excitation levels, yielding the MRCIS and MRCISD formalisms.

Density Functional Theory

A different route for solving the electronic Schrödinger equation has been formulated within the framework of density functional theory (DFT).[68,69] Here, the wave function as a driving factor for all equations is replaced by the easier graspable electron density ($\rho(\mathbf{r})$) which can be written as

$$\rho(\mathbf{r}) = n \int \mathrm{d}\mathbf{r}_2 \ldots \mathrm{d}\mathbf{r}_n |\Psi(\mathbf{r}, \mathbf{r}_2, \ldots \mathbf{r}_n)|^2 \tag{23}$$

reducing the manifold of explicit electron coordinates into three-dimensional space. Since the wave function is the integral element of $\rho(\mathbf{r})$, it is possible to calculate the energy not as a function of $\rho(\mathbf{r})$ but as a functional thereof, yielding:

$$E[\rho(\mathbf{r})] = T_r[\rho(\mathbf{r})] + V_{rr}[\rho(\mathbf{r})] + V_{rR}[\rho(\mathbf{r})] \tag{24}$$

with $T_r[\rho(\mathbf{r})]$ containing the kinetic energy of the electrons, $V_{rr}[\rho(\mathbf{r})]$ taking the electron-electron interaction into account, and $V_r R[\rho(\mathbf{r})]$ including the electron nucleus interactions.

Standard DFT has been shown to adhere to the variational principle and to uniquely link a density to the ground state Hamiltonian, meaning that no two ground state densities give rise to the same Hamiltonian.[69] To actually solve Equation 24 and derive functional forms for the terms therein, the Kohn-Sham (KS) formalism is employed.[70] Within the KS formalism, the real system of interacting electrons is replaced by a fictitious system of non-interacting electrons that still form the same density as the real system. This KS density is then constructed as a sum of contributions of one-electron KS orbitals $\phi^{KS}(\mathbf{r})$

$$\rho(\mathbf{r}) = \sum_k |\phi_k^{KS}(\mathbf{r})\rangle \, \langle \phi_k^{KS}(\mathbf{r})| \tag{25}$$

The needed Kohn-Sham orbitals fulfill a simple eigenvalue relation reminiscent of the HF equations (Equation 19):

$$\hat{h}_k^{KS} |\phi_k^{KS}(\mathbf{r})\rangle = \epsilon_k^{KS} |\phi_k^{KS}(\mathbf{r})\rangle \tag{26}$$

with the single electron operator $\hat{h}_k^{KS}$ being defined as

$$\hat{h}_k^{KS} = -\frac{1}{2}\nabla_k^2 - \sum_K^N \frac{Z_K}{|\mathbf{r}_k - \mathbf{R}_K|} + \int \frac{\rho(\mathbf{r}')}{|\mathbf{r}_k - \mathbf{r}'|} \mathrm{d}\mathbf{r}' + \frac{\partial E_{XC}^{KS}[\rho(\mathbf{r})]}{\partial \rho(\mathbf{r})} \tag{27}$$

where the first two terms are identical to contributions already known from Equation 8 while the third term describes a classical coulomb term where $\mathbf{r}'$ indicates the space of electronic coordinates. The final term is the derivative of the exchange-correlation energy $E_{XC}^{KS}[\rho(\mathbf{r})]$ which includes all terms arising from the initial neglect of the interacting nature of electrons. The exact form of $E_{XC}^{KS}[\rho(\mathbf{r})]$ is unknown and is approximated using one of many available exchange-correlation functionals – often the "exchange-correlation" is omitted and the term is shortened to just $functionals$ – that are often fitted for specific classes of molecular systems.

DFT has been extended to describe not only the electronic ground state but also excited states using a formalism known as time-dependent DFT (TDDFT).[71] Similar to DFT, TDDFT is built on two theorems – the Runge-Gross theorems[72] – that are strikingly similar to the Hohenberg-Kohn theorems with the difference of the use of time-dependent densities. First, a one-to-one relation between the time-dependent density $\rho(\mathbf{r}, t)$ and an time-dependent wave function derived from this density is established. Second, the time-dependent density is shown to be obtainable via minimization of the action integral $A[\rho(\mathbf{r}, t)]$ that includes the Dirac-Frenckel variational principle:

$$A[\rho(\mathbf{r}, t)] = \int_{t_0}^{t_1} \mathrm{d}t \left\langle \Psi[\rho(\mathbf{r}, t)] \middle| i\frac{\partial}{\partial t} - \hat{H}(\mathbf{r}, t) \middle| \Psi[\rho(\mathbf{r}, t)] \right\rangle \tag{28}$$

where the first Runge-Gross theorem is used to describe the time-dependent wave function as a functional of the time-dependent electron density and t_0 or t_1 are just two different values of time. Equation 28 can be used to obtain $\rho(\mathbf{r}, t)$ by determining the stationary states.

To solve these equations, a now time-dependent KS framework is used to obtain $\rho(\mathbf{r}, t)$, reducing the problem again to a set of single particle equations satisfying the respective TDSE:

$$\left(-\frac{1}{2}\nabla_k^2 - \sum_K^N \frac{Z_K}{|\mathbf{r}_k - \mathbf{R}_K|} + \int \frac{\rho(\mathbf{r}', t)}{|\mathbf{r}_k - \mathbf{r}'|}\mathrm{d}\mathbf{r}' + \frac{\partial E_{XC}^{KS}[\rho(\mathbf{r}, t)]}{\partial \rho(\mathbf{r}, t)} \right) |\phi_k^{KS}(\mathbf{r}, t)\rangle = i\frac{\partial}{\partial t}|\phi_k^{KS}(\mathbf{r}, t)\rangle \tag{29}$$

with the use of single-electron time-dependent KS orbitals $\phi_k^{KS}(\mathbf{r}, t)$. The terms for the kinetic energy and the interaction with the nuclei can already be found in Equation 27, however, for the last two terms an explicit time-dependence is encountered. For the Coulomb-repulsion, it is sufficient to only consider the instantaneous density while the time-dependent exchange-correlation term has been found to depend on preceding time steps, therefore exhibiting a memory-effect of previously visited densities. Nevertheless, the correlation with earlier densities is commonly neglected with the use of the so-called *adiabatic approximation*, enabling the use of DFT exchange-correlation functionals in TDDFT.

Two roads to solve the time-dependent KS equations are commonly explored: real-time propagation[73] and linear response[74,75] with the latter being the method that is used throughout this thesis. Here, information about excited states is obtained by evaluating the response of the system to a weak perturbation, truncating any expansion of the response after the linear term. After some lengthy algebra one ends up with a simple matrix formulation for the calculation of excited states in the linear response TDDFT framework:

$$\begin{bmatrix} \mathbf{A} & \mathbf{B} \\ -\mathbf{B}^* & -\mathbf{A}^* \end{bmatrix} \begin{bmatrix} \mathbf{X} \\ \mathbf{Y} \end{bmatrix} = \omega_k \begin{bmatrix} \mathbf{X} \\ \mathbf{Y} \end{bmatrix} \tag{30}$$

Here, ω_k amounts to the energy difference between the lowest energy state and state k and the respective matrix elements are defined as

$$\begin{aligned} A_{ia,kb} &= \delta_{ik}\delta_{ab}(\epsilon_a - \epsilon_i) + \langle ik|\hat{f}_{xc}^{KS}|ab\rangle \\ B_{ia,kb} &= \langle ib|\hat{f}_{xc}^{KS}|ak\rangle \end{aligned} \tag{31}$$

whith

$$\langle ik|\hat{f}_{xc}^{KS}|ab\rangle = \left\langle \phi_i^{KS}(\mathbf{r})\phi_k^{KS}(\mathbf{r}') \middle| \frac{1}{|\mathbf{r} - \mathbf{r}'|} + \frac{\partial^2 E_{XC}^{KS}[\rho(\mathbf{r}, t)]}{\partial \rho(\mathbf{r})\partial \rho(\mathbf{r}')} \middle| \phi_a^{KS}(\mathbf{r})\phi_b^{KS}(\mathbf{r}') \right\rangle \tag{32}$$

Here, a and b represent unoccupied orbitals while i and k are occupied in the reference configuration. It follows that $\mathbf{A}$ includes particle-hole excitations and $\mathbf{B}$ hole-particle excitations that are correlated via $\mathbf{X}$ and $\mathbf{Y}$. Within the Tamm-Dancoff approximation[76] the hole-particle excitations are disregarded, reducing Equation 30 to

$$\mathbf{AX} = \omega_k \mathbf{X} \tag{33}$$

TDDFT is found to be the most competitive method to approximately solve the electronic Schrödinger equation in the manifold of states.

2.2.2 *(Linear) Vibronic Coupling*

A completely different approach to provide the needed PESs consists in not computing the complete PES with a given electronic structure method but instead to approximate the PES in the region of interest based on few or a single evaluation of the electronic Schrödinger equation. One method envisioned to do exactly this is the vibronic coupling model.[18,19] These vibronic coupling models aim at providing a qualitative description of the PESs of multiple electronic states around a reference point $\mathbf{R}_0$ in a *diabatic* basis where the coupling between states is projected onto the off-diagonal potential energy terms, yielding a diabatic Hamiltonian $\hat{H}_{diab}(\mathbf{R}_0)$. Often $\mathbf{R}_0$ is chosen to be the minimum energy arrangement of nuclei but can be any point in coordinate space. This is achieved via a Taylor-expansion around $\mathbf{R}_0$ yielding the following series

$$\hat{H}_{diab}(\mathbf{R}_0) = (V_0 + \hat{T}_R(\mathbf{R}))\mathbf{1} + \mathbf{W}^{(0)}(\mathbf{R}_0) + \mathbf{W}^{(1)}(\mathbf{R}_0) + \mathbf{W}^{(2)}(\mathbf{R}_0) + \ldots \tag{34}$$

where $\mathbf{W}^{(y)}$ is the yth term in the respective Taylor expansion. The ground state potential V_0 can be approximated as a combination of harmonic oscillators in the basis of the $3N-5$ or $3N-6$ vibrational normal modes (Q_{max}) of the system

$$V_0 = \sum_{l}^{Q_{max}} \frac{\omega_l}{2} Q_l^2 \tag{35}$$

The normal mode displacement (Q_k) in mass-weighted and frequency-scaled coordinates describes a potential energy term encountered when moving away from $\mathbf{R}_0$.

It is important to note that within Equation 34 the shape of all excited state PESs is assumed to resemble V_0 as a very first approximation. The zeroth order expansion term $\mathbf{W}^{(0)}$ contains no dependence on the chosen coordinate basis but instead contains only the excitation energies at the reference point and other static couplings like spin-orbit couplings (SOCs, see the upcoming Section) η and can be written as:

$$\mathbf{W}^{(0)}_{mk}(\mathbf{R}_0) = E^{el}_m(\mathbf{R}_0)\delta_{mk} + \eta_{mk}(\mathbf{R}_0) \tag{36}$$

where m and k denote diabatic states. With $\mathbf{W}^{(1)}$ explicit coordinate dependence along Q_k is introduced giving rise to intra- and interstate couplings (κ and λ respectively) capable of describing the change of the PES along this coordinate as well as the interaction with other states:

$$\mathbf{W}^{(1)}_{mk}(\mathbf{R}_0) = \left(\sum_{l}^{Q_{max}} \kappa_l^{(m)}(\mathbf{R}_0)\delta_{mk} Q_l\right) + \left(\sum_{l}^{Q_{max}} \lambda_l^{(mk)}(\mathbf{R}_0)(1-\delta_{mk}) Q_l\right) \tag{37}$$

Truncating the expansion in Equation 34 after this term results in the linear vibronic coupling model (LVC), that can be used to describe the excited PESs close to $\mathbf{R}_0$ and includes the most important coupling terms needed for dynamics in this region. Going beyond $\mathbf{W}^{(1)}(\mathbf{R}_0)$ introduces cross-coupling elements between different normal modes, increasing the flexibility of the Hamiltonian. Throughout the present work, the LVC model will be used and any higher order terms are discarded.

Owing to the extensive use of the LVC model throughout the remainder of this thesis, a few of the limitations and caveats of the LVC model are listed.[77]
(i) The use of a harmonic normal mode basis breaks down in many cases including e.g. anharmonic PESs, dissociation, or rotations around molecular bonds that are wrongly described using a single linear normal mode displacement. To remedy this issue, different potential have been employed in the literature and even combined to fit the need of respective modes.[78,79]
(ii) Using the ground state normal modes to describe the excited state movement will be sub-optimal in many cases. The terms included in $\mathbf{W}^{(2)}(\mathbf{R}_0)$ would be needed to include state-specific changes to the otherwise rigid ground state normal mode basis.
(iii) Moving away from $\mathbf{R}_0$, a gradually worsening accuracy for the PESs is observed, limiting investigations to the region around the initial reference point.

2.2.3 *Spin-Orbit Couplings*

Up to here, the non-relativistic time-dependent Schrödinger equation has formed the basis for all presented methods and the computation of electronic states. Within the employed derivation, the electronic spin ($s = \pm\frac{1}{2}$) – an additional quantum number that does not describe any spatial position – of each considered particle was never explicitly stated nor included in the used equations. Indeed the dependence of the wave function on the spin is added here as an *ad hoc* correction, giving an explicit spin-dependence to the electronic wave function $\Psi^{el}(\mathbf{r}, s; \mathbf{R})$. Since the spin is not acted upon by $\hat{H}^{el}(\mathbf{r}; \mathbf{R})$, the spin-dependent part ($\Theta(s)$) can be separated to form a product of the already known $\Psi^{el}(\mathbf{r}; \mathbf{R})$ and $\Theta(s)$. With this, solutions for the electronic Schrödinger equation can be pursued as before with the limitation that the obtained $\Psi^{el}(\mathbf{r}, s; \mathbf{R})$ are eigenfunctions of both $\hat{H}^{el}(\mathbf{r}; \mathbf{R})$ and the spin-operators $\hat{s}_z(s)$ and $\hat{s}^2(s)$. Since the spin functions $\Theta(s)$ are orthonormal, any properties calculated between states of different overall spin are zero, effectively uncoupling those states making any transitions between those states impossible. In many real-life occasions, this imposed prohibition on multiplicity changes has been found to be violated, indicating that important aspects in this non-relativistic description have been neglected.[80]

When considering the *Dirac* equation[81] – a relativistic equation to describe particles – the spin appears naturally together with terms describing the interaction of different spins, giving rise to terms known as spin-orbit couplings (SOCs).[82] The interaction terms arising from this can be collected into a new coupling term $\hat{H}^{el}_{SOC}$ adding the respective SOCs as a perturbative correction to $\hat{H}^{el}(\mathbf{r}; \mathbf{R})$. One of the most common general forms of $\hat{H}^{el}_{SOC}$ is the Breit-Pauli Hamiltonian:

$$\hat{H}^{el}_{SOC} = \frac{1}{2C}\left[\sum_{K=1}^{N}\sum_{k=1}^{n}\frac{Z_K}{|\mathbf{r}_k - \mathbf{R}_K|^3}(\hat{r}_{kK} \times \hat{p}_k)\hat{s}_k - \sum_{k=1}^{n}\sum_{l\neq K}^{n}\frac{1}{|\mathbf{r}_k - \mathbf{r}_l|^3}(\hat{r}_{kl} \times \hat{p}_k)(\hat{s}_k + 2\hat{s}_l)\right] \tag{38}$$

Here, C is the speed of light, $\hat{r}_{kX} \times \hat{p}_k$ is the angular momentum of electron k with respect to particle X. The fundamental source of the SOCs therefore is the coupling of the angular momentum of the fast moving electrons with the electric field induced by orbiting around the nucleus. The first sum in Equation 38 includes the self interaction terms for each electron while the second sum includes the interaction due to the orbiting of all the other electrons, effectively shielding the nucleus. Applying $\hat{H}^{el}_{SOC}$ to the electronic wave functions obtained from $\hat{H}^{el}(\mathbf{r};\mathbf{R})$ yields off-diagonal elements in the matrix of electronic energies, effectively coupling states of different multiplicities. These couplings have been thought to be negligible for organic molecules and only to take considerable size for heavy elements due to the scaling with Z_k. However, throughout the last decade, considerable influence of SOCs on the excited state dynamics has been reported even for small molecules.[83,84]

In practice, Equation 38 is often simplified for heavy elements by including the shielding of the nucleus in a mean-field fashion, similar to the two-electron terms in HF.[85] Additionally, the explicit contributions can be collapsed into an effective charge (Z^{eff}_K) of the nucleus, reducing the computational load for obtaining the SOCs. This also allows the use of effective core potentials to describe the inner electronic shells of those molecules without interfering with the calculation of the respective SOCs.

2.3 NON-ADIABATIC DYNAMICS

The previous Section presented multiple pathways to approximately calculate $E^{el}(\mathbf{R})$ for many different states, on which the nuclear wave function can evolve on. With the PESs being known, Equation 17 can be solved via integration for an initial and a final time. In order to do this, a mathematical description of $\Psi^{nu}_a(\mathbf{R})$ is needed, realized in the so-called *standard* method of quantum dynamics by expanding it onto a basis of grid points (g) weighted by a time-dependent coefficient $c_k(\mathbf{R},t)$:

$$\Psi^{nu}_a(\mathbf{R}) = \sum_l^{Q_{max}} \sum_k^{g_{max}} c_{lk}(\mathbf{R},t) g_{lk} \tag{39}$$

For an accurate description of the nuclear time evolution via the coefficients, a sufficiently dense grid needs to be present, resulting in an total of $g^{Q_{max}}_{max}$ grid points for an evenly spaced grid. The unfavorable scaling of this space-spanning grid-based approach is termed the curse of dimensionality, rendering all but the smallest systems to computational nightmares.[86] Nevertheless, the standard method still sees some use either for benchmarking more approximate methods or to investigate systems in a reduced dimensionality, when nuclear quantum effects like tunneling and nuclear interference are of utmost importance. Different methods for reducing the dimensionality can be found employing either careful hand-[87] or automated selections[88–90] of the modes of movement driving the investigated process.

Since a complete quantum description of the nuclear dynamics in full dimensionality remains out of reach for most applications, different ways to reduce the number of needed grid points have been envisioned. One way to do so consists in removing the rigidness of the static grid, substituting it with a moving grid, that follows the evolution of the wave packet, providing enough grid points exactly where it is needed. This can be put to the extreme by using a set of classical trajectories evolving on the manifold of states, each independently trying to track the movement of the real quantum wave packet. The former method is realized in the multi-configurational time-dependent Hartree approach (MCTDH)[9] while the latter is termed fewest-switches surface hopping (SH)[22] both of which will be presented in the following.

2.3.1 *Multi-Configurational Time-Dependent Hartree*

In MCTDH the static grid of basis function is replaced by a time-dependent set of nuclear configurations $\Phi(\mathbf{R}, t)$ that consist of so-called single particle functions $\gamma(\mathbf{R}, t)$ (SPFs), yielding again a complete basis in the limit of infinite basis functions. Using a total of f degrees of freedom $\mathbf{x}_f$ (DOF) to describe the nuclear coordinates instead of $\mathbf{R}$, the wave function *ansatz* in MCTDH can be denoted as[91]

$$
\begin{aligned}
\Psi^{nu}(\mathbf{R}, t) &= \sum_K A_K(t)\Phi_K(\mathbf{x}_1, \dots, \mathbf{x}_f, t) && (40)\\
&= \sum_{k_1=1}^{o_1} \cdots \sum_{k_f=1}^{n_f} A_{k_1,\dots,k_{o_f}}(t) \prod_{l=1}^{f} \gamma_{k_l}^{(l)}(\mathbf{x}_l, t) && (41)
\end{aligned}
$$

where A_K is a complex coefficient for the configurations that themselves are Hartree products of SPFs. The number of basis functions for each considered degree of freedom enters via o_k. Each degree of freedom can either consist of a single or many vibrational modes at once in a process termed *mode combination* that allows pairing of similar behaving modes of movement into a single coordinate, lowering the computational burden.

Since the SPFs are not uniquely defined, a set of SPFs is chosen to be orthonormal so that

$$
\langle \gamma_k^{(l)} | \gamma_m^{(l)} \rangle = \delta_{km} \tag{42}
$$

to simplify all upcoming calculations. With a mathematical description of the grid at hand, the time-evolution of both the coefficients and the SPF basis can be derived using the Dirac-Frenckel variational principle (dropping explicit dependencies for brevity) to obtain the best possible variation of the wave function ($\delta\Psi$) still adhering to the variational principle

$$
\left\langle \delta\Psi \middle| i\frac{\partial}{\partial t} - \hat{H} \middle| \Psi \right\rangle \tag{43}
$$

where

$$
\delta\Psi = \sum_K \delta A_K \Phi_K + \sum_l \left(\sum_{m_l} \delta\gamma_{m_l}^{l} \kappa_{m_l}^{(l)} \right) \tag{44}
$$

with $\kappa_{m_l}^{(l)}$ being a single hole function. Now, variations of both the coefficients and the SPFs can be inserted in Equation 43, yielding the following equations of motions:

$$
\begin{aligned}
i\frac{\partial A_L}{\partial t} &= \sum_K \langle \Phi_L | \hat{H} | \Phi_K \rangle A_K && (45)\\
i\frac{\partial \boldsymbol{\gamma}^{(l)}}{\partial t} &= (\mathbf{1} - \hat{P}^{(l)})(\boldsymbol{\rho}^{(l)})^{-1} \hat{\boldsymbol{H}} \boldsymbol{\gamma}^{(l)} && (46)
\end{aligned}
$$

Hence, the coefficients are propagated depending on the Hamiltonian spanned by the nuclear configurations. The SPFs have been collected in a vector of SPFs $\boldsymbol{\gamma}^{(l)}$

for the respective propagation, with $\hat{P}^{(l)}$ being a projection operator to ensure the orthonormality constraint during the propagation. $\boldsymbol{\rho}^{(l)}$ contains the overlaps between single-hole functions as those are not orthonormal.

For integration of these equations of motion, the SPFs are expanded into a time-independent basis set using a discrete variable representation.[8] The Hamilton operator employed in MCTDH calculations is in most cases diabatic and requires precomputed PESs. If the used Hamiltonian can be decomposed into a sum of products form, efficient integration MCTDH has been shown to include up to 50 DOFs going far beyond the up to 5-6 DOFs possible in the standard method.[91] Inclusion of electronically excited states is straightforward via a separate degree of freedom where the respective SPFs can either be shared between or being optimized for each electronic state separately. The first case is termed single-set formalism that is suited if the nuclei move very similar on all populated electronic states. The second case is the multi-set formalism that in general results in faster converging results.

MCTDH has been been extended to use a basis of time-dependent Gaussian-functions,[14] inspiring the implementation of the variational multi-configurational Gaussian (vMCG)[15] method and its variation called direct-dynamics vMCG (DD-vMCG).[20] DD-vMCG features the capability to go beyond precomputed PES, relying only on a set of electronic structure properties that can be computed in every time step. The strength of MCTDH and all its derived methods is definitely found in the computational gain with respect to the standard wave packet dynamics method and the guarantee to converge to the real results given a sizeable enough basis, making those methods a widely used standard for investigations on the molecular level.

2.3.2 *Surface Hopping Dynamics*

MCTDH and its whole offspring of methods can be thought of as a well-mannered branch of the family tree emerging from the standard wave packet dynamics method, all retaining the basic principles and ideas with different sets of approximations that can always be traced back to the exact result. In this picture, SH is being conceived from *ad hoc* approximations and is therefore found far from the original roots of quantum dynamics. At the basis of SH lies a mixed quantum-classical description where the nuclei are propagated according to classical laws of motion, moving on a single PES at a time while the electronic dynamics is treated at a quantum level determining on which state the trajectory is evolving.[22,92,93] In doing so, the nuclear wave packet is collapsed to a single point in phase space that moves classically, alleviating the need to have a tedious quantum propagation of nuclei. Therefore, simulations using many more degrees of freedom are made viable. To retain some of the quantum features, like the splitting of the wave packet, a swarm of trajectories is employed, where each trajectory moves independently. In this section, the framework of SH is presented first, followed by shortcomings of the basic algorithms and methods to correct those.

SH Methodology

The classical nature of the nuclear movement in SH replaces the explicit quantum nuclear propagation by simple movement governed by Newton's second law:

$$\frac{\partial^2}{\partial t^2}\mathbf{R}_K(t) = -\frac{1}{M_K}\frac{\partial E_a^{el}(\mathbf{R})}{\partial \mathbf{R}_K(t)} \tag{47}$$

Here the nuclear wave function is replaced with the explicit coordinates of the ensemble of atoms, that are time-dependent with the movement of each atom depending on its mass and the gradient of the potential energy surface of the state the trajectory evolves on (a).[94] The most prominent way to actually propagate each trajectory is the velocity-Verlet algorithm[95,96] where both the positions and velocities are updated in each time step.

Up to here, the nuclear movement is dictated by the PES of the *active state*, raising the question how the active state can be changed throughout the dynamics to account for multiple PESs. The answer lies in the electronic wave function that is propagated simultaneously to the nuclei in each time step using an expansion into a set of electronic states that here are taken to be eigenfunctions of the electronic Hamiltonian weighted by a set of time-dependent coefficients ($c_k(t)$):

$$\Psi^{el}(\mathbf{r}, t; \mathbf{R}) = \sum_{k=1} c_k(t) \Psi_k^{el}(\mathbf{r}; \mathbf{R}) \tag{48}$$

The propagation of $c_k(t)$ can be obtained by inserting this expansion of the time-dependent electronic wave function in the time-dependent electronic Schrödinger equation after projecting onto a specific electronic state Ψ_m^{el} from the left

$$\frac{\partial c_m(t)}{\partial t} = -\sum_k \left[i \langle \Psi_m^{el} | \hat{H}^{tot}(\mathbf{r}, t; \mathbf{R}) | \Psi_k^{el} \rangle + \mathbf{v}\mathbf{h}_{mk} \right] c_k(t) \tag{49}$$

where the first term in the sum contains matrix elements of a total Hamiltonian ($\hat{H}^{tot}(\mathbf{r}, t; \mathbf{R})$) that can be written as

$$\hat{H}^{tot}(\mathbf{r}, t; \mathbf{R}) = \hat{H}^{el}(\mathbf{r}; \mathbf{R}) - \hat{\mu}^{el}(\mathbf{r}; \mathbf{R})\varepsilon(t) + \hat{H}_{SOC}^{el}(\mathbf{r}; \mathbf{R}) \tag{50}$$

Hence, this total Hamiltonian includes the electronic energies, the interaction of external laser pulses with those states, and the respective SOCs. The respective matrix with matrix elements H_{mk}^{tot} is diagonal in the basis of electronic eigenstates if no laser field and SOCs are present. The second term on the right-hand side in Equation 49 includes the nuclear velocities $\mathbf{v}$ and the NACs from now on defined as $\mathbf{h}_{mk} = \langle \Psi_m^{el} | \frac{\partial}{\partial \mathbf{R}} | \Psi_k^{el} \rangle$. With all these terms at hand, the electronic coefficients can be propagated and will be distributed across different states depending on the encountered couplings along the path of the trajectory. This distribution of the coefficients of the electronic wave function directly mimics how the nuclear wave packet should be distributed across the manifold of states, providing a target quantity to be exploited to determine the active state of each trajectory: The distribution of active states across the swarm of trajectories should match the distribution of the electronic coefficients. As each trajectory is independent of all the others, the selection of which state to follow is conducted stochastically via a hopping probability that is calculated in each time step. The probability to switch the active state $p_{a\rightarrow}$ is given as follows

$$p_{a\rightarrow} = -\frac{2\Delta t}{|c_a(t)|^2} \Re \left(c_a^*(t) \sum_b \left[i H_{ab}^{tot} + \mathbf{v}\mathbf{k}_{ab} \right] c_b(t) \right) \tag{51}$$

with the newly populated state being determine via a random number using as a probability for each state the contribution of the respective state to the sum in Equation 51. To reduce the number of hops to a minimum – hence, fewest-switches – the active state is only changed if the population ($|c_a(t)|^2$) of the active state decreased in the current time step. After a new active state has been determined, the classical trajectory instantaneously switches to this new state and continues the nuclear propagation from this new surface, conducting no changes to the electronic coefficients. These hops between surfaces coined the name for SH, which has risen to be one of the most widely used methods for simulating non-adiabatic processes.[23,97] Its success is owed to the low computational cost for the nuclear propagation while still providing qualitative results in most cases, allowing fast propagation of even thousands of atoms, almost completely eliminating the computational workload from the propagation itself, leaving only the computation of the needed PESs as the time-determining step. An additional benefit for SH can be found for the needed PESs: Since each trajectory only needs electronic structure properties like energies, gradients and couplings at the local position, it is possible to conduct SH on-the-fly without the need for precomputed potentials and to instead calculate the needed properties on each current position. However, all the benefits of SH come at a cost since SH is forever afflicted by the curse of *ad hoc* approximations that heralded its birth. As it is hard to establish a link between SH and the standard wave packet dynamics method, it is often not clear how justified the various *ad hoc* approximations are in SH. Nevertheless, recently the connection to the quantum-classical Liouville equation has been established[24,25] and the use of the exact factorization method offers a promising avenue to investigate the very nature of SH in more detail.[26] Some of the drawbacks and insufficiencies of SH will be discussed in the upcoming section together with different approaches to tackle the encountered issues, often introducing more *ad hoc* corrections. In addition to the upcoming issues, SH is unable to describe tunneling and contain zero-point energy, resulting in zero-point energy leakage[98] if this energy was initially sampled.

Velocity Adjustment

One of the first critical points that has already be tackled in the original formulations of the fewest-switches surface hopping methodology is the issue of total energy conservation.[22] Since an isolated system should retain its total energy throughout its dynamical evolution, the same should be the case for the ensemble of trajectories in SH. As each trajectory is independent of each other, the most straightforward way to ensure that criterion consists of enforcing energy conservation for each individual trajectory. Therefore, the instantaneous change in potential energy due to the switch of the active state has to be counteracted immediately by the respective trajectory, necessitating a change in the overall kinetic energy (E_{kin}). According to the original formulation of SH, the NAC vector between the two participating states plays a crucial role in this process, as adjusting the velocities along this vector has been found to resemble Pechukas force – a force encountered by classical nuclei while passing a crossing region between electronic states.[27,99] From this, it follows that hops to lower energy surfaces are accompanied by an increase in E_{kin} along the NAC vector and *vice versa*. In the reverse case, where E_{kin} is decreased, a situation might be encountered where adjusting E_{kin} would reduce it below zero. Therefore, the amount of available E_{kin} along the NAC vector has to be evaluated first:[27]

$$\Delta = 4\alpha(E_b - E_a) + \beta^2 \tag{52}$$

with

$$\alpha = \sum_{K}^{N} \frac{\mathbf{h}_{ab,K} \cdot \mathbf{h}_{ab,K}}{2m_K} \tag{53}$$

$$\beta = \sum_{K}^{N} \mathbf{v}_K \cdot \mathbf{h}_{ab,K} \tag{54}$$

If Δ is negative, then not enough energy is present along the NAC vector and the attempted hop is rejected and the dynamics continues on the old active state in a process termed $frustrated\ hop$ that has been found to be important to retain detailed balance.[100,101] It is also possible to inverse the velocities along the NAC vector in case such a frustrated hop is encountered[28,102] although it is not clear that this is always a beneficial route to take.[103] A way to introduce some more "quantumness" into the treatment of frustrated hops is the use of uncertainty for the hopping event, allowing each trajectory to jump not only at the time where a stochastic hop was encountered but a small time window around this event, smearing both the time and the needed energy gap according to the uncertainty principle.[104,105]

Once a jump is accepted (Δ in Equation 52 is positive or zero), the velocities are adapted to obtain the new velocities $\mathbf{v}'$:

$$\mathbf{v}'_K = \mathbf{v}_K - f\frac{\mathbf{h}_{ab,K}}{m_K} \tag{55}$$

with

$$f = \begin{cases} \frac{\beta+\sqrt{\Delta}}{2\alpha} & \text{if } \beta < 0 \\ \frac{\beta-\sqrt{\Delta}}{2\alpha} & \text{if } \beta \geq 0 \end{cases} \tag{56}$$

Although the use of the NAC vectors is theoretically well justified, these vectors are not available for all electronic structure methods and come at a considerable computational cost. Therefore, simulations often use propagation methods that do not rely on the calculation of explicit NAC vectors,[106] making those unavailable for the velocity adjustment. Then other vectors can be chosen to rescale the velocities along like the full velocity vector or the gradient difference vector ($\mathbf{g}_{ab}$)

$$\mathbf{g}_{ab} = \frac{\partial E_a^{el}}{\partial \mathbf{R}} - \frac{\partial E_b^{el}}{\partial \mathbf{R}} \tag{57}$$

Both of these vectors are simpler to calculate, coming at a lower cost but are found lacking in theoretical support. When using the full velocity vector, the amount of E_{kin} present will render almost all hops possible, especially for large systems. An alternate option would be to not adjust the E_{kin} at all during a hop, violating total energy conservation.

A special case for the velocity adjustment is the presence of external fields, as the total energy of the molecular system does not need to remain constant because energy can be absorbed or emitted as photons. Then a differentiation between field-induced hops and "standard" hops should be conducted, retaining the E_{kin} in the former case and rescaling it in the latter. The differentiation can be achieved by deducing the contribution of the field to the increase of population in the to-be-hopped-in state.[49] A simpler way consists in assigning each hop to be field-induced if the energy difference between the two participating states falls within a specified energy range around the central frequency, therefore assuming that all hops close to resonance frequency are field-induced.[57]

Overcoherence

The framework of SH allows for the description of transitions between electronic states, therefore bridging the chasm between electronic and nuclear movement introduced by the BOA. Indeed, SH has been shown to be capable of describing the passage through a single conical intersection – the form of the PES[107] where two or more surfaces are degenerate within the BOA and where the NACs are non-negligible – quite well:[22,32] The swarm of classical trajectories will branch close to the conical intersection, using the strength of the coupling via the electronic coefficients for a stochastic selection of states to propagate the nuclei in. However, the chimeric nature of SH is found to be at fault once the initial coupling region is surpassed: In a complete quantum description, the different parts of the wave packet will move apart from each other after branching, dephasing from one another. A similar picture is observed for the classical trajectories, that now move on different surfaces and will visit different parts of the phase space. The electronic coefficients inscribed to each trajectory, however, are distributed across many states, initially allowing for a correct stochastic selection at the branching region. After leaving the coupling region, these coefficients still resemble the original branching ratio, mimicking a scenario where the different parts of the electronic wave packet are moving at the same pace and visiting identical parts of the PES. Hence, every SH trajectory inherently carries overcoherent electronic coefficients along, resulting in a wrong description if another coupling region is encountered.[108,109]

To alleviate the overcoherence in SH, various *decoherence* corrections have been proposed that aim at removing spurious electronic coefficients using various degrees of physical justification for the adaption of the coefficients.[30,31,33,110,111] Some of those approaches try to track the explicit or approximate position and movement of wave packets that evolve on the non-active states. This can be realized with the help of auxiliary trajectories like in the augmented-fewest switches surface hopping approach (AFSSH).[33] In AFSSH, deviation in phase space and direction of movement for the active and auxiliary trajectories is used to determine if dephasing of the auxiliary wave packet should have occurred in which case the respective electronic coefficient is reset to zero. More simple approaches rely on the placement of Gaussians at branching points or gradients on different states to determine when decoherence should take effect.[31,111] Most decoherence methods rely on the calculation of additional properties, making these approaches inconvenient in cases where electronic structure evaluations are costly. Even simpler decoherence corrections have gained traction that do not rely on any additional properties, with the energy-based decoherence correction (EDC) proposed by Granucci and Persico being the most prominent.[30] Here, an adjustment to all non-active electronic populations[31] ($p_k(t)$) to yield decoherence corrected populations ($p'_k(t)$) is conducted in every single time step according to

$$p'_k(t) = p_k(t) \cdot \exp\left(-|E_k^{el} - E_a^{el}| \frac{E_{kin}}{E_{kin} + B}\right) \tag{58}$$

where B is a constant set to 0.1 a.u.[30] The population of the active state is adapted to conserve the norm of the overall population. It has to be noted, that throughout this thesis, two different implementations of the EDC are used: earlier work applies the exponential decay in Equation 58 not to the electronic populations but instead to the electronic coefficients. Which type of EDC correction is in use will be mentioned in the respective discussion sections. Following Equation 58, the EDC therefore simply depends on two parts: First, the energy difference to the active state with large differences yielding strong decoherence, indicating that the PES on very different states will look quite different as well. Second, E_{kin} plays an important factor as faster moving wave packets can move away faster, resulting in stronger decoherence. The latter factor has been criticized due to the lack of size consistency, meaning that the addition of a non-interacting heavy atom that is moving but far apart from the actual photoreactive site will affect the decoherence rate.[28]

Overall, the use of a decoherence correction has been found to be crucial in many SH calculations[28,29,112] with only very limited exceptions where the choice of a incompatible decoherence correction has been found to be detrimental.[90]

Choice of Basis

Until here, the eigenfunctions of the electronic Hamilton operator have served throughout all derivations as the basis for SH simulations. Nevertheless, SH can be performed regardless of the underlying basis, changing the respective elements in Equation 49 and shape of the PESs. In contrast to quantum dynamics, the resulting dynamics for two simulations using a different electronic basis will not be equivalent. This can be traced down to the classical propagation of the trajectories, forcing each trajectory to follow a single gradient at a time, allowing no linear combination of different gradients that could counteract the differently shaped PESs.[94] Additionally, the classical barriers that would need to be overcome can be smaller or larger, depending on the chosen basis, opening up the way for potentially large deviations if a barrier rises to be larger than the total energy in a trajectory in one representation but not the other.

It has been argued that the preferred choice for propagation for SH is a fully diagonal $\hat{H}^{tot}(\mathbf{r}, t; \mathbf{R})$ where all the additional couplings that are present are included in the definition of the basis, therefore localizing the coupling elements between states closely around the respective conical intersections.[25,58,113] Such a basis that includes SOCs and additional laser fields is commonly not provided by electronic structure codes, making a basis of electronic eigenfunctions with additional SOC and laser coupling elements the easiest and also most common choice. This non-diagonal $\hat{H}^{tot}(\mathbf{r}, t; \mathbf{R})$ (also termed molecular coulomb Hamiltonian, MCH) can be diagonalized in each time-step, providing a instantaneous diagonal basis.[57,113] In the presence of strong laser fields, this instantaneous diagonal basis has been found to be needed to hinder averaging of the gradients when trajectories are switching states often.[58] At the same time, the fully diagonal basis has been found to be flawed in other systems[59] where a Floquet Hamiltonian was able to give more satisfying agreement. A universally best performing basis has currently not been found, making the choice of an appropriate basis a system-dependent choice.

3

HIGH AMBITIONS: ACCURATE SIMULATIONS ON PYRROLE

In this chapter, investigations on the excited state dynamics of pyrrole are presented, featuring high-level electronic structure calculations and no explicit laser pulses. This molecule and its photodynamics are well understood both from an experimental point of view[114–121] and from a theoretical perspective,[51,122–134] making it a good system to try out laser control approaches. Therefore, the original intention for this work was to serve as the foundation for a subsequent study revolving around modification and control of the observed dynamics using external electric fields. During the exploration of the manifold of PESs, it quickly became clear that a high level of electronic structure theory is needed to correctly capture the shape of the PESs, which is discussed in more detail in Section 3.1. Since any desired control attempt using laser fields and SH would need multiple simulation runs – each featuring enough trajectories for statistical significance – to shape and design a good performing pulse, this original goal was abandoned and only the excited state dynamics in absence of external laser fields was studied. The resulting dynamics are presented in Section 3.2 and have been published together with the static calculations under the title "A XMS-CASPT2 non-adiabatic dynamics study on pyrrole" in *Comput. Theor. Chem.* 1155, 38-46 (find the respective reprint in Section A.1.1).

3.1 A TALE OF RYDBERG ORBITALS

After excitation with light, pyrrole has a very prominent deactivation channel at its disposal in the form of N–H bond cleavage, reminiscent of a whole range of planar heteroatomic organic compounds.[135] A remarkable feature observed in pyrrole is, that depending on the wave length of the exciting light, different time scales for this process can be observed, shedding light on the underlying PESs.[136] Three different excitation wave lengths (I, II, and III) are commonly used to probe the lowest-energy excited states: I) is shown in red in Figure 1 and corresponds to exciting in resonance to the lowest energy state, populates a dark $\pi\sigma^*$ state of A_2 symmetry. Upon N–H bond elongation, this state has to overcome a small energy barrier due to extensive σ-Rydberg mixing, rendering the otherwise repulsive A_2 state quasi-bound close to the equilibrium geometry where the mixing is strongest. The encountered barrier is small (around 0.08 eV[136]) that can be tunneled through, yielding a time constant of 126 ± 28 fs for dissociation. II) Increasing the wave length to correspond to the violet arrow in Figure 1 results in population of the vibrationally excited A_2 state, lending enough energy to overcome the small barrier, therefore leading to faster dissociation within 46 ± 22 fs, indicating that the photoreaction is ballistic and occurs within a single or two bond vibrations.[136] III) Increasing the wave length further (see the dark blue arrow in Figure 1) to be in resonance to the brightest state that is of $\pi\pi^*$ character and B_2 symmetry also shows ultrafast dissociation (52 ± 12 fs).[136] Therefore, a conical intersection to one of the close-lying $\pi\sigma^*$ states is readily accessible from the initially excited state, facilitating this fast reaction.

Previous theoretical simulations conducted on pyrrole found that the correct description of both the low-lying $\pi\sigma^*$ and the absorptive $\pi\pi^*$ states at the same time is not possible for most electronic structure methods: TDDFT based SH simulations have been employed, resulting either in a large amount of time spent in Rydberg

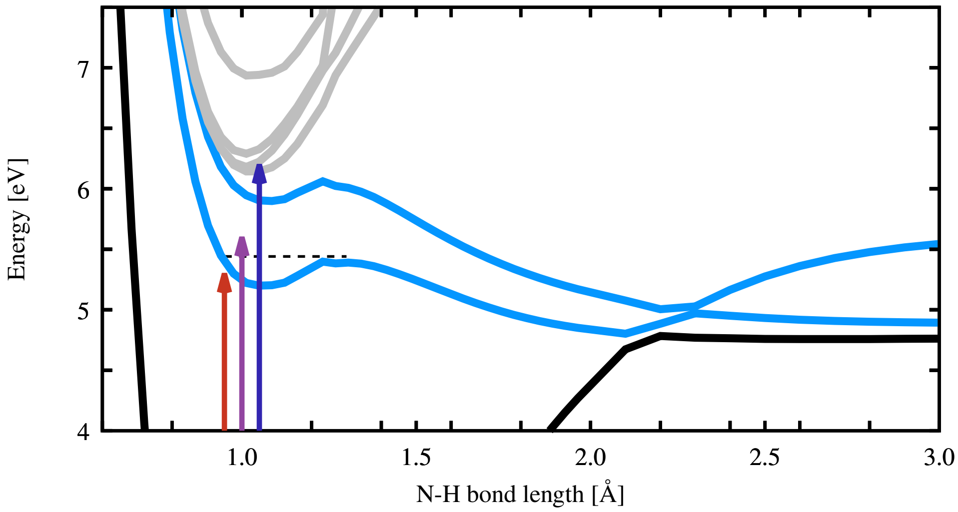

Figure 1: Depiction of the excited states along the N-H bond vector (see below for computational details). The lowest energy state (black), the two lowest excited states (blue), and other excited states (gray) are shown. Three different excitation wavelengths are indicated with arrows: red, violet and, blue. The energy needed to overcome the barrier along the N–H coordinate is indicated with a gray dashed line.

states[128] or the absence of the small barrier found in the lowest $\pi\sigma^*$ states.[130] Similar issues regarding Rydberg-valence mixing have been encountered using the algebraic diagrammatic construction of second order[137] in combination with SH.[130] These single-reference methods also suffer from the inability to correctly describe the S_0/S_1 conical intersection that should be encountered along the dissociative coordinate.

Multi-reference methods have been employed to study the excited states of pyrrole as well in the form of MRCI,[125] CASSCF,[131] and CASPT2.[122,129] Both MRCI and CASPT2 have been shown to be viable options for describing the PESs for all experimentally considered wave lengths while CASSCF overestimates the energies of $\pi\pi^*$ states. Based on these previous findings, the following conclusions are drawn and integrated into the methodological set of tools used for the present investigation of pyrrole: a) To be able to describe all relevant PESs qualitatively correctly, the extended multi state (XMS)[138–140] CASPT2 method is chosen. b) Since the description of Rydberg orbitals and their mixing with valence orbitals, additional diffuse functions $(8s, 8p, 8d) \rightarrow [1s, 1p, 1d]$ are added, centered at the nitrogen atom. The exponents for the diffuse functions are obtained from the Kaufmann series.[141]

Two different active spaces are explored, differing only in the number of included Rydberg orbitals: A large active space containing all π orbitals, the N–H σ bond and the $3p$ Rydberg orbitals (8 electrons in 10 orbitals, denoted (8,10) from now on) and a smaller active space, containing only one of the $3p$ Rydberg orbitals. Both active spaces are depicted in Figure 2 where the strong mixing of the σ^* orbital of the N–H bond with the $3s$ Rydberg orbital is evident. Additionally, it is found that the $3p_x$ orbital mixes with the π_1^* orbital, participating in the bright B_2 state. Removing this orbital from the active space results in an energy increase of 0.21 eV at the Franck-Condon geometry, explaining deviations in the calculated energies between previous CASPT2 investigations of pyrrole.[122,129] The larger active space has been used to optimize minimum energy conical intersections between the S_0 and the S_1 and the linearly interpolated pathways towards those. To facilitate on-the-fly

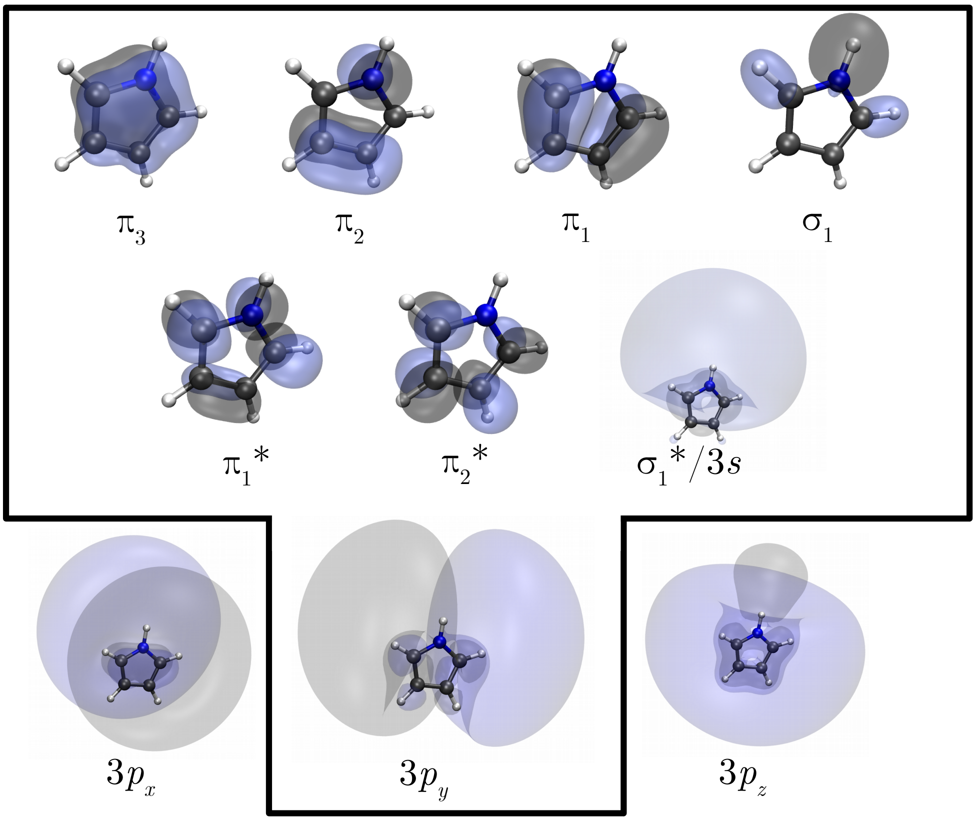

Figure 2: CASSCF orbitals comprising the (8,10) active space and their respective labels as obtained from a calculation averaging over 11 states [SA(11)]. The orbitals included in the smaller SA(7)-CAS(8,8)SCF active space are inside the black border. All calculations used the ANO-L basis set at double zeta quality plus the added diffuse functions (from now on denoted ANO-L+).

computations and the associated gradient calculations, the smaller active space was used in SH simulations. The PESs along the dissociative N–H coordinate using the smaller active space are shown in Figure 3, where the small barrier for the two lowest excited states and the energetic closeness of the second excited state to the $\pi\pi^*$ states (light gray in Figure 3) is visible.

The computational cost of CASSCF/CASPT2 calculations increases drastically with the size of the active space, making this the main bottleneck in the current investigation. Another factor entering into the scaling of these methods is the number of considered states, where a system-specific issue is encountered: CASSCF severely overestimates the energy of the lowest $\pi\pi^*$ states, placing them higher than the lowest two $\pi 3p_o$ states (where $o = \{x, y, z\}$, see). Although the correlation retrieved via XMS-CASPT2 corrects the erroneous placement of the $\pi\pi$ states, many more states need to be included in both the CASSCF and XMS-CASPT2 computation than will be actually relevant later on (the second set of Rydberg states is found at about 7 eV, one eV above the first set of Rydberg states). To allow efficient computation of the XMS-CASPT2 calculations for the SH dynamics, the program BAGEL[142] was interfaced during this project to the surface hopping code SHARC.[57,113,143] Although the parallelization provided by BAGEL allowed for the simulation of the excited state dynamics of pyrrole, the inclusion of laser fields would require the full interstate matrix of non-adiabatic coupling elements to provide correct XMS-CASPT2 transition dipole moments in every time step. As this would increase the computational effort immensely, the idea of performing laser control on this system was discarded.

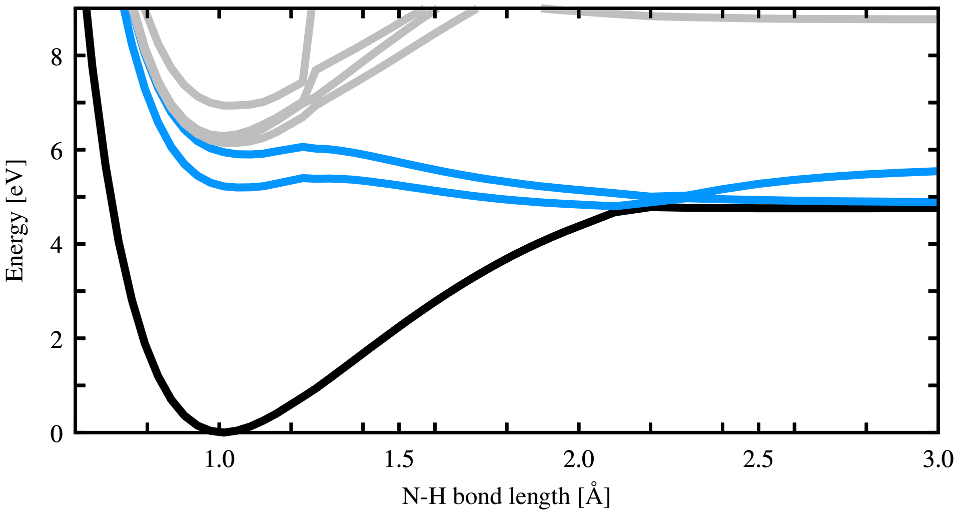

Figure 3: Rigid potential energy scan along the N-H bond vector at the XMS(7)-CASPT2(8,8)/ANO-L+ level of theory. The lowest energy state (black), the two lowest excited states (blue), and other excited states ($\pi\pi^*$ and Rydberg states, gray) are shown.

3.2 ULTRAFAST DISSOCIATION: DYNAMICS STARTING FROM $\pi\pi^*$ STATES

Having determined a suitable computational framework to calculate the electronic PESs of pyrrole, the respective excited state dynamics has been simulated using SH. A set of geometries and velocities has been sampled based on a Wigner distribution of the lowest vibrational state to cast the original quantum distribution into a set of classical snapshots.[144] In the absence of an explicit laser pulse to initiate the dynamics, a number of these initial conditions has been determined to start in a given excited state based on a stochastic procedure, taking into account the corresponding oscillator strength if the excitation energy falls within a predetermined window. An energy window of 6.1 to 6.3 eV was chosen for this, reminiscent of excitation into the $\pi\pi^*$ states. This type of excitation mimics interaction with an infinitely short optical δ-pulse with a well defined wavelength – such pulse cannot be realized in an experimental setup but is often employed in theoretical simulations. Due to the high computational cost, only a small number of only 23 trajectories was propagated, adding statistical noise to the observed results.

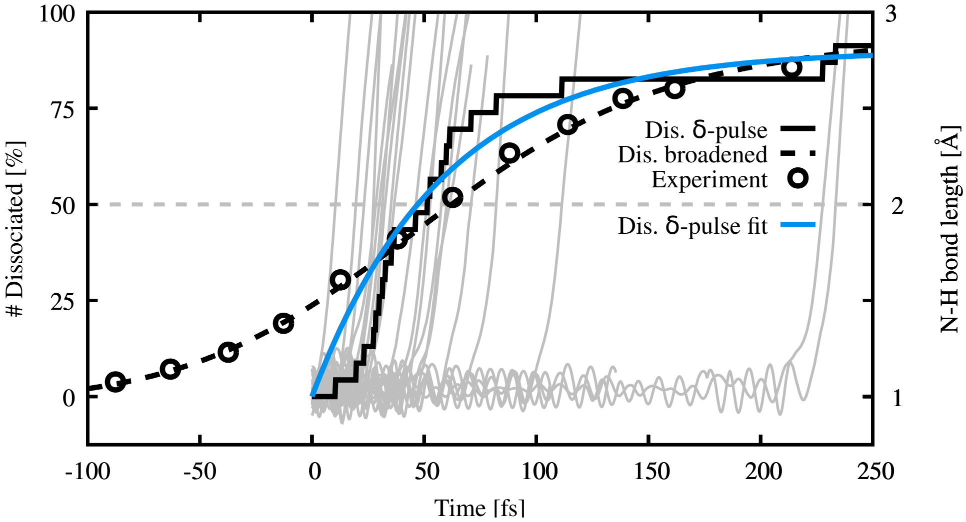

Figure 4: N–H dissociation dynamics of pyrrole simulated with SH using XMS(7)-CASPT2(8,8)/ANO-L+ to evaluate the electronic structure. The N–H bond length for each trajectory is given with light gray lines. The accumulated percentage of dissociated trajectories is given as a solid black line and a fit thereof is found in blue. Experimental[136] dissociation measurements are (black circles) can be compared to black dashed line representing a convolution of the δ-pulse dissociation with the envelope functions of the experimental laser pulses.

An overview of the resulting simulations, focusing on the N–H bond dissociation can be found in Figure 4. As can be seen there, the excited state dynamics of pyrrole is dominated by ultrafast N–H bond cleavage, placing most observed dissociation events well within the first 50 fs after excitation of the respective trajectories. To quantify this process, an arbitrary N–H bond length value of 2.00 Å was taken as a cutoff value to verify whether dissociation had occurred. A fit of the so-obtained dissociation curve yielded a time constant and associated uncertainty of 64 ± 13fs using bootstrapping of the set of trajectories. Experimental measurements of the N–H abstraction showed an associated time constant of 52 ± 12[136] agreeing very well with the present simulations. To allow for a better visual comparison between the simulations and the experimental results, the dissociation events have been smeared in time using the envelope functions of both the pump and the probe pulse used in experiment. In doing so, the time-delayed onset of the excited state dynamics can be taken into account to give a more realistic description.[145] Nevertheless, such *a posteriori* approaches to include the influence of laser pulses neglect all the finer interactions explicit excitation with a laser pulse introduces. One of the main differences encountered with no explicit laser pulse is that each trajectory is initialized with all electronic coefficients set to 0 except for the active state, where 100% of the population resides. An explicit laser pulse, however, would see partial population of other electronic states as well for each trajectory, therefore introducing potential differences at the onset of the dynamics.

Although N–H bond cleavage is the primary dissociation channel with 91% of trajectories following this pathway, different deactivation channels have been observed in the current and previous simulations:[126,128] Ring-puckering or ring-opening. The remaining simulated trajectories deactivated via ring-puckering, forming a hot ground state from where it is assumed that additional fragmentations or C–H bond cleavage can occur. Ring-opening was not observed for the set of simulated trajectories. Optimizations of minimal energy conical intersections between the S_0 and the S_1 have been conducted, followed by linear interpolations of internal coordinates to gain more insight into the deactivation pathways. From these pathways it was evident that ring-puckering is associated with rather flat changes in the PESs while ring-opening encounters steeper PESs, disfavoring this pathway in comparison to ring-puckering.

As a final note, the instability of the employed multi-reference calculations has to be mentioned: Due to the neglect of two of the $3p$ Rydberg orbitals in the active space used in the dynamics simulations, multiple interchanges of the one included $3p$ Rydberg orbital with the other two are observed. Additionally, a number of additional $\pi\sigma^*$ states enter the set of calculated states once N–H bond elongation is initiated, therefore giving more weight in the state-averaging to the participating orbitals, resulting in an additional stabilization of the low-lying $\pi\sigma$ states. The same holds true for the other deactivation channels. Nevertheless, due to the ballistic nature of the dissociation process and the ultrashort associated time scale, the influence of these instabilities on the current results are very limited.

3.3 INSIGHTS GAINED AND PLACE IN THE LARGER PICTURE

In conclusion: The excited state dynamics of pyrrole have been investigated in full dimensionality, employing high level electronic structure computations. A very good agreement with experimental observations for the time scale for N–H dissociation is obtained, highlighting the importance for the use of multi-reference methods even in the case of rather small molecules. Although the mingling of Rydberg and valence states that poses a serious problem in many computational setups can be overcome with diffuse basis sets and advanced computational methods, a serious toll in computational time is collected in return. This high cost for the use of state-of-the-art electronic structure methods prevents the use of such a computational setup for the original goal of laser control, which would need a large number of dynamics simulations with sufficient statistical significance. Additionally, the extra cost of calculating the transition dipole matrix at XMS-CASPT2 level in every time step would make such laser control approaches essentially not affordable, since this would raise the cost of the present dynamics by a factor of about 20 for each single trajectory. Therefore, the work on pyrrole initiated a rethinking regarding the approach to be used in this thesis: The use of lower-cost electronic energy evaluations would allow a more focused approach on the actual laser interaction and control aspect, which has always been the idealistic centerpiece of the thesis. As a consequence, in Chapter 4, the expensive on-the-fly evaluations are substituted by precomputed and approximated potentials.

4

SIMPLER SURFACES TO INVESTIGATE MORE COMPLEX DYNAMICS

The previous Chapter demonstrated the difficulties that can be encountered when describing the electronic states of molecules, sometimes necessitating a high level method to obtain qualitatively correct PESs. The high computational effort accompanying these methods paired with the still rather limited robustness of those surfaces makes investigations that revolve around the dynamical aspect as opposed to a highly accurate static description challenging. A simple remedy for these problems is to switch to precomputed surfaces that – once obtained – are nothing more than analytical functions that can be evaluated in less than a second and will be robust throughout the parametrized space. In doing so, the computational workload for the dynamic and the static part is essentially separated, opening up the road not only for the desired focus on the dynamical interaction with a laser pulse but also for a potential comparison of dynamics methods on the same set of PESs.

The route followed in this thesis to define and parametrize analytical potentials is the vibronic coupling model truncated at first order.[18,19] A detailed description of this framework including strong points and weaknesses thereof is given in Section 2.2.2. So obtained PESs are diabatic by construction and have seen a lot of use in the context of MCTDH simulations, where the complete PES needs to be known before running dynamics.[10,78,79] Recently, the LVC model has been used in our group in combination with SH to yield an extremely efficient simulation setup where both the static and the dynamical calculations are extremely cheap, scaling very well with the size of the investigated system, especially for the dynamical part.[28,77,146] Therefore, economical full-dimensional investigations of the excited state dynamics are made viable for transition metal complexes and other rigid systems of similar or even larger sizes that previously could only be simulated at very high computational cost.[147–151] With the detailed theoretical exploration of a range of transition metal complexes becoming reality,[152–155] the boundaries of what can possibly be investigated are pushed towards larger and larger systems with a pioneering spirit at heart. At the same time, expansion towards larger systems should always be supplemented by introspection, questioning the limitations and restrictions of the very approach that granted said expansion: On the one hand, the applicability and accuracy of SH is still a much debated topic, a fact that only gets more blurred when systems far beyond the capabilities of higher-level dynamics methods are simulated.[28] This seems to be even more severe in the presence of laser fields, where strong deviations between SH and higher-level methods can be encountered already for one-dimensional test systems,[49,55,59] making the blind use of LVC/SH for large molecular systems in the presence of laser fields questionable. On the other hand, these limitations are imposed by the approximate nature of the LVC model and its inability to go beyond the harmonic basis used to construct the respective PESs, rendering specific molecular movements and relaxation processes impossible.

The implications and difficulties encountered due to the approximation of the PESs with an LVC model will be touched upon in Chapter 5. In this chapter, the issue of the accuracy of SH will be treated in detail, putting special emphasis on the use of explicit laser fields within SH, going beyond the commonly employed one-dimensional test systems used to assess the validity. In a first step towards a comparison on an equal footing between SH and MCTDH, an iterative scheme is developed allowing for the automated reduction of the complete molecular Hamiltonian to the most important degrees of freedom and electronic states. This scheme is termed the SHARC-gym and makes use of the efficiency of the LVC/SH setup and the accuracy of MCTDH to provide the best of both worlds. The development of the SHARC-gym and the application thereof on the $[PtBr_6]^{2-}$ complex is presented in Section 4.1 and also published in *J. Phys. Chem. A* with the title "From surface hopping to quantum dynamics and back. Finding essential electronic and nuclear degrees of freedom and optimal surface hopping parameters" (reprinted in Section A.2). The SHARC-gym is subsequently employed in Section 4.2 to enable the comparison of SH in the presence of external laser fields to MCTDH and vMCG dynamics, benchmarking the validity of various SH protocols. The results of this benchmark on the SO_2 molecule and a 10-dimensional model system of 2-thiocytosine are published in *J. Chem. Phys.* titled "Validating fewest-switches surface hopping in the presence of laser fields" (see Section A.2 for a reprint). Here it is found that SH fails to quantitatively reproduce the interaction with the employed laser pulses, but nevertheless gives qualitative agreement for most SH protocols. With this knowledge at hand, the strengths of LVC/SH will be capitalized on in Chapter 5 to investigate and modify the excited state dynamics of a transition metal complex in 161 vibrational degrees of freedom.

4.1 THE ADVENT OF THE SHARC-GYM

Often, MCTDH and SH are treated as two different tools, each useful in its respective area with clearly defined strengths and weaknesses: MCTDH can be rigorously derived from exact propagations, converges to the exact solution given enough basis functions and is therefore capable of describing the whole plethora of nuclear quantum effects. This drawback is the need for a set of precomputed PESs and the unfavourable scaling of the computational effort with the number of included degrees of freedom. Contrary to this, SH has an extremely favorable scaling with the considered system size and only needs locally computed properties. The price to pay for this efficiency is paid in accuracy as most nuclear quantum effects are absent. Some of the deficiencies in SH are compensated by the use of *ad hoc* protocols that are useful in some cases but detrimental in others.

In most cases, either SH or MCTDH is chosen to investigate a given system, making use of the strength of the used method. Rarely though, SH and MCTDH are used in tandem to either determine the applicability of a new type of SH protocol or to use SH dynamics to trim a Hamiltonian down to the most reactive degrees of freedom that can then be used for MCTDH simulations.[89,156] In the spirit of the latter symbiotic approaches, a new way to intertwine SH and MCTDH is presented in this thesis that covers up the weak spots of both sides by utilizing the complementing strengths of the respective other method: the SHARC-gym. The SHARC-gym is an iterative procedure to obtain a reduced Hamiltonian on which high-level dynamics methods can be used on the one hand and a set of appropriate SH protocols on the other hand.

4.1.1 *An Iterative Scheme to Form a Symbiotic Relationship between Surface Hopping and MCTDH*

The SHARC-gym is a very general procedure that can be used to pair SH with any higher-level dynamics method using precomputed PESs or on-the-fly simulations if the higher-level dynamics allows to do so. For simplicity, from now on, only the specific case of pairing SH with MCTDH on PESs derived from an LVC model will be discussed since only this combination is used throughout this thesis.

To initialize the SHARC-gym, two ingredients are needed: a full-dimensional LVC Hamiltonian of the investigated system and an initial SH protocol containing a number of desired *ad hoc* corrections that can be optimized at a later stage. The subsequent workflow is depicted in Figure 5 and includes the following steps:

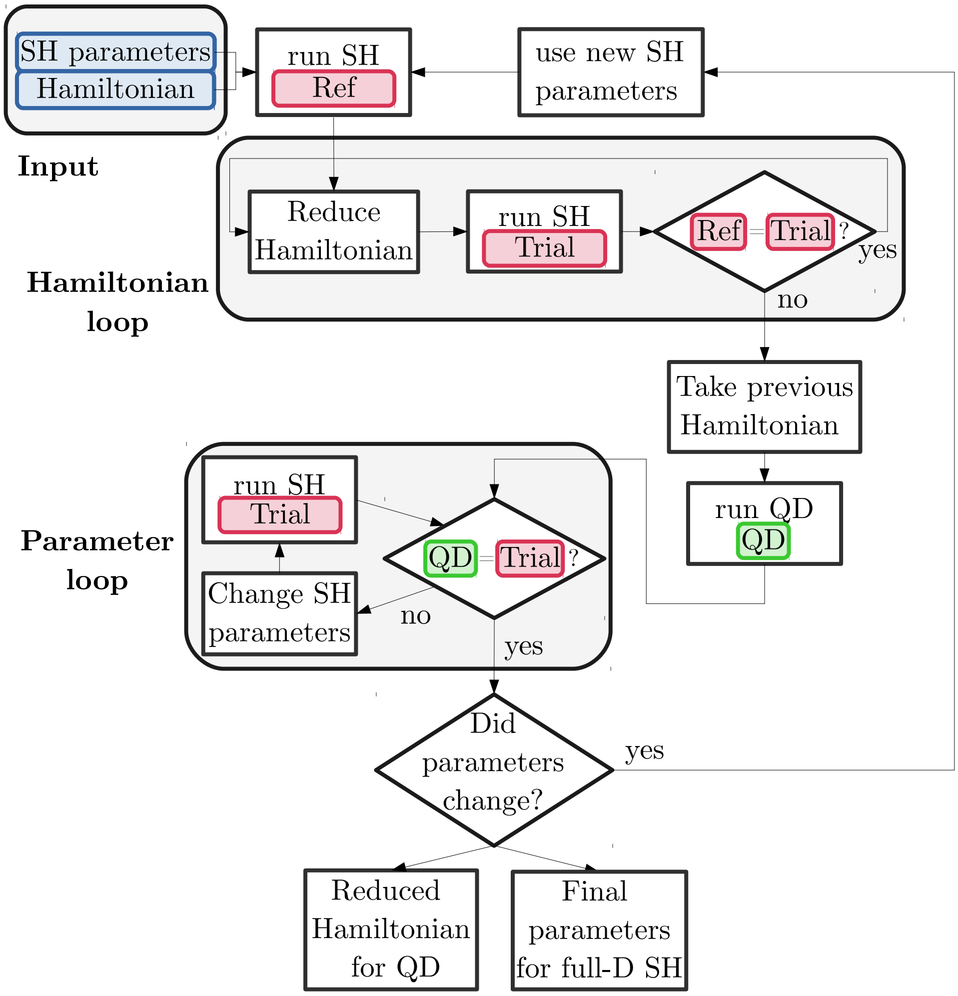

Figure 5: Overview of the different steps forming the SHARC-gym. Blue boxes represent initial parameters that enter the SHARC-gym, red boxes are results obtained from SH while green boxes are results obtained via a form of higher-level propagation method. The main building blocks that form the essential parts of the SHARC-gym procedures "Input", "Hamiltonian loop", and "Parameter loop" are grouped in grey boxes.

1) SH simulations are computed on the full-dimensional Hamiltonian using the initial SH protocol to yield a reference dynamics.

2) The *Hamiltonian loop* is entered that aims at reducing the size of the Hamiltonian by identifying superfluous electronic states and vibrational degrees of freedom. Having identified such states or modes via any method imaginable (excited state gradients, symmetry, principal component analysis of the reference dynamics, etc.), the respective degrees of freedom are removed and new SH dynamics with the same protocol calculated. If the new dynamics is in good agreement with the reference dynamics (using any numbers of measures to define the agreement), no important degrees of freedom have been cut and the reduction process can continue. If the new dynamics substantially deviates from the reference, the Hamiltonian prior to this reduction step is taken to either reduce some other states/modes or taken as the finally reduced Hamiltonian, which is when the Hamiltonian loop is exited.

3) The obtained reduced Hamiltonian is then used to run a MCTDH simulation, that should now be viable due to the reduce in considered system size. This MCTDH reference simulation is then used in the so-called *parameter loop* where the agreement between MCTDH and SH is scrutinized. If both methods agree to a certain threshold, no further steps need to be taken. However, the more probable case is that depending on the chosen *ad hoc* corrections, the agreement will vary, necessitating a screening of those corrections to find the best suited one. With a well-fitting SH protocol at hand, the parameter loop is exited.

4) If the SH protocol was changed in the parameter loop to increase the agreement with MCTDH, the overall process needs to be repeated starting again from step 1) using the newly obtained SH protocol from the beginning to reduce the Hamiltonian. If the protocol did not change, a self-consistent cycle has been reached that provides a reduced Hamiltonian for MCTDH and a set of *ad hoc* corrections for SH that are benchmarked against MCTDH on the reduced model of the investigated system, concluding the SHARC-gym.

This method is of course not without its flaws, as there is no guarantee that a reduction down to only a few degrees of freedom is possible and it might therefore be either impossible to perform MCTDH calculations or degrees of freedom important only in MCTDH are cut away. Even if a reduced Hamiltonian is found, it might turn out that MCTDH and SH give qualitatively different pictures, questioning the accuracy and validity of the selection via SH.

The simple beauty of the SHARC-gym lies in the very fast calculation of all the LVC/SH simulations, making a single cycle of the SHARC-gym even for a mode-by-mode reduction in the Hamiltonian loop or a screening of many different SH protocols in the parameter loop viable while still using a large number of trajectories for representative statistics. Obtaining both a reduced model system and an "optimal" protocol that can be used for the full-dimensional Hamiltonian is only made possible by interconnecting the strengths of both SH and MCTDH, showcasing how easily both methods can be bridged. As such, the SHARC-gym is the perfect device to devise low-dimensional test systems based on real molecules to benchmark SH against MCTDH. In the following, the SHARC-gym will be used to determine the most important electronic states and degrees of freedom for the $[PtBr_6]^{2-}$ complex.

4.1.2 *The First Member of the SHARC-gym: $[PtBr_6]^{2-}$*

Recently, the highly symmetrical $[PtBr_6]^{2-}$ complex has been shown to undergo ultrafast ISC in aqueous solution followed by a dissociation of a Br^-.[157,158] Although the number of participating atoms is very small, the density of electronic states is extremely high due to the heavy elements involved, placing more than 50 singlet and 50 triplet states within 7 eV from the electronic ground state. Such a high number of considered states is necessary to guarantee the inclusion of relevant states in the diabatic description of the LVC model. The presence of these heavy atoms also results in very strong SOCs, leading to the splitting of each triplet state into its respective components, effectively tripling the number of states for the triplet states. This high number of states makes the simulation of excited state dynamics in the full dimensionality of the molecule computational very expensive, even when considering the influence of the surrounding water on these dynamics only implicitly. Therefore, the SHARC-gym was employed to reduce the computational workload for MCTDH simulations and to identify suitable SH protocols for the dynamics of $[PtBr_6]^{2-}$.

The PESs of $[PtBr_6]^{2-}$ are described using an LVC model based on TDDFT calculations with the B3LYP functional[159] and the TZP basis set in ADF2017.[160] Relativistic effects have been included via the zero-order regular approximation and the octahedral symmetry of the molecule is neglected. The disregard of symmetry culminates in a different sorting of formally triply degenerate sets of states for calculations on different displaced geometries needed for a numerical differentiation of the LVC parameters. Wave function overlaps are exploited to correctly map the states in these cases and then obtain meaningful gradients and coupling parameters for all 50 singlet and 50 triplet states. When simulating the absorption spectrum of $[PtBr_6]^{2-}$ using a nuclear ensemble method we noted that the agreement with the experimental reference was poor, almost completely missing the experimental absorption peak at 4 eV. Although this indicates that the employed electronic structure setup is not capable of fully describing all excited states and therefore might be of limited predictive capacity, the Hamiltonian is used in the following as a proof of principle since the main main goal of the SHARC-gym revolves around selectively minimizing a given Hamiltonian.

With a full-dimensional LVC model at hand, a initial reference SH simulation is conducted using the following SH protocol (see Section 2.3.2 for details) that will be labelled SH^* in this section: Due to the strong SOCs, a diagonal basis for propagation is chosen initially, the total energy at a transition between surfaces is conserved by adapting the overall velocity vector of the molecule, and if insufficient energy is present to counteract the change in potential energy, the hop is rejected without any adjustments being made. The SH dynamics are initialized following instantaneous excitation of an Wigner ensemble of structures within an 0.2 eV window centered at 3.0 eV in a block-diagonal set of states, where all singlet and all triplet states are diagonal, respectively, and SOCs being off-diagonal elements (MCH). With singlet-triplet excitations being formally forbidden, only singlet states are populated at the onset of the dynamics. After only a few femtoseconds of evolution, ISC is visible due to the strong SOCs and energetic closeness of the states (see Figure 6a). A rapidly oscillating behavior of the singlet and triplet populations is observed before levelling off after about 40 fs with 72% of the electronic population being of singlet and 28% thereof being of triplet character. When comparing the time scale of the ultrafast ISC to the slow motion of the internal vibrational degrees of freedom, the ISC emerges as being driven almost exclusively by static coupling via the SOCs with nuclear relaxation playing only a minor role.

With the reference dynamics being conducted, the Hamiltonian loop of the SHARC-gym is entered, where the size of the Hamiltonian is reduced. The quantity chosen to determine if a diabatic excited state is important for the observed excited state

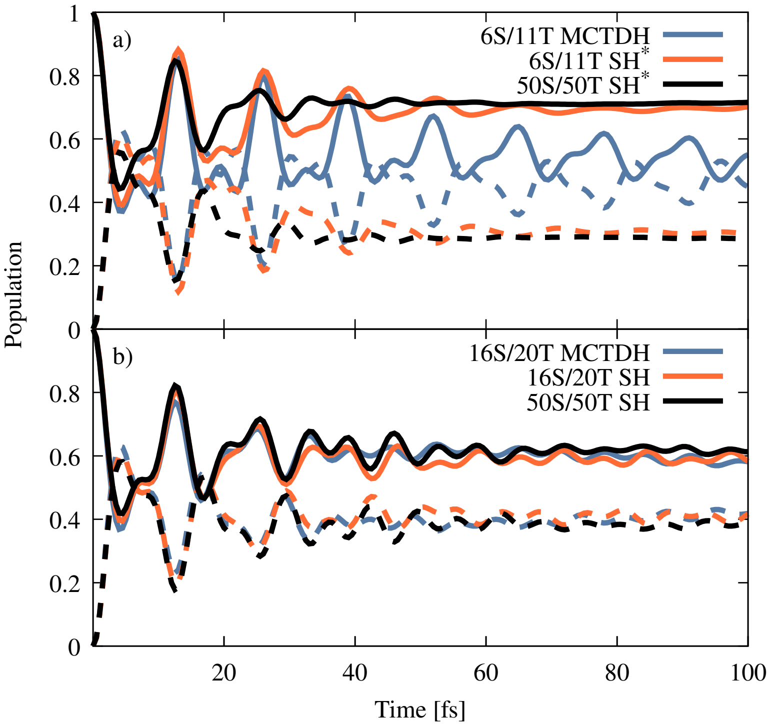

Figure 6: Sum of electronic singlet (solid lines) and triplet populations (dashed lines) throughout the first 100 fs of the excited state dynamics of $[PtBr_6]^{2-}$. The number of considered excited states for each Hamiltonian is denoted by the number of singlet (S) and triplet (T) states. The initial reference SH populations are shown in black, the SH populations for the derived and reduced Hamiltonian in orange while MCTDH populations using the reduced Hamiltonians are given in blue. Two different SH protocols have been used differing in one point: the EDC has been used (indicated by SH*) in panel a) while no decoherence correction has been used in panel b).

dynamics is the maximum population of a given state throughout the simulation. This way, all excited states could be sorted according to their maximum population throughout the dynamics and cutoff values for the maximum population be defined, which represent different truncation levels of the Hamiltonian. A drawback of this selection method is the possible neglect of states that are only transiently populated. Repeating the SH* simulations with these reduced Hamiltonians showed that the number of states can be reduced from 50 singlet and 50 triplet states down to 6 singlet states (S) and 11 triplet states (T) without considerable loss of accuracy. The obtained electronic populations are shown in Figure 6a, where small differences for the first 30 fs of the dynamics and an almost identical final ratio for the singlet and triplet populations is observed. More severe reductions of the Hamiltonian leads to substantial deviations from the reference populations, hence, the Hamiltonian loop was exited with this 6S/11T Hamiltonian, having cut the number of total states that need to be simulated from 200 to only 39, which can be efficiently be transferred to MCTDH.

When running MCTDH dynamics using the 6S/11T Hamiltonian and initializing the same populations as in the SH* setup, a more pronounced oscillatory behavior of the singlet-triple populations is observed that is damped for longer simulation times but seems to approach a 50:50 ratio between both multiplicities. This observation is in stark contrast to the SH* results, illustrating that the employed SH* protocol is

insufficient to describe the ensuing dynamics. The parameter loop of the SHARC-gym is then entered. Cycling through different SH protocols for dynamics, always changing only a single parameter with respect to the original SH* setup, with the 6S/11T Hamiltonian revealed the following:
(i) Switching the EDC for either AFSSH or no decoherence correction at all gives an almost perfect agreement with the MCTDH populations with no difference between AFSSH and no decoherence correction. This behavior can be traced back to a very coherent movement of the excited wave packet on the mainly involved excited states, where the different parts of the wave packet can interact with each other for a prolonged period of time. Contrary to this, the EDC acts in every time step to reduce coherence between parts of the wave packet, assuming that these should be moving apart oblivious of the similarly shaped PESs that are actually involved.
(ii) Changing the fully diagonal basis in the propagation for the MCH basis results in almost quantitative population of triplet states in stark contrast of only 30% seen in the SH* setup using the diagonal basis. It is found that the decisive factor for the differences is located at the synergy of the EDC paired with the MCH basis in this metal complex featuring strong SOCs: The extensive SOCs result in singlet-triplet hops between states with strongly differing potential energy. The strength of the EDC depends amongst others on the energy gap between the active state at the currently populated state, therefore acting strongly between largely separated states. Due to the diagonalization, smoother transitions between states occur, involving smaller energy gaps between populated states, resulting in a more consistent effect of the EDC on non-active states.
(iii) All other changes showed little to no impact on the electronic singlet and triplet populations.

Having determined a new set of SH parameters where no decoherence correction is used instead of the EDC (termed SH instead of SH*) that is capable of describing the evolution of the MCTDH populations in more detail, the parameter loop of the SHARC-gym is exited. Since a change in SH protocol was needed to better match the MCTDH results, the whole SHARC-gym needs to be repeated using the new SH protocol, starting from a new reference SH simulation. The new 50S/50T reference populations as well as the populations for the newly reduced 16S/20T Hamiltonian are shown in Figure 5b. Both Hamiltonians result in almost identical results, showing fast oscillations in the very first time steps before converging towards a population of 60% singlet and 40% triplet character. Running MCTDH dynamics on this Hamiltonian gives a very similar picture to the SH simulations, therefore no further changes to the SH setup have been conducted, therefore finishing both the Hamiltonian and parameter loops with success, concluding the SHARC-gym for the reduction of states. The SHARC-gym succeeded in identifying a weakness of the initially employed SH* protocol and managed to trim the number of considered electronic states with almost no loss in accuracy.

In a final step, the 16S/20T Hamiltonian was used to investigate which vibrational degrees of freedom can be omitted while not affecting the ISC and population dynamics. For this, MCTDH was used as a reference, since this calculation was already available. In the Hamiltonian loop a new criterion was used to select more important modes: The sum of κ and λ values has been taken to single out modes that contain a large amount of interstate couplings, feature strong gradients or have both of these features. While the intent of this criterion is plainly apparent, in hindsight a more appropriate mode of selection should have been chosen. As it stands, this criterion does treat couplings between weakly populated states on the same level as couplings between strongly populated states although the latter are more important for the overall course of the dynamics. Nevertheless, this criterion was able to identify the following most important modes: the totally symmetric mode q_{12} that contains a non-zero gradient in all excited states is found to be the highest ranking mode with this criterion followed by the Jahn-Teller modes q_{11} and q_{12} that contain the most and strongest interstate coupling elements. Using only these three modes, the ISC dynamics of $[\mathrm{PtBr_6}]^{2-}$ can be simulated quite well, with the main difference being an oscillation of the populations around the full-dimensional values. Inclusion of more vibrational normal modes reduces this oscillations.

4.1.3 *Insights Gained and Place in the Larger Picture*

The SHARC-gym represents a simple and intuitive framework to use the strengths of SH while at the same time revealing its weaknesses by providing simplified models of realistic test systems. Although the SHARC-gym itself is a simple and quite natural procedure, it was conceived by mere chance at the time, being born from the general euphoria surrounding the realization of the vast potential that was tapped when restricting SH dynamics to LVC PESs: While LVC/SH allows to reach for the stars by investigating bigger and bigger systems, the SHARC-gym also establishes a link between SH and higher-level methods for a harmonic cooperation, allowing for a comparison of both methods. The basics of the SHARC-gym and a first proof of concept thereof in the form of the $[\mathrm{PtBr_6}]^{2-}$ complex have been presented. For this complex, a possible reduction from 200 excited states and 15 vibrational modes down to 76 electronic states in 3 vibrational modes has been explored while at the same time identifying that the use of the EDC correction for this system leads to a systematic error as the evolution of the excited state wave packet is highly coherent.

In the following, the link between SH and higher-level methods that can be established with the SHARC-gym will be utilized to validate the capability of SH for a correct treatment of the interaction with a laser field, using multi-dimensional test systems. This comparison represents the basis for the final part of this thesis where a laser is used to excite and modify the excited state dynamics of a large transition metal complex.

4.2 PUTTING LASER-INDUCED SH TO THE TEST

Since the very first formulations of field-induced SH,[44,57] the accuracy of this methodology has been estimated by comparison with exact quantum dynamics simulations. These initial successes that show extremely good agreement with the reference method in the investigated one-dimensional test systems have been complemented by more critical studies that show partial or large deviations from reference calculations,[49,50,53,55,58,59,161] often showcasing a dependence on the used SH protocol: Sometimes choosing an adequate SH protocol is enough to recover most of the deviations[58,59] while in other cases, long laser pulses or low kinetic energies of the trajectories are found to still present a problem.[49,55] All of these comparisons - that were exclusively restricted to one-dimensional test systems - shine unfavourable light on field-induced SH, compromising any use of this method without further inspection. Therefore, the LVC/SH framework coupled to the SHARC-gym will be used to provide further insights into the deviations of field-induced SH from an exact reference method, supplementing previous investigations by going beyond one-dimensional to multi-mode test systems reminiscent of small molecules that are closer related to academic questions that are commonly tackled with SH.

4.2.1 *Setting the Stage: The Model Systems*

Two molecules are chosen as a reference for benchmarking the light-matter interaction in SH: SO_2 and 2-thiocytosine. A considerable number of studies employing both SH and MCTDH have been conducted on SO_2,[84,146,162,163] uncovering the complex and interwoven dynamics of close-lying singlet states accompanied by population of triplet states within a few hundred femtoseconds. This transfer to the triplet multiplicity is facilitated by the presence of the heavy sulfur atom, increasing the SOCs to a considerable amount in this molecule. Similarly, replacing a single oxygen in cytosine by a sulfur atom alters the dynamics of the molecule by enhancing the ISC rate as has been observed for 2-thiocytosine.[164] Both systems have previously been parametrized using an LVC model and SH simulations subsequently been conducted, revealing good agreement between the LVC-restricted approach and on-the-fly SH dynamics, especially for the first few hundred femtoseconds.[146] The biggest encountered difference to the on-the-fly dynamics is a slower population of the triplet states for both molecules, which can be attributed to the use of static SOCs that are only computed at the reference geometry, therefore neglecting any dynamical changes to these properties.

Outfitted with these LVC models, comparisons of the excited state dynamics in the absence of external laser fields are conducted first to be able to better separate deviations between SH and MCTDH due to the explicit light-matter interaction and the excited state dynamics following excitation. In the case of SO_2, this comparison is straightforward since the three vibrational modes present in SO_2 can readily be simulated using MCTDH. The populations obtained after starting in the brightest diabatic state are depicted in Figure 7a together with a combination of electronic and classical populations[165] from a SH simulation using the EDC, rescaling along the velocity vector, a completely diagonal representation and no adjusting or reflection of velocities if a frustrated hop is encountered. It can be seen that both methods predict a strong oscillatory behavior of the $^1B_1$ and the $^1A_2$ states that is found to be more pronounced in MCTDH than with this SH protocol. For longer time scales, a almost linear increase in population of the $^3B_2$ state is observed while MCTDH predicts a stagnation in the population of this triplet state after around 250 fs. To quantify the differences between SH and MCTDH, the deviation for each individual state is summed up and averaged over all time step, yielding an error ϵ between 0 and 2, amounting to $\epsilon = 0.248$ for this SH protocol. In a next step, not only one but many different SH protocols, differing in the treatment of overcoherence and frustrated hops, velocity rescaling and the basis for propagation are employed, and the respective ϵ values collected, providing a broader picture of the accuracy of SH and the influence of these options. For SO_2, the ϵ ranges from 0.240 to 0.384, where most of the error is amassed from having less pronounced oscillations of the two participating singlet states. The remainder of the error is found in differing population of triplet states, where SH protocols showed the largest deviations when combining the diagonal basis with a rescaling along the NAC or gradient difference vectors.

Performing the same analysis with 2-thiocytosine demands an additional step to trim the 33 vibrational degrees of freedom to be treatable with MCTDH. For this, the

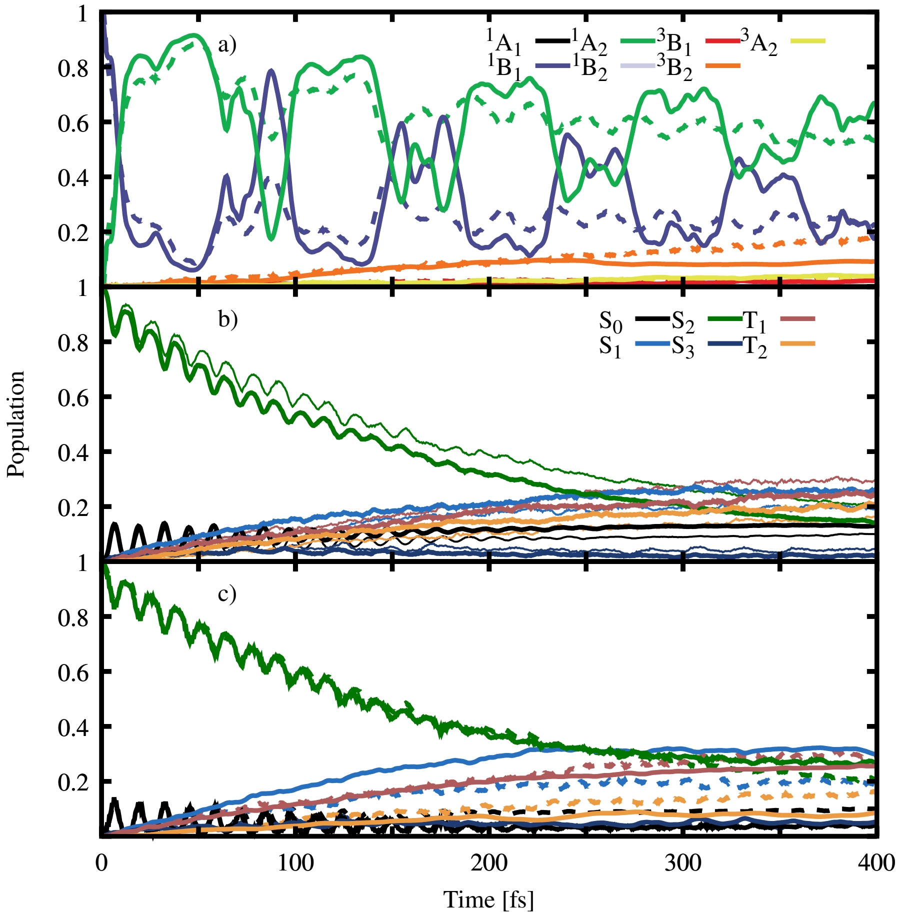

Figure 7: a) SH (dashed) and MCTDH (solid) populations for the excited state dynamics of SO_2 starting from the diabatic $^1B_1$ state. b) SH populations for a 33- (thick) and 10-dimensional (thin) LVC model of 2-thiocytosine starting from the diabatic S_2 state. c) SH (dashed) and MCTDH (solid) populations for the excited state dynamics of the 10-dimensional LVC Hamiltonian of 2-thiocytosine.

SHARC-gym was invoked. A new procedure was applied to assess the importance of a specific normal mode: For each normal mode, a separate SH dynamics was simulated with only this specific mode being deactivated, revealing the importance this mode had on the overall population dynamics. The differences to the reference dynamics are again quantified with the ϵ measure, providing a importance-weighted list of all normal modes. The populations obtained when using the top ten of these most important normal modes in a SH simulation are shown together with the data from the full-dimensional Hamiltonian in Figure 7b. In both cases, the dynamics is dominated by a decay from the initially populated S_2 state to a multitude of other diabatic states including the two triplet states. The observed differences amount to an ϵ value of 0.219.

With a suitable Hamiltonian available, MCTDH dynamics have been conducted, showing a decay of the S_2 population identical to the respective SH population but also differences in the ISC dynamics with SH overestimating the transfer to the T_2 state. The respective populations are plotted in Figure 7c. Iterating through the set of considered SH protocols provides an error range of 0.164 to 0.488 for this ten mode system, already showing a stronger dependency on the chosen protocol than SO_2. Rescaling along the gradient difference vector was found to result in large deviations for the singlet populations while using the NAC vector to adjust the velocities was again observed to yield unfavorable triplet populations when paired with the diagonal representation.

It has to be noted that not all possible combinations of SH options can be simulated, since NAC vectors between singlet and triplet states are not defined. Therefore, these quantities are unavailable for adjustments of the velocities if a block-diagonal basis is used for propagation. The unavailability of these quantities is especially intriguing since choosing the NAC vector for rescaling in the completely diagonal basis where singlet and triplet states as well as the respective NAC vectors are mixed was found to give large errors for the triplet populations. This suggests that the energy available along these mixed NAC vectors is often insufficient to accommodate a hop to a higher-lying state of a different multiplicity.

The excited state dynamics of the two model systems in the absence of explicit laser pulses has been analyzed, showing notable differences for changes in the SH protocol, some of them seeming to be systematic. Being equipped with the needed model systems and an overview of the accuracy of different SH protocols for the field-free non-adiabatic dynamics, explicit laser pulses are used in the following to initiate these dynamics.

4.2.2 *Dynamics Initiated by Explicit Laser Pulses*

Similar to the previous section, first the SO_2 model system is investigated and analyzed before moving to the larger 2-thiocytosine model.

To investigate the behavior of SH to model light-matter interaction in various scenarios, different pulse lengths have been employed to excite the SO_2 ground state population to the $^1B_1$ state. All these pulses are in resonance with the energy of the $^1B_1$ and have a normalized intensity so that in an ideal case, the same amount of population will be excited regardless of the pulse duration. The decline in the ground state population for three different laser lengths is shown in Figure 8a for three different propagation methods: SH, MCTDH and vMCG. For the full width at half maximum (FWHM) laser pulses of 17 and 50 fs, MCTDH and vMCG agree very well, both ending up with almost 60% of excited population. For the chosen SH protocol, only around 50% of population are excited at the end of the pulse for these pulses, with a slightly better agreement for the longer pulse.

When going to the longest considered pulse with a FWHM of 200 fs, MCTDH shows a diverging behavior compared to the previous pulses as population is transferred back to the ground state towards the end of the pulse, resulting in a final share of 21% excited state population. This peculiar behavior is found to be rooted in the return of excited population into the Franck-Condon region while the laser pulse is still active, introducing additional couplings between the still not excited and the returning excited population. The time needed for the excited state wave packet to traverse the excited state PESs until it enters the region around the ground state geometry again is found to amount to around 85 fs. Therefore this recurring wave packet does not affect the dynamics initiated by shorter laser pulses that cease to show intensity once the wave packet reappears. In the SH simulations that feature only independent trajectories, the interplay of the returning excited wave packet with the ground state population is completely absent and slightly more population than with the shorter pulses is excited. Therefore, a first conclusion from the SO_2 model can already be drawn: SH is capable to qualitatively capture the interaction with short pump pulses, but long pulses pose the threat of additional interactions with recurring parts of the wave packet that cannot be recovered with SH. In passing, it is noted that vMCG needs more than 100 Gaussian basis functions to qualitatively capture the returning wave packets for the FWHM= 200 fs pulse due to the permanent excitation of small portions of the ground state wave packet throughout the pulse duration, spreading the basis functions across a large part of configurational space.

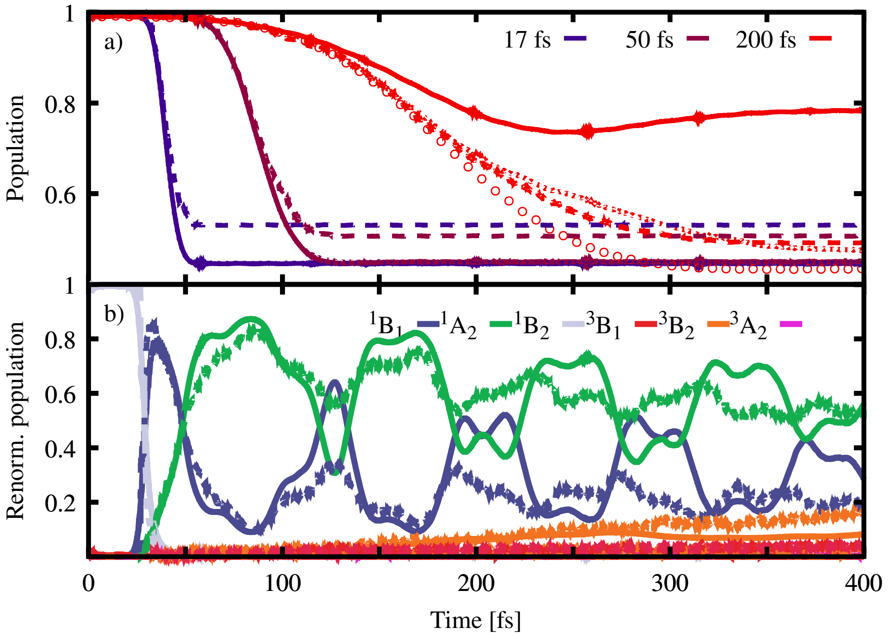

Figure 8: a) Ground state population of SO_2 for three different pulse lengths. For each of these pulse lengths populations obtained with SH (dashed), MCTDH (solid), and vMCG with 75 Gaussian basis functions (dotted) are shown. MCTDH populations for the FWHM= 200 fs pulse with complex absorbing potentials in the excited states are plotted with circles. b) renormalized excited state populations of SO_2 after excitation with a FWHM= 17 fs pump pulse for SH (dashed) and MCTDH (solid).

With this first analysis of the influence of the pulse length on the amount of excited population being finalized, in a next step a short pulse length of 17 fs is taken that is then used to compare the different SH protocols to the MCTDH reference. When comparing the influence of the SH protocols on the ground state population during the dynamics, it is found that not using a decoherence correction gives the largest deviations from the MCTDH; This can be attributed to the overcoherent dragging of S_0 population away from the Franck-Condon region. Fast convergence towards a pure state that does not retain ground state character therefore seems to be required to not be trapped in a cycle of excitation followed by deexcitation.

For the quantification of the ϵ values for the excited states, the difference in the total amount of excited population between MCTDH and SH is factored out, by renormalizing the excited state population in every time step for each method. An example for these renormalized populations is given in Figure 8b. The so-obtained error values are then found at similar values than without the initial laser excitation, sometimes even at lower values than before due to the loss of the fine structure of the rapid MCTDH oscillations caused by the delayed excitation for parts of the wave packet by the pulse. Combining all deviations, the neglect of decoherence is found to have the largest impact on the overall error followed by the use of the diagonal representation. For the former, the driving factor for the error is the description of the laser-trajectory interaction while the latter gives rise to the largest deviations in the triplet states.

For the 2-thiocytosine, the same set of analyses has been conducted, first treating the effect on the amount of the excited population followed by the dynamics within the excited states. The impact of the pulse duration on the transfer from the S_0 population is shown in Figure 9a for three different pulse lengths that each feature adapted amplitudes to yield the same intensity over the complete pulse duration. Depending on the duration of the pulse, MCTDH predicts a decrease down to 10-30% with longer pulses exciting more population and the 50 and 200 fs FWHM pulses exciting the same amount of population. Therefore, it the anomalous behavior observed for the longer pulses in SO_2 is not found in this model system of 2-thiocytosine, indicating the following: Either the excited state wave packet does not return in the Franck-Condon region within the duration of the pump pulse or the returning parts of the wave packet populate states of different energies that are not in resonance with the initial pump pulse, therefore minimizing additional coupling terms or a combination of both effects.

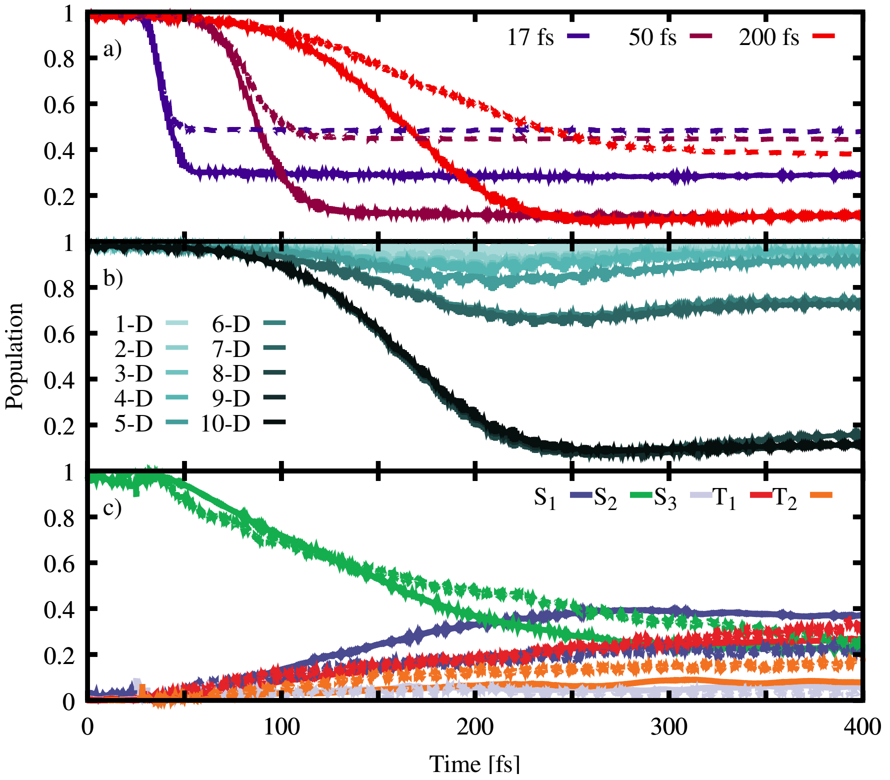

Figure 9: a) Ground state population of 2-thiocytosine for three different pulse lengths. For each of these pulse lengths populations obtained with SH (dashed) and MCTDH (solid) are shown. b) renormalized excited state populations of 2-thiocytosine after excitation with a FWHM= 17 fs pump pulse for SH (dashed) and MCTDH (solid). c) Ground state populations of truncated models of 2-thiocytosine ranging from containing only one to ten vibrational modes during excitation with a FWHM= 200 fs pulse, calculated with MCTDH.

The behavior of the S_0 population in the presence of the 200 fs FWHM pulse is investigated in more detail by repeating these MCTDH simulations for model systems of 2-thiocytosine containing different numbers of normal modes. To do so, the most important x vibrational modes have been taken to form new LVC Hamiltonians, with x ranging from one to ten. The obtained S_0 populations for these ten model systems are shown in Figure 9b. For very low-dimensional systems, almost all of the population that is excited throughout the dynamics is transferred back to the S_0 towards the end of the pulse duration. Increasing the number of vibrational modes opens up additional molecular movements in the excited states as well as increasing the interaction to other states, therefore increasing the time needed for a revival of the excited state wave packet. It is found that this increase in the revival time is not a step-wise increase where each added normal mode will finally result in a larger amount of excited population after the pulse but instead seems to be mostly bound to specific normal modes. Nevertheless, the overall trend is clear: The larger the investigated molecular system, the longer the time needed for a coherent revival of the excited state wave packet, therefore quenching the influence of this nuclear quantum effect.

When comparing the MCTDH populations to the respective SH simulations in Figure 9a to estimate the capability of SH to mimic the excitation process, a much less pronounced excitation for the SH dynamics is seen, exciting between 40 to 50% of S_0 population. Therefore the same trend as in SO_2 is found with SH underestimating the amount of excited population for all employed pulses. When inspecting the influence the choice of SH protocol has on the excitation of population for the FWHM= 17 fs pulse, it is found that the only considered choice that shows a systematic negative effect is neglect of a decoherence correction. It has to be noted that the large deviation between the SH and MCTDH populations in this work can partially be attributed to the large field strengths employed that were chosen so that around 50% of the SH population are excited to provide good statistics for the SH simulations. Since the amount of excited population is found to be higher in the MCTDH simulations, additional interference terms during the excitation process due to the strong laser field might be at work that are missed out on in SH.

Finally, the differences in the excited state dynamics following excitation have been investigated. Again, the differences due to the different amount of excited populations are removed by renormalizing the excited state populations in each time step. A depiction of the renormalized excited state populations for dynamics on the 2-thiocytosine model system for both MCTDH and a single SH protocol is shown in Figure 9c. Repeating these dynamics for a set of SH protocols, it is found that rescaling of the kinetic energy along the gradient difference vector has moved from being one of the worst choices to being the best available option. The MCH picture was found to be slightly favored to the completely diagonal represenation. All other protocols where found with very similar deviations from the MCTDH results.

4.2.3 *Insights Gained and Place in the Larger Picture*

Using simple analytical PESs constructed from a mapping of the full molecular configuration spaces onto LVC Hamiltonians allows for the side-by-side comparison of SH with higher-level reference methods for non-adiabatic dynamics in the absence and presence of external laser fields. The so-enabled benchmark of various SH protocols on the many-mode model potentials of SO_2 and 2-thiocytosine aims at estimating the accuracy of SH to describe the light-matter interaction in molecules, going beyond the commonly employed one-dimensional test systems where some of the deficiencies of SH have been highlighted.[49,50,53,55,59] Performing this benchmark revealed an underestimation of the amount of excited population for SH when compared to MCTDH dynamics for both systems. A driving factor for the deviations observed from the reference quantum results was the neglect of a treatment for the overcoherence inherent to SH. Furthermore, it was found to be problematic for SH when combining low-dimensional molecular systems with laser pulses long enough that they persist until parts of the excited state wave packet return to the Franck-Condon region. Apart from these issues, most SH protocols are able to at least qualitatively describe the evolution of the populations throughout the pump pulse and the subsequent excited state dynamics. The differences in deviations from the reference MCTDH results for good and bad performing SH protocols is found to be rather high, with good sets yielding only up to half the amount of the deviation of bad sets. Unfortunately, no overall best performing set can be identified but instead options have been identified that more often than not increase the agreement with reference simulations when compared to standard SH. Overall, the choice of the most appropriate SH protocol remains a system- and problem-dependent choice with some guide lines as to where some of the strengths and weaknesses of different options may be found and estimations on how large the deviation from the reference can be.

Although serving as a first benchmark of the laser-matter interaction for larger molecules, the current investigation is far from complete and should be expanded on in the future. Routes that should be considered in the future include the use of more test systems as well as the evaluation and comparison of additional electronic and nuclear observables to avoid the pitfall of coincidental good agreement in the one considered observable. Finally, the current set of considered SH protocols is missing the Floquet representation, which has recently been found to be a promising basis for SH, providing the closest match to quantum results.[55,59] Nevertheless, the presented investigation provides a reference for the simulation of SH dynamics in the presence of laser pulses for realistic molecular systems. While no clear conclusion on the best use of SH protocols can be drawn, an estimate on the shortcomings of SH can be made when treating systems too large to be treated with methods that include more nuclear quantum effects. As such, this work lays the foundation for the investigation of a large transition metal complex that will be the focal point of the next chapter of this thesis, making full use of the already successfully employed LVC potentials and the insights gained in this benchmark to use a meaningful SH protocol to simulate and modify the respective excited state dynamics.

5

THE LONG ROAD TO LASER CONTROL IN A PHOTOSENSITIZER

Having been confronted in Chapter 3 with an almost insurmountable obstacle in the form of computational cost to provide the PESs necessary for propagation thereon, the original goal of performing on-the-fly laser control simulations on pyrrole has been abandoned. This triggered the search for a simpler way to represent the PESs in order to focus on the aspect of simulating the interaction of matter with laser pulses. Such a method was found in the form of LVC potentials where the possibility to utilize these analytical expressions to compare SH to reference methods was explored extensively in Chapter 4. Being supplied after this detour from the original goals with both the LVC potentials for fast evaluations of the PESs and estimates of the issues encountered in SH when including laser fields in the simulation, the final Chapter now returns to the original roots of this thesis: The excited state dynamics of the transition metal photosensitizer $[\mathrm{Ru}(^{\mathrm{S-S}}\mathrm{bpy})(\mathrm{bpy})_2]^{2+}$ (bpy=2,2'-bipyridine) featuring a sulfur-bridged ligand[166] are investigated in detail and control pulses are proposed to slow down or even halt the prevalent relaxation mechanism. All these detailed simulations are made possible by the use of the combined LVC/SH approach, allowing for remarkably fast calculations even for systems as large as $[\mathrm{Ru}(^{\mathrm{S-S}}\mathrm{bpy})(\mathrm{bpy})_2]^{2+}$.

The initial characterization of $[\mathrm{Ru}(^{\mathrm{S-S}}\mathrm{bpy})(\mathrm{bpy})_2]^{2+}$ has been conducted in close collaboration with experimental collaborators and is published in *Inorg. Chem.* with the title "Electrochemical and photophysical properties of ruthenium(II) complexes equipped with sulfurated bipyridine ligands". For this investigation of the properties of the complex around the ground state minimum energy geometry, only static calculations have been employed. This endeavour is followed by a parametrization of a LVC model that is subsequently used to perform SH dynamics starting from excited states of two different excitation windows without explicit laser pulses. These excitation windows represent excitation into two contrasting initial states where the excited electron is either located at one of the bpy or the $^{\mathrm{S-S}}$bpy ligand. The details and results to these simulations are also published in *Inorg. Chem.* titled "Excited-state dynamics of $[\mathrm{Ru}(^{\mathrm{S-S}}\mathrm{bpy})(\mathrm{bpy})_2]^{2+}$ to form long-lived localized triplet states". With the natural non-adiabatic dynamics of the complex being known, explicit laser pulses are employed to excite the ground state population and to design pulse schemes capable of driving the excited state dynamics away from their natural evolution. The employed pulses are able to trap the excited state population in a pump-relaxation-pump circle as long as the laser pulse is acting on the system. These findings are currently submitted to *J. Phys. Chem. Lett.* and represent the final culmination of this work in presenting the tools to steer the excited state dynamics of a transition metal complex in 161 vibrational degrees of freedom and a set of 79 electronic states.

5.1 $[\mathrm{RU}(^{\mathrm{S-S}}\mathrm{BPY})(\mathrm{BPY})_2]^{2+}$, A NOVEL PHOTOSENSITIZER

One of the archetypical photosensitizers extensively used is $[\mathrm{Ru}(\mathrm{bpy})_3]^{2+}$, capable of absorbing light in the blue part of the visible spectrum of light and subsequently transferring the energy from a long-lived triplet state to other molecules.[167–172]

Due to this long ancestry, $[Ru(bpy)_3]^{2+}$ serves as a prototype for many derived photosensitizers that try to either enhance or supplement the functionality already found in the unmodified transition metal complex. One such modification is the addition of a disulfide bridge to the backbone of one of the bpy ligands, thereby introducing the possibility to harbor electrons and protons on the new functionality by cleavage of the disulfide bond.[166]

To assess the properties of this $[Ru(^{S-S}bpy)(bpy)_2]^{2+}$ complex, a combined experimental and theoretical study has been conducted. Here, two features are investigated: On the one hand, the absorptive features are elucidated in detail using both experimental and theoretical data. On the other hand, the capabilities to store additional electrons on the modified ligand are determined using electrochemical measurements. The electrochemical data provided by a research team of the University of Göttingen showed that a reversible uptake of up to two electrons on the newly introduced $^{S-S}$bpy ligand can be achieved to form the neutral $[Ru(^{S-S}bpy)(bpy)_2]$ complex. However, this neutral complex decomposes at room temperature in the used acetonitrile solvent by extrusion of a sulfide ion (S^{2-}) to form $[Ru(^{S}bpy)(bpy)_2]^{2+}$ where the single sulfur now connects to both pyridine rings. At lower temperatures, this decay path was no longer observed and the neutral complex was found to be stable.

5.1.1 *The Dual Nature of the Absorption of* $[Ru(^{S-S}bpy)(bpy)_2]^{2+}$

When measuring absorption spectra of $[Ru(^{S-S}bpy)(bpy)_2]^{2+}$ and $[Ru(^{S}bpy)(bpy)_2]^{2+}$, an interesting observation was made: The absorption of the new $[Ru(^{S-S}bpy)(bpy)_2]^{2+}$ complex in acetonitrile shows an additional low energy shoulder when compared to the absorption spectrum of the parent $[Ru(bpy)_3]^{2+}$ complex. This shoulder is absent for the electrochemical decomposition product $[Ru(^{S}bpy)(bpy)_2]^{2+}$ that is found with an absorption spectrum that is essentially identical to the one of $[Ru(bpy)_3]^{2+}$. Theoretical calculations at the TDDFT level have been carried out investigate the processes leading to the changes in the absorption spectra. The calculated excited states are analysed based on the distribution of the electron that is excited with respect to the ground state configuration, taking into account both from where (labelled *hole*) and to where (labelled *electron*) the electron is excited. For this, four fragments are defined and a short-hand notation introduced that will see use throughout this whole chapter: The central ruthenium atom (M), each bpy ligand (L), and the modified ligand (S) being either $^{S-S}$bpy or ^{S}bpy. If an excitation has both the electron and the hole on the same fragment, this is a fragment-centered excitation (C), e.g. a ruthenium-centered excitation will be written as MC. The opposite case, where the electron is transferred from one fragment to another is a charge-transfer excitation (CT). Here, the hole-fragment will be written in front followed by the electron-fragment which is then followed by CT, giving rise to labels like MSCT to indicate a transfer of an electron from the ruthenium to the $^{S-S}$bpy or ^{S}bpy ligands. A depiction of all 10 possibilities to characterize an excitation using this scheme is given in Figure 10.

The absorption spectrum of the two transition metal complexes has been calculated by generating an ensemble of geometries based on a Wigner distribution and calculating the excited states for each of these structures. Using the scheme presented above, analysis of all excited states based on the type of excitation allows for dividing the total absorption onto the different types of states. The simulated absorption spectrum including this separation into different contributions is shown

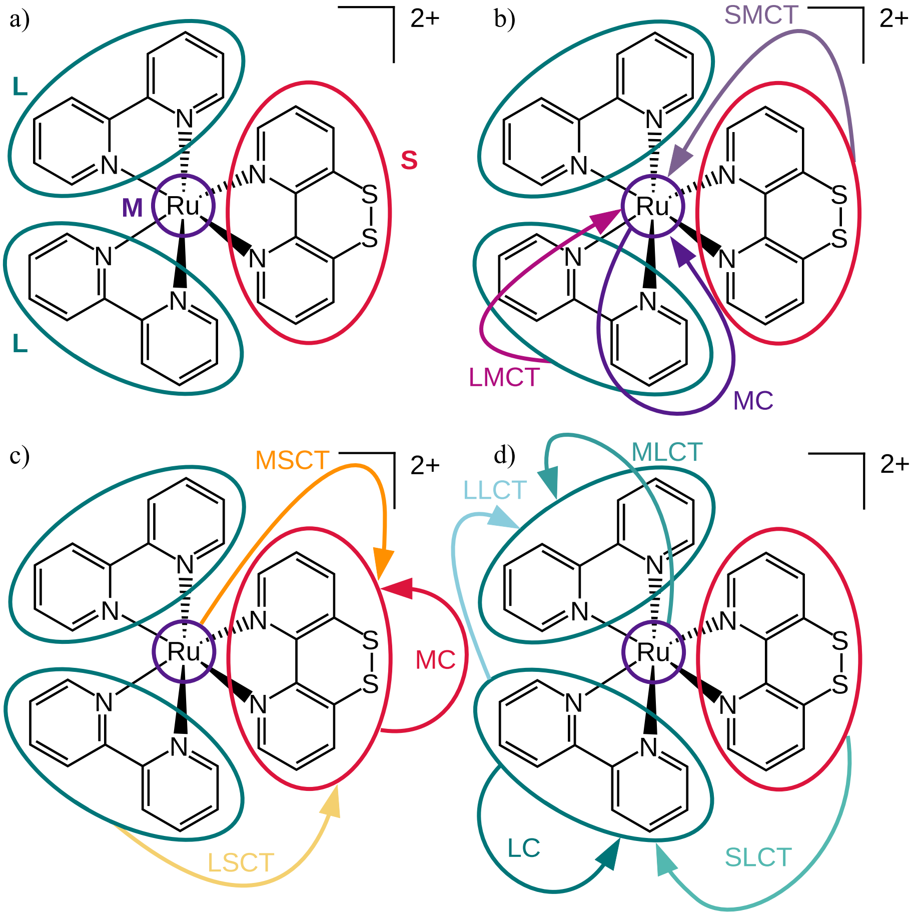

Figure 10: The different fragments used for the analysis of the possible excitations present in [Ru($^{S-S}$bpy)(bpy)$_2$]$^{2+}$ and [Ru(^{S}bpy)(bpy)$_2$]$^{2+}$ are shown with their respective labels and colors that will be used in this chapter. Arrows indicate excitations with the base of the arrow being the hole fragment and the tip of the arrow pointing to the electron fragment. a) Definition of the fragments. b) All possible excitations where the excited electron ends up on the central metal atom. c) All possible excitations where the excited electron ends up on the [Ru($^{S-S}$bpy)(bpy)$_2$]$^{2+}$ or [Ru(^{S}bpy)(bpy)$_2$]$^{2+}$ ligand. d) All possible excitations where the excited electron ends up on one of the two bpy ligands.

in Figure 11. Here it can be seen that the shape of the calculated spectrum closely matches the experimental reference, predicting the shoulder at low energy as well as the main absorption peak and the high energy shoulder located at 400 nm. The biggest deviation from the experiment is a slightly larger absorbance of the low energy shoulder which in the theoretical calculations is predicted as a separate peak. When decomposing the spectrum with respect to the character of the absorbing states, it is found that the low energy shoulder consists almost exclusively of SC and MSCT states with a small contribution of MLCT states. The reverse is true for the main absorptive feature that almost exclusively consists of absorption into MLCT states with a small participation of LC and MSCT states. Therefore, it can be concluded that the low energy shoulder is due to the presence of the disulfide bridge at the backbone of the $^{S-S}$bpy ligand, locating the absorptive excited states of this ligand at lower energies than the corresponding states at the bare bpy ligands. The absorptive properties of the other bpy ligands are not affected by the modification of

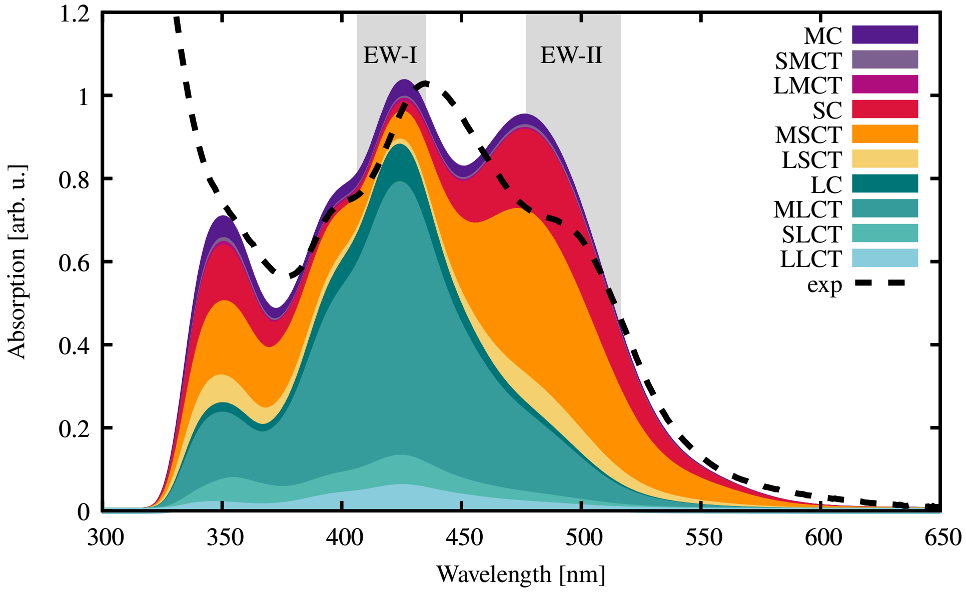

Figure 11: Experimental (black dashed) and simulated absorption spectrum (filled) of $[Ru(^{S-S}bpy)(bpy)_2]^{2+}$. The theoretical spectrum is subdivided into the contribution of the different types of excitations towards the total spectrum (see Figure 10 for the different possibilities) that are stacked on top of each other in the plot. In addition, the energy ranges that are later used to initialize excited trajectories are indicated in gray and labelled as EW-I (excitation window 1) and EW-II (excitation window 2).

a single bpy ligand and are found to still absorb at similar wave lengths as for the unmodified $[Ru(bpy)_3]^{2+}$ complex.

Interestingly, the low energy shoulder almost completely vanishes if the calculations are repeated in gas phase. Hence, the lowering of the energy of absorptive states that locate the excited electron at the $^{S-S}$bpy ligand is due to interactions with the polar solvent. Similar to the experimental observations, no redshifted shoulder is observed for $[Ru(^{S}bpy)(bpy)_2]^{2+}$, indicating that the energy-lowering feature observed before is solely due to the disulfide bridge and its interactions with the surrounding solvent. On a side note, these calculations have been repeated using ORCA 4.2[173] instead of Gaussian09,[174] to test the influence of the different implicit solvent models in these programs on the observed results. Here it has been found that the low energy shoulder was less pronounced when using ORCA, highlighting how small differences in how the implicit solvent is modelled can change the energetic shift of the states involving the $^{S-S}$bpy ligand.

Overall, for the photophysical properties it is found that addition of a bridging disulfide to one of the bpy ligands extends the absorptive range towards lower energies. This feature is solvent dependent and lost upon loss of a sulfur atom. Disentangling the absorption spectrum into different classes of states depending on the location of the excited electron before and after the excitation shows that both the main absorption feature as well as the low energy shoulder are dominated by specific types of excited states. The distinct spectral separation between states that locate the excited electron either at the sulfurated or the default bpy ligand opens up the possibility for selective excitation into one of both sets of states, potentially triggering different excited state dynamics. Since different possible pathways for dynamics could limit or even enhance the applicability of the investigated photosensitizer, this possibility needs to be explored in more detail. To gain insight into the dynamics initiated by excitation into the two differing sets of states, the subsequent excited state dynamics needs to be simulated. Since this separation between the states was not found in [Ru(^{S}bpy)(bpy)$_2$]$^{2+}$, this complex is not investigated further.

5.1.2 *Parametrizing a Giant: LVC Model for [Ru($^{S-S}$bpy)(bpy)$_2$]$^{2+}$*

The full-dimensional simulation of the excited state dynamics of a system as large as [Ru($^{S-S}$bpy)(bpy)$_2$]$^{2+}$ poses a serious challenge, straining both the limits of the electronic structure method and the dynamics method employed. As shown in the previous chapter, the workload for such an endeavor can be drastically reduced by precomputing a set of PESs. Following suit with the previous chapter, we use the LVC model for the approximation of the complete PESs, an approach that is often used for similar rigid complexes.[10,175,176] Since the previously employed TDDFT protocol is able to correctly predict the shape of the absorptive features between 600 and 400 nm and places the absorption energies close to experimental values, the same level of theory is used to parametrize the LVC model. Nevertheless, it should be noted that a good agreement for the description of the bright singlet states is probably not sufficient when ISC dynamics will be simulated especially since different TDDFT functionals can give quite different results for the singlet-triplet energy gaps, hence influencing the observed ISC rates.[177]

The parametrized full-dimensional LVC model features 177 normal modes and 21 singlet plus 20 triplet states. With this LVC model it was possible to reproduce the main features of the absorption spectrum apart from a shift to higher energies for the absorption peak associated with ecxitation into MLCT states. When investigating the excited state PESs in more detail - prior to dynamics simulations - it became evident that the full LVC template is flawed in its description of the expected photodynamics: When optimizing the lowest energy structure of the lowest energy triplet state (T_1) using TDDFT, it was found that the S–S bond is drastically weakened in the final structure, increasing from 2.11 Å to 2.57 Å. Since the LVC model only guarantees a reasonable description of the PESs close to the reference point (in this case the ground state equilibrium geometry), the LVC PESs will most likely be unable to describe structures further away from the reference point like the observed T_1 minimum energy structure. As the strong SOCs in the [Ru($^{S-S}$bpy)(bpy)$_2$]$^{2+}$ complex will result in a fast population of triplet states including the T_1, extra measures have been taken to identify the normal modes responsible for the largest deviations from the expected T_1 minimum structure and the TDDFT S_0-T_1 energy difference between the respective optimized structures. For this, the lowest frequency normal modes have been successively deactivated (i.e. first deactivating only the lowest energy mode, then deactivating the lowest two and so on) and the T_1 minimum energy structure optimized, keeping track of the S_0-T_1 energy gap, the final S–S bond length and other geometrical deviations from the TDFFT structure. The reason to specifically target low-energy modes is that these modes often describe rotations around bonds that cannot be described properly with the employed harmonic potentials, therefore introducing potentially large errors. In the light of this analysis, 16 vibrational modes and one triplet state have been removed from the LVC model. With this reduced LVC model featuring 166 vibrational normal modes, 21 singlet and 19 triplet states, the T_1 minimum energy structure features a S–S bond length of 2.34 Å and a energy difference of 1.57 eV to the S_0 energy at the equilibrium geometry compared to a disulfide bond of 2.57 Å and an energy of 1.41 eV for the T_1 geometry directly minimized with TDDFT. Although this agreement is more qualitative than quantitative, it represents the best compromise between being able to describe the encountered structural change and not cutting away too many modes that could be relevant for other pathways.

5.1.3 *Selective Excitation - Initiating Dynamics from Two Different Sets of States*

To investigate the possibly different excited state dynamics after exciting into different parts of the low energy absorptive feature of $[\mathrm{Ru}(^{\mathrm{S-S}}\mathrm{bpy})(\mathrm{bpy})_2]^{2+}$, SH dynamics are employed using the LVC model that has been adjusted in the previous section. Initial conditions for the dynamics are generated from a set of 10,000 nuclear geometries taken from a ground state Wigner distribution. No explicit laser was used in this part of the thesis to excite the molecule; instead instantaneous excitation using a stochastic selection based on the oscillator strength of excited states that fall within a given energy range was employed. Two of those excitation windows (EW) were chosen that are also depicted in Figure 11: A high energy window (EW-I) between 2.85-3.05 eV that includes the absorption peak and mostly excites into MLCT states. A lower energy window (EW-II) that excites into the red shoulder consisting mostly of excitation into either SC or MSCT states. Using this excitation scheme, a total of 5125 trajectories are excited for EW-I and 3838 in EW-II. All excited trajectories are used in the subsequent SH dynamics, hence providing way more trajectories and statistical significance than would be possible if one would not use precomputed PESs. The simulated evolution from these two different starting points is analyzed considering three main aspects to shed light onto the excited state pathways of $[\mathrm{Ru}(^{\mathrm{S-S}}\mathrm{bpy})(\mathrm{bpy})_2]^{2+}$: First, the singlet to triplet crossing rate is inspected. Second, the progression of the different excited state characters is considered to gain insight into the location of both the hole and the excited electron throughout the dynamics. Lastly, the dynamical structural relaxation into the T_1 minimum energy structure is studied.

A graphical overview of the ISC dynamics starting from both EWs is shown in Figure 12a and 12b. Here it can be seen that initially, all population resides in singlet states. This is due to the chosen mode of excitation as only singlet states have a non-vanishing oscillator strength with the singlet ground state and spin-mixing due to the SOCs was neglected throughout the excitation process. Once the dynamics starts, the singlet population declines rapidly throughout the first few femtoseconds before slowing down a bit after around 50 fs. Overall, both dynamics show a very similar behavior for the ISC evolution and end up with very similar final triplet populations of 80% (EW-I) and 86% (EW-II) after 250 fs of simulated dynamics. The transfer to the triplet manifold therefore occurs on an ultrafast timescale with an almost quantitative yield. The obtained singlet and triplet populations have been fitted using a kinetic model involving three species: A fast ($^{\mathrm{fast}}\mathrm{S}$) and a slow reacting singlet component ($^{\mathrm{slow}}\mathrm{S}$), and the triplet states. It was assumed that $^{\mathrm{fast}}\mathrm{S}$ is interconnected via internal conversion to $^{\mathrm{slow}}\mathrm{S}$ with a time constant k^{IC}. The triplet states can be accessed via ISC from both singlet components with the time constants $k^{\mathrm{ISC,fast}}$ and $k^{\mathrm{ISC,slow}}$. Using this scheme, ISC from $^{\mathrm{fast}}\mathrm{S}$ was observed with 46 fs (EW-I) and 43 fs (EW-II) while $k^{\mathrm{ISC,slow}}$ amounts to 337 fs (EW-I) and 256 fs (EW-II). In an attempt to understand the two singlet components and their respective transfer towards the triplet in greater detail, the SH simulations were repeated but this time the geometries were frozen, preventing any movement away from the initial Wigner-sampled geometry. In this

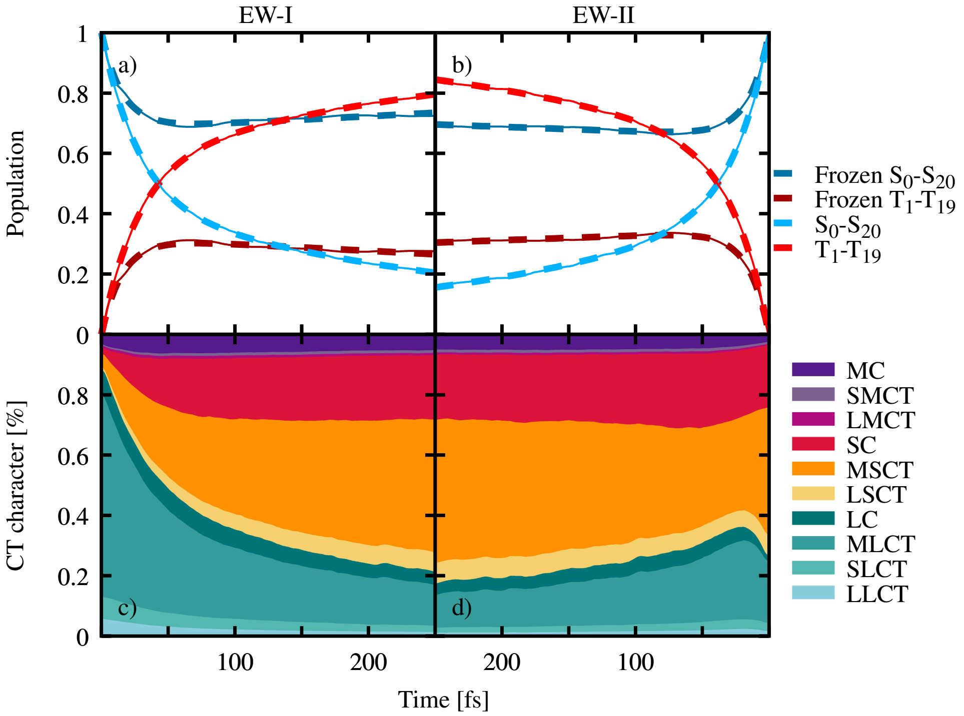

Figure 12: Overview over the evolution of states in the dynamics of the [Ru($^{S-S}$bpy)(bpy)$_2$]$^{2+}$ complex initiated in two different excitation windows (EW-I on the left and EW-II on the right). Note the reversed time axis for the right panels to better compare the final populations at the end of the simulations. a) and b) Sum of singlet (blue) and triplet (red) populations (dashed). Populations obtained from frozen dynamics are depicted in dark blue (singlets) and dark red (triplets). The fitted population evolution is shown as thin solid line in the respective colors. c) and d) Share of the respective CT character along the dynamics as a stacked plot.

way, the original Gaussian-shape of the Wigner distribution in all normal modes is kept while the electronic wave function evolves for each geometry. The resulting singlet and triplet populations are fitted using the same three-component scheme as before, yielding $k^{\mathrm{ISC,fast}}$ values of 49 fs (EW-I) and 44 fs (EW-II), very much in agreement with the unfrozen dynamics. For the ISC rate from the $^{\mathrm{slow}}$S component, however, time constants of -3189 fs (EW-I) and -4377 fs (EW-II) are found, indicating a very slow repopulation of $^{\mathrm{slow}}$S. Since restraining any nuclear movement did not affect the transfer due to the fast ISC component blocks the ISC from $^{\mathrm{slow}}$S, $k^{\mathrm{ISC,fast}}$ is caused exclusively by electronic mixing of the states due to the strong SOCs and the presence of triplet states in the close vicninity of the initially excited states. Therefore, $k^{\mathrm{ISC,slow}}$ represents ISC due to structural relaxation that is absent in the frozen dynamics. With this realization, the spotlight can be moved away from the finer details of the ISC dynamics towards a comparison of the obtained speed for ISC: A collaboration with experimental partners in Göttingen using femtosecond transient absorption spectroscopy to measure the time scale of relaxation processes in [Ru($^{S-S}$bpy)(bpy)$_2$]$^{2+}$ in acetonitrile revealed that the population of triplet states occurs within less than 80 fs, therefore agreeing very well with the theoretical simulations. These numbers can then be compared to the ISC dynamics of the parent compound [Ru(bpy)$_3$]$^{2+}$. Previous experimental[178,179] and other theoretical investigations[148,149] on this compund locate the time needed for ISC below 100 fs, most of them even below 50 fs. Therefore, the ISC occurs for both complexes at very similar time scales with limited influence of the modified ligand.

Next, the nature of the excited states is investigated. For this, the evolution of the swarm of trajectories is cast into the CT description introduced in Section 5.1.1, analyzing each populated state based on the fragments where the excited electron is transferred from and to. The initial distribution of populated states for EW-I locates almost 90% of the excited electron on one of the two bpy ligands with most of the contribution coming from MLCT states. With the onset of the dynamics a rapid transfer towards SC and MSCT states is observed, leaving only around 20% of the population in MLCT or LC states after 250 fs of simulation. After its initial increase, the SC population stagnates at around 20% after 100 fs leaving only the MSCT character to increase considerably afterwards. At the end of the simulation time, no equilibrium for the CT characters is reached, but most of the transfer seems to have concluded. A completely different starting setup is found for EW-II since this window excites into the low energy shoulder, harboring mainly states where the excited electron is located on the $^{S-S}$bpy ligand: A large portion of the excited electron is already located in SC and MSCT states with only 25% being found on the bpy ligands. The first few femtoseconds of dynamics see a short increase in MLCT and LC states, followed by a slow decline of these contributions starting after 20 fs. Similar to EW-I, the SC population increases and stagnates already after only 50 fs, the MSCT contribution increases until the end of the simulation. When comparing the final distribution of the hole and the excited electron, almost identical values are found for both EWs. Therefore, it can be concluded that predominantly MSCT and SC states are populated throughout the dynamics, indicating that the lower energy associated with these states leads to a fast population of those states. The reversibility of the population transfer is decreased due to nuclear relaxation in the low-lying MSCT and SC states. Finally, it should be noted that the changes in population within the very first tens of femtoseconds are due only to electronic coupling of the states without any additional nuclear relaxation and happen on almost the same timescale as the previously observed $k^{\mathrm{ISC,fast}}$. The high density of states - layering state upon state like in a Dobos cake - therefore allows for an almost immediate mixing of states once SOCs are included.

Having investigated the evolution of the electronic wave function by itself, the electronic character will now be linked to the most important nuclear rearrangement that is observed throughout the dynamics: the elongation of the S–S bond at the $^{S-S}$bpy ligand. As elongation of this bond is the defining geometrical feature of the T_1 minimum energy structure, such an analysis will reveal how fast the T_1 structure can be accessed. A depiction of a few snapshots of the combined dynamics starting from EW-I and EW-II is shown in Figure 13 where the swarms of trajectories are plotted against the S–S bond length and the energy gap defined by the energetic difference of the currently active state and the ground state. From this analysis it can be seen that the initial S–S bond lengths at $t = 0$ fs gets elongated during the dynamics for almost all trajectories due to slightly elongated equilibrium S–S bond lengths in most excited states. After around 100 fs, a few trajectories are found with a disulfide bond length that matches the T_1 minimum energy structure. These trajectories are found with a very small energy gap to the ground state due to the destabilization of the ground state upon elongation of the S–S bond. A few trajectories even undergo hops to the ground state that are labelled erroneous since the respective non-adiabatic couplings to the ground state are not included in the used LVC model. When going to later simulation times, the amount of trajectories revolving around the T_1 equilibrium S–S

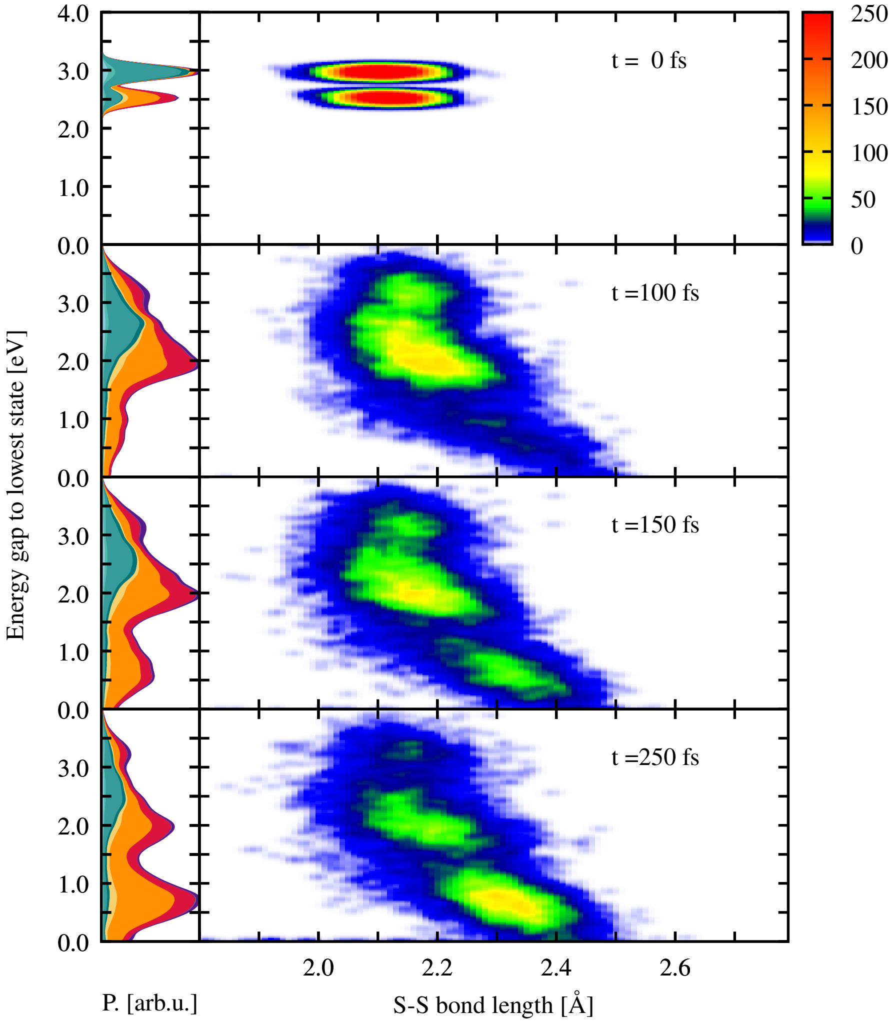

Figure 13: Analysis of the excited state dynamics of [Ru($^{S-S}$bpy)(bpy)$_2$]$^{2+}$ starting from both EWs. Left-hand side panels show the distribution of the wave function character against the energy gap between the classical active state and the lowest singlet state. The density is normalized in every time-step. On the right-hand side, a convoluted scatter plot of the SS bond length with the corresponding energy gaps to the lowest state is given.

bond length increases until it is the most abundant molecular configuration. Pairing this analysis with the distribution of the different CT characters shows that there seem to exist different minima that can be accessed throughout the dynamics each characterized by a specific mix of wave function character and a specific energy gap to the lowest energy state: A high-energy minimum located at an energy gap of around 3.3 eV that consists of an almost equal mixture of MLCT, MSCT, SC and MC states that sees some population throughout the complete dynamics that only slowly drains towards lower energy structures. Two minima at intermediate energy gaps of 2.6 and 2.0 eV with the former being of predominantly MLCT and the latter of MSCT and SC character. The T_1 associated minimum that is located at an energy gap of 0.7 eV in the dynamics with the excited electron residing on the $^{S-S}$bpy ligand. The same analysis for both EWs predicts very similar results, which was the reason why only the combined analysis was plotted here.

5.1.4 *Insights Gained and Place in the Larger Picture*

$[\mathrm{Ru}(^{\mathrm{S-S}}\mathrm{bpy})(\mathrm{bpy})_2]^{2+}$ showed two distinctly different excited state compositions within its first absorption band: At wave lengths very close to the first absorption maximum of the parent $[\mathrm{Ru}(\mathrm{bpy})_3]^{2+}$ complex, this absorption is dominated by MLCT states. The low-energy shoulder to this absorption peak is found to consist of excitation into states that locate the excited electron at the $^{\mathrm{S-S}}$bpy ligand. Combining the results from the three analyses conducted in the previous Section, it can be gathered that $[\mathrm{Ru}(^{\mathrm{S-S}}\mathrm{bpy})(\mathrm{bpy})_2]^{2+}$ undergoes ultrafast ISC within less than 50 fs, resulting in almost quantitative population of the T_1 minimum within 250 fs. These processes are observed regardless of the used wavelength for excitation, showing only slight differences in the ISC rates and how fast the excited electron will be located at the $^{\mathrm{S-S}}$bpy ligand. From a practical point of view, this means that the excited electron will always be located on the sulfurated ligand, reaching the same T_1 minimum energy structure from where the energy can be transferred towards other species. The introduction of the $^{\mathrm{S-S}}$bpy ligand therefore just extends the absorptive range towards the red part of the spectrum when compared to the parent $[\mathrm{Ru}(\mathrm{bpy})_3]^{2+}$ without introducing additional wavelength dependent deactivation channels that could possibly interfere with its use as a photosensitizer. The presented dynamics highlights the strengths of the LVC/SH approach in making these dynamics accessible while at the same time show the drawbacks associated with this methodology in the form of the manual reduction of the model to be able to describe the T_1 minimum energy structure and how to tackle these obstacles.

The parametrization and evaluation of the LVC model for $[\mathrm{Ru}(^{\mathrm{S-S}}\mathrm{bpy})(\mathrm{bpy})_2]^{2+}$ provides the key ingredients for the final part of this thesis. Being equipped both with a LVC Hamiltonian and knowledge of the natural excited state dynamics of this complex, an in depth study of the excited state dynamics under the influence of explicit external fields can be conducted. Similar to Section 4.2.2, the LVC model enables such investigations that would require a large number of trajectories and a plethora of electronic structure evaluations to treat the rapidly oscillating fields correctly.

5.2 EXPLICIT FIELDS: EXCITATION AND CONTROL OF THE PHOTODYNAMICS OF $[\mathrm{RU}(^{\mathrm{S-S}}\mathrm{BPY})(\mathrm{BPY})_2]^{2+}$

The previous section laid out and traversed the path to simulate the excited state dynamics of $[\mathrm{Ru}(^{\mathrm{S-S}}\mathrm{bpy})(\mathrm{bpy})_2]^{2+}$ starting from a set of excited states mimicking excitation into two different parts of the low-energy absorption peak. Ultrafast ISC was observed followed by a relaxation towards states that feature the excited electron on the $^{\mathrm{S-S}}$bpy ligand, resulting in a weakening of the S–S bond, further stabilizing the corresponding states, yielding the lowest energy geometry of the T_1 state. Comparison with experimental measurements showed a general agreement with the simulations for the observed time scales, however the details of the ultrafast dynamics largely remained hidden in the time-resolution of the experimental setup.

An important next step is modelling the external fields that are involved explicitly. In doing so, observables that can be directly compared to experiment are obtained since the spectral and temporal broadening introduced by the use of non-inifintesimal pulses is then also included in the theoretical estimations. In addition to this, laser fields allow for modification of the observed excited state dynamics. In the following, both of these avenues are explored, discussing first the influence of including explicit pump pulses for the excitation of $[\mathrm{Ru}(^{\mathrm{S-S}}\mathrm{bpy})(\mathrm{bpy})_2]^{2+}$. Later, different pulse sequences to modify the prevalent excited state relaxation pathway therein are discussed and put to the test. The focus for the latter task was put on finding very simple pulse shapes and sequences to achieve this task. On the one hand this allows for a easy reproduction in an experimental setup. On the other hand, the employed LVC/SH setup contains inaccuracies in both the electronic structure as well as the dynamical propagation parts, rendering any over-detailed fitting of laser pulses based on LVC/SH probably useless in a potential experimental setup.

5.2.1 *Excitation using Explicit Laser Fields*

For the explicit excitation process of $[\mathrm{Ru}(^{\mathrm{S-S}}\mathrm{bpy})(\mathrm{bpy})_2]^{2+}$, a pump pulse was defined with a Gaussian envelope function following Equation 10. Since the previous section revealed that initial excitation into EW-I and EW-II yield almost identical final states after 250 fs, this section focuses solely on excitation into EW-I with a central frequency of 2.95 eV. The temporal width of the pulse is defined by $t_{\mathrm{FWHM}} = 50$ fs and the center of the pulse set to $t_0 = 75$ fs. For the polarization of the pulse the coordinate axis along which the transition dipole moments from the ground state are the largest has been chosen. For the parametrized LVC model this axis is along x, pointing from the central ruthenium towards $^{\mathrm{S-S}}$bpy. Different values for the amplitude of the pulse have been tested before settling on a field strength that corresponds to a peak intensity of 75 GW/cm^2 (corresponds to $1.46\cdot10^{-3}$ a.u. maximum amplitude of the electric field). With this field strength, 41% of the trajectories could be excited in test calculations. Although a lower ratio of excited trajectories would be sufficient to investigate the results of explicit excitation on the excited state dynamics, the higher ratio is preferred to provide more potential targets for the subsequent control laser that will be introduced later.

With the pump pulse defined above, SH simulations using the same LVC Hamiltonian as in the previous section have been conducted with a set of 4000 initial conditions from a Wigner sampling of the vibrational ground state. The following SH protocol has been applied: nuclear and electronic propagation was performed in the completely diagonal basis where both the off-diagonal coupling terms of the transition dipole moments with the external field and the spin-orbit couplings are projected onto the diagonal of the Hamiltonian, forming a set of spin-mixed states.[57,143] In the context of laser fields, such a procedure is known as instantaneous adiabatic representation or instantaneous Born-Oppenheimer representation.[59] Such a basis has been found to be beneficial compared to keeping the laser interactions as off-diagonal elements in the presence of strong external fields[58] but has also been shown to give unphysical results in other cases where a Floquet basis was found to be superior.[50,55,59] In the current case - similar to the previous section - this diagonal picture is chosen to better account for the strong SOCs in the present complex. A time step of 0.25 fs has been employed for the nuclear propagation while the electronic wave function was propagated using time steps of 0.01 fs in a locally diabatic basis.[106] The size of the nuclear time step has been chosen based on a set of simulations employing differently sized time steps ranging from 0.5 fs to 0.1 fs, finding essentially identical populations for time steps of 0.25 and 0.1 fs with some small deviations for the largest considered time step. With the chosen time step, a maximum simulation time of 350 fs is propagated, equating to 1400 nuclear and 35,000 electronic time steps per trajectory. Following the results obtained in Section 4.2, decoherence of the electronic wave function on different states has been accounted for using an energy-based criterion acting in every time step with a decoherence parameter of 0.1 Hartree.[30,31] For the conservation of the total energy, a special situation is encountered: In the presence of laser fields, energy conservation within a trajectory is complicated by the fact that energy uptake or dissipation in the form of photon absorption or stimulated emission is now possible and will result in changes to the total energy. As discussed before, a differentiation into field-induced and "standard" hops would be needed to decide if velocity adjustment should be conducted or not. However,different possibilities that have been proposed[49,57] for this purpose were found unsuited for the investigated transition metal complex using the diagonal representation and the sets of pulses employed: i) Using a criterion that defines all hops between surfaces where the energy-gap is close to the employed pulse[57] runs into issues when low energy pulses are used as a lot of "standard" surface hops will fall into this energy range. Since the control pulses employed later will use very low energies, this option is unsuited in the current investigation. ii) Another route would consist in looking at the population transfer induced by the field and comparing to the field-free transfer. The larger of these two contributions then decides if a hop would be field-induced or not. Due to the use of the fully diagonal representation in which the basis of states is field-dependent, such a separation is made impossible. Due to these complications, the kinetic energy at a transition between states is not adapted although this decision has been found[27,28,32] to result in larger deviations from quantum simulations and is in general a very undesirable choice. All dynamics simulations have been run using SHARC 2.1.[143]

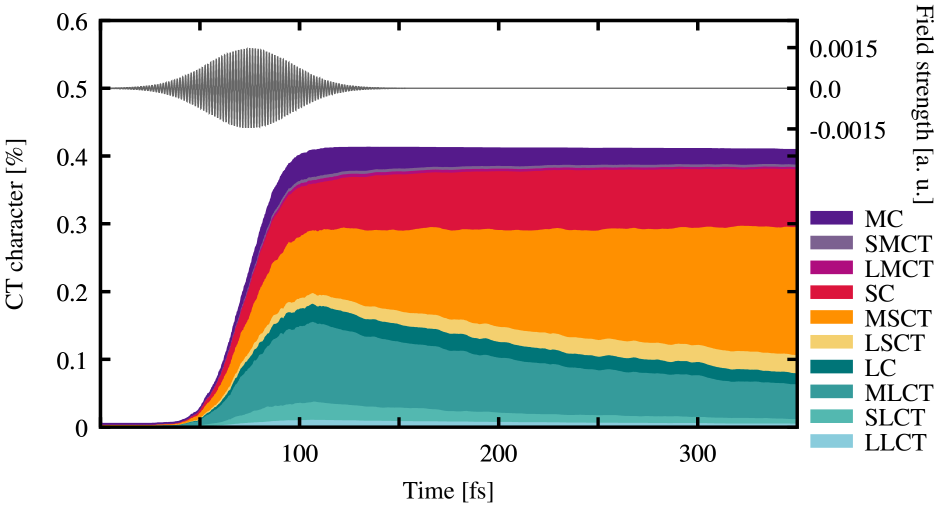

Figure 14: Evolution of the CT character in [Ru($^{S-S}$bpy)(bpy)$_2$]$^{2+}$ after being subject to a pump pulse resonant to the center of EW-I. All the contributions to the CT character are stacked on top of each other. The pump pulse is shown in gray with the corresponding y-axis containing the amplitude being located to the right.

The electronic localization obtained from simulating the LVC/SH dynamics of [Ru($^{S-S}$bpy)(bpy)$_2$]$^{2+}$ starting from the lowest energy state in the presence of an explicit pump pulse exciting into EW-I is shown in Figure 14. As expected, most population is excited around the center of the pulse where the intensity is highest, exciting a total of 41% of trajectories. A difference to the dynamics using instantaneous excitation that have been discussed in Section 5.1.3 is found when looking at the very onset of the dynamics. When using instantaneous excitation, the initial distribution of CT states is almost exclusively dominated by MLCT states which then undergo ultrafast transfer into MSCT states. In the field-induced dynamics, an almost equal mixture of MSCT+SC and MLCT states is present and the peak of the pulse. The difference in the distribution of population at the beginning of the simulations can be explained by the delayed excitation present in the dynamics using a pump pulse: Any excited trajectory will already start the ultrafast relaxation towards MSCT states while other trajectories are only excited later, resulting in a mixture of population at the peak maximum of the pulse. Towards the end of the dynamics a distribution reminiscent of the final mixture of states obtained from the dynamics using instantaneous excitation is found.

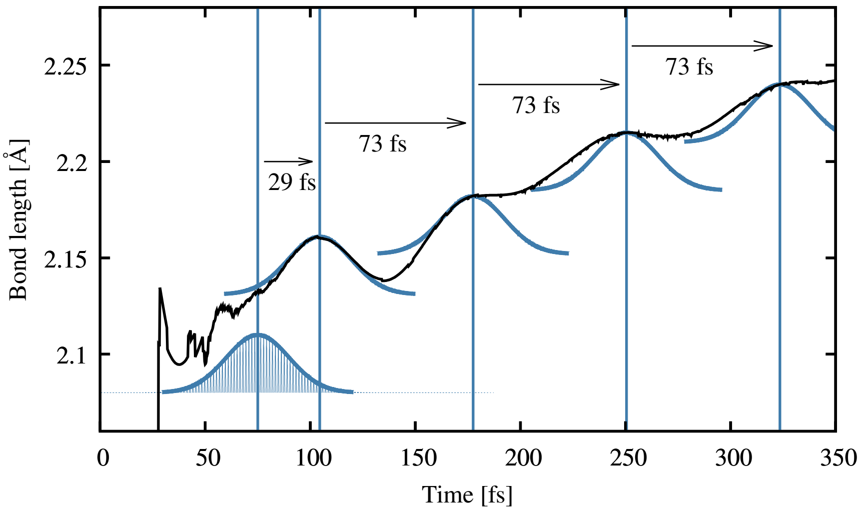

Figure 15: Average S–S bond length of all excited trajectories of $[\text{Ru}(^{\text{S–S}}\text{bpy})(\text{bpy})_2]^{2+}$ (black) using a single pump pulse for excitation. The intensity of the laser field is plotted in blue with the envelope thereof being depicted as a thick blue line. This envelope line is then used to match the approximate local maxima of the average disulfide bond length. The temporal displacement between the centers of the envelope functions (marked by vertical lines) is indicated with arrows.

The field-free investigation of $[\text{Ru}(^{\text{S–S}}\text{bpy})(\text{bpy})_2]^{2+}$ presented in Section 5.1.3 revealed that the most important nuclear motion occurring within the excited states is the elongation of the S–S bond at the $^{\text{S–S}}$bpy ligand. Tracking this movement for the average of all excited trajectories gives the curve shown in Figure 15. As soon as the pump pulse starts to excite a statistically significant amount of trajectories, the bond length starts to increase from the equilibrium bond length of 2.11 Å. Throughout the dynamics, the average of the S–S bond length undergoes a few oscillatory motions that are found at more and more extended S–S bond lengths. The first of these local maxima in the evolution of the bond length is found at 104.5 fs after which they seem to occur roughly every 73 fs. When investigating this oscillatory behavior, it is found that the first oscillation of the average bond length almost exactly coincides with the shape of the applied intensity I ($I \propto \epsilon(t)^2$). A two-fold mechanism is at work here: I) The amount of excited trajectories is changing in every time step during the duration of the pump pulse. Each excited trajectory therefore initiates the excited state dynamics at a different point in time, resulting in different absolute time scales until when the T_1 minimum can be reached. The more trajectories get excited in a single time step, the stronger the influence of these coherently excited trajectories on the average S–S bond length, resulting in an intensity shaped oscillation. II) Coherent movement of the S–S bond length in the initially excited states also contributes to this behavior, inducing a coherent motion of the disulfide bond in the beginning of the dynamics in those states. The oscillation is found to have a recurrence time of around 73 fs which is very close to experimentally determined disulfide bridge bond vibrations which are commonly found in a range between 65-77 fs.[180] For prolonged dynamics, the oscillations are flattening out as more and more trajectories follow different excited state pathways, resulting in slightly shorter or longer bond oscillations with more trajectories showing longer bond oscillations as the S–S bond is weakened in most of the trajectories. Finally, the reader is reminded that the employed setup is not well suited to describe this bond elongation in full detail as the LVC model is harmonic by construction, therefore obfuscating any potential excited state pathways that include a complete cleavage thereof (see Sections 2.2.2 for the theory of the LVC model and Section 5.1.1 for the obstacles encountered in describing the T_1 minimum energy structure).

With the electronic evolution being discussed in terms of CT character and the nuclear evolution being investigated in the form of the disulfide bond length, it can be concluded that the dynamics initiated by an explicit laser pulse undergo very similar pathways to the field-free case. The main difference to the dynamics starting from instantaneous excitation is the temporal broadening of the onset of the dynamics for each trajectory. A first important step towards the simulation of a close-to-experiment pulse sequence in $[\mathrm{Ru}(^{\mathrm{S-S}}\mathrm{bpy})(\mathrm{bpy})_2]^{2+}$, including both the pump pulse and any additional control pulses has been undertaken. Thus, this thesis finally is able to reach into the depths of laser control, representing the initially set goal.

5.2.2 *Control using Explicit Laser Fields*

This section is dedicated to finding pulses capable of introducing changes to the excited-state dynamics of $[\mathrm{Ru}(^{\mathrm{S-S}}\mathrm{bpy})(\mathrm{bpy})_2]^{2+}$ after excitation with an explicit laser pulse. Control of chemical or physical processes via a single or a sequence of laser pulses is a rather delicate matter, requiring to take into account the delicate interplay of the used laser pulse with the wave packet evolving on the set of excited states.[5,181] A classification into weak- and strong-field effects is commonly undertaken where weak-field pulses induce transitions between states but do not change the shape of the respective PESs while strong-field pulses influence the dynamics by introducing a time-dependence in the PESs. Numerous successful applications for both types of pulses have been demonstrated although both effects cannot be strictly separated.[42,43,58,182–187]

Regarding how to design suitable control pulses for simulations, two main schools of thought do exist: On the one hand, knowledge of the respective potential energy surfaces can be exploited to pinpoint sites where specific laser pulses can promote desired transition effectively. On the other hand automated control theories can be applied in the form of optimal or local control theory. In optimal control theory, a desired product state or property is maximized over the course of the complete dynamics, relying on a multitude of runs, resulting in an iteratively adapting pulse.[181,182] Contrary to this, local control theory tries to maximize the chosen state or property in each time step, requiring only a single simulation to yield a locally optimized pulse shape.[42,43,47,188] A downside of the use of these forms of control theory is the non-analytical shape of the resulting fine-tuned pulses oftentimes hindering physical interpretation of the excited state mechanisms at work and complicating experimental realization of these pulses. The fine-tuning of these optimal or local control pulses poses another problem in the form of likely incompatibility between theory and experiment: Any fine-tuned laser pulse obtained from theoretical simulations will not result in a similarly good control rate in experiment, due to the approximations introduced via the electronic structure description or the propagation method chosen or environmental factors that have not been included in the simulations. To circumvent this issue, only very simple forms of control pulses will be used that will most likely achieve very similar results in experimental setups.

An important question not raised so far is: What should be the goal of the modification in the current application? The natural excited state dynamics indicates that given enough simulation time, all the population ends up in the T_1 minimum energy structure from where phosphorescence occurs. Therefore, the following goal is set for the control via additional pulses: The employed control pulse(s) should be capable of slowing down or even completely hindering the population of the T_1 minimum energy structure.

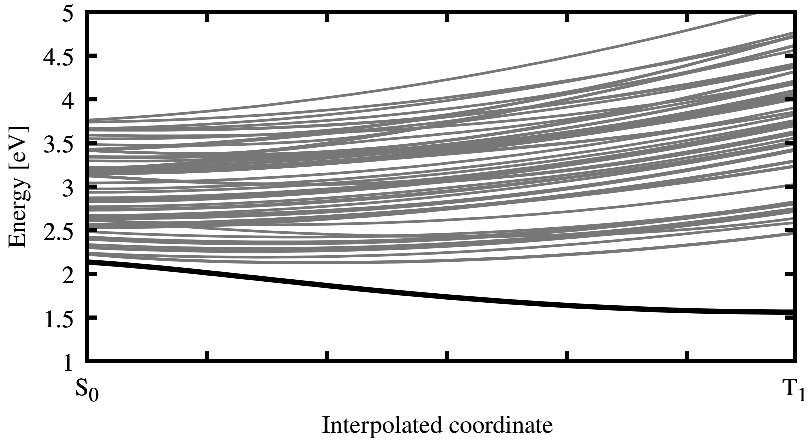

Figure 16: Potential energy plot for all considered states of $[\mathrm{Ru}(^{\mathrm{S-S}}\mathrm{bpy})(\mathrm{bpy})_2]^{2+}$ along the interpolation of internal coordinates from the S_0 to the T_1 minimum energy geometry. The potential energy surfaces are shown in the block-diagonal form, keeping the SOCs as off-diagonal elements between the singlet and triplet blocks. The T_1 state is marked in black. Note that the ground state is outside of the shown energetic window.

With the aim of the control being defined, the search for a suitable control sequence is started by investigating in detail the transition of the initial S_0 structure to the T_1 minimum energy structure. The PESs for all excited states in the employed LVC model are shown for a linear interpolation of internal coordinates between those two structures (using the LVC optimized structures as start and end points) in Figure 16. It can be seen that once the T_1 state is populated, barrierless access to the T_1 state is granted, explaining the very fast population of this minimum. All other states are destabilized when going towards the T_1 minimum, rendering any repopulation of other states rather unlikely due to a separation of at least 0.9 eV from higher-lying states. A way to hinder quantitative population of the T_1 minimum would be to employ control lasers capable of exciting trajectories moving along the T_1 state to higher-lying states from where the structural relaxation will be reversed. This could in principle be achieved at any point throughout the T_1 relaxation by excitation to any higher-lying state. To obtain more control about the dynamics following such a transient excitation, the available excited states are analyzed: At the T_1 minimum, a lower- and a higher-lying band of states can be observed. Closer inspection reveals that the lower-lying band of states consists mainly of MSCT and SC states while the higher-lying band is comprised of mainly MLCT states. Transient excitation from the T_1 state to an MLCT state would induce a drastic change in the localization of the excited electron that could be easily followed using the CT analysis that has already been employed for this complex, allowing for an easy verification if the control pulse works as intended. In addition, it would be desirable to try to act on the still relaxing trajectories since the LVC model struggles with the description of largely elongated bond lengths as would be the case in the T_1 minimum. Therefore, the choice was made to employ control pulses that transiently excite population from the T_1 or other low-lying states to MLCT states, preferably before reaching the T_1 structure. Such a goal is complicated due to the high number of states, different onset times and possible routes of the relaxation dynamics. Therefore, a procedure based on running non-controlled dynamics was employed to come up with a suitable pulse – borrowing from the idea of local control theory.[41] First, a target quantity $p_L(E_{ab}, t)$ was defined as

$$p_L(E_{ab}, t) = |\mu_{x,ab}| \cdot \mathrm{MLCT}_b^2 \tag{59}$$

with a being the active excited state in current surface hopping trajectory and b being another excited state with the respective percentage of MLCT character in this state (MLCT_b). The transition dipole element between a and b ($\mu_{x,ab}$) along x is proportional to the ease of transition between both states and E_{ab} is the energy difference between the active state and state a and therefore reminiscent of the frequency needed for resonance between a and b. This time-dependent measure can be evaluated for each state and each time step for all trajectories to obtain a time-dependent map showcasing which energy for a laser pulses are the most likely to excite population to the MLCT band. To further increase selectivity between MLCT and MSCT or SC states, the quantity $p_L(E_{ab}, t)$ is expanded to $p(E_{ab}, t)$ defined as:

$$p(E_{ab}, t) = |\mu_{x,ab}| \cdot (\mathrm{MLCT}_b^2 - \mathrm{MSCT}_b^2 - \mathrm{SC}_b^2) \tag{60}$$

where MSCT_b and SC_b are the contributions of MSCT and SC character to excited state b. Using this formulation, the probability to excite towards states that are mainly MSCT or SC states contributes negatively to the overall target quantity.

With the target quantity $p(E_{ab}, t)$ being defined, a set of 1000 trajectories has been run for 250 fs, starting in the S_0, using the simulation setup described in the previous section including the pump pulse that excites into EW-I. The resulting values have been convoluted in energy with Gaussian functions featuring a t_{FWHM} of 0.3 eV, yielding Figure 17. Right at the beginning of the dynamics in the excited states (close to the center of the pump pulse), MLCT bands that are located 0.5 eV above and below the currently active states are observed that could be transiently excited. MSCT+SC states are found at even lower energies (1.2 eV below the active states), highlighting the overall lower energy of MSCT+SC states when compared to the initially excited MLCT states. Throughout the dynamics, these lower energy MLCT and MSCT+SC bands stay present, fading out slowly towards the end of the dynamics as they represent lower energy states accessible from rather high energy states. These higher energy states get more and more depleted the longer the dynamics continues due to non-adiabatic relaxation to lower energy states. An additional MSCT+SC band

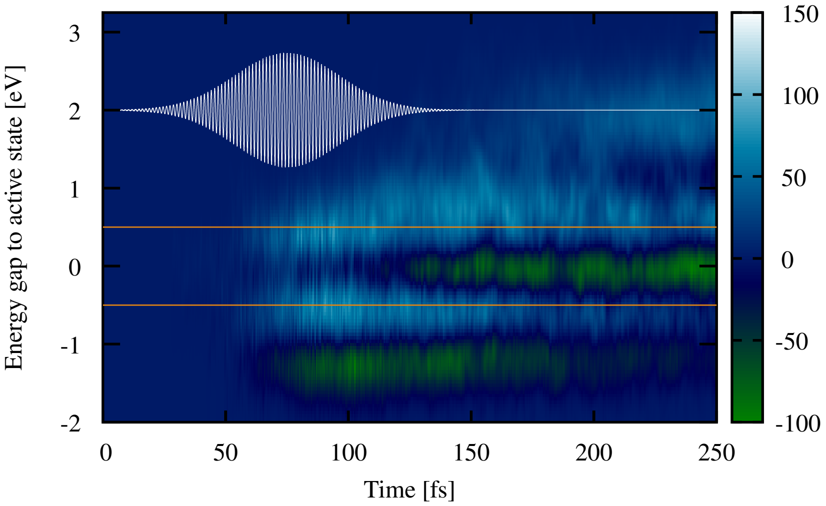

Figure 17: $p(E_{ab}, t)$ values along dynamics initiated by the pump pulse, reminiscent of the density of trajectories that could transiently be excited from the current active state to either MLCT states (light blue to white) or MSCT+SC states (green). The y-axis is the respective energy needed for a resonant transition. The pump pulse is depicted in white and a viable laser frequency to transiently excite MLCT states in gold.

appears at the same energy as the active states throughout the dynamics, due to the fact that the MSCT+SC band gets more and more populated, with other MSCT+SC states in close vicinity. A MLCT band appears towards the end of the dynamics 2 eV higher than the active states. This additional band represents trajectories that are very close to the T_1 minimum energy geometry from where the MLCT band is far away in energy.

Two pulses for controlling the excited state dynamics of $[\mathrm{Ru}(^{\mathrm{S-S}}\mathrm{bpy})(\mathrm{bpy})_2]^{2+}$ can be deduced from Figure 17: A pulse with frequency of 2 eV could be used to excite trajectories close to the T_1 minimum geometry back to MLCT states, from where the S–S bond would contract. The second pulse would act at a much lower frequency (0.5 eV) and target trajectories which are in the process of descending down the ladder of states towards the low-lying MSCT+SC states. The 2 eV pulse was discarded and the infrared 0.5 eV pulse will be used throughout the remainder of the work based on the following reasons: First, a 2 eV pulse would also act as a pump pulse for the S_0 population, further complicating the ensuing dynamics by exciting more trajectories from the ground state population. Second, the use of a control pulse with about 2 eV would also allow trajectories currently not residing in the T_1 minimum to be excited to higher-lying states with the problem arising that only the lowest 21 singlet and 19 triplet states are considered in the current model. Therefore, possible interactions with higher-lying states will be neglected. With the low-energy pulse, a much smaller span of states can be bridged, minimizing the influence of omitting those high-energy states.

Being equipped now with a frequency to adapt the excited state dynamics in the desired way, a two pulse setup is used: The same pump pulse used previously to excite population from the S_0 is used, followed by a second pulse which uses again a t_{FWHM} 50 fs gaussian envelope and a maximum intensity of 75 GW/cm^2 (corresponds to 1.46·10^{-3} a.u. maximum amplitude of the electric field). It has to be noted that the involved transition dipole moments for the investigated transition metal complex are very large compared to the systems investigated in Section 4.2 and paired with an intense laser field. Hence, any observed modification of the dynamics will be a combination of weak- and strong-field effects.

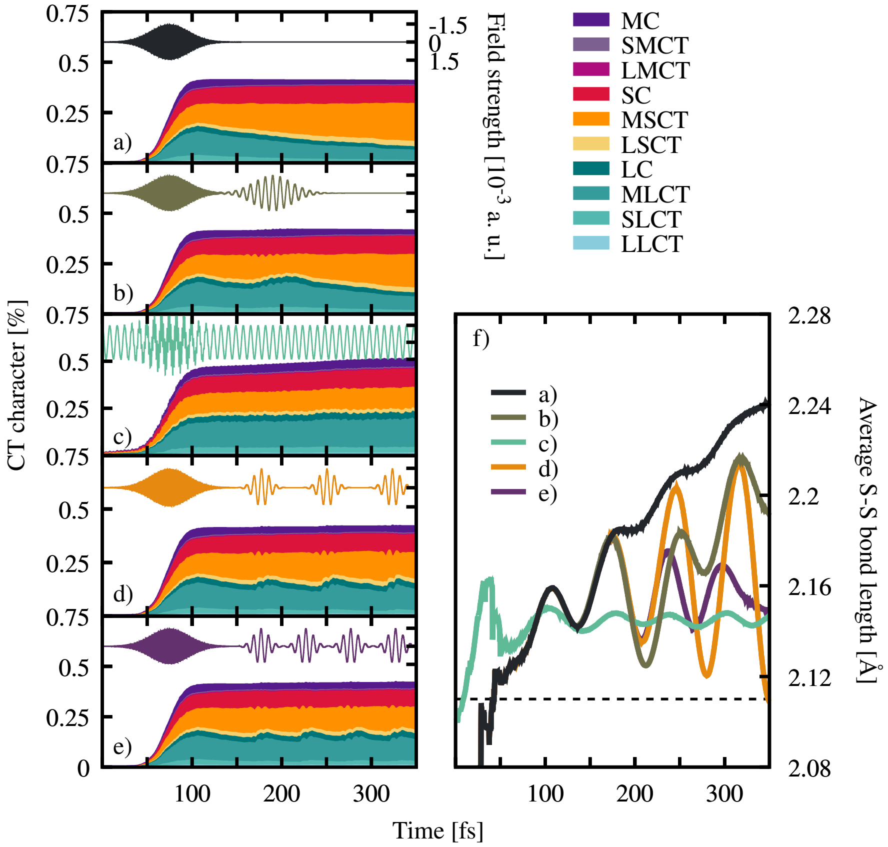

Figure 18: a-e) Charge-transfer characters for all simulated trajectories for LVC/SH dynamics using pulse sequences that are depicted in the respective pictures. f) Average S–S bond length for all excited trajectories simulated using the pulse sequences depicted in a)-e). The equilibrium bond length in the S_0 state is indicated by a black dashed line.

Different delays τ between the centers of the pump and the control pulse have been tested (95,115, and 135 fs) with a smaller set of 300 trajectories before setting τ to 115 fs. For all considered delay times, a sizeable effect on the average disulfide bond length is seen, resulting in a reduction thereof during the control pulse. Using this delay between both pulses, LVC/SH dynamics have been run with the complete set of 4000 trajectories, the results of which are shown in Figure 18b. During the duration of the control pulse, an increase of MLCT character is visible accompanied by a decrease of MSCT character, resulting in a distribution of MLCT to MSCT+SC characters similar to the distribution at the end of the first pump pulse. The employed control pulse therefore successfully couples MSCT and SC states to MLCT states, allowing the desired transient excitation. When looking at the average S–S bond length of excited trajectories (shown in Figure 18f), a strong reduction of the average S–S bond length is observed during the time the second pulse acts on the system.

Transient excitation by the control pulse therefore leads to S–S bond hardening, pushing the wave packet away from the T_1 minimum energy structure. However, the moment the second pulse subsides, the already known excited state dynamics prevails, and a repopulation of MSCT states is observed paired with an increase in the average S–S bond length. The latter observation comes at no surprise since none of the other accessible excited state minima can compete with the relaxation towards the T_1 minimum, leading to an efficient transfer towards the T_1 minimum after the control pulse fades away.

To verify if the decay towards the T_1 state can be halted completely, the second pump pulse was substituted with a continuous wave of frequency 0.5 eV providing a permanent source of MSCT to MLCT transitions. The resulting excited state evolution can be seen in Figure 18c with the influences on the disulfide bond being shown in Figure 18f. The infrared wave acts throughout the whole simulation time, resulting in the excitation of a few trajectories at times earlier than for the dynamics in Figure 18a and 18b. Additionally, after the pump pulse fades out, slowly, more and more trajectories are excited with a total of 51% of trajectories being excited at the end of the simulations. When looking at the character of the excited states, it is seen that the decay of the MLCT character is completely halted and the ratio of all charge-transfer contributions stays constant after the maximum of the initial pump pulse due to the permanent coupling introduced by the continous wave. Furthermore, the S–S bond length for excited trajectories oscillates around a value of 2.145 Å, a much lower value than for the other dynamics and only slightly elongated with respect to the ground state value (2.11 Å) and far away from the T_1 equilibrium bond length that with the current LVC model amounts to 2.34 Å. Applying a permanent control pulse therefore traps the excited population effectively in a mixture of states where the electron is located at any of the three ligands without relaxing quantitatively to the T_1 minimum structure, achieving the set goal for the control of the excited state dynamics.

Having achieved the desired success with a simple continuous wave, the continuous wave was replaced by a sequence of short pulses, allowing for a more targeted modulation of the excited state dynamics. Each single infrared pulse would then promote population of MLCT states accompanied by a reduction of the S–S bond, which would between pulses be reverted back to MSCT states and possible weakening of the sulfur to sulfur bond For the placement of the position of the individual control pulses, the oscillations of the average of the S–S bond length in the control-free case were used as a basis and pump pulses placed at the respective maxima (remember Figure 15 where the different maxima and their placement is shown in more detail). Therefore, three infrared pulses with a FWHM of 20 fs were used, separated from each other by 73 fs with the first pulse acting with a τ of 102 fs between the center of the pump pulse and the center of the first infrared pulse. The resulting dynamics are shown in Figure 18d where it can be seen that the MLCT character increases during the duration of all three laser pulses at the expense of MSCT contribution. When considering the S–S bond elongation, a strong decrease is observed during the time each pulse is acting on the system. However, each decrease in the average S–S bond length is followed by a stronger increase of the average, resulting in a build up of an even stronger coherent oscillation after each pulse. This can be explained by two effects: for one there is the timing of the pulses, which act at the maximum of the S–S bond length for most trajectories, promoting them to MLCT states. First, the accompanying hardening of the bond will result in a gain of kinetic energy along the S–S bond vibration, resulting in a situation best compared to a swing on a playground where extra force is best applied when the maximum height is reached. Second, the strong infrared pulses can increase the synchronization between more and more trajectories as the PESs are varying with the time-dependent slow oscillations of the pulse. The employed pulse sequence is found to be unfit to preserve a shorter S–S bond length in the excited wave packet and modifications need to be performed to provide a suitable pulse sequence. A simple adaption would be to set the centers of the short pulses asynchronous to the S–S bond oscillation to obtain the opposite of the swing-effect described above by applying the pushing force while the swing is still trying to reach the maximum amplitude. To see the effect of such an approach, another pulse sequence was simulated, starting from the same first infrared pulse with all subsequent laser pulses acting with a τ of only 50 fs. This way, the first infrared pulse still initiates this swing like behavior which is then damped by the next pulse acting before a full oscillation of the S–S bond can be completed, effectively removing kinetic energy from the vibration. Using such a setup of control pulses, the effect on the distribution of charge-transfer character (see Figure 18e) of each pulse is still similar to the other pulse, resulting in a larger proportion of MLCT states during the pulse duartion. For the average S–S bond length, a decrease of the average S–S bond length is observed when compared to the previous pulse sequence as soon as the second infrared pulse influences the system. Using this asynchronous timing of the control pulses, the average S–S bond length for the excited trajectories seems to oscillate around a value of around 2.16 Å, showing only a very minor elongation when compared to the equilibrium S_0 bond length.

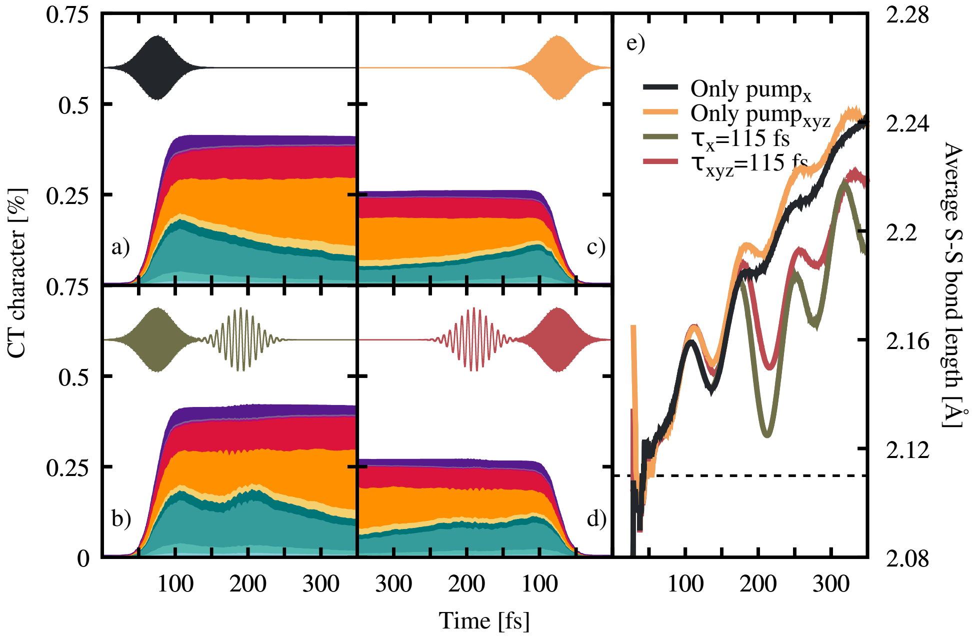

Figure 19: a)-d) Charge-transfer characters for all simulated trajectories for LVC/SH dynamics using pulse sequences that are depicted in the respective pictures. The polarization of the complete pulse sequence is always along x in a) (Only pump$_x$) and b) (τ_x = 115 fs), making these two panels identical to Figure 18a and 18b. c) (Only pump$_{xyz}$) and d) (τ_{xyz} = 115 fs) use a different random polarization for each trajectory. f) Average S–S bond length for all excited trajectories simulated using the pulse sequences depicted in a)-d). The equilibrium bond length in the S_0 state is indicated by a black dashed line.

The desired goal of finding control pulses capable of slowing and reversing the prevalent relaxation towards the T_1 minimum in $[\mathrm{Ru}(^{\mathrm{S-S}}\mathrm{bpy})(\mathrm{bpy})_2]^{2+}$ has been achieved using a single control pulse, a continuous wave, and a sequence of ultrashort few-cycle pulses. All employed control pulses could in principle be used in experimental setups with one important caveat: Every one of these simulations assume that the laser polarization always points along the same molecular axis (the x-axis in the used LVC model). In an experimental environment this would necessitate that all $[\mathrm{Ru}(^{\mathrm{S-S}}\mathrm{bpy})(\mathrm{bpy})_2]^{2+}$ would need to be pre-aligned, imposing the same spatial orientation on all complexes. A more straightforward comparison between theory and experiment would be enabled if a random orientation of each molecule at the start of the simulations is assumed. Therefore, as a final step to estimate how big of a difference between the previously shown results and an experimental setup is to be expected if no pre-alignment is conducted, two additional simulations have been run, including this factor: A simulation in the presence of just the pump pulse and a simulation also including a single pump and a single control pulse. For simplicity, the molecules have not been rotated in space but instead the polarization vector of the complete pulse sequence for each trajectory has been randomized, achieving the same effect without the need to remap the normal modes of the LVC model for each trajectory. The polarization vector has been normalized so that the peak intensity still amounts to 75 GW/cm^2 as in the previous simulations. Apart from this, the two simulations use the same SH protocol as the previous dynamics, again employing 4000 trajectories. The resulting charge transfer characters can be found in Figure 19 where panels a and b show the dynamics obtained for similar setups using only electric fields polarized along x (these panels are identical to Figure 18a and 18b) while panels c and d are obtained in the presence of randomly polarized pulses. For the simulations just featuring the pump laser, a reduction in the amount of excited population is observed with randomly polarized light (26 % compared to 41 %), demonstrating what has been known before: The largest transition dipole moments are located along x and a reduction in intensity along this direction results in a drop in the amount of excited trajectories. The charge-transfer character between both simulations (polarized along x or randomly) are very similar, therefore no distinctly different sets of states are initially excited and visited throughout the dynamics. When looking at the S–S bond length for the excited trajectories in Figure 19e, a slightly larger average is found for simulations using a randomly orientated electric field but overall, very similar dynamics are observed.

For the simulations using both a pulse for excitation and a pulse for subsequent modification of the excited state dynamics, the following observations can be made:
i) The amount of excited trajectories is reduced when using randomized polarization vectors when compared to an electric field that acts exclusively from x.
ii) The infrared pulse which is now also randomized in its polarization vector, results in a smaller increase of MLCT character than for a similar pulse exclusively along x, showing therefore a little less of the desired quality to excite population from MSCT and SC states towards MLCT states.
iii) The average S–S bond length of excited trajectories is also less influenced by the acting infrared pulse but still yields qualitatively similar results as during the control pulse the average disulfide bond length is decreasing.

Overall, the previously taken choice of the x direction for the electric field in this investigation results in a more quantitative interaction with the ruthenium complex that allows for a better control of the dynamics. Nevertheless, the used pulses with randomized polarization are also able to induce very similar changes as the x polarized pulses but just to a weaker extent. Therefore it can be concluded that the found pulse sequences will be able to modify the excited state dynamics of $[\mathrm{Ru}(^{\mathrm{S-S}}\mathrm{bpy})(\mathrm{bpy})_2]^{2+}$ regardless of the molecular alignment albeit at various degrees of effectiveness.

5.2.3 *Insights Gained and Place in the Larger Picture*

The excited state dynamics of $[\mathrm{Ru}(^{\mathrm{S-S}}\mathrm{bpy})(\mathrm{bpy})_2]^{2+}$ in the presence of laser fields to both initiate and to modify the excited state dynamics have been investigated. It has been shown that it is possible to slow down and reverse the dominant relaxation pathway towards the T_1 state using low-energy control pulses that transiently excite population from MSCT and SC states towards higher-lying MLCT states. In doing so, the disulfide bond weakening that occurs in low-lying MSCT and SC states is halted due to the lower equilibrium S–S bond lengths in the so-excited MLCT states. However, since no MLCT minimum can compete with the deactivation pathway available in the form of relaxation towards the T_1, any progress to reverse this relaxation process via a control pulse will be made undone the moment the laser subsides. Employing a sequence of control pulses or a continuous wave has been shown to be circumvent this issue by effectively trapping the excited state population in a never-ending cycle of relaxing towards the T_1 minimum, being transiently excited, and starting the whole journey again. A slight bias in the simulations has been revealed when moving away from a picture of pre-aligned $[\mathrm{Ru}(^{\mathrm{S-S}}\mathrm{bpy})(\mathrm{bpy})_2]^{2+}$ complexes towards randomly oriented ones: Using a set of randomly oriented complexes, the ability of the pulse sequence to excite and modify the excited state dynamics is reduced but still clearly visible.

The presented results have only been attainable through a gradual build up using all previous parts: Chapter 3 revealed the obstacles one needs to face when trying to run dynamics using a high level of electronic structure method, inducing the search for a faster and more robust way of simulation. This would allow for a more explicit focus on the inclusion with external fields and the treatment thereof in SH. Such a methodology was found in the form of the LVC model capable of running very fast dynamics, opening up the route for the investigation of large systems as shown in Section 4.1. A small benchmark of the ability of different SH protocols to handle the interaction with laser fields against MCTDH dynamics has been conducted in Section 4.2, showcasing some of the deficiencies of SH. Being equipped with this knowledge and a suitable LVC model plus the field free dynamics both obtained in Section 5.1, this Section finally achieves the goal this thesis originally set out to tackle: Using laser pulses in SH dynamics to control the excited state dynamics of a system. With the finally investigated system being a 161-mode behemoth featuring a set of 79 excited states in the diagonal representation, the initial expectations for the tackled system size have been exceeded by far due to the usage of the efficient LVC/SH methodology.

6

CONCLUSION

Chemical and physical processes initiated by absorption of photons span a are numerous in number and unrivaled in potential. To gain insight into and to allow deliberate modification of the mechanisms at work in such light-induced processes, theoretical simulations can be conducted in the multitude of excited states. Currently, such non-adiabatic dynamics simulations are mostly conducted without the inclusion of the explicit light source, therefore neglecting possible interactions and missing out on the ability to actively reshape the excited state dynamics using control pulses. In addition, such investigations are commonly restrained to small molecules or a subset of modes of movement of larger systems due to computational restraints. The current thesis set out to use approximate surface hopping (SH) dynamics in combination with laser pump and control pulses to validate the ability of SH to describe the interaction with a laser in more detail than has been done previously with a special emphasis on going to realistically sized molecules.

The route to achieve the stated goal has not been without obstacles and detours that in the end resulted in a much more concise and straightforward way to achieve the stated goal. The very first step along this journey is the investigation of pyrrole where it was found that the on-the-fly computation of electronic properties for each trajectory posed a serious problem due to a set of Rydberg states requiring a high-level method to get a correct description. Here, first simulations without any explicit laser pulses that were intended to be a precursor to a laser control study showed excellent agreement with experimental measurements from the literature. However, the computational cost such a large-scale investigation using multiple laser pulses would bring resulted in a drastic rethinking of how to tackle the initial goal of the thesis.

A solution to this problem has been found in the use of approximate and precomputed potential energy surfaces (PESs) via linear vibronic coupling (LVC) models. The so-obtained PESs are robust and consistent throughout the dynamics while at the same time amounting to almost no computational power to evaluate, therefore allowing to investigate much larger systems. An additional benefit of such precomputed surfaces consists in the now available comparison to high-level dynamics simulation methods using the same set of precomputed PESs. This aspect has been exploited to the fullest in the development and use of the SHARC-gym in the context of the thesis. The SHARC-gym is an iterative scheme coupling SH and more accurate simulations simulations in a symbiotic fashion, profiting from the computational speed of SH to trim larger systems down to the most important degrees of freedom while using the accuracy of the other method to validate SH. This methodology has been employed as a proof of concept to determine the most relevant excited states and normal modes of $[\mathrm{PtBr_6}]^{2-}$, showing that the excited state dynamics using a full set of 200 electronic states in 15 vibrational normal modes can be reasonably well reproduced using 76 electronic states and three normal modes. At the same time, the SHARC-gym revealed that the excited state motion is very coherent, therefore the use of decoherence corrections that do not take into account the gradients in the different excited states will give wrong results.

With a tried and tested tool to compare the validity of SH dynamics at hand, the ability of SH to capture the influence of a laser pulse is put to the test using LVC models that were parametrized on SO_2 and 2-thiocytosine the latter of which has been reduced to a 10-mode system based on an automatic reduction. An extensive set of different SH protocols and combinations thereof has been used and benchmarked against multi-configurational time-dependent Hartree results, giving at least qualitative agreement with the reference dynamics for most SH protocols. While the achieved qualitative agreement is a rather pleasant result, none of the used protocols was able to achieve quantitative agreement for the treatment of the laser interaction, highlighting the need for additional investigations. One such avenue would be the inclusion of the Floquet representation in this benchmark.

Having established the usefulness of a combined LVC and SH approach as well as the at least qualitative agreement of SH with reference dynamics when it comes to laser pulses, the *magnum opus* of this thesis consists in a detailed dynamics study of the $[\mathrm{Ru}(^{\mathrm{S-S}}\mathrm{bpy})(\mathrm{bpy})_2]^{2+}$ (bpy=2,2'-bipyridine). Here, computations revealed that the two types of ligands present can be specifically excited into using slightly different excitation wave lengths. Subsequent field-free dynamics on a LVC model containing a total of 161 normal modes and 79 electronic states starting from both excitation windows showed ultrafast intersystem crossing into the triplet manifold. When following the evolution of the excited electron, it is found that the localization of the electron on the ligand featuring a disulfide bond increases throughout the dynamics, where finally a state is populated where the S–S bond is considerably weakened, resulting in a strong stabilization of the T_1 state. All these observations have been made irrespective of which of the two excitation windows has been used, showcasing the speed of the internal conversions and intersystem crossings involved. Finally, explicit laser pulses have been used to initiate the excited state dynamics followed by a single or a set of control pulses that have been designed to counteract the ultrafast population of the T_1 state. These control pulses use very simple analytical forms to allow easy reproduction in experiment and are designed to relocate the excited electron from the $^{\mathrm{S-S}}$bpy to a common bpy ligand, therefore hindering the S–S bond elongation. All employed control pulse sequences have been shown to have the desired effect therefore achieving laser control using SH. Therefore, this work hopefully raises awareness for both the issues surrounding SH due to the many available protocols and the strengths thereof to simulate the control of systems out of reach for most other simulation methods.

7

ACKNOWLEDGMENTS

Writing acknowledgments to commemorate something that lasted for so long and was so deeply intertwined with almost all aspects of my life will always lack completeness. Similar to showing pictures of an impressive journey that will never convey the feeling of experiencing the sights and sounds first hand, mere words cannot describe the extent of my gratitude towards the many people that accompanied me on my journey. Nevertheless, mere words have to suffice here, hopefully invoking the memories shared along this mutual path.

First of all I want to express my thanks to Leticia González who was my gateway to the scientific world, motivating me to push to greater heights when I was aiming too low while keeping me earthbound when I was about to be carried away by my ideas. Without this guidance, this thesis would have been much shorter as I would have been lost being side-tracked in the wonderful but labyrinthine woods of science.

The largest of all thanks however, goes to all the group, making the time at and after work a really enjoyable time, even when steering through a pandemic, therefore thanks to Markus, Markus, Dimitri, Simon, Denis, Monika, Sophie, Sebastian, Philipp, Patrick, Julia, Richard, Nadja, Ludwig, David, Richard, Dóra, Madlen, Severin, Max, Brigitta, Boris, Omar, Leopold, Lukas, Robert, Anna, Leon, Michael, Clemens, Francesco, Martina, Max, Sandra, Julia, Davide, Gustavo, Felix, David, Pedro, Anna, Jin, Mikhail, Lisa, Vera, Mona and some more.

A very pragmatic but heartfelt thanks goes to the many people that I had the pleasure of annoying with my computer or administrative issues: Markus, Markus, Dimitri, Simon, Denis, Monika, and Sophie. Sebastian and Patrick both showed eternal patience and a talent for finding simple words for abstract concepts when it came to explaining and discussing various concepts and ideas. The switch to LVC potentials in this thesis was originally not planned and has been initiated by working together with Sandra. For this I am forever thankful but much more for all the shared morning teas and discussions. A shared dream of making a lot of ca$h is what united me with Max and Lea, showing me that although we did not get a single penny, that fun and science go well together. In addition I want to thank Max for all his support plus coding advice and Lea for all the shared chaos, making me feel more at ease with my messy table. I am grateful for all the shared time, table space, and struggle for the perfect room temperature with Davide and the shared birthday and interests with Gustavo. Julia started this journey together with me and I really appreciated the sincerity of discussions and teaching we had. A very special thanks goes to the newer additions of the group that despite very difficult times managed to bring back joy and companionship even in times of staring at faces on the screen.

Finally I want to thank all the people outside the group for the shared time that helped make this whole journey enjoyable both in times of hardship and success. My final thanks is dedicated to my family that always supported me before and throughout my studies.

A APPENDIX: REPRINTED PUBLICATIONS

Reprints of the various publications that are the foundations of the current thesis are listed in this appendix. The single paper discussing the on-the-fly excited state dynamics on pyrrole is found in Appendix A.1.1. Appendix A.2 then shows the first use of the LVC model both in the absence and presence of laser pulses to provide a playing ground for the comparison of different dynamics simulation methods. Finally, Appendix A.3 shows the step-by-step analysis and simulation of a ruthenium photosensitizer, demonstrating the strength of the LVC model for simulation of large molecules in the manifold of states.

APPENDIX A.1 FINDING A SYSTEM

APPENDIX A.1.1

A XMS-CASPT2 Non-adiabatic Dynamics Study on Pyrrole

MORITZ HEINDL AND LETICIA GONZÁLEZ

Comput. Theor. Chem., **1155**, 38-46 (2019).
`https://doi.org/10.1016/j.comptc.2019.03.012`

Contributions:

MORITZ HEINDL implemented the BAGEL-SHARC interface, performed the calculations and wrote the draft for the manuscript.

LETICIA GONZÁLEZ envisioned and supervised the project. Co-wrote the manuscript.

Reprinted with permission from *Comput. Theor. Chem.*, **1155**, 38-46 (2019).

Computational and Theoretical Chemistry 1155 (2019) 38–46

Contents lists available at ScienceDirect

Computational and Theoretical Chemistry

journal homepage: www.elsevier.com/locate/comptc

A XMS-CASPT2 non-adiabatic dynamics study on pyrrole

Moritz Heindl, Leticia González*

Institute of Theoretical Chemistry, Faculty of Chemistry, University of Vienna, Währinger Strasse 17, 1090 Vienna, Austria

ARTICLE INFO

Keywords:
Pyrrole
Non-adiabatic dynamics
SHARC
CASPT2

ABSTRACT

The photoinduced dynamics of pyrrole is revisited employing the independent trajectory surface hopping methodology based on extended multi-state second order perturbation theory (XMS-CASPT2). Excitation at 200 nm into a high density of states region gives rise to ultrafast deactivation via internal conversion. The primary dissociation channel was found to be N—H hydrogen abstraction, resulting in pyrrolyl radical formation. The associated time constant for hydrogen dissociation was determined to be 64 ± 13 fs, in good agreement with the experimental value of 52 ± 12 fs (Roberts et al., 2013). A total kinetic energy spectrum was also computed, that is in qualitative agreement with experiment. Radiationless decay via the ring-puckering crossing seam was identified as a minor deactivation channel.

1. Introduction

The role of pyrrole was found to be more than just one of a mere bystander in the quest of unraveling the intricate interactions and properties of biomolecules, leading to a better understanding of life itself. While pyrrole is no biomolecule itself, this five-membered ring is a important sub-unit of chlorophyll a, tryptophane and the porphyrine ring found in heme. In an attempt to gain insight into the mechanisms at work in these larger molecules, pyrrole has been the subject of extensive investigations [1–25]. Moreover, with the discovery of an easily accessible conical intersection between the ground state and $\pi\sigma^*$ states along elongation of the heteroatom-hydrogen bond in pyrrole, as well as in other aromatic heterocycles [11], its photoinduced dynamics became the center of attention. Experimental [1,3–10] and theoretical investigations [12–24] provided a comprehensive understanding of the dynamics of the system after photoexcitation to the lowest-lying electronically excited state (S_1), which is of $\pi\sigma^*$ character. In agreement with the general mechanism proposed by Sobolewski and Domcke [11], ultrafast N—H bond dissociation was determined to be the main deactivation mechanism in gas phase.

Time-resolved pump-probe experiments by Roberts et al. [6] yielded a time constant of $\tau = 126 \pm 28$ fs for the deactivation via hydrogen abstraction after resonant excitation to the S_1 at 250 nm. In their paper, 2 + 1 resonance-enhanced multi photon ionization was used to measure the time-dependent rise of the amount of dissociated hydrogen atoms, which was then used to obtain the given time constant. Deuterating the hydrogen atom of the N—H bond resulted in a large primary kinetic isotope effect, indicating that the S_1 is not completely repulsive upon N—H bond elongation. By increasing the excitation energy to 238 nm the S_1 is populated in a vibrational excited state, lending enough energy to overcome the barrier encountered upon dissociation. The corresponding dissociation time constant of $\tau = 46 \pm 22$ fs [6] represents an almost instantaneous deactivation. When instead, higher-lying $\pi\pi^*$ states are excited at 200 nm, two types of dissociated hydrogen atoms were differentiated based on the kinetic energy in each of the detected hydrogen atoms. The high kinetic energy hydrogen atoms yielded an associated time constant of $\tau = 52 \pm 12$ fs [6] while two time constants were fitted for the low-energy hydrogen atoms. The first of these low-energy time constants with a value of $\tau = 108 \pm 20$ fs [6] was assigned to undesired multiphoton ionization while the second time constant of $\tau = 1.0 \pm 0.4$ ns [6] was attributed to C—H bond cleavage from hot ground state molecules.

In an attempt to describe the photodynamics starting from the $\pi\pi^*$ states, a number of dynamical simulations have been carried out employing mixed quantum-classical methods via fewest switches surface hopping [26] paired with various electronic structure methods. Vazdar et al. [16] obtained an average dissociation time of 54 fs by using multireference configuration interaction singles-doubles (MR-CISD) and starting all trajectories in the adiabatic S_4 state. This value is in very good agreement with the experimental measured time constant but the authors state that due to the mode of excitation, the amount of trajectories already starting in a $\pi\sigma^*$ state is overestimated. Time-dependent density functional theory (TDDFT) has been also used for dynamics at the PBE0 [18] and B3LYP [20] levels of theory, after excitation to 211/193 nm and 200 nm, respectively. PBE0 predicted time constants for dissociation of 166/184 fs [18] while B3LYP resulted

---

* Corresponding author.
E-mail address: leticia.gonzalez@univie.ac.at (L. González).

https://doi.org/10.1016/j.comptc.2019.03.012
Received 1 February 2019; Received in revised form 11 March 2019; Accepted 12 March 2019

in a dissociation time of 48 fs [20]. PBE0 drastically overestimates the time needed for dissociation, due to trapping in Rydberg states [18]. In contrast, the B3LYP dynamics are able to reproduce the experimental time constant for dissociation, albeit the same setup could not describe the dynamics after excitation into lower-lying states due to the absence of the dissociation barrier that should be present in the $\pi\sigma^*$ states. In their endeavor to investigate the influence of Rydberg states onto the excited state dynamics of pyrrole, Sapunar et al. [20] also performed dynamical simulations using the algebraic diagrammatic construction scheme of second order (ADC(2)). However, ADC(2) is prone to Rydberg-valence mixing and they obtained a large overestimation ($\tau > 150$ fs) of the time needed for N—H bond dissociation, which was attributed to erroneous mixing between the $\pi\pi^*$ and $3p_x$ states. One should furthermore note that, both, ADC(2) and TDDFT, are single-reference methods and therefore unable to formally describe conical intersections with the ground state. Hence, these methods are incapable of describing the final product formation and branching ratio of the dissociative pathway.

One method capable of treating Rydberg and valence states on an equal footing while being multireference in character, is multi-state complete active space self-consistent field second-order perturbation theory (MS-CASPT2) [27–29] as well as its extended formulation XMS-CASPT2 [30]. Indeed, CASPT2 calculations have been done on pyrrole, both statically [12] and within the framework of multi-configuration time-dependent Hartree (MCTDH) wavepacket dynamics [19]. For MCTDH simulations a vibronic coupling Hamiltonian based upon CASPT2 potential energies was employed in reduced dimensionality using up to 10 normal modes. These MCTDH dynamics were employed to calculate an absorption spectrum that resulted in excellent agreement with the experimental one [2]. This made that over the last few years, this CASPT2 model Hamiltonian has been employed successfully to interpret a range of combined experimental-theoretical studies on pyrrole, investigating dissociation in the low-lying $\pi\sigma^*$ states, photoelectron spectra and excited state populations after excitation into the $\pi\pi^*$ states [8–10]. However, the reduced set of normal modes included in this model prevents one to describe properly the dynamics of pyrrole after few femtoseconds and relaxation mechanisms triggered by strong molecular deformations, which are beyond the reach of the fitted potential energy surfaces (PES) obtained. Hence, energy dissipation via internal relaxation mechanisms like ring-puckering and ring-opening mechanisms that do not include N—H bond fission cannot be treated in this model. These deactivation pathways, however, open up the road to HCN dissociation and C_3H_4 formation, as it was observed in photofragment translational spectroscopy [1].

On-the-fly dynamics in full dimensionality at the CASPT2 level of theory should be able to overcome these limitations and this is the motivation behind the present work. Given the large computational expense of the required nuclear gradients, the number of on-the-fly dynamical studies performed at CASPT2 level of theory is rather limited [31–33]. However, the recent development of efficient nuclear gradient routines for XMS-CASPT2 [34,35] and the implementation of these in BAGEL [36,37] hold promises for the field for trajectory-based CASPT2 dynamics with medium sized molecules, employing several electronic states and not very large active spaces. The present paper aims at proving the versatility of this approach by performing surface-hopping dynamics simulations of pyrrole at the XMS-CASPT2 level of theory, also extending the active space as well as the number of calculated states in comparison with those previously employed in previous stationary CASPT2 studies [33]. Pyrrole itself is an ideal testbed for this purpose, as there exists a large number of surface-hopping simulations performed with different methods providing different results, and CASPT2 is one method that provides a robust description of the associated electronic structure [19].

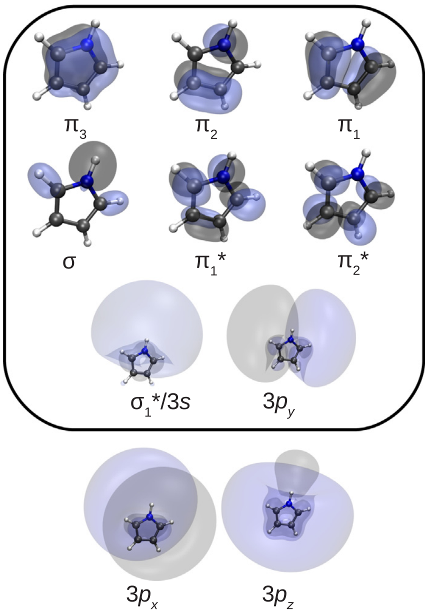

Fig. 1. The black box indicates orbitals included in the (8,8) active space while the complete set forms the (8,10) active space. An isovalue of 0.05 is shown for the π, π^* and the σ orbital. The isovalue was set to 0.005 for the $\sigma^*/3s$ and $3p$ orbitals in order to visualize the Rydberg character. A strong Rydberg mixing between the 3s and the $3p_z$ orbitals that are of the same symmetry is visible.

2. Computational details

2.1. Electronic structure calculations

Multi-state complete active space second-order perturbation theory (MS-CASPT2) [27–29] calculations have been performed on pyrrole, using the extended multi-state (XMS-CASPT2) [30,35,33] formalism that is based on extended quasi-degenerate perturbation theory [38] using the BAGEL [36,37] program package. State-specific first order interaction spaces were constructed in the CASPT2 calculations to reduce the computational cost as implemented in BAGEL via the single-state single-reference scheme [35].

The complete active space self consistent field (CASSCF) [27] method was used as a multiconfigurational basis for subsequent correlated calculations. An active space of 8 electrons in 10 orbitals has been used as a reference and for the optimization of minimum energy conical intersections (MECIs). The absorption spectrum and the dynamics calculations have been carried out with a smaller active space, that only includes 8 electrons in 8 orbitals (see Fig. 1), for computational reasons. Both active spaces contained the 3 π orbitals, the bonding and antibonding orbitals of the N—H bond, 2 π^* orbitals and the Rydberg-3p_y orbital. The antibonding N—H orbital is strongly mixed with the Rydberg-3s orbital in the Franck-Condon (FC) region. The larger CAS(8,10) also includes the 3p_x and 3p_z orbitals. This set of orbitals was chosen based on the character of the excited states that contribute to the lowest-energy part of the absorption spectrum (4–6 eV).

Using the (8,8) active space, state averaging with equal weight was performed over seven states, that included the ground state, two $\pi\sigma^*$, two $\pi\pi^*$ and two $\pi 3p_y$ states. To alleviate the presence of intruder states, a level shift [39] of 0.5 H_a was necessary. Even with this high value, some intruder states are inevitable during the dynamics and the calculation of high-lying electronic states, as it will be evident in the next section.

The ANO-L [40] basis set was used with double zeta quality for all atoms. Diffuse functions (8s,8p,8d)→[1s,1p,1d] were added to the nitrogen to describe the Rydberg orbitals. The additional diffuse functions were obtained using exponents from the Kaufmann series [41] and coefficients obtained from the genano module in MOLCAS [42]. This basis set will be denoted as ANO-L+ throughout this paper.

The ground state geometry of pyrrole was optimized at the MP2/aug-cc-pVTZ level of theory and frequency calculations that confirm the structure to be a minimum have been carried out at the same level of theory.

2.2. Non-adiabatic molecular dynamics

Molecular dynamics including excited states were simulated in the mixed quantum-classical framework of fewest switches trajectory surface hopping [26] using the SHARC [43,44] program package. A set of 1000 initial conditions was generated from an uncorrelated Wigner sampling [45,46] of the vibrational ground state of pyrrole using the Hessian obtained at the MP2/aug-cc-pVTZ level of theory. This ensemble was used to calculate an absorption spectrum of the lowest energy part, as described in Ref. [47], performing single point XMS(7)-CASPT2(8,8) calculations at every geometry of the initial conditions. The obtained pairs of oscillator strengths and excitation energies for every geometry were then convoluted with a gaussian function with a FWHM of 0.05. For the initial excitation, an energy window ranging from 6.1 to 6.3 eV was chosen. This energy window corresponds to a broad pulse excitation at 200 nm. For the determination of the initially excited state in every trajectory, an algorithm stochastically selected trajectories to start in a specific excited state [48] according to the relative oscillator strength in the chosen energy window. This selection resulted in 97 active trajectories, from which 23 were propagated using SHARC at the XMS(7)-CASPT2(8,8) level of theory. Of the 23 simulated trajectories, 6 were started in the adiabatic S_3, 14 in the S_4 and 3 in the S_5. At this point it should be noted that this excitation procedure formally equates to a delta-pulse excitation in a limited energy window. This chimera between a long pulse with a defined energy and a delta-pulse accompanied by an undefined energy is an often invoked *ad hoc* assumption in the setup of trajectory-based non-adiabatic dynamics. The interested reader is referred to recent publications [23,24], where the laser field is included in the non-adiabatic dynamics of pyrrole. The classical nuclei were propagated using the velocity-Verlet algorithm employing a 0.25 fs time step, which was found to result in more robust dynamics with regard to intruder states than the usually employed time step of 0.5 fs [44]. The electronic wavefunctions were propagated using a local diabatization scheme [49,50] in interpolated sub-time steps of 0.01 fs. At each nuclear step, energies and analytical gradients were calculated by BAGEL, while non-adiabatic couplings were approximated using wavefunction overlaps, as described in Ref. [50]. The energy-based decoherence scheme of Granucci and Persico [51] with a value $\alpha = 0.1\ H_a$ was used to account for the effects of overcoherence. Trajectories were terminated after either 300 fs total runtime, or 25 fs in the lowest energy state or after a N—H separation of more than 3 Å.

3. Results and discussion

3.1. Single point calculations

The simplicity of pyrrole is deceptive. Pyrrole exhibits a set of features that make the computation of its low-lying excited states non-straightforward, especially when employing methods based on active spaces. The most striking of these features is the interlacing of the two lowest $\pi\pi^*$ states in the first band of π-Rydberg transitions, resulting in a high density of states around 6 eV at the FC geometry that generates controversies about the ordering of the states.

Within the CASSCF method, inclusion of Rydberg orbitals in the active space is accompanied by a twofold rise in computational cost. First, extension of the active space leads to an factorial increase in the number of determinants that need to be considered. Second, inclusion of any of the 3rd row-Rydberg orbitals gives rise to two π-Rydberg states that are lower in energy at the CASSCF level of theory than the $\pi\pi^*$ states, which are the states of interest. This is due to an overestimation of the energy of the $\pi\pi^*$ states at the CASSCF level. Within the subsequent CASPT2, the $\pi\pi^*$ states retain more correlation energy than the Rydberg states, shifting the $\pi\pi^*$ states at the or below the level of the first Rydberg band. Thus, as the $\pi\pi^*$ states can obviously only be affected by CASPT2 if they are present in the state-averaged CASSCF calculation, for every Rydberg orbital included in the active space, two additional states need to be calculated. This makes the calculation quickly computationally expensive. At the same time, it is desirable to keep the minimum of Rydberg orbitals in the CAS space if dynamics calculations are going to be performed. Therefore, some compromises are necessary in the composition of the CAS space.

In order to estimate the value and cost of including different Rydberg orbitals, a reference calculation including all $3p$-Rydberg orbitals is compared to one with a smaller active space that only includes the $3p_y$ orbital. The choice of the $3p_y$ orbital is based on previous assignments [19] that clearly associate a $\pi 3p_y$ state to a distinct peak in the absorption spectrum at 5.85 eV.

Table 1 collects the excited states obtained with XMS(7)-CASPT2(8,8) compared with the reference XMS(11)-CASPT2(8,10) calculation. As it can be appreciated, the influence of the two additional $3p$ Rydberg orbitals in the CAS(8,10) space is small on the states S_1-S_4 and S_6, as deviations in the excitation energies lie in the range of 0.03–0.07 eV (well below the accepted error range of CASPT2 methods of 0.2 eV [52]), and oscillator strengths remain almost the same. The bright S_5 state of $\pi\pi^*$ character, however, is found to be stabilized by 0.21 eV in the larger active space via mixing with a $\pi 3p_x$ Rydberg state, which is now included in the calculation. Compared to the CAS(8,8) calculation, the oscillator strength is found to be 20% lower, which can also be attributed to the gain in Rydberg-character.

In the light of these results, previous CASPT2 calculations from Roos et al. [12] and Neville and Worth [19] that resulted in vertical excitation energies for the bright S_5 of 5.87 and 6.24 eV, respectively, can be better understood: the work of Roos et al. [12] included the $3p_x$ orbital and corresponding state in the active space, allowing for the mixing of the two states, while this orbital was omitted in the potential energy calculations of Neville and Worth [19], resulting in a pure $\pi\pi^*$ state located higher in energy than the Rydberg-mixed $\pi\pi^*$ state. Curiously, the absorption spectrum obtained by Neville and Worth is nevertheless in unmatched agreement with the experimental reference. As this spectrum was obtained from a Fourier transform of the wavepacket autocorrelation function in the corresponding states, in this work we assume that the influence of the Rydberg-$3p_x$ state mixing with the S_5 can be safely neglected for the dynamics simulations with CASPT2 (as implied in the work of Neville and Worth [19]). It is fair to note, however, that this very same mixing was proposed to be the source of

Table 1

Energies, oscillator strengths and dominantly contributing configurations for the excited states obtained at the XMS(7)-CASPT2(8,8)/ANO-L+//MP2/aug-cc-pvtz level of theory. The right-hand side shows the same properties for the corresponding excited states from the XMS(11)-CASPT2(8,10) reference calculation including all three $3p$ Rydberg-orbitals. Excitation energies (E_{exc}) are given in eV and oscillator strengths (f_{osc}) in a. u.

XMS(7)-CASPT2(8,8)				XMS(11)-CASPT2(8,10)		
f_{osc}	Character	E_{exc}	Label/Sym	E_{exc}	Character	f_{osc}
0.000	$\pi_1\sigma^*$	5.23	S_1/A_2	5.27	$\pi_1\sigma^*$	0.000
0.001	$\pi_2\sigma^*$	5.95	S_2/B_1	6.00	$\pi_2\sigma^*$	0.003
0.032	$\pi_1 3p_y$	6.16	S_3/B_1	6.21	$\pi_1 3p_y$	0.036
0.009	$\pi_2\pi_1^* + \pi_1\pi_2^*$	6.18	S_4/A_1	6.15	$\pi_2\pi_1^*$	0.010
0.163	$\pi_1\pi_1^*$	6.29	S_5/B_2	6.08	$\pi_1\pi_1^* + \pi_1 3p_x$	0.130
0.000	$\pi_2 3p_y$	6.96	S_6/A_2	7.03	$\pi_2 3p_y$	0.000

Table 2
Comparison of various vertical excitation energies [eV] of pyrrole in the current work and previous studies. The first four entries represent CASPT2 calculations denoted by the active space employed. Current excitation energies have been obtained at the XMS(7)-CASPT2(8,8)/ANO-L+ and XMS(11)-CASPT2(8,10)/ANO-L+ levels of theory.

State	(8,8)[a]	(8,10)[a]	(6,14)[b]	(8,8)[c]	ADC(2)[d]	PBE0[e]
$S_1/A_2(\pi\sigma^*)$	5.23	5.27	5.22	5.06	5.13	5.04
$S_2/B_1(\pi\sigma^*)$	5.95	6.00		5.86	5.75	5.75
$S_3/B_1(\pi 3p_y^*)$	6.16	6.21	5.87	6.00[f]	5.89	5.92
$S_4/A_1(\pi\pi^*)$	6.18	6.15	5.82	6.01	6.49	5.81
$S_5/B_2(\pi\pi^*)$	6.29	6.08	5.87	6.24	6.35	5.99
$S_6/A_2(\pi 3p_y^*)$	6.96	7.03			6.65	

[a] Present work.
[b] Ref. [12].
[c] Ref. [19].
[d] Ref. [20].
[e] Ref. [18].
[f] This value was obtained via EOM-CCSD.

the overestimation of the dissociation time constant obtained by Sapunar et al. [20] but using ADC(2).

Given the plethora of calculated vertical excitation energies available in pyrrole, we consider it useful to collect the most relevant ones in Table 2. The broad range of excitation energies illustrates the sensitivity of the excited states of pyrrole with respect to the chosen method, basis set and active space. The excitation energies of the present work adhere to the general trends and energy ranges attributed to specific states in pyrrole except for the S_3 state, which is overestimated by around 0.2 eV with respect to the other methods presented.

Another peculiarity of the excited states of pyrrole is the strong mixing of the anti-bonding σ^* orbital and the 3*s* Rydberg orbital at the FC geometry. The effects of this mixing can be visualized in a scan along the N—H bond (see the top part of Fig. 2). Upon elongation of the N—H bond, the bonding 3*s* character decreases until the orbital is purely antibonding. This behavior results in quasi-bound $\pi\sigma^*$ states that exhibit a small barrier at a slightly elongated N—H bond distance (1.3 Å) before dissociating downhill on the repulsive surface. This barrier is experimentally accessible for the S_1 state, where it was determined to be in the order of 0.08 eV [6]. Such a small barrier towards hydrogen dissociation can be readily overcome via tunneling.

The N—H bond scan also reveals a difficulty of dealing with state-averaged methods: At $r = 1.25$ Å a change in the set of averaged states occurs as another state of $\pi\sigma^*$ character intrudes in the calculation, resulting in a drastic increase of the energy of the highest-lying state, i.e. the state has changed character. As at this point, there is one state of $\pi\sigma^*$ character more, their weight increases in the optimization of the state-averaged orbitals, and the energy of the two low-lying dissociative states that are also mainly of $\pi\sigma^*$ character decreases, thereby slightly modifying the barrier height.

A further complication is that the character of the 3*p* Rydberg orbital included into the active space was found to change from the $3p_y$ to the $3p_x$ and $3p_z$ orbitals along N—H bond elongation coordinate. Gratefully, despite the included $3p_y$-Rydberg orbital (and therefore the states involved) is often exchanged by another Rydberg orbital, the corresponding N—H dissociating potential energy curves behave smoothly. This interchange between Rydberg orbital character is also observed during the dynamics simulations (vide infra), indicating that the Rydberg orbitals are adapting themselves within the active space as necessary. Based on the aforementioned observation that an interchange of Rydberg orbitals did hardly affect the PES, we assumed that excluding the $3p_x$- and $3p_z$-Rydberg states from the active space would have a limited effect on the dynamics, at least as long as 3*p*-Rydberg states are not heavily involved during the dynamics. According to Geng et al. [9], Rydberg states can be visited only for a short amount of time during photodynamics in pyrrole. Therefore, we contented to keep only the $3p_y$-Rydberg orbital in the CAS space that is used for the SHARC dynamical simulations. We are certainly aware that it would have been more desirable to include the complete set of 3*p* Rydberg orbitals in the active space during the dynamics. However, the computational workload of adding the two remaining 3*p*-Rydberg orbitals makes the analytical CASPT2 gradient calculation far too expensive to run dynamics feasibly.

The absorption spectrum computed using XMS(7)-CASPT2(8,8)/ANO-L+ on the set of 1000 initial conditions is shown in Fig. 3 together with the experimental absorption spectrum of Palmer and coworkers [2]. The low energy absorption band is in qualitative agreement with the experiment, albeit a blue-shift of 0.2 eV is visible. This energy shift can be attributed to the missing mixing of the bright $\pi\pi^*$ state with the $\pi 3p_x$ state in the CAS(8,8). Furthermore, the $\pi 3p_y$ state, which is the source of the sharp absorption located at 5.85 eV in the experimental spectrum, is overestimated in our calculations by about 0.2 eV.

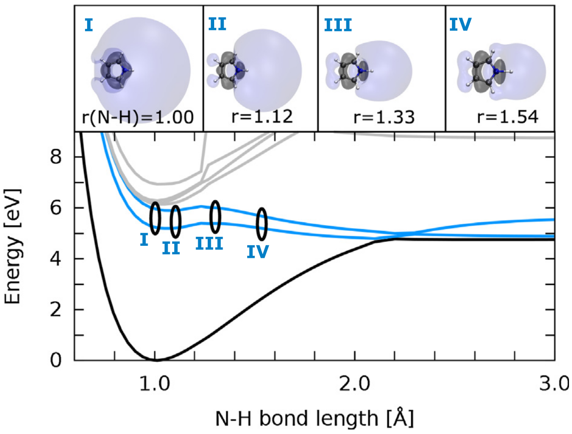

Fig. 2. Rigid energy scan along the N—H bond length, showing the adiabatic states at the XMS(7)-CASPT2(8,8)/ANO-L+ level of theory. The Black circles denote N—H bond lengths for which the $\sigma^*/3s$ orbital is depicted in the top panel with the corresponding number. The circles are placed on the blue-labeled S_1 and S_2 states which are of $\pi\sigma^*$ character. The depicted demixing of the 3*s*-Rydberg and the σ^* orbital is the cause for the small barrier observed in these two states.

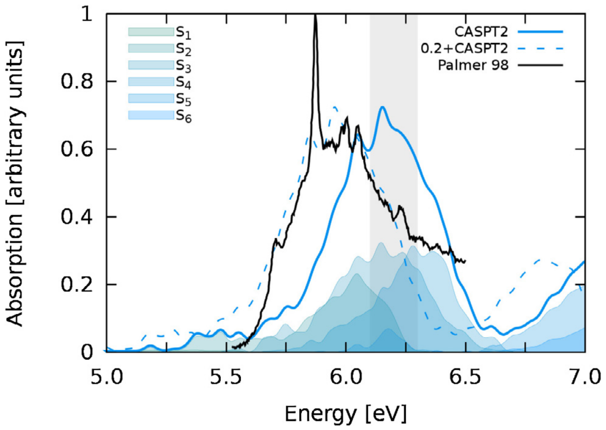

Fig. 3. Simulated absorption spectrum of pyrrole at the XMS(7)-CASPT2(8,8)/ANO-L+ level of theory (solid) and shifted by 0.2 eV (dashed). The spectrum is decomposed in the contributions of the different adiabatic states (shaded areas). The experimental spectrum [2] (black) is shown as a reference. The excitation window for the sampling of initial states of the trajectories is shown in gray and corresponds to a 200 nm (6.2 eV) excitation wavelength.

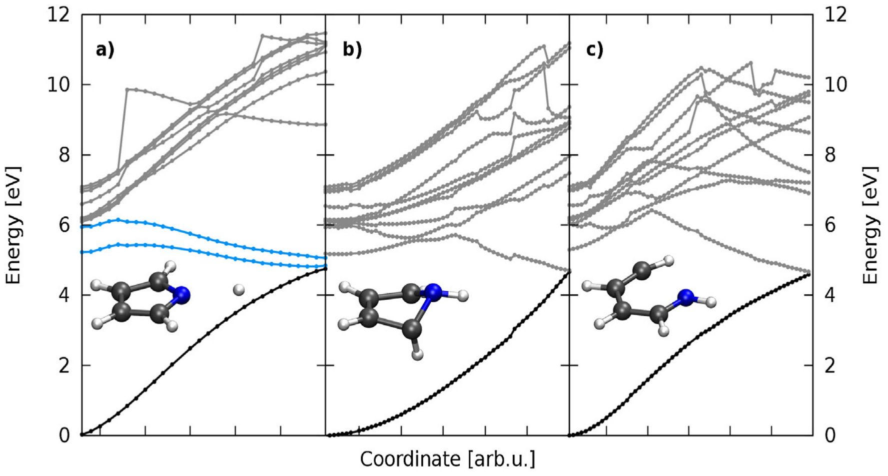

Fig. 4. Potential energy scans from the Franck-Condon geometry to the S_0/S_1 conical intersections obtained at the XMS(11)-CASPT2(10,8)/ANO-L+ level of theory using linear interpolation of internal coordinates. Panel (a) depicts the pathway towards $MECI_{NH}$ with the low-lying dissociative states being labeled in blue in accordance with Fig. 2, while panels (b) and (c) show $MECI_{puck}$ and $MECI_{open}$ pathways, respectively. The minimum energy conical intersection geometries are shown on the left of the respective panels.

3.2. Reaction pathways

The mechanisms behind the S_0/S_1 internal conversion deactivation in pyrrole are known to involve N−H bond dissociation as well as ring-puckering and ring-opening [16,18]. The three MECI geometries associated with these distortions and the potential energy surfaces connecting the equilibrium (FC) and the three MECI points are presented in Fig. 4. The $MECI_{NH}$ (panel 4a) was optimized from the geometry with the smallest S_0-S_1 energy gap in the rigid energy scan of Fig. 2. The $MECI_{puck}$ (panel 4b) corresponding to the ring-puckering was optimized starting from an initial guess of the dynamics simulation while the $MECI_{open}$ geometry (panel 4c) was started using a C−N bond distance obtained from Ref. [16].

In the dissociative deactivation mechanism, deactivation can occur in any of the two low-lying $\pi\sigma^*$ states that get stabilized upon N−H bond elongation. At the FC geometry, the S_2 is interwoven in the band of states while the S_1 is separated by 0.8 eV from other states. Hence, for population transfer to occur towards the S_1, a coupling via other molecular movements is needed. The S_2 on the other hand can be populated right away due to the energetic proximity to initially excited states. Once the small exit barrier in one of the two $\pi\sigma^*$ states is overcome, rapid dissociation will occur as all other states increase in energy. This pathway is in agreement with previous characterizations of the N−H dissociation at the PBE0 [18] and MR-CISD + Q [16] levels of theory. During the scan, two intruder states of $\pi\sigma^*$ character are observed.

The ring-puckering mechanism consists in a crossing of the $\pi\pi^*$ state of B_2 symmetry with the lower-lying $\pi\sigma^*$ states. Such a crossing facilitates population transfer towards one of these $\pi\sigma^*$ states, impeding deactivation through the ring-puckering mechanism. Once the last of the $\pi\sigma^*$ states is crossed, the $\pi\pi^*$ state is the first excited state which proceeds downhill towards the MECI. This final part of the deactivation pathway is different from the flat surface obtained by the PBE0 calculations, [18] while the MR-CISD + Q calculations [16] also show this repulsive behavior. This scan was found to suffer from a surprising large amount of spurious irregularities. The underlying CASSCF potentials (not shown) are smooth except for two intruder states that are encountered close to the $MECI_{puck}$ (the first one being clearly visible due to the small jump in the ground state PES and almost all excited state PES). The reference weights in the CASPT2 calculations do not indicate anything unusual though.

Characterization of the mechanism towards the $MECI_{open}$ is not straightforward. For this C−N bond cleavage to occur, rearrangements of the active space are needed to include the anti-bonding σ^*(C−N) orbital. The active space, however, is found to adapt correspondingly to allow description of such a process. As can be seen in Fig. 4c, a total of 6 new states are intruding along the scanned set of internal coordinates, resulting in a set of spikes in the PESs. These states can be identified by their strong energy lowering when approaching the $MECI_{open}$. Comparison of the potential energy surfaces in the ring-opening mechanism with the ring-puckering ones reveals the presence of much steeper potentials in the initial steps towards the corresponding MECIs. Based upon this, it is assumed that the ring-opening mechanism is less readily activated.

3.3. Excited state dynamics

All the trajectories simulated deactivated to the electronic ground state or underwent N−H dissociation below 250 fs, so that none of the launched trajectories reached the maximum simulation time of 300 fs. Specifically, the analysis of the classical populations (see Fig. 5a) shows that 83% of trajectories end in the S_0 while the S_1 and the S_2 are populated with 13% and 4% respectively. These S_1 and S_2 populations represent formation of the pyrrolyl radical in an excited state.

The primary relaxation path (91%) observed is N−H bond cleavage, while the remaining two trajectories (9%) deactivated via ring-puckering (see Section 3.2). The expectation value for the N−H bond length of the set of trajectories is depicted in Fig. 5b. After exceeding a N−H bond length of 2 Å, the N−H bond is considered broken. Comparing these ’raw’ dissociation events to experimental measurements is challenging. This is due to the preparation of initial conditions using a delta-pulse like excitation as opposed to the fs-laser pulses employed in experimental studies. To facilitate a comparison between experiment and theoretical predictions, a smoothing technique has been proposed recently to include at least the broadening caused by the laser pulses *a posteriori* in the calculations [53,25]. For this, the obtained discrete dissociation times for every trajectory are subsequently convoluted with gaussian functions representing the pump and the probe pulse. The FWHM of 160 fs for the pump laser was taken from Ref. [6] while the FWHM for the probe laser is approximated to be 70 fs. Summing over all the convoluted trajectories now gives the ’laser’-driven dissociation times. Applying this broadening results in a tail into negative pump-probe delay times as can be observed experimentally. Furthermore, a smearing of the raw dissociation events due to the convolution with the laser pulses is observable that results in very good agreement with experimental data. Setting a threshold of 2 Å to consider that the bond is broken, an associated dissociation time constant (τ_{dis}) of 64 ± 13 fs is obtained from an exponential fit. The error estimate is obtained from bootstrapping the set of trajectories. This value of τ_{dis} is in good agreement with that of τ_{dis} = 52 ± 12 fs measures by Roberts et al. [6] Kirkby et al. [10] observed a sub 50 fs population decay based on time-resolved photoelectron imaging, attributing two ultrafast lifetimes to

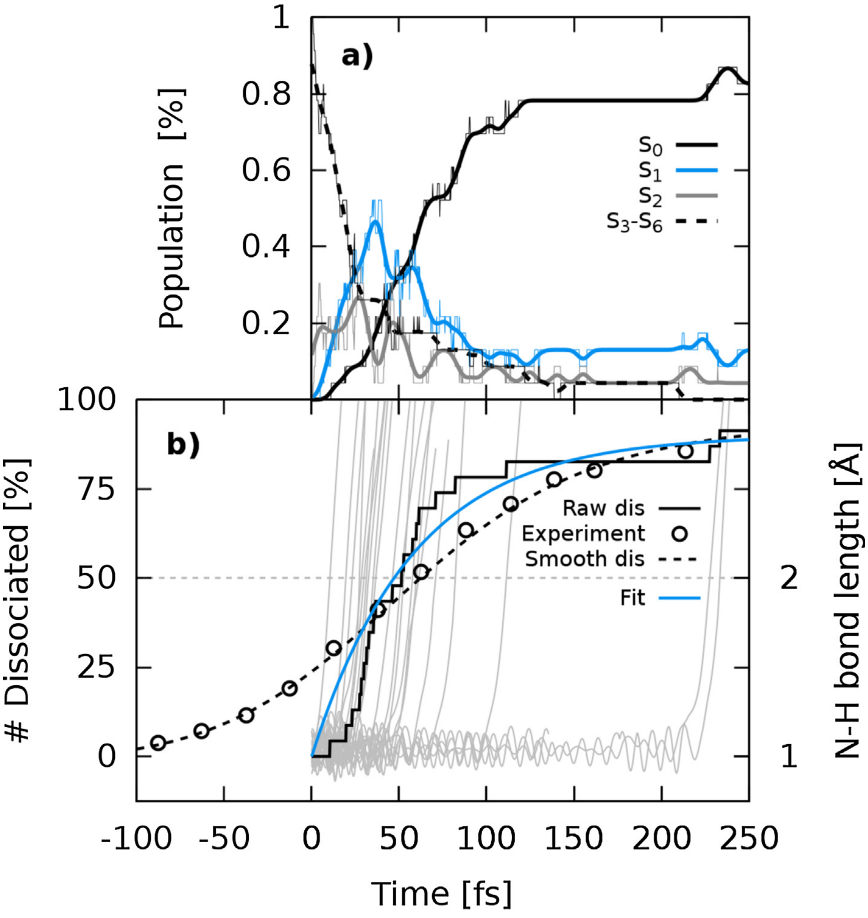

Fig. 5. (a) Time evolution of the classical adiabatic populations. Populations of trajectories that ended prematurely were continued in the last active state. For better readability, smoothed populations are represented by thick lines while the corresponding non-smoothed populations are visualized as thin lines. (b) Expectation value of the N—H bond length versus propagation time. The percentage of trajectories that exceeded a N—H bond length of 2 Å (represented by the dashed horizontal gray line) is visualized by the solid black line. The blue line represents an exponential fit of the raw dissociation times that yields a time constant for deactivation of 64 ± 13 fs. Black circles mark measurements obtained in Ref. [6] that were renormalized to the 91% dissociation observed in the simulations.

specific state-state deactivation channels with 27 ± 1 fs and 34 ± 12 fs. The slight overestimation of the current theoretical work can be attributed to the semi-classical nature of the dynamics, which misses tunneling over the slight barrier of the dissociative states.

The kinetic energy of the dissociating hydrogen atoms at the threshold of 2 Å is collected in Fig. 6a) and was used to get a qualitative estimation of the corresponding kinetic energy distribution measured in total kinetic energy (TKER) experiments [6,4]. While the experimental

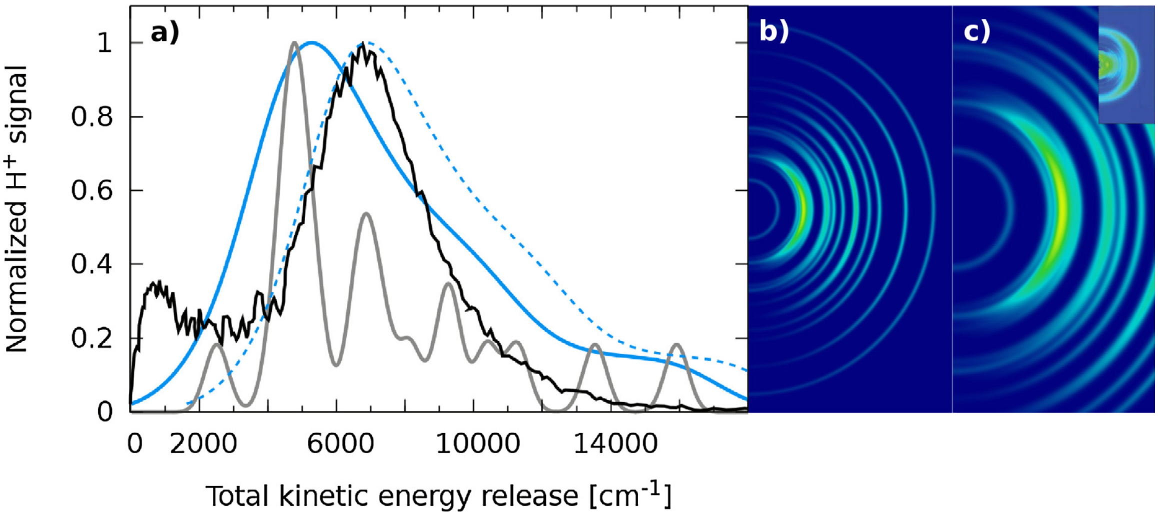

Fig. 6. (a) Total kinetic energy spectrum as obtained from the XMS(7)-CASPT2(8,8) simulations after excitation at 200 nm. Kinetic energies of the trajectories were broadened with gaussian function of FWHM 0.4 eV (blue) and 0.1 eV (gray). The dashed blue line represents a 0.2 eV shifted spectrum. The experimental TKER spectrum [6] after excitation at 200 nm taken at a 1 ps pump-probe delay is shown in black. (b) Complete simulated velocity map image as obtained from the 250 fs dynamics. (c) Detail of the simulated velocity image map on the same scale as the experimental one. The experimental velocity map image with a pump-probe delay time of 1 ps is shown in the inset. This inset has been adapted from Ref. [6] with permission from The Royal Society of Chemistry.

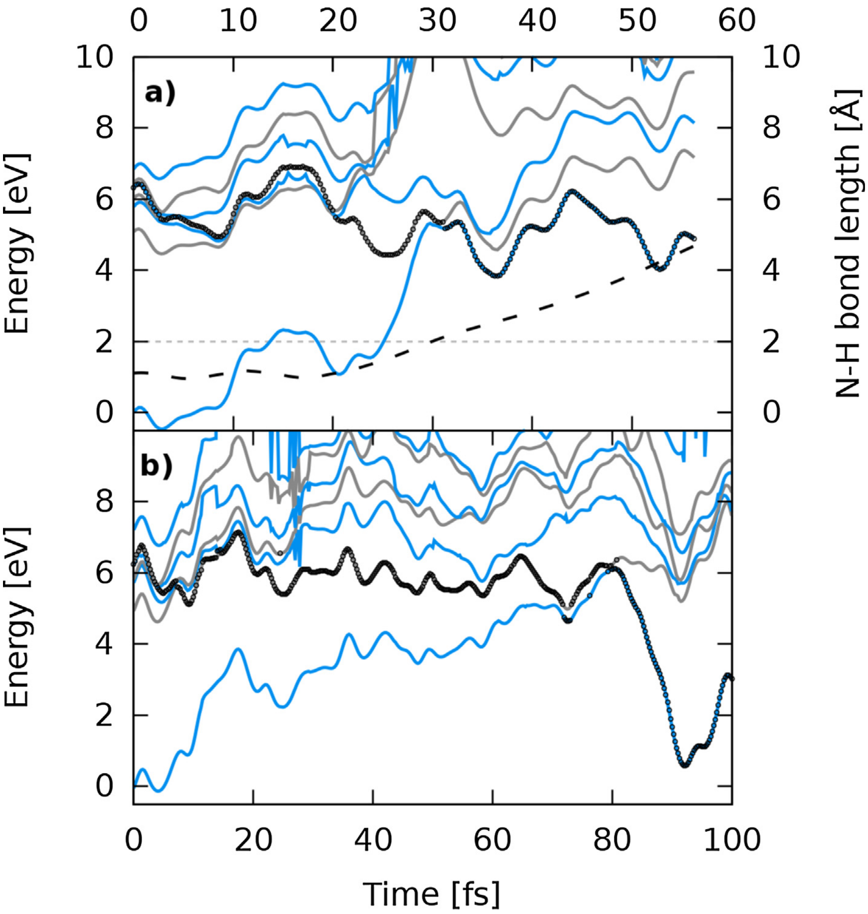

Fig. 7. Representative trajectories for the two deactivation channels observed. Adiabatic states are alternatingly colored in blue and dark gray. The active state in each time step is marked with a black circle. (a) shows N—H bond dissociation. Here the N—H bond distance as a function of time is plotted as a dashed black line. The set threshold for dissociation at 2 Å is marked as a dashed horizontal gray line. (b) depicts a trajectory deactivating via ring-puckering. Note the different time axes for both trajectories.

TKER spectrum (black line) displays two peaks, a small one below 4000 cm^{-1}, mainly caused by C—H bond breaking and multiphoton ionization [6], and a large one centered at 7000 cm^{-1} with a long high-energy tail, the calculated spectrum results in a single peak centered at 5200 cm^{-1} that slowly decays towards the high energy region. Note that the absence of the low-energy peak is expected. First, because we are not simulating the multiphoton ionization signal. Second, and most importantly, because the C—H bond breaking was measured to occur with a time constant of $\tau = 1.0 \pm 0.4$ ns –well beyond the propagation regime considered here. The calculated TKER spectrum seems to be red-shifted by 0.2 eV with respect to the experimental one. Due to the small number of trajectories on which this number is based, this shift has to be taken with a grain of salt. Makhov et al. [21] observed a blue-shift of the same order of magnitude in their simulated TKER spectra using CASSCF potentials and starting in the S$_1$ state. They concluded that the observed overestimation of kinetic energy on the dissociated hydrogen atoms was based on the inaccuracy of the employed CASSCF calculations as compared to reference CASPT2 calculations. Unfortunately, employing exactly these CASPT2 potentials results in a red-shifted spectrum. However, this red-shift in kinetic energies of the dissociated hydrogens could be explained with the energy of the excited state PES: In Section 3.1 the calculated absorption spectrum was found to be shifted to higher energies by 0.2 eV. Hence, the potential energy of absorbing states are shifted by 0.2 eV with respect to experiment. Therefore it can be assumed that the overestimation of PES hinders transfer of energy into kinetic energy at the dissociated hydrogen atom, which is then dissociated on an overestimated PES, resulting in the observed shift of 0.2 eV.

Another observable in the experimental setup is the velocity map imaging technique, which allows for a mapping of the kinetic energy at the dissociated hydrogen atoms against the angular distribution with respect to the laser pulse polarization. It can be obtained from

$$I\left(r, \phi\right) \propto \exp\left(-\frac{(r - |\boldsymbol{v}|)^2}{2\sigma^2}\right)\left(\cos^2(\theta)\cos^2(\phi) + \frac{1}{2}\sin^2(\theta)\sin^2(\phi)\right) \tag{1}$$

where every velocity vector $\boldsymbol{v}$ is broadened by a gaussian function with a width of $\sigma = 0.015$ Å/fs. The angle θ is the inclusion between $\boldsymbol{v}$ and the transition dipole moment. The calculated velocity map image is shown in Fig. 6b) and c). Across all energy ranges the hydrogen atoms were found to dissociate perpendicular to the transition dipole moment. A high intensity feature is visible at low velocities followed by a distribution of medium energy hydrogen atoms and two high-energy ones. In comparison, the experimental [6] velocity map image taken 1 ps after excitation shows a distinct and isotropic feature for low kinetic energies followed by a perpendicular blurry region of medium intensity and a main feature at high velocities. The absence of the low-energy feature in the simulations has already been discussed above. The high energy feature of the experimental velocity map image is split into two signals in the simulations followed by additional peaks arising from the high-energy tail of the spectrum.

Two representative trajectories are shown in Fig. 7: one undergoing N—H bond cleavage in 32 fs (panel a) and one evolving via the ring-puckering mechanism (panel b). In the N—H dissociating trajectory, the first 20 fs are dominated by a rapid decrease in the energy separation of the initially populated S$_5$ and the S$_1$. After 22 fs, the repulsive part of the $\pi\sigma^*$ state is reached and the N—H bond distance increases, which leads to a separation from the bound states. A hop to the S$_0$, which is now of $\pi\sigma^*$ character occurs at 31.25 fs at a N—H bond length of 2.11 Å. Pyrrole then continues on the lowest energy dissociation product channel. Inspection of the smoothness of the potential energy curves for the excited states for the complete trajectory reveals irregularities due to intruder states related to the Rydberg states. Intruder states become more severe once the dissociation process is initiated because another repulsive state enters in the state-averaging procedure, as it has been discussed in Section 3.1.

The ring-puckering deactivation trajectory (Fig. 7b) share some similarities to the dissociating one. Starting from the S_5, the first few fs are governed by a stabilization in potential energy of the active state, leading to multiple state crossings due to the high density of states in the proximity of the active state. Within 20 fs, the active S_1 state separates from the higher-lying excited states while the S_0-S_1 energy gap decreases steadily until a final hop to the S_0 occurs.

4. Conclusions

The photodeactivation of pyrrole after excitation to 200 nm has been simulated in the framework of full-dimensional non-adiabatic surface hopping dynamics. The on-the-fly electronic structure calculations were carried out at the complete active space self-consistent field second-order perturbation theory (CASPT2) level of theory using the extended multistate scheme (XMS-CASPT2). The simulations show that the dominating (91%) deactivation channel is N—H bond dissociation, taking place with a time scale of 64 ± 13 fs. Previous experimental measurements [6] obtained a time constant of 52 ± 12 fs for hydrogen abstraction, which compares well with that obtained in simulations, particularly considering the inability of quantum-classical methods to describe tunneling –a mechanism that should be also partially operating in pyrrole. The remaining 9% of trajectories deactivated via ring-puckering to the closed-shell ground state, as it was found in previous surface hopping simulations carried out at lower levels of theory, [16,18] and no dynamical event was found to occur through ring-opening. Both operating deactivation channels were found to be completed after 230 fs in all trajectories. The total kinetic energy (TKER) spectrum simulated from the dissociating trajectories qualitatively describes the features visible in the experimental TKER with exception of the low-energy peak which is due to multiphoton ionization in the experiment.

Although the number of trajectories simulated cannot provide statistical robustness, the very good agreement with the experiment demonstrates the feasibility of CASPT2 in combination with surface hopping to provide reliable insight into deactivation mechanisms. The complicated intertwining of valence and Rydberg states of pyrrole also illustrates the limitations that current high-level multiconfigurational methods face to perform extending dynamical simulations.

References

[1] D.A. Blank, S.W. North, Y.T. Lee, The ultraviolet photodissociation dynamics of pyrrole, Chem. Phys. 187 (1-2) (1994) 35–47.
[2] M.H. Palmer, I.C. Walker, M.F. Guest, The electronic states of pyrrole studied by optical (VUV) absorption, near-threshold electron energy-loss (EEL) spectroscopy and ab initio multi-reference configuration interaction calculations, Chem. Phys. 238 (2) (1998) 179–199.
[3] J. Wei, A. Kuczmann, J. Riedel, F. Renth, F. Temps, Photofragment velocity map imaging of H atom elimination in the first excited state of pyrrole, Phys. Chem. Chem. Phys. 5 (2) (2003) 315–320.
[4] B. Cronin, M.G.D. Nix, R.H. Qadiri, M.N.R. Ashfold, High resolution photofragment translational spectroscopy studies of the near ultraviolet photolysis of pyrrole, Phys. Chem. Chem. Phys. 6 (21) (2004) 5031–5041.
[5] H. Lippert, H.-H. Ritze, I.-V. Hertel, W. Radloff, Femtosecond time-resolved hydrogen-atom elimination from photoexcited pyrrole molecules, ChemPhysChem 5 (9) (2004) 1423–1427.
[6] G.M. Roberts, C.A. Williams, H. Yu, A.S. Chatterley, J.D. Young, S. Ullrich, V.G. Stavros, Probing ultrafast dynamics in photoexcited pyrrole: timescales for $^1\pi\sigma^*$ mediated H-atom elimination, Faraday Discuss. 163 (0) (2013) 95–116.
[7] M. Staniforth, J.D. Young, D.R. Cole, T.N.V. Karsili, M.N.R. Ashfold, V.G. Stavros, Ultrafast excited-state dynamics of 2,4-dimethylpyrrole, J. Phys. Chem. A 118 (46) (2014) 10909–10918.
[8] G. Wu, S.P. Neville, O. Schalk, T. Sekikawa, M.N.R. Ashfold, G.A. Worth, A. Stolow, Excited state non-adiabatic dynamics of pyrrole: a time-resolved photoelectron spectroscopy and quantum dynamics study, J. Chem. Phys. 142 (7) (2015) 074302.
[9] T. Geng, O. Schalk, S.P. Neville, T. Hansson, R.D. Thomas, Dynamics in higher lying excited states: Valence to Rydberg transitions in the relaxation paths of pyrrole and methylated derivatives, J. Chem. Phys. 146 (14) (2017) 144307.
[10] O.M. Kirkby, M.A. Parkes, S.P. Neville, G.A. Worth, H.H. Fielding, Non-radiative relaxation dynamics of pyrrole following excitation in the range 249.5–200 nm, Chem. Phys. Lett. 683 (Supplement C) (2017) 179–185.
[11] A.L. Sobolewski, W. Domcke, Conical intersections induced by repulsive $^1\pi\sigma^*$ states in planar organic molecules: malonaldehyde, pyrrole and chlorobenzene as photochemical model systems, Chem. Phys. 259 (2) (2000) 181–191.
[12] B.O. Roos, P.-Å. Malmqvist, V. Molina, L. Serrano-Andrés, M. Merchán, Theoretical characterization of the lowest-energy absorption band of pyrrole, J. Chem. Phys. 116 (17) (2002) 7526–7536.
[13] V. Vallet, Z. Lan, S. Mahapatra, A.L. Sobolewski, W. Domcke, Time-dependent quantum wave-packet description of the $^1\pi\sigma^*$ photochemistry of pyrrole, Faraday Discuss. 127 (0) (2004) 283–293.
[14] V. Vallet, Z. Lan, S. Mahapatra, A.L. Sobolewski, W. Domcke, Photochemistry of pyrrole: Time-dependent quantum wave-packet description of the dynamics at the $\pi_1\sigma^*$-S_0 conical intersections, J. Chem. Phys. 123 (14) (2005) 144307.
[15] M. Barbatti, M. Vazdar, A.J.A. Aquino, M. Eckert-Maksic, H. Lischka, The non-adiabatic deactivation paths of pyrrole, J. Chem. Phys. 125 (16) (2006) 164323.
[16] M. Vazdar, M. Eckert-Maksic, M. Barbatti, H. Lischka, Excited-state non-adiabatic dynamics simulations of pyrrole, Mol. Phys. 107 (8–12) (2009) 845–854.
[17] B. Sellner, M. Barbatti, H. Lischka, Dynamics starting at a conical intersection: application to the photochemistry of pyrrole, J. Chem. Phys. 131 (2) (2009) 024312.
[18] M. Barbatti, J. Pittner, M. Pederzoli, U. Werner, R. Mitric, V. Bonacic-Koutecý, H. Lischka, Non-adiabatic dynamics of pyrrole: dependence of deactivation mechanisms on the excitation energy, Chem. Phys. 375 (1) (2010) 26–34.
[19] S.P. Neville, G.A. Worth, A reinterpretation of the electronic spectrum of pyrrole: a quantum dynamics study, J. Chem. Phys. 140 (3) (2014) 034317.
[20] M. Sapunar, A. Ponzi, S. Chaiwongwattana, M. Mališ, A. Prlj, P. Decleva, N. Došlic, Timescales of N–H bond dissociation in pyrrole: a nonadiabatic dynamics study, Phys. Chem. Chem. Phys. 17 (29) (2015) 19012–19020.
[21] D.V. Makhov, K. Saita, T.J. Martínez, D.V. Shalashilin, Ab initio multiple cloning simulations of pyrrole photodissociation: TKER spectra and velocity map imaging, Phys. Chem. Chem. Phys. 17 (5) (2015) 3316–3325.
[22] K.R. Nandipati, Z. Lan, H. Singh, S. Mahapatra, An alternative laser driven photodissociation mechanism of pyrrole via $\pi\sigma_1^*$ S_0 conical intersection, J. Chem. Phys. 146 (21) (2017) 214304.
[23] D.V. Makhov, D.V. Shalashilin, Floquet Hamiltonian for incorporating electronic excitation by a laser pulse into simulations of non-adiabatic dynamics, Chem. Phys. 515 (2018) 46–51.
[24] D. Picconi, S.Y. Grebenshchikov, Photodissociation dynamics in the first absorption band of pyrrole. II. Photofragment distributions for the $^1A_2(\pi\sigma^*) \leftarrow \widetilde{X}\,^1A_1(\pi\pi)$ transition, J. Chem. Phys. 148 (10) (2018) 104104.
[25] J.A. Green, D.V. Makhov, N.C. Cole-Filipiak, C. Symonds, V.G. Stavros, D.V. Shalashilin, Ultrafast photodissociation dynamics of 2-ethylpyrrole: adding insight to experiment with ab initio multiple cloning, Phys. Chem. Chem. Phys. 21 (2019) 3832–3841.
[26] J.C. Tully, Molecular dynamics with electronic transitions, J. Chem. Phys. 93 (2) (1990) 1061–1071.
[27] B.O. Roos, P.R. Taylor, P.E.M. Siegbahn, A complete active space SCF method (CASSCF) using a density matrix formulated super-CI approach, Chem. Phys. 48 (2) (1980) 157–173.
[28] K. Andersson, P.-Å. Malmqvist, B.O. Roos, Second-order perturbation theory with a complete active space self-consistent field reference function, J. Chem. Phys. 96 (2) (1992) 1218–1226.
[29] J. Finley, P.-Å. Malmqvist, B.O. Roos, L. Serrano-Andrés, The multi-state CASPT2 method, Chem. Phys. Lett. 288 (2) (1998) 299–306.
[30] T. Shiozaki, W. Gyorffy, P. Celani, H.-J. Werner, Communication: extended multi-state complete active space second-order perturbation theory: energy and nuclear gradients, J. Chem. Phys 135 (8) (2011) 081106.
[31] H. Tao, B.G. Levine, T.J. Martínez, Ab initio multiple spawning dynamics using multi-state second-order perturbation theory, J. Phys. Chem. A 113 (49) (2009) 13656–13662.
[32] S. Mai, P. Marquetand, L. González, Intersystem crossing pathways in the non-canonical nucleobase 2-thiouracil: a time-dependent picture, J. Phys. Chem. Lett. 7 (11) (2016) 1978–1983.
[33] J.W. Park, T. Shiozaki, Analytical derivative coupling for multistate CASPT2 theory, J. Chem. Theory Comput. 13 (6) (2017) 2561–2570.
[34] M.K. MacLeod, T. Shiozaki, Communication: automatic code generation enables nuclear gradient computations for fully internally contracted multireference theory, J. Chem. Phys 142 (5) (2015) 051103.
[35] B. Vlaisavljevich, T. Shiozaki, Nuclear energy gradients for internally contracted complete active space second-order perturbation theory: multistate extensions, J. Chem. Theory Comput. 12 (8) (2016) 3781–3787.
[36] T. Shiozaki, BAGEL brilliantly advanced general electronic-structure library, WIREs Comput. Mol. Sci. 8 (1) (2018) e1331.
[37] BAGEL Brilliantly Advanced General Electronic-structure Library, http://www.nubakery.org under the GNU General Public License.
[38] A.A. Granovsky, Extended multi-configuration quasi-degenerate perturbation theory: the new approach to multi-state multi-reference perturbation theory, J. Chem. Phys. 134 (21) (2011) 214113.
[39] B.O. Roos, K. Andersson, Multiconfigurational perturbation theory with level shift — the Cr_2 potential revisited, Chem. Phys. Lett. 245 (2) (1995) 215–223.

[40] P.-O. Widmark, P.-Å. Malmqvist, B.O. Roos, Density matrix averaged atomic natural orbital (ANO) basis sets for correlated molecular wave functions, Theoret. Chim. Acta 77 (5) (1990) 291–306.

[41] K. Kaufmann, W. Baumeister, M. Jungen, Universal Gaussian basis sets for an optimum representation of Rydberg and continuum wavefunctions, J. Phys. B 22 (1989) 2223–2240.

[42] F. Aquilante, J. Autschbach, R.K. Carlson, L.F. Chibotaru, M.G. Delcey, L. De Vico, I. Fdez. Galván, N. Ferré, L.M. Frutos, L. Gagliardi, M. Garavelli, A. Giussani, C.E. Hoyer, G. Li Manni, H. Lischka, D. Ma, P-Å. Malmqvist, T. Müller, A. Nenov, M. Olivucci, T.B. Pedersen, D. Peng, F. Plasser, B. Pritchard, M. Reiher, I. Rivalta, I. Schapiro, J. Segarra-Martí, M. Stenrup, D.G. Truhlar, L. Ungur, A. Valentini, S. Vancoillie, V. Veryazov, V.P. Vysotskiy, O. Weingart, F. Zapata, R. Lindh, Molcas 8: new capabilities for multiconfigurational quantum chemical calculations across the periodic table, J. Comput. Chem. 37 (5) (2016) 506–541.

[43] S. Mai, M. Richter, M. Heindl, M.F.S.J. Menger, A. Atkins, M. Ruckenbauer, F. Plasser, M. Oppel, P. Marquetand, and L. González, SHARC2.0: Surface Hopping Including Arbitrary Couplings — Program Package for Non-Adiabatic Dynamics, 2018. < sharc-md.org > .

[44] Sebastian Mai, Philipp Marquetand, Leticia González, Nonadiabatic dynamics: the SHARC approach, WIREs Comput. Mol. Sci. 8 (6) (2018) e1370.

[45] E. Wigner, On the quantum correction for thermodynamic equilibrium, Phys. Rev. 40 (5) (1932) 749–759.

[46] J.P. Dahl, M. Springborg, The Morse oscillator in position space, momentum space, and phase space, J. Chem. Phys. 88 (7) (1988) 4535–4547.

[47] R. Crespo-Otero, M. Barbatti, Spectrum simulation and decomposition with nuclear ensemble: formal derivation and application to benzene, furan and 2-phenylfuran, Theor. Chem. Acc. 131 (6) (2012) 1237.

[48] M. Barbatti, G. Granucci, M. Persico, M. Ruckenbauer, M. Vazdar, M. Eckert-Maksic, H. Lischka, The on-the-fly surface-hopping program system Newton-X: application to ab initio simulation of the nonadiabatic photodynamics of benchmark systems, J. Photochem. Photobiol. A 190 (2) (2007) 228–240.

[49] G. Granucci, M. Persico, A. Toniolo, Direct semiclassical simulation of photochemical processes with semiempirical wave functions, J. Chem. Phys. 114 (24) (2001) 10608–10615.

[50] F. Plasser, G. Granucci, J. Pittner, M. Barbatti, M. Persico, H. Lischka, Surface hopping dynamics using a locally diabatic formalism: charge transfer in the ethylene dimer cation and excited state dynamics in the 2-pyridone dimer, J. Chem. Phys. 137 (22) (2012) 22A514.

[51] G. Granucci, M. Persico, Critical appraisal of the fewest switches algorithm for surface hopping, J. Chem. Phys. 126 (13) (2007) 134114.

[52] J.P. Zobel, J.J. Nogueira, L. González, The IPEA dilemma in CASPT2, Chem. Sci. 8 (2) (2017) 1482–1499.

[53] N.d.N. Rodrigues, N.C. Cole-Filipiak, K.N. Blodgett, C. Abeysekera, T.S. Zwier, V.G. Stavros, Wavepacket insights into the photoprotection mechanism of the uv filter methyl anthranilate, Nat. Commun. 9 (2018) 5188.

APPENDIX A.2 ADVENT OF THE LVC MODEL

APPENDIX A.2.1

From Surface Hopping to Quantum Dynamics and Back. Finding Essential Electronic and Nuclear Degrees of Freedom and Optimal Surface Hopping Parameters

Sandra Gómez, Moritz Heindl, András Szabadi and Leticia González

J. Phys. Chem. A, **123**, 8321-8332 (2019).
`https://doi.org/10.1021/acs.jpca.9b06103`

Contributions:

Sandra Gómez performed single point computations, ran MCTDH and SH simulations analyzed the results, co-supervised the project, and wrote the first draft and the refinement of the manuscript.

Moritz Heindl performed SH dynamics simulations, implemented iterative selection scheme, contributed to the initial draft manuscript

András Szabadi parametrized the potential energy surface.

Leticia González conceived and supervised the project, analyzed the results and contributed to the writing and refinement of the manuscript.

THE JOURNAL OF PHYSICAL CHEMISTRY A
Article
Cite This: J. Phys. Chem. A 2019, 123, 8321−8332
pubs.acs.org/JPCA

From Surface Hopping to Quantum Dynamics and Back. Finding Essential Electronic and Nuclear Degrees of Freedom and Optimal Surface Hopping Parameters

Published as part of The Journal of Physical Chemistry virtual special issue "F. Javier Aoiz Festschrift".

Sandra Gómez, Moritz Heindl, András Szabadi, and Leticia González*

Institute of Theoretical Chemistry, Faculty of Chemistry, University of Vienna, 1010 Vienna, Austria

Supporting Information

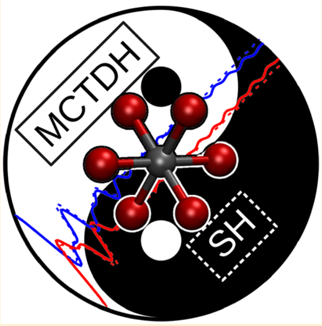

ABSTRACT: We report an efficient iterative procedure that exploits surface-hopping trajectory methods and quantum dynamics to achieve two complementary purposes: to identify the minimum dimensionality of a molecular Hamiltonian in terms of electronic and nuclear degrees of freedom to study radiationless relaxation mechanisms as well as to provide a reference quantum dynamical calculation that allows assessing of the validity of surface-hopping parameters. This double goal is achieved by a feedback loop between surface hopping and MCTDH calculations based on potential energy surfaces parametrized with a linear vibronic coupling method. Initially, a surface hopping calculation in full dimensionality with a chosen set of parameters is performed, and it is repeated, gradually reducing its dimensionality until divergence with the initial calculation is observed or the system is small enough to be treated quantum dynamically. A comparison between the quantum dynamics and surface hopping simulations dictates the validity of the surface hopping parameters. Using these new parameters, the reduction loop is started again, until convergence. As an example, this strategy is applied to simulate the ultrafast intersystem crossing dynamics of $[PtBr_6]^{2-}$ in solution. The 15-dimensional space initially including 200 electronic states is reduced to a 9-dimensional problem with 76 electronic states, without a considerable loss of accuracy.

1. INTRODUCTION

The study of light-induced processes is key to advance many fields.[1] Ideally, the evolution of a molecule after light irradiation can be studied by solving the nuclear time-dependent Schrödinger equation. However, the underlying calculation of the global configurational space in which a wavepacket can potentially evolve precludes the application of this equation to large molecules, e.g., large transition metal complexes. The multiconfigurational time-dependent Hartree method (MCTDH)[2,3] can alleviate this hurdle by optimizing configurations variationally, reducing considerably the size of the problem to solve. Although current extensions of MCTDH, such as the multilayer approach (ML),[4] can be pushed to treat considerable large systems,[5] the family of MCTDH methods is still applied to systems with a limited number of degrees of freedom (DOFs). An additional cost in MCTDH calculations comes from the number of diabatic states considered. Like the full-dimensional space of nuclear configurations, the inclusion of the complete set of electronically excited states is unfeasible, and current computational resources impose a limitation on the number of low-lying electronic excited states. More often than not, choosing few lowest electronic states as a reference point for the diabatization can prove to be insufficient as states not included initially stabilize during the ensuing dynamics, leading to artifacts.

During the last decades, a number of strategies emerged with the aim of reducing the cost of quantum dynamical calculations. A popular way to simplify the calculations is to propagate wavepackets on the orthogonal basis spanned by the vibrational normal modes of the molecule.[6−8] If symmetry is available, a symmetry analysis of the normal modes and the partaking excited states also allows separating between so-called driving and spectator modes, based on their ability to influence the dynamics. A separation of normal modes into photoactive, photoinactive, and neutral bath modes is also possible, taking advantage of excited-state properties at the Franck−Condon geometry, such as excited-state gradients, energy-difference Hessians, and nonadiabatic coupling vectors.[9,10]

An alternative procedure to identify important DOFs that then are used explicitly in a quantum dynamics calculation (e.g., MCTDH or ML-MCTDH) with a limited number of DOFs is to first employ lower-level dynamics methods. Obviously, the limitation of this approach is the innate assumption that the quality of the preliminary dynamics is sufficient to describe the path that quantum dynamics would take. However, there are promising steps in this direction, e.g.,

Received: June 26, 2019
Revised: August 29, 2019
Published: September 3, 2019

DOI: 10.1021/acs.jpca.9b06103

conducting a principal component analysis of quantum−classical surface hopping (SH) trajectory dynamics[11] to guide a MCTDH calculation in reduced dimensionality.[12,13] The appeal of SH to perform nonadiabatic dynamics is based upon its computational efficiency, accuracy, and the fact that it can be implemented on-the-fly, without depending on a given set of reduced coordinates or precomputed potential energy surfaces (PESs), making it a powerful tool to study light-induced processes in molecular systems.[14] This flexibility comes at a considerable cost as SH can be unreliable in a number of cases, such as in extended coupling regions[11] or wavepacket recoherence,[15] to name a few. To extend the applicability of SH beyond the limitations imposed by its intrinsic classical treatment of the nuclei and the lack of a rigorous derivation, various SH schemes, decoherence corrections, and velocity rescaling choices have been proposed. Despite the fact that most SH studies employ default SH parameters, we have recently shown that this choice can substantially affect the outcome of the dynamics.[16] To overcome these uncertainties, the best solution would be to use a high-level dynamics method, such as MCTDH, as a benchmark for comparison, which seemingly opposes the idea of using SH as a guide to determine the normal modes and states that could be selected to carry out a meaningful MCTDH reduced dynamics.

In this contribution, we propose an efficient iterative methodology between SH and MCTCH to overcome this apparent contradiction. The proposed approach exploits the efficiency of our recently developed SH method with a linear vibronic coupling Hamiltonian (LVC).[17] With LVC, the wings of SH are clipped by restricting the dynamics to precomputed approximated potentials, but in return, one achieves enormous computational efficiency that can be translated in a substantial increase of system size, be it the number of atoms and/or states that can be considered.

Using a diabatic and a normal mode basis for SH dynamics allows for a direct and easy comparison between SH and MCTDH calculations with exactly the same Hamiltonian. Such comparison offers an opportunity to exploit the best of both methods as it enables an iterative process that provides (i) the most important normal modes to be included in MCTDH and at the same time (ii) the best SH parameters one should use to treat the system. In short, the strategy is based on the following: Starting from full dimensionality and a sufficiently large number of electronic states, a comparison of successive SH dynamical simulations with progressively fewer degrees of electronic and/or nuclear freedom is performed. If the obtained dynamics resembles the one simulated in full dimensionality and after the system is hopefully modest enough to be tractable quantum dynamically, a MCTDH calculation is performed and compared to the last SH run. This closed loop approach has two-fold applicability: On the one hand, it allows reduction of the system dimensionality until an affordable MCTDH or ML-MCTDH calculation can be set up. On the other hand, it allows benchmarking the choice of SH parameters that could be used in a full-dimensional simulation without the restriction of a LVC model. The proposed approach is conceptually simple, unbiased, and attractive as it is generally applicable in a black-box fashion. While it has the potential to treat more generalized problems than the one presented below, it also provides an ideal setup to deal with LVC models.

To test this procedure, we study the early photodynamics of the $[\mathrm{PtBr_6}]^{2-}$ transition metal complex in water, which undergoes singlet−triplet intersystem crossing (ISC) within 150 fs, as recently demonstrated experimentally.[18,19]

2. METHODS

2.1. Potential Energy Surfaces. The diabatic PESs **W** are approximated using a LVC[20−22] model, i.e., a Taylor expansion around the equilibrium geometry truncated at first order in the basis of the ground-state normal mode coordinates q_i. In matrix notation:

$$\mathbf{W} = \begin{bmatrix} E^{(0)} & \cdots & 0 \\ \vdots & \ddots & \vdots \\ 0 & \cdots & E^{(n)} \end{bmatrix} + \frac{1}{2}\sum_{i=1}^{\text{modes}} \begin{bmatrix} \omega_i \mathrm{q}_i{}^2 & \cdots & 0 \\ \vdots & \ddots & \vdots \\ 0 & \cdots & \omega_i \mathrm{q}_i{}^2 \end{bmatrix} + \sum_{i=1}^{\text{modes}} \begin{bmatrix} \kappa_i^{(0)}\mathrm{q}_i & \cdots & \lambda_i^{(0n)}\mathrm{q}_i \\ \vdots & \ddots & \vdots \\ \lambda_i^{(n0)}\mathrm{q}_i & \cdots & \kappa_i^{(n)}\mathrm{q}_i \end{bmatrix} \tag{1}$$

The index n goes from zero (ground state) to the number of electronically excited states under consideration. $E^{(n)}$ are the vertical excited-state energies calculated from a single point performed at the optimized geometry. The parametrization is performed in the basis of the ground-state harmonic frequencies ω_i at the optimized geometry. The intrastate coupling κ and interstate coupling λ are calculated from the gradients and nonadiabatic couplings, respectively. If the quantum chemical method of choice cannot calculate analytical gradients or nonadiabatic couplings or if the number of electronic states is remarkably high to perform this task efficiently, the intrastate and interstate couplings can be obtained via numerical derivatives based on the overlap of electronic wave functions calculated at different normal mode displacements.[23] Alternatively, they can also be calculated at the vicinity of a conical intersection using energies and the Hessian.[24,25]

The spin−orbit coupling (SOC) matrix elements calculated at the minimum geometry are added as a constant matrix to the Hamiltonian (zero-order approach).[26]

2.2. Nuclear Dynamics Methods. In this section, we recap essential features of the MCTDH and SH methods, as used here. In MCTDH,[3,27] a linear combination of Hartree products of time-dependent basis functions (known as single-particle functions or SPFs) defines the multidimensional wave function, carrying the correlation between DOFs. This wave function is propagated on diabatic potentials according to the Dirac−Frenkel variational principle. In contrast, the SH[11] method is based on a classical description of the nuclei, collapsing the probability distribution in position space on a single distinct value. In order to mimic a wavepacket, multiple independent trajectories are propagated from initial geometries and velocities, e.g., from a Wigner distribution that correlates position and momentum.[28] A trajectory can perform transitions between different states based on a stochastic selection and the current nonadiabatic coupling elements.

SH can be implemented on-the-fly to profit from the locality of the electronic properties needed every time step. The propagation can use the molecular coulomb Hamiltonian (MCH or spin diabatic) representation or, in the presence of

DOI: 10.1021/acs.jpca.9b06103
J. Phys. Chem. A 2019, 123, 8321−8332

SOCs, the basis composed of the eigenstates of the total Hamiltonian including spin.[29,30]

In both MCTDH and SH methods, the electronic wave function is represented as a sum of electronic states with time-dependent coefficients. In the MCTDH wave function, these electronic coefficients are time-dependent high-dimensional nuclear wave functions associated with each electronic state. In SH, we obtain one time-dependent coefficient per state and per trajectory from the electronic Schrödinger equation.

A trajectory located on an electronic state trails the gradient of that one state but carries the coefficients of all others. Electronic population transfer may occur after two electronic states come close, causing a change on their coefficients that is carried along the trajectory. When the states come close repeatedly, the coefficients change accordingly, simulating an interference process between two parts of a split wavepacket. However, as a trajectory only follows the gradient of the active state, this population transfer occurs as if both parts of the wavepacket were moving with the same velocity, in a nonphysical manner. In order to correct for this improper description, different approaches have been devised. Ideally, one would divide the trajectory at the splitting point in two and follow every gradient separately.[31−33] This is partially realized in the augmented fewest switches surface hopping (AFSSH)[34,35] approach, where auxiliary trajectories in all but the active state are propagated using gradients calculated at the geometry determined by the active state. Once an auxiliary trajectory diverges too far away from the current geometry, the population in this state is deemed to be dephased, and the population in this state collapses toward the active state. Less demanding computationally and thus widely extended is the use of exponential damping for the amplitude of nonactive states depending on the kinetic energy and the energy gap, as in the so-called energy-based decoherence (EDC) scheme of Granucci et al.[36]

2.3. SH-MCTDH Workflow. Here we describe in detail the workflow proposed to identify relevant electronic states and nuclear DOFs playing a role in the deactivation dynamics of a high-dimensional molecular system, as well as suitable SH parameters.

A preliminary harmonic frequency calculation and a single-point calculation (or $3N - 6$ for nonlinear molecules if numerical derivatives are required) are performed with a chosen electronic structure level of theory. These calculations serve to parametrize the full-dimensional PES, i.e., the LVC model to be used for both the MCTDH and SH dynamics. Depicted in Figure 1, the workflow consists of the following steps:

(1) An initial run using SH dynamics is carried out using any choice of SH parameters, such as hopping algorithms, decoherence corrections, velocity rescaling, treatment of frustrated hops, etc. The obtained dynamics serves as a reference ("Ref") for the upcoming Hamiltonian loop in steps 2 and 3.

(2) This is the start of the Hamiltonian loop: Selected nuclear DOFs or electronic excited states can now be deleted systematically from the previous Hamiltonian. The selection can be based on any imaginable criterion: e.g., a priori approaches, based on symmetry, chemical intuition, excited-state properties in the model Hamiltonian like excited-state gradients, and coupling elements, or a posteriori approaches that rely on previously run dynamics, like principal component analysis, identifying modes that do not drive the dynamics toward crossing points, searching for diabatic excited states that are not populated at all during the dynamics, etc. The efficiency of LVC-SH dynamics is such that even the brute force approach of running a whole simulation deactivating one DOF at a time is possible. After selecting which diabatic states or nuclear DOFs remain, SH simulations are rerun with this reduced model Hamiltonian.

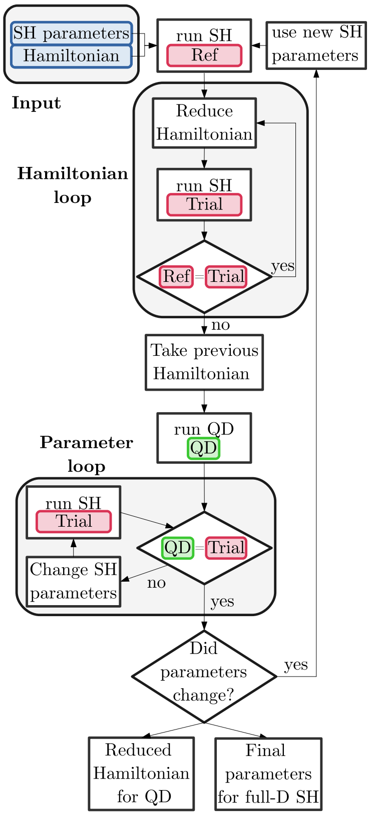

Figure 1. Proposed workflow to identify (i) a reduced Hamiltonian that can be employed in a quantum dynamical (QD) simulation and (ii) suitable surface hopping (SH) parameters for a full-dimensional calculation. See details in the text.

(3) A comparison of the dynamics run with a reduced Hamiltonian ("Trial") against the full Ref dynamics of step 1 provides an estimation of the validity of the reduced Hamiltonian. As observable one can quantify errors in the time evolution of the state populations, errors in decay times, etc., within a certain threshold. If the observables of the Trial dynamics agree reasonably well with those of the Ref dynamics, the Hamiltonian can be further reduced by returning to step 2. This iterative reduction can be repeated until the obtained Trial dynamics diverges from the Ref dynamics, indicating an improper description of the system. At that point, the Hamiltonian loop is finished and the last iteration that produced results in accordance with the reference is chosen for the next step.

(4) The Hamiltonian obtained in the Hamiltonian loop is, hopefully, small enough to be treated using MCTDH. This quantum dynamics simulation will now be taken as a quantum dynamical reference ("QD") to benchmark an appropriate set of SH parameters in the parameter loop.

(5) Parameter loop: The SH dynamics are repeated using various sets of parameters, keeping the same reduced Hamiltonian. The obtained dynamics is then compared to the QD reference. This comparison returns the set of SH parameters that gives the best correspondence to the QD results.

(6) If the set of parameters differs from the one used to calculate the Ref dynamics and the one used in the Hamiltonian loop, an additional step is in order: If a posteriori criteria were applied to reduce the size of the Hamiltonian, this reduction was based on an improper set of SH parameters. Therefore, it is mandatory to restart the whole process again starting from step 1, this time using the freshly optimized set of SH parameters.

Once convergence toward a set of SH parameters is reached, both goals of this symbiotic approach are reached: a Hamiltonian sufficiently reduced in both nuclear DOFs and number of states that can be used to run quantum dynamics simulations is found, and a set of SH parameters that suits the system at hand best is available. This set of SH parameters can now be taken to run full-dimensional dynamics, e.g., on nonparametrized potentials. As pointed out in the Introduction, the applicability of this approach is based on the presumption that SH can provide a reasonable description of the investigated dynamics. Hence, in cases where nuclear quantum effects dominate parts of the dynamics, this recipe will more often than not result in a wrong set of states and modes. However, strong discrepancies between QD and SH results could also be used to identify problematic cases and help to narrow down and understand the nature of these deviations.

3. COMPUTATIONAL DETAILS

$[PtBr_6]^{2-}$ belongs to the octahedral O_h point group, thus posing the particularly tricky challenge of possessing a high density of triple degenerate singlet and triplet states in the lower-energy region of the absorption spectrum. The totally symmetric (A_{1g}) normal mode has a nonzero gradient for every excited state, while all gerade normal modes (symmetric with respect to the inversion center) could have a nonzero gradient in states that belong to higher-dimensional irreducible representations (E_g, T_{1g}, T_{1u}, T_{2g}, and T_{2u}).

3.1. LVC Parametrization. The PESs of $[PtBr_6]^{2-}$ were parametrized using (i) density functional theory (DFT) to optimize the ground-state equilibrium geometry and obtain its harmonic frequencies and (ii) its time-dependent version (TD-DFT) to obtain excitation energies and couplings. All calculations were done without symmetry constraints. In particular, we employed the B3LYP hybrid functional,[37] as implemented in the ADF code,[38] together with the TZP basis set. This choice was motivated by ref 39, which shows that hybrid functionals, such as B3LYP, give accurate results for Pt and Ir complexes, while more recent functionals like M06-2X or CAM-B3LYP overestimate the excitation energies and BP86 or M06-L underestimate them. To allow for electronic wave function overlap calculations, all of the electrons are considered in the Pt atom. The Tamm−Dancoff approximation (TDA)[40] and the Grimme D3 correction[41] were used. The zero-order regular approximation (ZORA) was employed to include relativistic effects. A total of 50 singlet and 50 triplet states spanning from 2.37 to 6.90 eV, dipole moments, and SOC terms were calculated, i.e., a total number of 200 spin states was considered as a sufficiently large number of states approximating the infinite limit. The influence of the surrounding water as solvent was modeled using the conductor-like screening model (COSMO) approach.[42] The parameters of the so-obtained LVC Hamiltonian can be found in the SI. The normal modes of $[PtBr_6]^{2-}$ are displayed in Figure 2 together with their corresponding irreducible representation.

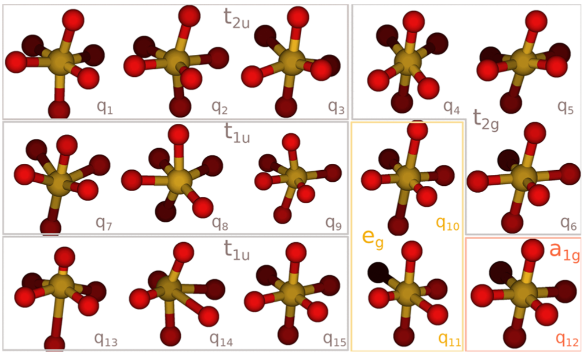

Figure 2. Normal modes of $[PtBr_6]^{2-}$ and their symmetry. An animation of the normal modes can be found in the Supporting Information under the name modes.gif.

As the calculation of the LVC parameters is done via numerical differences, particular attention is needed due to the inherent high symmetry of the molecule. When the molecule has degenerate electronic states—as is the case here—an inversion of the order of states might occur due to numerical noise associated with the calculated energies, yielding spurious couplings when differentiating. For example, in the case of a T_{1g} state, three degenerate states are expected; however, as symmetry is neglected, these states have slightly varying energies due to numerical noise. At a displaced geometry, this numerical noise can result in a different ordering of these degenerate states, which in turn will result in strong artificial coupling parameters in the LVC parametrization. This problem is best visualized in Figure 3a, which shows a zoom in of the overlap matrix between electronic wave functions at the optimized and displaced geometries for the totally symmetric stretching mode (q_{12}). Some of the larger overlaps are located at off-diagonal positions, indicating an exchange of electronic states. This problem was solved reordering carefully the states with respect to the optimized structure in the cases where the electronic states were still degenerate at the displaced geometry; see Figure 3b. Note that this process does not involve any diagonalization because this would annihilate the diabatic couplings between electronic states.

3.2. Nonadiabatic Dynamics Methods. The MCTDH quantum dynamics simulations were performed using the quantics[43] program package. Different SPFs were optimized for every electronic state, following a multiset formalism. The maximum number of SPFs, the primitive basis, and the mode combination in MCTDH required for the convergence of the different calculations are given in Table 1.

The initial condition for the MCTDH dynamics is a wave function constructed as the Hartree product of the harmonic oscillator eigenstates for each DOF of the electronic ground state placed on the states corresponding to the T_{1g} energy level.

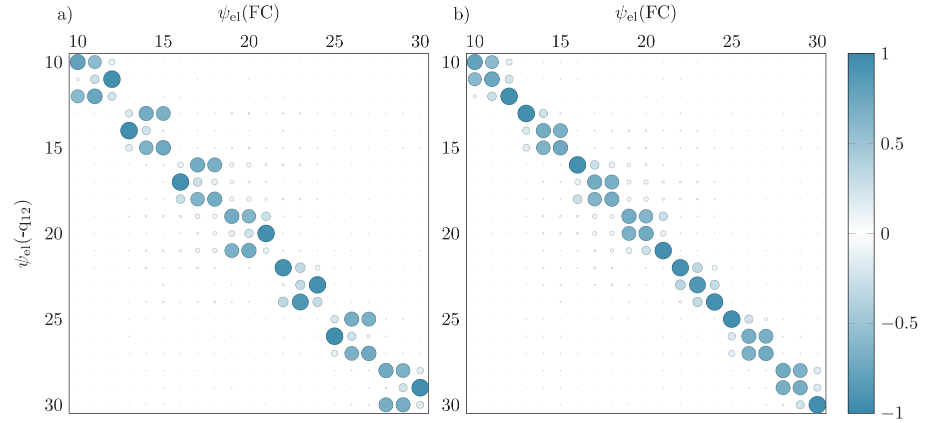

Figure 3. Zoom in of the overlap matrices for 20 electronic states (from the 10th singlet to the 30th) at the optimized geometry and a displaced one along the totally symmetric normal mode q_{12}, before (a) and after (b) correction.

Table 1. Basis Needed for Convergence of the MCTDH Wavepacket Propagations[a]

simulation	particle	N_i	n_{max}
6S/11T/15modes	el		39
	q_1,q_2,q_3	11,11,11	2
	q_4,q_5,q_6	11,11,11	5
	q_7,q_8,q_9	11,11,11	2
	q_{10},q_{11}	35,35	5
	q_{12}	77	2
	q_{13},q_{14},q_{15}	11,11,11	2
16S/20T/15modes	el		76
	q_1,q_2,q_3	11,11,11	6
	q_4,q_5,q_6	11,11,11	5
	q_7,q_8,q_9	11,11,11	3
	q_{10},q_{11}	37,37	6
	q_{12}	119	3
	q_{13},q_{14},q_{15}	11,11,11	4
16S/20T/9modes	el		76
	q_1,q_3	11,11,11	3
	q_4	11,11,11	4
	q_{10},q_{11}	27,27	4
	q_{12}	103	3
	q_{13},q_{14},q_{15}	11,11,11	4
16S/20T/6modes	el		76
	q_1	11,11,11	3
	q_5	11,11,11	4
	q_{10},q_{11}	35,35	4
	q_{12}	105	3
	q_{13}	11,11,11	3
16S/20T/3modes	el		76
	q_{10},q_{11}	37,37	3
	q_{12}	99	2
16S/20T/1modes	el		76
	q_{12}	256	1

[a] In the column labeled "simulation", the number of singlet (S) and triplet (T) states and normal modes is specified. The grid type was harmonic oscillator DVR[44] with N_i basis functions for every MCTDH run. n_{max} is the maximum number of SPFs used for each state in a multiset formulation. This number is optimized for every electronic state; however, only the maximum value is written due to space limitations. Note that in the case of only a single mode exact dynamics has been conducted.

For the SH, a development version of the SHARC suite of programs[45] was used. The SHARC implementation propagates the nuclei classically using as a basis the diagonalized sum of the electronic Hamiltonian and the SOC Hamiltonian.[17] The electronic wave function was propagated using the local diabatization method[46] with a 0.02 fs time step. Initially, the default parameters were used; therefore, nuclei were propagated in the diagonal basis, and the EDC correction[36] was employed with a parameter C of 0.1 Hartree. To conserve the total energy, the full velocity vector was rescaled in the event of a hop. No special actions were conducted in the case of frustrated hops. The SHARC hopping scheme was used to determine if a hop occurs.[30] Nonadiabatic coupling elements were not included in the gradient transformation.

The initial positions and velocities for the initial SH trajectories were sampled according to oscillator strengths[47] from a Wigner distribution of 1000 geometries using the same frequency calculation as used for the parametrization of the PESs. The vertical excitations of triplets and singlets calculated from the optimized geometry are shown in Figure 4a. Every histogram bar corresponds to a 0.01 eV interval, showing the high degeneracy and density of states presented by this molecular system.

Two state representations are possible, either performing a diagonalization of the total Hamiltonian including SOCs (diagonal representation) or without diagonalization (spin-diabatic or MCH representation). The density of states for this molecule is obtained by convoluting the vertical energies for every state from the Wigner distribution with Gaussian functions with a full width at half-maximum of 0.2 eV. The result, shown in Figure 4b, illustrates that the densities of singlet and triplet states (in the MCH picture) are overlapping throughout the complete energy range. Vertical excitations were calculated for each geometry to generate an absorption spectrum from the oscillator strengths[48] using the LVC parametrized surfaces. The resulting absorption spectrum using 1000 geometries is shown in Figure 4c. The difference between spectra in diagonal and MCH pictures suggests that ISC could occur without the need for strong structural rearrangements beforehand. For the highest and lowest peaks of the spectra, the agreement between calculations and experiment is reasonable. However, TDDFT fails to assign nonvanishing oscillator strengths to the states corresponding to

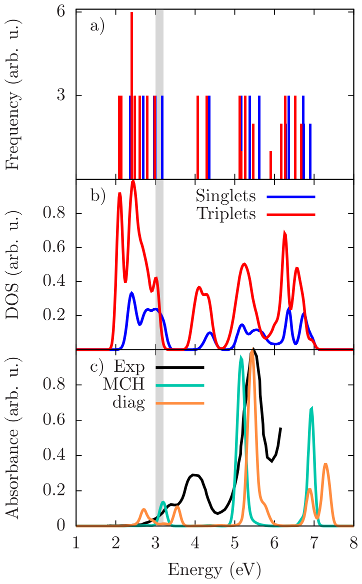

Figure 4. (a) Histogram of vertical energies in the MCH picture calculated from the optimized geometry. The number of states in every 0.01 eV interval is shown on the *y* axis. (b) Density of states (DOS) of $[PtBr_6]^{2-}$ in the MCH picture, calculated from vertical energies calculated with the LVC model of the Wigner distribution of 1000 geometries. (c) LVC absorption spectra of $[PtBr_6]^{2-}$ calculated via excited-state calculations from an ensemble of 1000 geometries, either in the MCH (teal) or the diagonal representation (orange). The absorption spectra are compared to the experimental one of ref 49. (black). The excitation window is marked in gray.

the middle peak at about 4 eV (note that there are states in this energy range, Figure 4, panel b).

For the initial excitation, we assume a delta-pulse excitation, and therefore, we excite in the MCH picture. Absorption in the range of 420 nm was simulated by doing an oscillator strength-weighted stochastic selection of initial states in a window between 3.0 and 3.2 eV, following experiments published in ref 49. This energy range is shadowed in gray in Figure 4. This window corresponds to an excitation to the first T_{1g} spectroscopic state, forbidden for the optimized geometry due to the Laporte rule (because the ground state is A_{1g} and the dipole moment operator belongs to the T_{1u} irreducible representation). Symmetry breaking along the six ungerade modes allows the transition to occur via vibronic coupling, also known as the Herzberg–Teller effect. After excitation to the T_{1g} spectroscopic state, the molecule moves along the normal modes that have a nonzero gradient on this state. According to symmetry, these normal modes belong to the irreducible representations contained in the direct product $T_{1g} \times T_{1g}$, i.e., a_{1g}, e_g, and t_{2g}. The totally symmetric mode q_{12} is the mode that has a nonzero gradient in every electronic state and therefore leads the molecular movement. Ungerade modes have zero intrastate couplings but can be active in coupling gerade and ungerade states.

For the Hamiltonian loop, it was found that already 50 SH trajectories are sufficient to get an indication of the ensuing dynamics. In the parameter loop, 300 SH trajectories are necessary to get converged results before comparing to the MCTDH calculations.

4. RESULTS AND DISCUSSION

Even though $[PtBr_6]^{2-}$ is a small molecule, converging a MCTDH dynamics calculation containing all 15 normal modes and 200 electronic states is not feasible. It can however be easily done with the help of LVC-SHARC. As documented in ref 16, different choices of SH parameters can lead to different results, particularly with different decoherence correction setups. Thus, we start by investigating the effect of the EDC in the dynamics of $[PtBr_6]^{2-}$ in H_2O.

Figure 5 compares the SH dynamics with (a) and without (b) EDC using the full LVC Hamiltonian. For simplicity, we focus on the collective evolution of all 50 singlets (dark blue) and all 50 triplets (red) summed together. Initially, both dynamics agree well, showing strong population oscillations between singlet and triplet states. However, these oscillations get dampened faster using EDC, and after 100 fs, the final triplet population is lower by 10% with EDC than that without. At this point, we do not have a criterion to judge which simulation is better. Because EDC was originally designed to correct for overcoherence, we decide to take the dynamics with EDC as the first reference Ref, with which we shall start the first Hamiltonian loop (recall Figure 1).

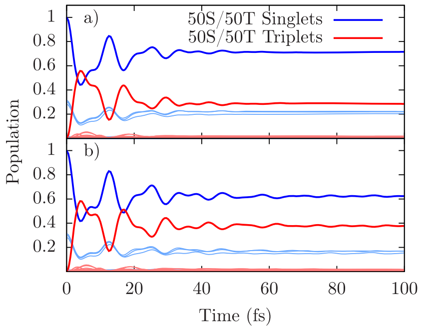

Figure 5. LVC-SHARC dynamics using 50 singlets and 50 triplet states (50S/50T), with (a) and without (b) EDC. The time evolutions of the singlet and triplet states are depicted in blue and red, respectively—in light color for the actual states and in dark for the sum over all of the singlets and triplets states.

The system at hand can be reduced both in the number of nuclear DOFs and/or in the number of electronic states. First, we shall investigate how to reduce the number of states up to an amount that can be handled by MCTDH, and afterward the number of DOFs will be decreased.

4.1. Reduction of Electronic States. In order to investigate whether all 200 mixed electronic states are necessary to describe the relaxation of $[PtBr_6]^{2-}$ in H_2O, the maximum amount of electronic population (square of the time-dependent coefficient) present during the Ref dynamics was screened for every diabatic state, allowing identification of states that were less frequently or not populated during the dynamics. Different cutoffs of this a posteriori population criterion have been employed to reduce the Hamiltonian. The results are shown in Figure 6, which collects populations and errors with respect to the Ref dynamics using different thresholds (0.01, 0.3, 1.2, 5, and 10%, which correspond to sets of 31S/30T, 16S/21T, 6S/11T, 4S/5T, and 4S/1T states, respectively) of the total maximum electronic state population in every state (all m_s components of triplets of each state were summed). Using as a measure the deviation with respect to Ref

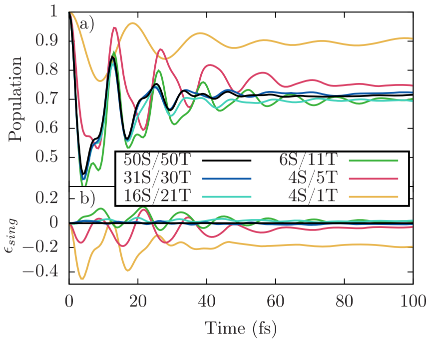

Figure 6. Hamiltonian loop: reducing the number of states. (a) Time evolution of the sum of population in all singlet states obtained with SH at various numbers of singlet and triplet states (the triplet population is complementary to the singlet and thus not shown for clarity). EDC was used for all calculations. (b) Time-dependent deviation ($\epsilon_{\text{sing}}(t)$) in the total singlet population for all considered Hamiltonians with respect to the reference $\epsilon_{\text{sing}}(t) = \sum_i^{50} P_{i;\text{ref}}(t) - \sum_i^{n} P_i(t)$.

in the total population of singlet and triplet states, one can see that the Hamiltonian consisting of 6S and 11T states (39 electronic states) is a reasonably good compromise between accuracy and computational effort. Therefore, the first iteration in the Hamiltonian loop was exited with a Hamiltonian that was reduced by 161 electronic states.

As a MCTDH calculation with 39 states and all 15 normal modes is feasible, we use this calculation to provide a QD reference. The comparison of the QD results against the SH counterpart is shown in Figure 7. Interestingly, both populations agree very well during the first 20 fs but diverge afterward when the EDC starts to damp population from the triplet states back to the singlets. At this point, two scenarios are possible: Either the MCTDH dynamics shows quantum features that are not recovered by SH or the set of SH parameters is not ideally suited to describe the solvated $[\text{PtBr}_6]^{2-}$ complex.

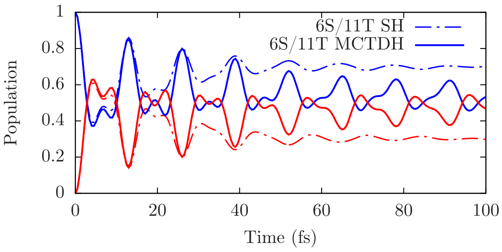

Figure 7. SH and MCTDH time evolution of all of the singlet (blue) and triplet (red) states, using a reduced Hamiltonian of 6 singlets (S) and 11 triplets (T).

In order to investigate which of these possibilities holds, the parameter loop is entered. Accordingly, we now investigate the effect of decoherence and other SH parameters on this reduced Hamiltonian by changing the default set of SH parameters ("Default" in Figure 8), explained in the Computational Details section. Regarding decoherence corrections, we investigate the performance of the AFSSH method as well as the effect of not using decoherence correction at all ("No deco").

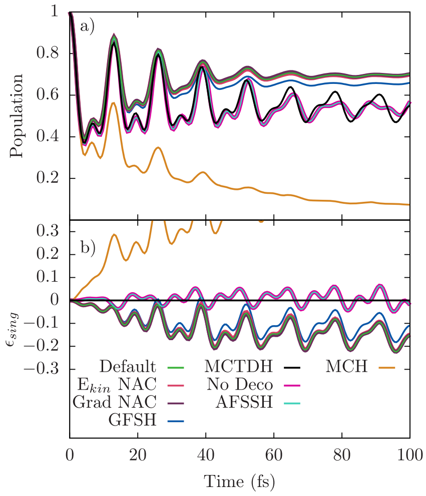

Figure 8. Parameter loop: (a) Sum of the singlet quantum population obtained by changing single parameters in the SH dynamics of the reduced 6S/11T system against the reference MCTDH using the same number of states (black). Lines of different thickness were used to make almost identical lines distinguishable. Default is the set of parameters described in the Computational Details. MCH uses a spin-diabatic basis in the propagation. GFSH stands for the global flux hopping scheme. Different ways to take into account the nonadiabatic coupling vector have been used: E_{kin} NAC indicates that velocities were rescaled along the NAC vector after a surface hop, while Grad-NAC included the NAC vectors in the gradient transformation. AFSSH stands for augmented fewest switches surface hopping, and No Deco means that no decoherence correction has been used. (b) Time-dependent deviation ($\epsilon_{\text{sing}}(t)$) in the total singlet population for all considered parameters with respect to the MCTDH reference $\epsilon_{\text{sing}}(t) = \sum_i^{6} P_{i;\text{ref}}(t) - \sum_i^{6} P_i(t)$.

The global flux surface hopping scheme[50] (GFSH) was tested to estimate the influence of superexchange on the dynamics, which is poorly accounted for in standard SH. Additionally, the influence of rescaling the kinetic energies after a hop along the NAC vector (E_{kin} NAC) and including the NAC vectors in the gradient transformation (Grad-NAC) has been studied. Finally, the changes connected to switching from propagating using the total diagonal basis to using the spin-diabatic basis of the molecular Coulomb Hamiltonian (MCH) were investigated. Figure 8 shows the population evolution in each case (panel a) as well as the differences against the reference QD calculation (panel b). Three different population behaviors are visible: (i) simulations using EDC and propagated in the diagonal picture (Default, E_{kin} NAC, Grad-NAC, and GFSH); (ii) results using other decoherence corrections excluding EDC propagated in the diagonal picture (No deco, AFSSH); and (iii) results coming from propagating in the spin-diabatic basis using EDC (MCH).

The group of dynamics in set (i) agrees nicely with the MCTDH reference during the first 15 fs. After this time, the populations start to diverge: the strong initial oscillations are damped, leading to a converged final singlet population of 70%, in contrast to the still oscillating MCTDH population that oscillates around a value of 55%. Inclusion of the NAC vectors in both the gradient transformation and the velocity rescaling results in almost identical dynamics. Changing the hopping algorithm to the GFSH variant[50] only improves the final population by about 3% toward the MCTDH results.

Set (ii) of the calculations shows remarkably good agreement with the MCTDH reference, so that mild dephasing of the oscillations starts only after 70 fs and very similar final population values are obtained. Interestingly, the dynamics employing the AFSSH decoherence variant behaves identically to the simulations in the absence of any decoherence correction. This behavior is due to the moderate number of hops experienced by every single trajectory, which forces the current implementation of the AFSSH formalism to reset the auxiliary trajectories in every other state before they can diverge too far from the trajectory in the active state. Additionally, the observed dynamics occurs very coherently, as indicated by the agreement of the dynamics deprived of any decoherence correction with MCTDH.

The last branch, (iii), (MCH in Figure 8) shows the largest deviation from the MCTDH reference and starts diverging after a few fs, resulting in a dramatic overestimation of the ISC rate with a final singlet population of only 7%. This disagreement is due to the delocalized SOC present in the spin-diabatic representation in combination with the EDC. To gain some understanding of the reasons why this combination of input parameters fails in the present case, a more detailed look at the EDC is needed. In the EDC formalism, the electronic coefficients c_α in all nonactive states are damped according to

$$c_\alpha' = c_\alpha \cdot f_{\text{EDC}}$$

$$f_{\text{EDC}} = \exp\left[-\Delta t \frac{\Delta E}{\hbar}\left(1 + \frac{C}{E_{\text{kin}}}\right)^{-1}\right] \qquad (2)$$

where α is a nonactive state, f_{EDC} is the final damping factor of the population in this state, ΔE is the absolute energy difference between the active state and state α, C is an input parameter given in units of energy, and E_{kin} is the kinetic energy. The value of f_{EDC} depends on two variables during a single simulation, which are ΔE and E_{kin}. The evolution of both of these parameter and the resulting damping factor for the electronic population in the initially excited state along a single trajectory are visualized in Figure 9. Panel (a) shows how the strong but delocalized coupling results in fast hops across the set of considered states. During each hop, conservation of total energy is enforced by rescaling the kinetic energy correspondingly, leading to a rapid change of both the kinetic energy (E_{kin}) and the energy gap ($\Delta E = |E_{\text{init}} - E_{\text{ref}}|$) between the currently active state (black) and the initially populated state (teal). The impact of these parameters on f_{EDC} is depicted in Figure 9b: after the first hop to a low-lying triplet state, the population in the initially active state is dampened by a factor of about 0.93 during every time step, resulting in a cumulative damping of 60% due to the EDC before encountering the next hopping event. Hence, the EDC results in a very fast drain of the high-lying initial singlet population, which is in disagreement with the QD reference.

The results of the parameter loop can be summarized as follows: The choice of decoherence correction together with the choice of a good representation has the largest impact on the dynamics for this molecule. In particular, we found that the diagonal picture outperforms the spin-diabatic one, especially in the presence of EDC.

It is peculiar in the first place that the EDC has a detrimental influence on the dynamics as it results in a strong overall dampening. Accordingly, the best results are obtained when no decoherence correction is included. Although AFSSH gives the same results as using no decoherence correction, the latter was chosen as a preferred parameter in the parameter loop as it is conceptually easier to understand and imposes no additional cost as opposed to AFSSH. All other parameters, like changing to the GFSH, turning on the rescaling of kinetic energies along the NAC vectors after a hop, and taking the NAC vectors in the gradient transformation into account, were found to yield negligible differences. Even switching to the MCH basis yields only small deviations from the totally diagonal dynamics once no decoherence correction is used. We therefore consider that a first set of "quantum-based" SH parameters has been found and the parameter loop is finished. The SH parameters are those of the default setup, except for the decoherence correction, which is turned off as it provides much better agreement with the MCTDH dynamics. However, as the initial reduction of the states was based on a reference SH dynamics that used a different set of SH parameters, i.e., included EDC, a new reduction of the problem needs to be done starting from the SH calculation without EDC (cf. Figure 5b).

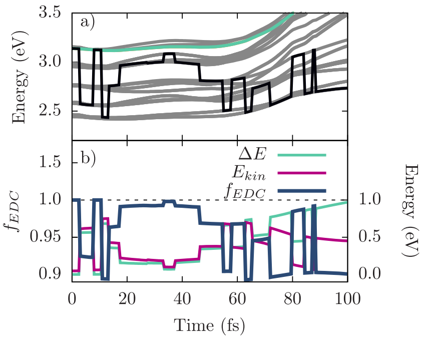

Figure 9. Evolution of one example trajectory in the spin-diabatic basis using EDC. (a) Excited-state energies (gray) during the simulation. The active state is traced in black, while the initially excited state is marked in teal. (b) Strength of the EDC term (f_{EDC}) on the electronic population in the initially excited state along the trajectory. f_{EDC} depends on both the kinetic energy of the trajectory (E_{kin}) and the energy separation between the state in question (the initially excited state) and the active state according to $\Delta E = |E_{\text{init}} - E_{\text{ref}}|$.

Accordingly, using the diabatic state population of this new Ref dynamics, the Hamiltonian loop is entered for a second time, starting from the full Hamiltonian with all of the electronic states. The results of this second iteration through the Hamiltonian loop are presented in Figure 10. In this case, a Hamiltonian with 16 singlets and 20 triplets states (76 electronic states) is deemed the best compromise. Using this number of states, a new converged MCTDH calculation is obtained to compare again against SH; see Figure 11. As can be seen, very good agreement between both dynamics is obtained during the first 40 fs, with some slight differences afterward. As the SH dynamics agrees well with the MCTDH reference dynamics, we consider the reduction of electronic states converged in this second iteration. At the same time, a set of quantum-based SH parameters has been obtained.

Now we turn our attention to understanding the role played by decoherence in the simulations of this complex by examining the reference MCTDH calculations. To this aim, we plot in Figure 12 the position expectation value of the totally symmetric mode (q_{12}) for the simulations including 6S/

DOI: 10.1021/acs.jpca.9b06103
J. Phys. Chem. A 2019, 123, 8321−8332

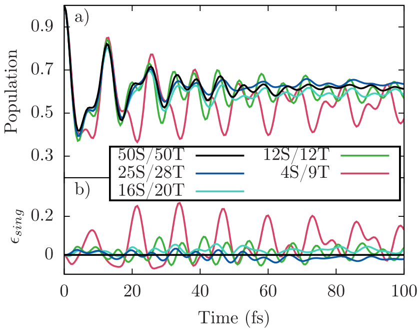

Figure 10. Hamiltonian loop: reducing the number of states without decoherence correction. (a) Time evolution of the sum of population in all singlet states obtained with SH at various numbers of singlet and triplet states. (b) Time-dependent deviation ($\epsilon_{\text{sing}}(t)$) in the total singlet population for all considered Hamiltonians with respect to the reference $\epsilon_{\text{sing}}(t) = \sum_i^{50} P_{i;\text{ref}}(t) - \sum_i^n P_i(t)$.

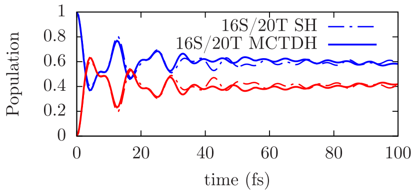

Figure 11. SH and MCTDH time evolution of all of the singlets (blue) and triplet (red) states, using 16 singlets (S) and 20 triplet (T) states. No decoherence correction is used for SH dynamics.

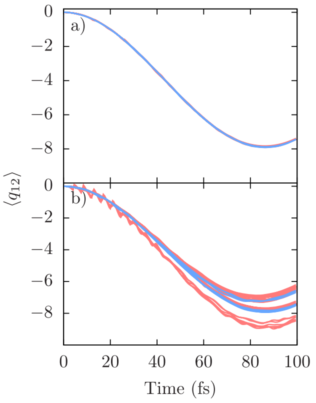

Figure 12. Expectation value of the totally symmetric mode q_{12} in mass-weighted normal mode coordinates for all MCTDH excited singlet (blue) and triplet (red) states for (a) 6S/11T (essential states after the first iteration) and (b) 16S/20T (essential states after the second iteration of the Hamiltonian loop).

11T (panel a) and 16S/20T (panel b) states. The q_{12} mode is by far the most active mode, having strong gradients for every considered state. Interestingly, these gradients show the same sign and almost the same magnitude in all of the states, resulting in similar initial movement of the wavepacket of every state in this mode. For this reason, all of the curves of Figure 12a overlap, indicating coherent movement in every electronic state and explaining why no decoherence correction is needed here, i.e., the electronic population transfer occurs coherently along this mode. Because this mode is the one that couples a large number of states and extends up to 8 units of normal mode coordinates, it is the most active normal mode and therefore responsible for most of the vibronic coupling between states. With the larger set of 16 singlet and 20 triplet states, the agreement between MCTDH and SH decreases (recall Figure 10). This deterioration is at least partially explained by Figure 12b. After 40 fs, two and later three groups of expectation values with different oscillating periods can be observed; this indicates that the wavepacket interference between parts located at different electronic states does not occur at the same time, suggesting the need for a decoherence correction, leading to the partial disagreement at and after 40 fs. This indicates that better decoherence correction models need to be developed.

In summary, the calculations suggest the following intermediate conclusions: (1) the lowest 16 singlets and 20 triplets seem to be sufficient to describe the ISC dynamics of $[\text{PtBr}_6]^{2-}$ in implicit H_2O during the first 100 fs, and (2) no decoherence is necessary to run SH in full dimensionality in this system. With this information at hand, we now proceed to investigate how many nuclear DOFs are important for the early relaxation of the system.

4.2. Reduction of Nuclear Degrees of Freedom. As in this case we already have a reference MCTDH calculation, there is no further need to rely on SH calculations as a reference. Here we shall employ the sum of absolute κ and λ values associated with a given normal mode to investigate whether a particular mode is important, but any other criteria could be used instead. If both of these sums fall below the cutoff threshold, the corresponding normal mode is removed from the Hamiltonian. The threshold values of 1.05, 1.1, 1.175, 1.3, and 4 were chosen to subsequently reduce the set of normal modes by 3 in each iteration, resulting in 12, 9, 6, 3, and 1 normal modes. A complete list of the neglected modes and the MCTDH parameters employed is collected in Table 1.

Figure 13 shows the populations obtained from the MCTDH calculations with all 15 modes, 12, 9, 6, 3, and 1. Initially and during the first 10 fs, the dynamics is found to be almost identical in all cases, showing that the effect of nuclear movement is negligible on this time scale and electronic-driven ISC dominates.

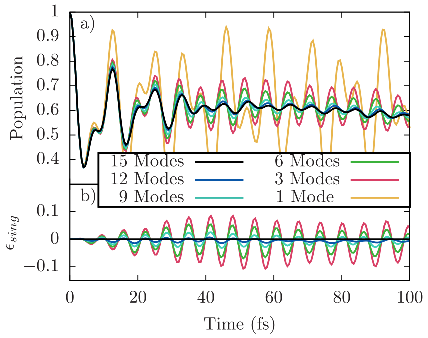

Figure 13. Hamiltonian loop: reducing the number of nuclear DOFs using MCTDH. (a) Time evolution of the sum of population in all singlet states obtained with various numbers of normal modes, as indicated. (b) Time-dependent deviation ($\epsilon_{\text{sing}}(t)$) in the total singlet population for all considered Hamiltonians with respect to the reference MCTDH calculation using all normal modes $\epsilon_{\text{sing}}(t) = \sum_i^{16} P_{i;\text{ref}}(t) - \sum_i^{16} P_i(t)$.

Then, a gradual attenuation of the oscillations is visible in going from 15- (full-dimensional) to lower-dimensional cases. Having all of the normal modes available allows for faster internal vibrational redistribution of the energy, i.e., faster loss of coherence. Subsequently reducing the number of normal modes down to only three modes still results in total state population errors of 10% of the total population. However, when going down to one single normal mode (the totally symmetric q_{12}), one observes stronger population oscillations and a dephasing that sets in after 30 fs. This large deviation from the three-mode case is due to the nature of the mode: q_{12} is the mode that contains the largest κ values and, therefore, the initial gradients that the dynamics is subject to after excitation. However, while q_{12} induces the largest movement with respect to geometric parameters, as is evident in Figure 12, it contains only a small set of λ values. Therefore, the influence of q_{12} on the total singlet population is rather small, although it is the mode that experiences the strongest displacement. It can be then concluded that the description of the initial dynamics occurring in solvated $[PtBr_6]^{2-}$ can be qualitatively described by three modes: the degenerate q_{10} and q_{11} modes (belonging to the e_g irreducible representation) that give the largest Jahn−Teller interstate couplings, and q_{12}, which is essential to describe the movement of the molecule. Striving for quantitative agreement, one could yet consider that a good agreement in the population oscillations can be achieved using nine normal modes.

4.3. Intersystem Crossing Dynamics of $[PtBr_6]^{2-}$ in Water.

Finally, this section is devoted to discuss the early excited-state dynamics of solvated $[PtBr_6]^{2-}$ using the optimized Hamiltonian of 16S/20T states and a set of validated SH parameters.

Initial excitation at about 3.1 eV leads to population of the first set of triple degenerate $^1T_{1g}$ states. From there, ultrafast electronic ISC occurs mostly uncoupled from the nuclear motion needing only three normal modes to describe the essential dynamics, as shown above. This electronic ISC is a concluding result from both the full-dimensional MCTDH calculations with 16S/20T states and the SH calculation using no decoherence correction, both with 16S/20T or 50S/50T. During the first 100 fs, ISC results in a population transfer of 40% toward the triplet states. Experimental data for the complete dissociation mechanism followed by water association returned a quantum yield of about 40%,[51] although it has been suggested that initial transfer toward the triplet states should yield almost quantitative population transfer.[18]

Our simulations show that the nuclear dynamics of the $[PtBr_6]^{2-}$ complex is governed by Pt−Br bond elongations that are mainly driven by the totally symmetric q_{12} mode. Due to the inherent limitation of the LVC model, which approximates PESs by displaced harmonic oscillators, dissociation of Br is not possible. However, the concerted motion initiated in all of the trajectories toward dissociation is still apparent, as can be seen in Figure 14, which shows the Pt−Br bond that undergoes the maximum elongation for every trajectory. The maximum elongation of Pt−Br (about 2.72 Å) is reached at 85 fs. At this point, the harmonic nature of the potentials hinders dissociation and the bond length shortens again, so that the simulations cannot be considered reliable anymore. Longer simulations would require a nuclear Hamiltonian for MCTDH beyond the local harmonic approximation or on-the-fly SH simulations using a multiconfigurational method that includes statical electronic correlation.

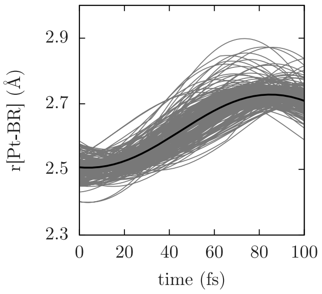

Figure 14. Most active Pt−Br bond distance for the ensemble of trajectories (gray) and the corresponding average (black).

5. CONCLUSIONS

A simple procedure to identify the essential electronic and nuclear DOFs of a system has been devised, profiting from a feedback loop between SH and QD simulations using a LVC method. The method is general and extendable to any analytical potential that can be used within quantum dynamics (in this case we use MCTDH) and to any criteria to reduce electronic states and/or normal modes. This approach could be used to provide a starting point for a reduced Hamiltonian to be treated with quantum dynamics. This model Hamiltonian should afterward be accordingly extended to account for effects that might not be recovered by a LVC Hamiltonian. Furthermore, our procedure is also able to provide the best set of parameters to run SH simulations based on a comparison with a quantum reference.

The reduction of electronic and nuclear DOFs is done as follows. First, SH dynamics simulations are carried out on the complete system with a particular choice of parameters. As the LVC Hamiltonian is analytical, solving the Newton equations of motion is done extremely efficiently, so that gradually nonpopulated electronic states are eliminated from the nuclear Hamiltonian until finding the optimal system that conserves the characteristics of the full-dimensional dynamics (in this case we look at the electronic populations) with the lowest number of DOFs. When this reduced system is found, a QD (e.g., MCTDH) calculation is performed and compared to the last SH dynamics to assess the validity of the SH parameters. Particular attention should be paid to decoherence corrections, the hopping algorithm, and velocity rescaling as we have recently shown that they can have a drastic effect on the outcome of SH.[16] If a different set of SH parameters is found, the reduction step needs to be performed again because before it was based on the wrong choice of SH parameters. A further comparison with the quantum dynamics indicates if convergence is achieved. After finding the optimal reduced set of DOFs and optimal SH parameters, it is possible to refine the reduced system with a higher level of quantum dynamics simulations or to run full-dimensional on-the-fly SH dynamics simulations with better suited parameters.

In line with previous results from some of us,[16] the present calculations emphasize that the SH parameters are not universally valid, and caution should be exerted. Better decoherence correction schemes should be developed. In the present example, employing no decoherence was best suited to describe ISC because this occurred without strong involvement of nuclear motion, but other systems could behave differently and will have different requirements. Given the large usability that SH has in the community in many different fields, the

DOI: 10.1021/acs.jpca.9b06103
J. Phys. Chem. A 2019, 123, 8321−8332

present method offers a simple way to validate a given choice of SH parameters.

Here, the ultrafast ISC in the $[PtBr_6]^{2-}$ in implicit water has been studied as a test case. This is a realistic system with many DOFs that a priori asks to involve a large number of degenerate and pseudodegenerate electronic states. Starting with 50 triplets and 50 singlets (200 coupled electronic states) and 15 nuclear DOFs described by a LVC model, we found that 16 singlets and 20 triplets and 9 nuclear DOFs are enough to describe the early ISC of the system after excitation to the T_{1g} singlet manifold, without a considerable loss of accuracy. In particular, the early ISC of $[PtBr_6]^{2-}$ is mainly an electronic process, and during the first 100 fs, there is no large effect of nuclear motion, as has been demonstrated in other transition metal complexes.[52]

■ ASSOCIATED CONTENT

Supporting Information

The Supporting Information is available free of charge on the ACS Publications website at DOI: 10.1021/acs.jpca.9b06103.

> LVC parametrization data, normal mode gif, and MCTDH data necessary to reproduce the results (ZIP)

■ AUTHOR INFORMATION

Corresponding Author

*E-mail: leticia.gonzalez@univie.ac.at.

ORCID

Leticia González: 0000-0001-5112-794X

Notes

The authors declare no competing financial interest.

■ ACKNOWLEDGMENTS

Funding from the Deutsche Forschungsgemeinschaft [DFG, Priority Program SPP 2102 Light-controlled reactivity of metal complexes (GO 1059/8-1)] and the University of Vienna is gratefully acknowledged. The authors thank Graham A. Worth for fruitful discussions. This paper is dedicated to J. Aoiz, whom SG is especially grateful for his excellent spectroscopy lectures at the UCM. Part of the calculations have been obtained using the Vienna Scientific Cluster.

■ REFERENCES

(1) González, L.; Escudero, D.; Serrano-Andrés, L. Progress and challenges in the calculation of electronic excited states. *ChemPhysChem* **2012**, *13*, 28−51.

(2) Meyer, H.-D.; Manthe, U.; Cederbaum, L. The multi-configurational time-dependent Hartree approach. *Chem. Phys. Lett.* **1990**, *165*, 73−78.

(3) Gatti, F.; Lasorne, B.; Meyer, H.-D.; Nauts, A. Applications of Quantum Dynamics in Chemistry. *Lectures Notes in Chemistry*; Springer: Heidelberg, 2017; Vol. *98*.

(4) Wang, H.; Thoss, M. Multilayer formulation of the multi-configuration time-dependent Hartree theory. *J. Chem. Phys.* **2003**, *119*, 1289−1299.

(5) Falahati, K.; Tamura, H.; Burghardt, I.; Huix-Rotllant, M. Ultrafast carbon monoxide photolysis and heme spin-crossover in myoglobin via nonadiabatic quantum dynamics. *Nat. Commun.* **2018**, *9*, 4502.

(6) Hammerich, A. D.; Manthe, U.; Kosloff, R.; Meyer, H.-D.; Cederbaum, L. S. Time-dependent photodissociation of methyl iodide with five active modes. *J. Chem. Phys.* **1994**, *101*, 5623−5646.

(7) Worth, G. A.; Meyer, H.-D.; Cederbaum, L. S. The effect of a model environment on the S_2 absorption spectrum of pyrazine: A wavepacket study treating all 24 vibrational modes. *J. Chem. Phys.* **1996**, *105*, 4412−4426.

(8) Mahapatra, S.; Worth, G. A.; Meyer, H. D.; Cederbaum, L. S.; Köppel, H. The $\tilde{A}^2E$ $\tilde{B}^2B_2$ photoelectron bands of allene beyond the linear coupling scheme: An *ab initio* dynamical study including all fifteen vibrational modes. *J. Phys. Chem. A* **2001**, *105*, 5567−5576.

(9) Lasorne, B.; Sicilia, F.; Bearpark, M. J.; Robb, M. A.; Worth, G. A.; Blancafort, L. Automatic generation of active coordinates for quantum dynamics calculations: Application to the dynamics of benzene photochemistry. *J. Chem. Phys.* **2008**, *128*, 124307.

(10) Richings, G.; Robertson, C.; Habershon, S. Can we use on-the-fly quantum simulations to connect molecular structure and sunscreen action? *Faraday Discuss.* **2019**, *216*, 476−493.

(11) Tully, J. C. Molecular-dynamics with electronic-transitions. *J. Chem. Phys.* **1990**, *93*, 1061−1071.

(12) Capano, G.; Penfold, T. J.; Chergui, M.; Tavernelli, I. Photophysics of a copper phenanthroline elucidated by trajectory and wavepacket-based quantum dynamics: a synergetic approach. *Phys. Chem. Chem. Phys.* **2017**, *19*, 19590−19600.

(13) Tavadze, P.; Avendaño Franco, G.; Ren, P.; Wen, X.; Li, Y.; Lewis, J. P. A machine-driven hunt for global reaction coordinates of azobenzene photoisomerization. *J. Am. Chem. Soc.* **2018**, *140*, 285−290.

(14) Barbatti, M. Nonadiabatic dynamics with trajectory surface hopping method. *WIREs: Comput. Mol. Sci.* **2011**, *1*, 620−633.

(15) Miao, G.; Subotnik, J. Revisiting the recoherence problem in the fewest switches surface hopping algorithm. *J. Phys. Chem. A* **2019**, *123*, 5428−5435.

(16) Plasser, F.; Mai, S.; Fumanal, M.; Gindensperger, E.; Daniel, C.; González, L. Strong influence of decoherence corrections and momentum rescaling in surface hopping dynamics of transition metal complexes. *J. Chem. Theory Comput.* **2019** DOI: 10.1021/acs.jctc.9b00525 (in press).

(17) Plasser, F.; Gómez, S.; Menger, M. F. S. J.; Mai, S.; González, L. Highly efficient surface hopping dynamics using a linear vibronic coupling model. *Phys. Chem. Chem. Phys.* **2019**, *21*, 57−69.

(18) Zheldakov, I. L. *Ultrafast photophysics and photochemistry of hexacoordinated bromides of Pt(IV), Os(IV), and Ir(IV) in the condensed phase studied by femtosecond pump-probe spectroscopy*. Ph.D. thesis, 2010.

(19) Zheldakov, I. L.; N. Ryazantsev, M.; Tarnovsky, A. N. Wavepacket motion via a conical intersection in the photochemistry of aqueous transition-metal dianions. *J. Phys. Chem. Lett.* **2011**, *2*, 1540−1545.

(20) Köppel, H.; Domcke, W.; Cederbaum, L. S. *Advances in Chemical Physics*; John Wiley & Sons, Ltd., 2007.

(21) Köppel, H.; Domcke, W. *Encyclopedia in Computational Chemistry*; John Wiley & Sons, Ltd., 1998.

(22) Worth, G. A.; Cederbaum, L. S. Beyond Born-Oppenheimer: Molecular dynamics through a conical intersection. *Annu. Rev. Phys. Chem.* **2004**, *55*, 127−158.

(23) Plasser, F.; Ruckenbauer, M.; Mai, S.; Oppel, M.; Marquetand, P.; González, L. Efficient and flexible computation of many-electron wavefunction overlaps. *J. Chem. Theory Comput.* **2016**, *12*, 1207−1219.

(24) Gonon, B.; Perveaux, A.; Gatti, F.; Lauvergnat, D.; Lasorne, B. On the applicability of a wavefunction-free, energy-based procedure for generating first-order non-adiabatic couplings around conical intersections. *J. Chem. Phys.* **2017**, *147*, 114114.

(25) Kammeraad, J. A.; Zimmerman, P. M. Estimating the derivative coupling vector using gradients. *J. Phys. Chem. Lett.* **2016**, *7*, 5074−5079.

(26) Marian, C. M. Spin-orbit coupling and intersystem crossing in molecules. *WIREs: Comput. Mol. Sci.* **2012**, *2*, 187−203.

(27) Beck, M. H.; Jäckle, A.; Worth, G. A.; Meyer, H.-D. The multiconfiguration time-dependent Hartree (MCTDH) method: a

highly efficient algorithm for propagating wavepackets. *Phys. Rep.* **2000**, *324*, 1−105.

(28) Sun, L.; Hase, W. L. Comparisons of classical and Wigner sampling of transition state energy levels for quasiclassical trajectory chemical dynamics simulations. *J. Chem. Phys.* **2010**, *133*, 044313.

(29) Mai, S.; Marquetand, P.; González, L. A general method to describe intersystem crossing dynamics in trajectory surface hopping. *Int. J. Quantum Chem.* **2015**, *115*, 1215−1231.

(30) Mai, S.; Marquetand, P.; González, L. Nonadiabatic dynamics: The SHARC approach. *WIREs: Comput. Mol. Sci.* **2018**, *8*, No. e1370.

(31) Cheng, S. C.; Zhu, C.; Liang, K. K.; Lin, S. H.; Truhlar, D. G. Algorithmic decoherence time for decay-of-mixing non-Born-Oppenheimer dynamics. *J. Chem. Phys.* **2008**, *129*, 024112.

(32) Subotnik, J. E.; Jain, A.; Landry, B.; Petit, A.; Ouyang, W.; Bellonzi, N. Understanding the surface hopping view of electronic transitions and decoherence. *Annu. Rev. Phys. Chem.* **2016**, *67*, 387−417.

(33) Ha, J.-K.; Lee, I. S.; Min, S. K. Surface hopping dynamics beyond nonadiabatic couplings for quantum coherence. *J. Phys. Chem. Lett.* **2018**, *9*, 1097−1104.

(34) Subotnik, J. E.; Shenvi, N. A new approach to decoherence and momentum rescaling in the surface hopping algorithm. *J. Chem. Phys.* **2011**, *134*, 024105.

(35) Jain, A.; Alguire, E.; Subotnik, J. E. An efficient, augmented surface hopping algorithm that includes decoherence for use in large-scale simulations. *J. Chem. Theory Comput.* **2016**, *12*, 5256−5268.

(36) Granucci, G.; Persico, M.; Zoccante, A. Including quantum decoherence in surface hopping. *J. Chem. Phys.* **2010**, *133*, 134111.

(37) Stephens, P. J.; Devlin, F. J.; Chabalowski, C. F.; Frisch, M. J. Ab initio calculation of vibrational absorption and circular dichroism spectra using density functional force fields. *J. Phys. Chem.* **1994**, *98*, 11623−11627.

(38) Baerends, E. J. et al. *ADF2017, SCM, Theoretical Chemistry*; Vrije Universiteit, Amsterdam, The Netherlands; https://www.scm.com.

(39) Latouche, C.; Skouteris, D.; Palazzetti, F.; Barone, V. TD-DFT Benchmark on Inorganic Pt(II) and Ir(III) Complexes. *J. Chem. Theory Comput.* **2015**, *11*, 3281−3289.

(40) Hirata, S.; Head-Gordon, M. Time-dependent density functional theory within the Tamm−Dancoff approximation. *Chem. Phys. Lett.* **1999**, *314*, 291−299.

(41) Grimme, S.; Antony, J.; Ehrlich, S.; Krieg, H. A consistent and accurate ab initio parametrization of density functional dispersion correction (DFT-D) for the 94 elements H-Pu. *J. Chem. Phys.* **2010**, *132*, 154104.

(42) Pye, C. C.; Ziegler, T. An implementation of the conductor-like screening model of solvation within the Amsterdam density functional package. *Theor. Chem. Acc.* **1999**, *101*, 396−408.

(43) Worth, G. A.; Giri, K.; Richings, G. W.; Beck, M. H.; Jäckle, A.; Meyer, H.-D. *QUANTICS, a suite of programs for molecular QUANTum dynamICS simulations*, version 1.1; 2015.

(44) Light, J. C.; Hamilton, I. P.; Lill, J. V. Generalized discrete variable approximation in quantum mechanics. *J. Chem. Phys.* **1985**, *82*, 1400−1409.

(45) Mai, S.; Richter, M.; Heindl, M.; Menger, M. F. S. J.; Atkins, A.; Ruckenbauer, M.; Plasser, F.; Oppel, M.; Marquetand, P.; González, L. *SHARC2.0: Surface hopping including arbitrary couplings Program package for non-adiabatic dynamics.* sharc-md.org (2018).

(46) Granucci, G.; Persico, M.; Toniolo, A. Direct semiclassical simulation of photochemical processes with semiempirical wave functions. *J. Chem. Phys.* **2001**, *114*, 10608−10615.

(47) Barbatti, M.; Ruckenbauer, M.; Plasser, F.; Pittner, J.; Granucci, G.; Persico, M.; Lischka, H. Newton-X: a surface-hopping program for nonadiabatic molecular dynamics. *WIREs: Comput. Mol. Sci.* **2014**, *4*, 26−33.

(48) Crespo-Otero, R.; Barbatti, M. Spectrum simulation and decomposition with nuclear ensemble: formal derivation and application to benzene, furan and 2-phenylfuran. *Theor. Chem. Acc.* **2012**, *131*, 1237.

(49) Pozdnyakov, I. P.; Glebov, E. M.; Matveeva, S. G.; Plyusnin, V. F.; Melńikov, A. A.; Chekalin, S. V. Primary photophysical and photochemical processes upon UV excitation of $PtBr_6^{2-}$ and $PtCl_6^{2-}$ complexes in water and methanol. *Russ. Chem. Bull.* **2015**, *64*, 1784−1795.

(50) Wang, L.; Trivedi, D.; Prezhdo, O. V. Global flux surface hopping approach for mixed quantum-classical dynamics. *J. Chem. Theory Comput.* **2014**, *10*, 3598−3605.

(51) Balzani, V.; Manfrin, M. F.; Moggi, L. Photochemistry of coordination compounds. XVI. Hexabromoplatinate(IV) and hexaiodoplatinate(IV) ions. *Inorg. Chem.* **1967**, *6*, 354−358.

(52) Atkins, A. J.; González, L. Trajectory surface-hopping dynamics including intersystem crossing in $[Ru(bpy)_3]^{2+}$. *J. Phys. Chem. Lett.* **2017**, *8*, 3840−3845.

APPENDIX A.2.2

Validating Fewest-switches Surface Hopping in the Presence of Laser Fields

MORITZ HEINDL AND LETICIA GONZÁLEZ

J. Chem. Phys. , **154**, 144102 (2021).
`https://doi.org/10.1063/5.0044807`

Contributions:

MORITZ HEINDL performed the surface hopping simulations, analyzed the results and contributed to the initial draft of the manuscript.

LETICIA GONZÁLEZ conceived and supervised the project and contributed to the writing of the manuscript.

The Journal of Chemical Physics ARTICLE scitation.org/journal/jcp

Validating fewest-switches surface hopping in the presence of laser fields

Cite as: J. Chem. Phys. **154**, 144102 (2021); doi: 10.1063/5.0044807
Submitted: 19 January 2021 • Accepted: 23 March 2021 •

Moritz Heindl and Leticia González[a)]

AFFILIATIONS

Institute of Theoretical Chemistry, Faculty of Chemistry, University of Vienna, Währingerstr. 17, 1090 Vienna, Austria

Note: This paper is part of the JCP Special Topic on Quantum Dynamics with *Ab Initio* Potentials.
[a)] **Author to whom correspondence should be addressed:** leticia.gonzalez@univie.ac.at

ABSTRACT

The capability of fewest-switches surface hopping (FSSH) to describe non-adiabatic dynamics under explicit excitation with external fields is evaluated. Different FSSH parameters are benchmarked against multi-configurational time dependent Hartree (MCTDH) reference calculations using SO_2 and 2-thiocytosine as model, yet realistic, molecular systems. Qualitatively, FSSH is able to reproduce the trends in the MCTDH dynamics with (also without) an explicit external field; however, no set of FSSH parameters is ideal. The adequate treatment of the overcoherence in FSSH is revealed as the driving factor to improve the description of the excitation process with respect to the MCTDH reference. Here, two corrections were tested: the augmented-FSSH (AFSSH) correction and the energy-based decoherence correction. A dependence on the employed basis is detected in AFSSH, performing better when spin–orbit and external laser field couplings are treated as off-diagonal elements instead of projecting them onto the diagonal of the Hamilton operator. In the presence of an electric field, the excited state dynamics was found to depend strongly on the vector used to rescale the kinetic energy along after a transition between surfaces. For SO_2, recurrence of the excited wave packet throughout the duration of the applied laser pulse is observed for laser pulses (>100 fs), resulting in additional interferences missed by FSSH and only visible in variational multi-configurational Gaussian when utilizing a large number of Gaussian basis functions. This feature vanishes when going toward larger molecules, such as 2-thiocytosine, where this effect is barely visible in a laser pulse 200 fs long.

I. INTRODUCTION

Femtosecond time-resolved spectroscopy has progressed drastically throughout the past decades,[1] challenging the computational excited state dynamics simulations to explicitly include laser pulses.[2–12] Following a laser excitation to some high-lying electronic state, a wave packet can evolve through different potential energy surfaces (PESs), ultimately deactivating to the electronic ground state by radiationless or radiative processes. The characterization of these dynamical processes requires the consideration of coupled nuclear–electronic motion, reaching beyond the Born–Oppenheimer approximation. If one also includes the interaction with the laser pulse, the ensuing excited state dynamics will be influenced according to the pulse amplitude and duration, thereby further challenging the calculations as compared to the case of dynamics in the absence of explicit external fields.

Even without explicit laser pulses, the exact quantum treatment of all degrees of freedom in non-adiabatic dynamics is a considerable burden for systems containing more than few atoms. From the large number of methods that proliferated,[13] the so-called mixed quantum–classical methods employ trajectories as basis functions, moving according to the classical laws of motion to describe the nuclei. Present in this category are the Ehrenfest,[14] *ab initio* multiple spawning[15] (AIMS), or fewest-switches surface hopping[16,17] (FSSH) dynamics. These methods show a favorable scaling with the molecular size at the cost of some quantum effects and thus accuracy in comparison to methods that more readily converge to the exact result like multi-configurational time-dependent Hartree[18] (MCTDH), variational multi-configurational Gaussian[19,20] (vMCG), or full multiple spawning[21,22] (FMS). Contrary to Ehrenfest dynamics and AIMS, FSSH is not directly derived from first principles; instead, it is based on straightforward assumptions that allow a classical trajectory to describe movement and transitions within and between different electronic states. Although recent investigations employing exact factorization[23–25] and the quantum–classical Liouville equation[26–28] have shed light on the nature of FSSH and make clear the use of the non-adiabatic coupling (NAC) vector as the proper direction for adapting the nuclear velocities at a hopping event, a proper derivation of FSSH does not exist. Therefore, systematic improvements of the FSSH algorithm are scarce, and known issues, such as the inherent overcoherence,[29,30] are treated by *ad hoc* corrections that while remedying the issue at hand in some test cases fail in others. The resulting abundance of the available options with different parameters to choose from—some of which should be more accurate while others aim to extend the applicability of this method to larger and more complex systems—both redeems and curses FSSH. On the one hand, an appropriate choice of parameters enables at least qualitative accuracy. On the other hand, most of these parameters are devised on one- or low-dimensional models, far away from reality, and, when applied in real systems, can dramatically affect dynamics.[31]

The inclusion of explicit laser pulses in the Hamiltonian is straightforward in wave packet dynamical calculations, but due to the exponential scaling, such simulations are done only in reduced dimensionality. Extensions beyond are offered by modified versions of MCTDH,[10] vMCG,[9] *ab initio* multiple cloning,[7] or AIMS,[6] showcasing the capabilities of these methods to cope with this additional coupling taking into account many degrees of freedom. The implementation of explicit laser pulses in FSSH is also possible.[2,3,32] However, recent comparisons of FSSH to exact quantum results have revealed a strong dependence on the chosen representation of the interaction with the laser pulse. Wrong representations were found to fail even for H_2^+[5,33] where only a set of Floquet states was able to correctly follow the trends of the quantum results. Similar shortcomings were found for the dissociation dynamics of LiF[6] and for single and dual avoided crossing problems employing a set of Floquet states,[12] showing that no general methodology could be devised so far to treat the coupling correctly. Overall, it seems that including a laser field into FSSH simulations provides an additional uncertainty as to which parameters are more suitable to use.

This paper is spurred on bridging recent investigations[33] that highlighted errors present in FSSH and more apparently in the presence of laser fields and the more pragmatic aim of striving to increase the comparability with experimental data by including laser fields in realistic molecular studies. With this in mind, we use two model systems, SO_2 and 2-thiocytosine, to test the influence of different FSSH parameters dealing with decoherence, representations, and rescaling options of the kinetic energy after a change between PESs or a frustrated hop. These tests are conducted both using an explicit laser pulse to excite the system and the much more common approach of neglecting any external field and just placing the wave packet directly in the optical bright state at the beginning of the dynamics. As a reference, MCTDH (also vMCG) calculations are used to verify the validity of the FSSH simulations and estimate errors for a given set of parameters, thus showing the grade of applicability of FSSH in realistic molecules.

The remainder of this paper is organized as follows: In Sec. II, the framework of FSSH and the various options available therein are presented. Dynamics methods that go beyond FSSH are introduced in Sec. III. Section IV describes the nomenclature employed and the methodological details. Finally, the numerical results are presented in Sec. V followed by the conclusions in Sec. VI.

II. FEWEST-SWITCHES SURFACE HOPPING BACKGROUND

Since its original formulation[16] as an improvement to the existing surface hopping methodologies,[34,35] FSSH has seen a multitude of adjustments to overcome some of its inherent limitations.[17,36–38] The most severe ones concern energy conservation and the fact that a single independent classical trajectory is unable to describe branching and interference correctly.[30] Instead, the whole wave packet is piggybacking on a single trajectory, resulting in a phenomenon termed overcoherence. In the following, a short overview of the FSSH methodology with its deficiencies and remedies is given to provide a background for the parameters that will be used in the subsequent dynamical simulations.

At the core of each FSSH scheme is a classical propagation of the nuclei coupled to a quantum propagation of the electronic wave function bound to the classical trajectory. In both cases, the propagation is based on a set of electronic states $|\Phi(\mathbf{r},\mathbf{R})_\alpha\rangle$ that are commonly obtained from solving the electronic Schrödinger equation. Surface hopping is not restricted to the adiabatic basis, and different sets of states can serve as a basis[39] (see section below). For now, a general non-diagonal basis will be assumed although it has been argued that the adiabatic representation is most fitting for the FSSH methodology.[40]

The electronic wave function $[|\Psi(\mathbf{r},\mathbf{R},t)\rangle]$ along each trajectory can then be written as

$$|\Psi(\mathbf{r},\mathbf{R},t)\rangle\!\rangle = \sum_\alpha c_\alpha(t)|\Phi_\alpha(\mathbf{r},\mathbf{R})\rangle\!\rangle, \tag{1}$$

where c_α are the coefficients for each electronic state. Their time dependence is given by

$$i\hbar\frac{\mathrm{d}c_\beta}{\mathrm{d}t} = \sum_\alpha\left(H^d_{\beta\alpha}(\mathbf{R},t) - i\hbar\frac{\mathrm{d}\mathbf{R}}{\mathrm{d}t}\cdot\mathbf{h}_{\beta\alpha}(\mathbf{R})\cdot\right)c_\alpha. \tag{2}$$

Here, $\mathbf{h}_{\beta\alpha}(\mathbf{R})$ is the non-adiabatic coupling (NAC) vector $\langle\Phi_\beta(\mathbf{r},\mathbf{R})|\frac{\partial\hat{H}_{el}}{\partial\mathbf{R}}|\Phi_\alpha(\mathbf{r},\mathbf{R})\rangle$ that indicates the change in the electronic wave function with variation of the nuclear coordinates. $H^d_{\beta\alpha}$ is the matrix element of a complete Hamiltonian that contains any arbitrary coupling and can be written as

$$H^d_{\beta\alpha}(\mathbf{R},t) = H_{\beta\alpha}(\mathbf{R}) - \hat{\mu}_{\beta\alpha}(\mathbf{R})\varepsilon(t) + H^{SOC}_{\beta\alpha}(\mathbf{R}). \tag{3}$$

The dipole operator $\hat{\mu}_{\beta\alpha}(\mathbf{R})$ mediates coupling between states α and β with an external laser field $\varepsilon(t)$, and H^{SOC} couples states of different multiplicity (here singlet and triplet states) via relativistic spin–orbit coupling (SOC). $H_{\beta\alpha}(\mathbf{R})$ is the matrix element of the electronic Hamiltonian in the absence of laser and SO couplings. In the case of an adiabatic basis, $H_{\beta\alpha}(\mathbf{R})$ equals zero for $\alpha \neq \beta$.

Contrary to the coefficients of the electronic wave function that can be distributed over multiple states at once and that will fluctuate across a simulation, the nuclei are restricted to move on only one of the PES in each time step, termed the *active state*. Non-adiabatic effects are included in FSSH simulations via instantaneous switches between PESs when the active state changes. Multiple algorithms to determine when the active state should be switched have been proposed—most of them adhering to the concept that the number of switches that occur during a simulation run of a single trajectory should be minimized, thus coining the term *fewest-switches*.[16,41] Since a single trajectory is only able to follow one distinct nuclear rearrangement at a time, swarms of trajectories are employed to mimic a nuclear wave packet and obtain meaningful branching ratios or excited state deactivation times.

One of the flaws of FSSH can be readily seen in the use of a set of independent classical trajectories, which prevents the simulation of nuclear quantum phenomena such as tunneling or interference. The advantages of surface hopping, however, rely on its on-the-fly application as a time step in every trajectory only needs to evaluate properties that can be obtained from a single quantum chemistry calculation. The upside is that the algorithm itself scales well with the size of the system, only depending on the cost of the corresponding quantum chemistry calculation. As running FSSH simulations necessitates the calculation of multiple trajectories at once, but the independent trajectory approximation inherent to FSSH allows for all trajectories to be computed independently, it is trivial to parallelize.

A. The choice of representation

When performing FSSH simulations, different sets of electronic basis states—termed representations—are available. While exact wave packet quantum dynamics in a complete basis is invariant to the choice of representation, FSSH is not. The nuclei of each trajectory are propagated on the PES of the active electronic state, and thus, changing the definition of the electronic states will change the PES the nuclei evolve on and, in turn, the observed dynamics.

The most accessible representation is the so-called molecular Coulomb Hamiltonian (MCH)[32,39,42] in which no coupling between states of different multiplicity and no external field is considered. Solving the electronic Schrödinger equation with the MCH yields a set of diagonal and non-crossing states within each multiplicity. Additional coupling elements such as SOCs or external fields can then be included as off-diagonal elements in the MCH picture. This MCH set of states can be transformed to a new non-diagonal set of states by a diabatization.[43] The PES of diabatic states can be chosen to be smoothly varying and can cross without showing avoided crossings. For a polyatomic molecule, no unique diabatic transformation exists[44] and the transformation should be chosen as to minimize kinetic-energy coupling and retain a set of chemically relevant states obtained at a reference geometry or to other relevant observable. A third representation is the one considered in the surface hopping including arbitrary couplings (SHARC) approach:[32,42] here, the complete Hamiltonian $\mathbf{H}^{\mathbf{d}}$ with matrix elements $H^{d}_{\alpha\beta}$ as in Eq. (3) is diagonalized. In this completely diagonal picture (DIAG), the amount of small coupling regions is reduced in favor of more strongly coupled avoided crossings. In this work, this DIAG representation will include both coupling with an external field and SOC, although it is conceivable to include only one of those couplings in the diagonalization while keeping the other as off-diagonal elements.

A fourth representation that has been employed when it comes to include external fields is the Floquet representation.[4,12,45] In the Floquet representation, a set of time-independent states is obtained for a continuous wave by diagonalizing the Floquet Hamiltonian.[46,47] For each state in the original basis a set of infinite new states is created in the Floquet picture that represents the original PES shifted by [−n, −n + 1, . . ., n] times $h\omega$, where ω corresponds to the frequency of the applied field. These surfaces are not simply shifted by this amount but show additional avoided crossings at the intersection of states with different photon numbers. Performing surface hopping simulations employing a reduced set of Floquet states has been shown to result in surfaces that can coincide with those obtained from exact factorization[33] and thus give the best description for H_2^+ in the presence of laser fields—a system where all other representations were found to fail.[5] Floquet theory, however, is not guaranteed to give the best FSSH results[12] and is only exact in the regime of continuous external fields, breaking down in the regime of ultra-short few-cycle pulses. Thus, the Floquet representation will not be applied in the current work.

B. Electronic decoherence

A wave packet traversing a conical intersection branches into a part continuing on the upper state and another propagating on the lower state. The two parts can reach different regions of phase space or could interact at a later time.

When it comes to mixed quantum–classical simulation methods, description of a passage through a conical intersection is one of the most decisive steps. The FSSH formalism mimics the splitting of the wave packet into two parts while traversing a single conical intersection as a swarm of trajectories that split in two sets following one or the other state.[48] Interestingly, the challenge of FSSH to represent the quantum behavior does not lie on the hopping itself, but on the subsequent evolution. To picture this, we take a look at the evolution of a single trajectory. When passing through the strong coupling region, the classical trajectory will end up in one of two states, randomly selected based on the coupling strength. While the classical part of this trajectory is subject to a binary choice, namely which gradient the nuclei will follow, the electronic part tells another story. The propagation of the electronic coefficients leads to a ratio of state occupations that resembles the branching ratio of the complete wave packet at the conical intersection. This distribution of electronic occupations is necessary to ensure a binary hopping choice that resembles the real wave packet so that the swarm of trajectories undergoes a reasonable splitting although every trajectory has no information on any other trajectory. Following the conical intersection, every trajectory is subject to a discrepancy between the classical population (100% in the currently active state) and the electronic populations, which are a distribution between the two states involved in the strong coupling. Doing this, the electronic population of a single trajectory mimics both parts of the wave packet at once although the nuclear movement is dictated by the active state and therefore only reminiscent of this single branch of the wave packet. Dragging this "wrong" part of the wave packet along is termed *overcoherence*. When another coupling region is encountered, there is interaction with both the "right" and the "wrong" parts of the wave packet and wrong hopping probabilities will be predicted, as the presence of this second part of the wave packet is nonphysical.

In the past decades, a plethora of modifications (decoherence methods) to the plain surface hopping have been presented to remedy overcoherence, i.e., trying to adapt the electronic populations in a more or less physical way to resemble the quantum dynamical results. In this work, we will work with two decoherence methods: the energy-based decoherence correction (EDC)[37] and the augmented fewest switches surface-hopping (AFSSH).[49,50] EDC is based on the simple assumption that the branched part of the wave packet in another state will dephase and move into another spatial part where the interactions between these two wave packet parts vanish. For a single trajectory, this means that electronic population in non-active states should slowly decay because any branched part of the wave packet in another state will dephase and move into another spatial part where the interactions between these two wave packet parts vanish. This decay is realized by modifying the electronic populations[51] (p_i) of every non-active state in every time step via

$$p_i' = p_i \cdot exp\left(-\frac{|E_i - E_\alpha|}{\hbar}\frac{E_{kin}}{E_{kin} + C}\right), \tag{4}$$

where E_i and E_α are the energy of the ith non-active and the currently active state, respectively. E_{kin} is the kinetic energy and C is a parameter commonly set[52] to 0.1 E_h. Any population that is reduced from non-active states is added to the population of the active state to keep the overall population constant. The modified populations (p_i') are then used subsequently. The AFSSH mechanism[50] is more intricate as it tries to track where any part of the wave packet in a non-active state is moving to. In every time step, gradients in the non-active states are collected and auxiliary trajectories propagated in those states. If the trajectories deviate too far or too fast from the active trajectory, the population in this non-active state is considered dephased and set to 0.

Both EDC and AFSSH decoherence corrections have been shown to improve dynamics over the case of using no decoherence correction at all in a set of test cases without including laser fields.[37,49,50] The EDC has been applied to the excited state dynamics of LiF in the presence of different laser pulses, where no significant improvement over the basic FSSH algorithm without any treatment of the overcoherence was observed when compared to the exact quantum simulations.[6] Yet, one should keep in mind that the presented decoherence corrections only explicitly tackle the problem of overcoherence but do not improve FSSH results when it comes to a wave packet recombination event. These recombination events can be important in very specific systems but have minor influence in most cases.[17]

C. Energy conservation

Propagating a swarm of non-interacting trajectories raises an important issue when it comes to energy conservation throughout the dynamics. The total energy contained within the system should not change in the course of the dynamics. This energy can be distributed into kinetic and potential energy in all nuclear and electronic degrees of freedom. When a hop between PES occurs, the potential energy of the trajectory undergoes an instantaneous change because the active state is switched. This behavior would cause discontinuities in the total energy of the single trajectory and possibly even in that of the total ensemble. To ensure energy conservation of the total ensemble, one typically enforces total energy conservation along each individual trajectory. For this, every change in the potential energy of the trajectory induced by a surface hop is compensated by adapting the kinetic energy correspondingly. In Tully's original prescription,[16] only the nuclear momenta parallel to the NAC vector $\mathbf{h}_{\alpha\beta}$ are rescaled. The use of the $\mathbf{h}$ vectors as the best possible option has subsequently been confirmed through work connecting the FSSH algorithm to the quantum–classical Liouville equation.[27,28] In the case where NAC vectors are either unavailable within the employed electronic structure method or computationally limited, the gradient difference vector $\mathbf{g}$ can be used as a substitute,

$$\mathbf{g}_{\alpha\beta} = \mathbf{F}_\beta - \mathbf{F}_\alpha, \tag{5}$$

with $\mathbf{F}_\alpha$ and $\mathbf{F}_\beta$ being the gradient in the active state and the non-active state, respectively. It has been found that the differences between using $\mathbf{h}$ and $\mathbf{g}$ are negligible in the case of large nuclear momenta in some systems but become more apparent when these are small,[53,54] highlighting the more rigorous derivation of the $\mathbf{h}$ vector to adjust the kinetic energy after a hop. An even more approximate method is to rescale the full nuclear momentum, which offers an intriguing simplicity where no additional properties need to be computed.

Hops to a lower PES result in an increase in the kinetic energy, while transitions to higher-lying PESs are accompanied by a reduction in the kinetic energy of the system. When trying to enforce any of the mentioned energy conservation procedures, a special case can be encountered if the FSSH algorithm wants to switch the active state to a higher energy PES, but the kinetic energy in the system is insufficient to bridge the energy gap to this PES. Such an attempt at hopping is rejected by most algorithms and fittingly coined as a *frustrated hop*. The presence of frustrated hops has been noted early on, and it was found that they are necessary to retain detailed balance within surface hopping simulations.[55,56] However, the number of observed frustrated hops can vary significantly, depending on which of the rescaling schemes is employed. This is due to the different amounts of available kinetic energy in rescaling along $\mathbf{h}$ or rescaling along the full velocity vector. More energy is available in the full velocity vector, as the velocity component along the NAC vector is included therein. Using the full kinetic energy rescaling scheme, i.e., enlarging a system, e.g., by including additional non-interacting molecules at large distances, increases the total kinetic energy, thus enabling the possibility to jump to higher-lying states than when non-interacting molecules are absent. If rescaling along $\mathbf{h}$ is used, inclusion of additional non- or weakly interacting molecules has no or limited influence on the NAC vector, and thus, the same amount of energy as without the additional molecules is available for hopping to surfaces of higher energy. Rescaling along the NAC vectors has been found to give results that are in best agreement with quantum dynamics and is then treated as the preferred option when NAC vectors are available.[31,56] Additional care has to be taken when using the NAC vectors to adapt the nuclear momenta when a complex Hamiltonian is employed. In this case, additional measures have to be employed to guarantee a meaningful choice of the phase, which is not arbitrary anymore.[57]

Unfortunately, the concept of strict energy conservation throughout the dynamics does not hold in the presence of an external field, which stimulates absorption or emission of photons, adding or subtracting energy to the system. When an external field is applied, two options are available to deal with this flow of energy: one is to suspend the conservation of the total energy for the duration of the pulse. Then, the nuclear momenta will not be adapted at a surface hopping event, and the trajectory will be propagated on a different PES using the same nuclear momenta. Therefore, any changes in the potential energy are also found in the total energy. Another option is to find criteria to verify whether a hop is laser-induced. This can be realized by tracking the change in the electronic coefficients due to the laser coupling as opposed to changes in the coefficients due to NACs.[58] Alternatively, one can set an energy interval around the center frequency of the external field,[32] and if the energy gap at a hopping event falls within this interval, the hop is labeled field-induced and, thus, no rescaling of the velocities is performed.

III. REFERENCE METHODS

A. Multi-configurational time-dependent Hartree

Introduced in 1990, the MCTDH[18,59,60] method is one of the most versatile methods to simulate non-adiabatic processes due to the inherent possibility to converge toward the exact solution. Briefly, MCTDH is based on an expansion of the wave function using a time-dependent basis of single-particle functions (SPFs), $|\varphi\rangle$,

$$\begin{aligned}|\Psi(q_1,\dots q_f,t)\rangle\!\rangle &= \sum_{j_1=1}^{n_1}\cdots\sum_{j_p=1}^{n_p} A_{j_1\dots j_p}(t)|\varphi^{(1)}_{j_1}(Q_1,t)\dots\varphi^{(p)}_{j_p}(Q_p,t)\rangle\!\rangle\\ &= \sum_J A_J\Phi_J, \end{aligned}\tag{6}$$

where the coordinates of Ψ are f explicit degrees of freedom (q_f), which can be combined to form a set of actual coordinates Q_i. Each Q_i then represents one or more degrees of freedom at once in a process called "mode combination." Φ_J is a single Hartree product preceded by its corresponding coefficient A_J. Through the Dirac–Frenkel variational principle, the best suited expansion coefficients and SPFs can be determined directly for each time step. Therefore, MCTDH can be understood as a method that allows describing the evolving wave packet in a reduced number of used basis functions for each time step, thereby minimizing the computational effort while maintaining a maximum amount of accuracy.

B. Variational multiconfigurational Gaussian

A drawback of MCTDH is that the SPFs themselves still use a static grid and the whole method therefore relies on a functional form of the PES. Subsequent, alternative formulations have been proposed, resulting in the development of the vMCG[19,20] method, where frozen Gaussians are used as basis functions instead of SPFs. In short, the wave function ansatz for Ψ then reads

$$|\Psi(\mathbf{r},\mathbf{R},t)\rangle\!\rangle = \sum_i A_i^{(s)}(t)|\varphi^{(\alpha)}(\mathbf{r};\mathbf{R})\chi_j^{(\alpha)}(\mathbf{R},t)\rangle\!\rangle, \tag{7}$$

where the electronic wave function for a state α, $|\varphi^{(\alpha)}(\mathbf{r};\mathbf{R})\rangle$, is multiplied by a set of Gaussian basis functions (GBFs) $|\chi_j^{(\alpha)}\rangle$ and time-dependent expansion coefficients $A_j^{(s)}$. As in MCTDH, the equations of motion can be derived variationally and result in the propagation of both the expansion coefficients and the parameters of the GBFs. The coupled motion of both the coefficients and the GBF parameters results in a "quantum" movement that goes beyond simple classical motion. Also similar to MCTDH, in the limit of infinite basis functions (SPFs for MCTDH and GBFs in vMCG), the complete space is covered in basis functions and the exact dynamics is obtained. The vMCG algorithm has the advantage that it can be employed in an on-the-fly fashion without relying on precomputed PESs.[61]

IV. COMPUTATIONAL DETAILS

A. Nomenclature

In order to distinguish between the different combinations of FSSH parameters employed in this work, the following short-hand notation will be used:

$$^{\text{REPRESENTATION}}\text{DECOHERENCE}^{\text{frustrate hops}}_{\text{rescaling}}. \tag{8}$$

The possible options for each of the keywords are listed in Table I and explained as follows:

- (i) Representation: two representations for the propagation are used, the MCH or the completely diagonal picture (DIAG) previously introduced in Sec. II A.
- (ii) Decoherence: to correct for overcoherence, we use AFSSH or EDC (see Sec. II B). Additionally, the NONE option indicates that no decoherence correction is included.
- (iii) Rescaling after a surface hop: for the treatment of velocity rescaling after a transition between states, we rescale the velocity vector after a hopping event along the full velocity vector (v), the non-adiabatic coupling vector of the involved states (h), or the gradient difference vector (g), or we do not rescale the momenta at all, therefore violating the energy conservation within each trajectory (none).

TABLE I. FSSH options employed for dynamics.

Representation	Decoherence	Rescaling	Frustrated hops
MCH	AFSSH	v	−v
DIAG	EDC	h	−h
	NONE	g	−g
		none	+

(iv) Frustrated hops: if an insufficient amount of kinetic energy is available to compensate for a hop to a higher-lying PES during the rescaling process, the hop is canceled and termed frustrated. At such frustrated hops, the velocities of the trajectory can be reflected. The same set of vectors as in (iii) is available to reflect the momenta, resulting in the options −v, −h, and −g, where the minus indicates the reflection event. Alternatively, the velocities can be kept at a frustrated hop without any reflection, which is labeled "+."

Using this notation, a FSSH setup in the diagonal representation, using the AFFSH decoherence correction and rescaling along the NAC vectors at hopping events and no reflection at frustrated hops would be denoted as $^{\mathrm{DIAG}}AFSSH_h^+$. Note that not all combinations of these parameters result in stable setups for FSSH dynamics: for example, in the MCH representation, the non-adiabatic coupling vector **h** between singlet and triplet states is zero and therefore cannot be used as a direction to rescale the velocities along in simulations including singlet and triplet states. Apart from these incompatibilities, all possible combinations between options (i)–(iii) have been used. Throughout this work, a consistent pairing of the used vectors in (iii) and (iv) has been used: This means that when using the gradient difference vector in (iii), reflection of frustrated hops in (iv) cannot be conducted along −v or −h but has to occur along −g. Using the option to not rescale the kinetic energy at all in (iii) leads to zero frustrated hops and is therefore only paired with "+" for the treatment of frustrated hops. The option "+" in (iv), however, can be paired with all rescaling vectors (iii) to shed light on the difference between dynamics where reflection takes place at frustrated hops compared to dynamics, where the same trajectory is not reflected at this point.

B. Error quantification

To quantify the difference between a reference MCTDH calculation and a FSSH calculation with a particular set of parameters, we define an error ε calculated as

$$\varepsilon = \frac{max_t}{\Delta t} \sum_{t}^{max_t} \sum_{i=1}^{n_{states}} |p_{i,t} - p_{i,t,ref}|, \tag{9}$$

where max_t is the final simulated time, Δt is the employed time step, and $p_{i,t}$ and $p_{i,t,ref}$ are the populations of state i taken from the investigated and the reference dynamics at time t, respectively. If the populations of the reference and the investigated dynamics are identical for all time steps, ε equals zero. The maximum value of this error is achieved only if for every time step of the dynamics, all of the population in the investigated dynamics is found in states that are not populated at all in the reference dynamics. For example, if all of the population in the reference dynamics is in state a, while the investigated dynamics always run in state b, the finale error equates to $|p_a - p_{a,ref}| + |p_b - p_{b,ref}| + \sum_{i\neq a,b}^{n_states-2} |0 - 0| = 2$. The error is further split into contributions from the singlet and triplet states by summing the errors over all singlet (ε_{sing}) and all triplet states (ε_{trip}), respectively.

The error measure in Eq. (9) is not well suited to describe the error in the dynamics if a laser pulse is present: As mentioned above, the maximum error is 2, achieved if all the population is found in differing states for both the reference and the investigated dynamics. However, when we imagine an extreme case, where a weak laser excites only 1% of the ground state population to higher-lying states in both the reference and the investigated dynamics, one would obtain a maximum error of 0.02 due to the agreement in the 99% of population staying correctly in the S_0 ground state. Therefore, we use two differently calculated errors for simulations that include laser fields in order to provide errors that can be compared to errors from dynamics without a laser field: First, the deviation in the ground state population (ε_{S_0}) is calculated according to Eq. (9) only using the ground state population; this will indicate the capability of a given set of FSSH parameters to describe the initial excitation process. To factor out the differences in the excitation process itself from the subsequent excited state dynamics, the error in the excited state populations (ε^r) is calculated using a renormalized excited state population. This is done by renormalizing the population in the excited states in every time step to 1 for both the reference and the FSSH dynamics, yielding ε^r (the superscript thus indicates the renormalization within this error measure),

$$\varepsilon^r = \frac{max_t}{\Delta t} \sum_{t}^{max_t} \sum_{i=2}^{n_{states}-1} \left| \frac{p_i, t}{1 - p_{S_0,t}} - \frac{p_{i,t,ref}}{1 - p_{S_0,t,ref}} \right|. \tag{10}$$

To avoid numerical instabilities where the denominator in $\frac{p_i,t}{1-p_{S_0,t}}$ or $\frac{p_{i,t,ref}}{1-p_{S_0,t,ref}}$ is close to zero, ε^r is only calculated for time steps where the S_0 populations in both dynamics are below 0.98.

To compare the diabatic MCTDH (also vMCG populations) to FSSH populations and to obtain diabatic populations for FSSH dynamics that contain both information about the distribution of active surfaces and the corresponding electronic populations at the same time, the methodology applied in Ref. 62 has been employed.

C. Dynamical propagations

The FSSH simulations have been carried out with the SHARC[39,63] program suite using pySHARC[64] to drastically reduce I/O overhead. A set of 1000 nuclear initial conditions obtained from a ground state Wigner sampling[65] is used for both SO_2 and 2-thiocytosine. The simulations employed a time step of 0.5 fs for the nuclear propagation in the field-free case and a nuclear time step of 0.05 fs in the presence of an external field. The electronic wavefunction is propagated in a locally diabatic basis with nuclear time steps of 0.02 and 0.002 fs in the field-free and field-including case, respectively.[66] The reduction of step size when including an electromagnetic field is necessary to capture the rapidly oscillating field.

As explained above, various FSSH options and modifications will be tested and compared to reference quantum dynamical results. Note, however, that the representation in which FSSH is performed is never the purely diabatic representation of the linear vibronic coupling (LVC) model (see below). Two different sets of initial electronic coefficients have been employed: For the simulations without an explicit laser field, the initially active electronic state at the start of the FSSH dynamics is set to the MCH state that has the largest overlap with the diabatic bright state of SO_2 and 2-thiocytosine for each initial condition. After setting the initial electronic state, the electronic coefficients are adapted correspondingly so that the initial electronic population at the start of the dynamics amounts to 1 for the diabatic bright state. This methodology represents an instantaneous excitation of the complete ground state wave packet to a single diabatic bright state, as it would follow an ideal instantaneous δ-pulse. For simulations in the presence of a laser field, the initial electronic state was set to the lowest energy state, and no modification of the initial electronic coefficients was done.

The QUANTICS package has been employed to run MCTDH and vMCG dynamics.[67] In MCTDH, the Adams–Bashforth–Molton predictor–corrector integrator of sixth order and the multi-set formalism have been used. Convergence of MCTDH dynamics was deemed to be reached if both of the following criteria have been met: First, the weight of the last SPF assigned to a degree of freedom did not exceed a value of 0.001 and, second, the number of grid points in a mode was taken to be sufficient if it was larger than $\langle n\rangle + 3\cdot\langle dn\rangle$ for all states and time steps, where $\langle n\rangle$ and $\langle dn\rangle$ are the position expectation value and the corresponding standard deviation, respectively.

vMCG calculations were run in a single-set formalism, which was found to be computationally more efficient than the multi-set formalism and converged faster to the MCTDH results as well, which is in line with previous observations.[9] Integrals between Gaussian wave packets have been calculated up to fourth order. The Runge–Kutta integrator of fifth order has been used. The number of considered Gaussian basis functions in vMCG ranged from 10 to 100. For both vMCG and MCTDH, initial conditions were obtained by populating the vibrational ground state of the lowest-energy electronic state of all normal modes considered. In simulations without an external field, this initial wave packet was set to start in the diabatic bright state, while for simulations in the presence of an external field, no additional steps were taken. The input and operator files used can be found in the supplementary material.

All FSSH, MCTDH, and vMCG simulations were run for 400 fs.

D. Definition of the laser pulse

The coupling with the external field is described within the semi-classical dipole approximation and can be written as $-\hat{\mu}_{\beta\alpha}(\mathbf{R})\varepsilon(t)$, neglecting any further interaction terms. The pulse has a Gaussian shape, defined as

$$\varepsilon(t) = \mathbf{e}_i\varepsilon^0_{t_p}\cos(\omega_i(t-t_0)+\eta)exp\left[-4\ln 2\left(\frac{t-t_0}{t_p}\right)^2\right], \qquad (11)$$

with field amplitude $\varepsilon^0_{t_p}$, carrier frequency ω_i, carrier envelop phase η, and pulse duration t_p equivalent to the full width at half-maximum (FWHM). We assume a linearly polarized pulse along the x-direction ($\mathbf{e}_i = x$) of the transition dipole moment and a phase $\eta = 0$. The frequency is set to be in resonance with the brightest state of the corresponding molecules: 4.49 eV for SO_2 and 3.92 eV for 2-thiocytosine. Seven different values for t_p are used with the corresponding centers of the pulse (t_0) in parentheses: 2 fs (t_0 = 10 fs), 10 fs (t_0 = 30 fs), 17 fs (t_0 = 40 fs), 30 fs (t_0 = 70 fs), 50 fs (t_0 = 90 fs), 100 fs (t_0 = 140 fs), and 200 fs (t_0 = 200 fs).

The field amplitude of the laser field for a given t_p, $\varepsilon^0_{t_p}$, was varied for different lengths of the laser pulse according to $\varepsilon^0_{t_p} = \varepsilon^0_{17}\cdot\sqrt{\frac{17}{t_p}}$. In this way, the pulse energy (area of intensity throughout the pulse duration) for different laser pulse lengths is kept constant. The pulses with a t_p of 17 fs serve as reference pulses for the determination of the field amplitudes for other pulse lengths and were set to $\varepsilon^0_{17} = 0.03$ a.u. (15.44 GV/m) for SO_2 and $\varepsilon^0_{17} = 0.01$ a.u. (5.15 GV/m) for 2-thiocytosine. Using these amplitudes, about half of the S_0 population in the FSSH simulations was excited in both molecules, which was deemed a good tradeoff between minimizing non-linear behavior and Rabi-oscillations while still exciting enough population in FSSH to yield reasonable statistics.

E. LVC model

The PES employed for the dynamical simulations are parameterized using a linear vibronic coupling (LVC) model.[68] Vibronic coupling models are diabatic representations of the electronic states close to a reference point and capable of describing dynamics and conical intersections close to the reference point. A suitable reference point capable of describing interactions with all excited states directly after initial photoexcitation is the ground state equilibrium geometry. The spatial dependence of the excited states is then cast into mass-frequency scaled normal mode coordinates using the normal modes of the ground state as a basis. When truncating this Taylor expansion at first-order, only linear terms that depend on a single normal mode displacement Q_i are obtained, resulting in

$$\mathbf{H}_{LVC} = \mathbf{H}^{(0)} + \mathbf{W}^{(1)}, \qquad (12)$$

where $\mathbf{H}_{LVC}$ is the diabatic LVC Hamiltonian and $\mathbf{H}^{(0)}$ contains the zero-order harmonic potential approximations to the PES

$$\mathbf{H}^{(0)} = V_0\mathbf{1}, V_0 = \sum_i \frac{\hbar\omega}{2}Q_i^2. \qquad (13)$$

Here, V_0 is the harmonic ground state potential along every normal mode i. The first order terms in $\mathbf{W}^{(1)}$ are state-specific and consist of electronic energy shifts ε, intrastate gradients κ, and couplings between two states λ,

$$W^{(1)}_{nn} = \varepsilon_n + \sum_i \kappa_i^{(n)}Q_i, \qquad (14)$$

$$W^{(1)}_{mn} = \sum_i \lambda_i^{(mn)}Q_i. \qquad (15)$$

Truncating the Hamiltonian after the first-order terms results in a rather crude PES able to accurately capture the form of potential only near the reference point. Parameters for the systems investigated here were taken from Ref. 64, which also demonstrates that the LVC approximation is able to reproduce the main characteristics of the corresponding on-the-fly dynamics. Note that all spin orbit coupling elements entering the employed LVC model Hamiltonian have no imaginary parts.

For use in the remainder of the work, the diabatic states and properties were transformed to either the MCH or completely diagonal representation during the propagation.

V. RESULTS AND DISCUSSION

A. SO_2

The excited state dynamics of SO_2 after irradiation has been extensively investigated in the past decade, illustrating a complex interplay between singlet and triplet states.[69–71] In this work, we use a LVC Hamiltonian that contains four singlet and three triplet states obtained with multi-reference configuration interaction including single excitations, which is able to reproduce the main features of the full-dimensional excited state dynamics.[64] In order to find an optimal set of surface hopping parameters able to describe the excited states dynamics of SO_2 *in the presence* of an explicit laser pulse, we first validate different parameter sets for the ensuing excited state dynamics *in the absence* of the laser field.

1. SO_2 dynamics in the absence of a laser field

To simulate the non-adiabatic dynamics of SO_2 without an explicit laser pulse excitation, the ground state nuclear wave packet is vertically placed in the bright $^1B_1$ state. Figure 1 shows the results obtained with MCTDH, vMCG, and FSSH dynamics. The MCTDH dynamics [Fig. 1(a)], which will serve as a reference throughout, shows ultrafast population transfer from the initially populated $^1B_1$ state to the $^1A_2$ state. Within the first 50 fs, there is almost complete depletion of the $^1B_1$ population, which then oscillates on par with that of the $^1A_2$ during the rest of the propagation. This oscillatory behavior is due to the closeness of the respective minima in both energy and phase space. Therefore, only limited stabilization of one diabatic state with respect to the other can take place, resulting in the repeating pattern that gets more complex over time. During the first 400 fs, about 10% of the population crosses to the triplet manifold, where the $^3B_2$ state is populated almost exclusively—in line with the also MCTDH simulations performed on *ab initio* potentials by Lévêque *et al.*[69]

The vMCG dynamics using 75 GBFs [Fig. 1(b)] show only small differences compared to the MCTDH reference. The excellent agreement of the vMCG singlet populations with the MCTDH ones illustrates the strength of the method. The oscillating behavior between the $^1B_1$ and the $^1A_2$ states is very well reproduced, with minor deviations at later times. The differences in the triplet states, however, are more pronounced. There is a continuous transfer to the triplet states, mostly to the $^3B_2$ state, which is not observed in the MCTDH dynamics in which the population in this state stagnates after 250 fs. To quantify the differences between vMCG and MCTDH dynamics, we calculate the error ε following Eq. (9). This results in the average deviation between the reference populations and the dynamics in question in each time step. The so-derived error is $\varepsilon = 0.069$ and it is attributed almost equally to the $^1B_1$, the $^1A_2$, and the $^3B_2$ states. Increasing the number of used GBFs is expected to decrease the error until convergence toward the exact result (see Sec. S1 C of the supplementary material for the ε values for simulations using different numbers of GBFs).

The FSSH simulations yield different results depending on the choice of the parameters discussed above (representation, decoherence correction, rescaling of the kinetic energy after a hopping event, and reflection of the kinetic energy after a frustrated hop). For the sake of briefness, we show in Fig. 1(c) only the populations for a single parameter set: $^{\mathrm{DIAG}}\mathrm{EDC}_V^+$. Compared to the MCTDH reference, the FSSH dynamics start with a similar transfer between the $^1B_1$ and the $^1A_2$ state, matching the time needed for this transfer. However, after the initial 50 fs, the oscillatory transfer between both states is far less pronounced than it was in MCTDH. The damped oscillations in FSSH follow the general trend of the MCTDH populations, with a slow decline in $^1A_2$ population at later times. The triplet state population is reminiscent of the vMCG dynamics with a continuous transfer to the $^3B_2$ state. The error associated with this simulation gives $\varepsilon = 0.248$, with the damped oscillations and the transfer to the $^3B_2$ state being the main sources of error. Unsurprisingly, FSSH has a larger error than vMCG (approximately three times larger).

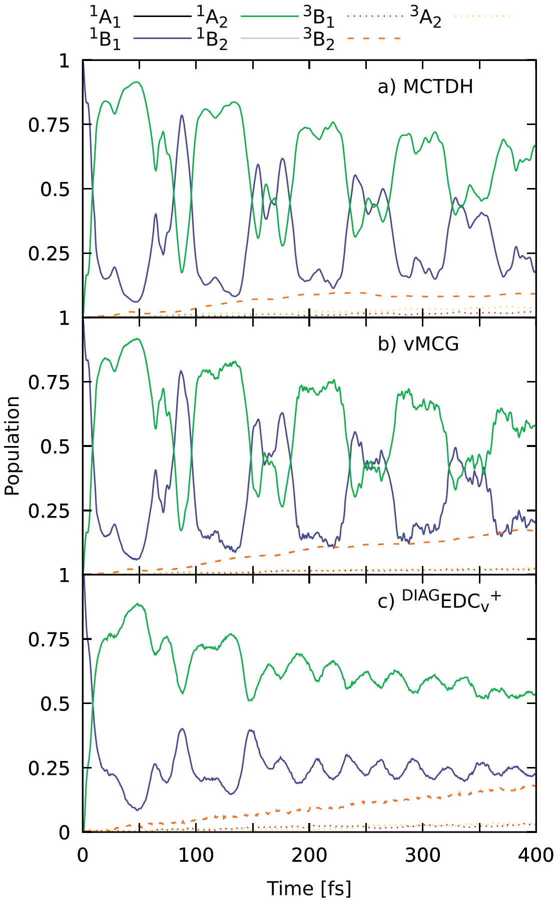

FIG. 1. Time-resolved population of the electronic states involved in the excited state dynamics of SO_2 starting from the diabatic $^1B_1$ state using different methods: (a) MCTDH, (b) vMCG dynamics using 75 GBFs, and (c) FSSH with the parameter set $^{\mathrm{DIAG}}\mathrm{EDC}_V^+$. Singlet states are depicted by solid lines, and triplet states are depicted in dashed lines.

In order to investigate the influence of different FSSH parameters, all sensible combinations of parameters according to Sec. IV A have been used to run FSSH dynamics. Figure 2 collects all the deviations against the MCTDH reference for each set. See Tables

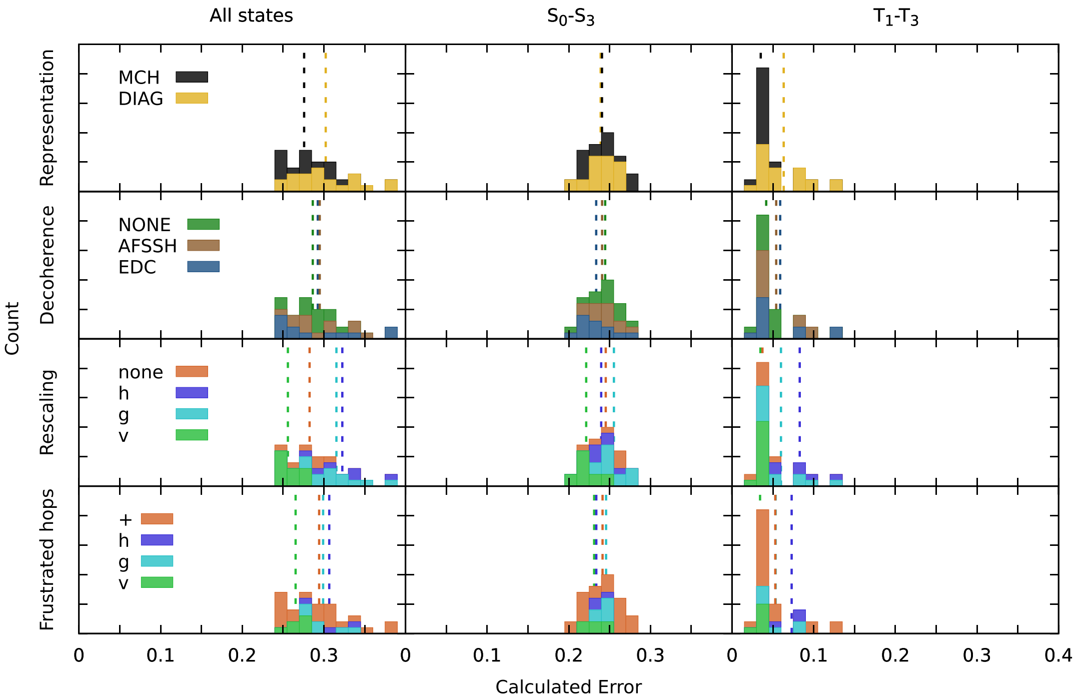

FIG. 2. Calculated ε values for each set of surface hopping parameters employed for the simulation of SO_2 represented by a stacked histogram combining errors that fall into bins of size 0.015. The contribution of each parameter toward the histogram is colored correspondingly. The dashed lines represent the average error associated with the identical colored parameter for the given panel. Each row displays the contribution of all parameters associated with a specific setting, as indicated in the label. The left panel shows the combined error (ε) running over all states, while the middle and right panels display the calculated error over singlet (ε_{sing}) and triplet states (ε_{trip}), respectively.

SI–SIII of the supplementary material for a list of all obtained ε values.

The ε ranges from 0.240 to 0.383, meaning that an unsuitable combination of surface hopping parameters can increase the error with respect to the best possible set by 50%. Each column of Fig. 2 gives the stacked error summed over all the states, singlet and triplet states, respectively, while each row depicts the influence of a particular option in the FSSH algorithm.

When comparing the influence of the representation on the errors, it is found that using the MCH representation gives smaller deviations than its completely diagonal counterpart. While this does not hold for ε_{sing}, where the average errors obtained using either representation are almost identical, big differences can be observed in ε_{trip}: all MCH simulations yield an almost identical error, while only half of the simulations employing the diagonal representation yield comparable errors. The difference observed in the average error due to the representation is therefore due to the better performance of the MCH representation to describe the triplet state populations. The decoherence correction inflicts very small differences among the three different parameters investigated. However, the FSSH dynamics on the investigated SO_2 model system is very sensitive to the choice of the vector along which rescaling of the kinetic energy should be conducted. Here, two clear favorites emerge, of which rescaling along the total velocity vector outperforms the crude option of not changing the velocities at all after switching to the active state. Yet, both of these parameters are found with significantly smaller average error than rescaling along the non-adiabatic coupling vector (**h**) or the gradient difference vector (**g**), which gives the highest average error of all investigated options for all parameters. The bad performance of the **h** and **g** parameters is mainly due to the triplet states, where they are the cause for almost all large deviations from the MCTDH reference. This is surprising, as adapting the kinetic energy along the NAC vectors was considered the option closest to real quantum dynamics, both from a theoretical point of view[27,28] and in a set of practical applications.[31,56] A possible explanation is that choosing to rescale along **h** or **g** significantly reduces the amount of available kinetic energy that can be used to reach a higher-lying surface, as compared to the option of rescaling along the complete velocity vector and, of course, the option of not adapting the energies at all. When comparing the number of successful and frustrated hops for two sets of parameters that differ only in the rescaling vector, e.g., **v** and **g**, a total of 3629 executed vs 3833 frustrated hops is found for ${}^{\text{MCH}}\text{EDC}_g^+$, while 7484 hops against only 1041 frustrated hops are found for ${}^{\text{MCH}}\text{EDC}_v^+$

on the complete set of 1000 trajectories. Thus, the higher available kinetic energy in the complete kinetic energy vector enables a lot of jumps that are otherwise forbidden when the non-adiabatic coupling or the gradient difference vector for rescaling is used. This increased number of frustrated hops might account for the discrepancies detected when rescaling the velocities along **h** or **g**, despite the fact that these options are both more physically sound and should have resulted in better adapted velocities after a successful hop than the full velocity vector or not rescaling the velocities at all. A possible remedy is the use of a modified FSSH algorithm that employs a time-uncertainty scheme, which can allow hops otherwise forbidden—as proposed by Truhlar and co-workers.[72] We noted that switching to the diagonal basis increases the total number of observed hops drastically (39 908 for $^{\text{DIAG}}\text{EDC}_g^+$ and 41 738 for $^{\text{MCH}}\text{EDC}_v^+$) due to the presence of more trivial and avoided crossings, as the triplet states are split into their respective components. Although the total number of hops increases in the diagonal picture, the amount of frustrated hops stays on a comparable level, with 4664 frustrated hops ($^{\text{DIAG}}\text{EDC}_g^+$) and 859 ($^{\text{DIAG}}\text{EDC}_v^+$). This might shed some light on why the largest errors are associated with using either of the two decoherence corrections in the diagonal representation along with rescaling the kinetic energy after a hop along **h** or **g**, as an increased number of hops slows down both types of decoherence corrections. In general, for the treatment of frustrated hops, reflection of the full velocity vector results in the lowest average error. As this option is always tied to using the full velocity vector for estimating if sufficient kinetic energy is present, which is the largest amount of available energy apart from not rescaling the energy at all, the number of frustrated hops is very low in these dynamics. The notion that "few frustrated hops equal better agreement between populations" is reinforced when realizing that most best-performing sets did not reflect frustrated hops at all. However, combinations of rescaling along **h** or **g** with a complete neglect of frustrated hops gave the highest disagreement for singlet and triplet populations, showcasing that a correct treatment of frustrated hops is needed in these cases.

The findings can be summarized as follows: (i) The MCH picture results in a stable description of the triplet population. (ii) No real favorite decoherence correction emerges. (iii) Rescaling along one of the physically more sound options, **h** or **g** results in larger deviations from the MCTDH dynamics, especially when paired with the parameter of not reflecting frustrated hops. Good results were achieved when using **v** for rescaling the kinetic energy combined with a continuation along the current velocity when encountering frustrated hops. (iv) A very bad combination of parameters for the description of the triplet states emerges in the form of using a decoherence correction in the diagonal representation and rescaling along **h** or **g** using non-reflected frustrated hops.

2. SO$_2$ dynamics in the presence of a laser field

In the presence of a laser field, both the excitation and the subsequent excited state evolution of the population are influenced by the laser pulse. We shall investigate both processes separately, starting with the excitation process itself. The effect of applying longer pulses to excite population from the $^1A_1$ ground state is shown in Fig. 3. Before discussing the details of the observed trends, note that laser pulses of different lengths employ different field amplitudes $\varepsilon^0_{t_p}$ [see Eq. (11)] to carry the same total energy.

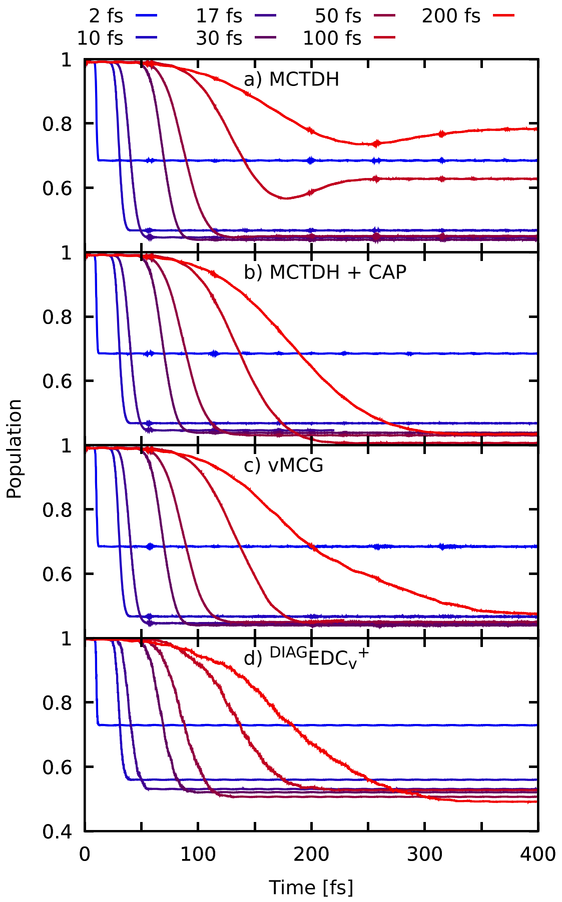

FIG. 3. Time-resolved S$_0$ population for seven different sets of dynamics employing laser pulses differing in the t_p of the envelope function and the field amplitude $\varepsilon^0_{t_p}$ [see Eq. (11)]. Panel (a) displays the MCTDH dynamics, while panels (b) and (c) show surface hopping dynamics with the parameter set $^{\text{DIAG}}\text{EDC}_v^+$ and vMCG dynamics using 75 GBFs.

Within MCTDH, three different dynamical regimes are observed: (i) the shortest pulse (t_p = 2 fs) excites around 30% of the population to higher-lying states, (ii) laser pulses with a t_p between 10 and 50 fs excite about 55% of the population, and (iii) very long pulses beyond a t_p of 100 fs induce a diverging behavior, where the ground state is repopulated at later times where the laser is still active. The reduced excitation in the dynamics including the very short t_p = 2 fs laser pulse is due to the fact that the pulse carries only few cycles. This results in a higher uncertainty for the energy, and interference effects are increased as the amplitude of the laser field ($\varepsilon^0_{t_p}$) is adapted to pack the same amount of energy as the longer pulses in this short laser pulse. When comparing the excitation process of the t_p = 10 fs laser pulse to the t_p = 17 fs, t_p = 30 fs, or

t_p = 50 fs dynamics, most of the effects hindering the excitation toward excited states present in the t_p = 2 fs case are gone, and an almost identical level of excited population is achieved. This excitation of an identical amount of population is reminiscent of an ideal non-interacting case where dynamics in the excited states initiated at the start of the laser pulse does not enhance or hamper further excitation during the duration of the laser pulse. When going to the t_p = 100 and t_p = 200 fs laser pulses, this ideal picture does not hold true anymore, and a more complex S_0 population behavior is observed.

Inspection of the nuclear wave function for the dynamics using t_p = 100 and t_p = 200 fs lasers reveals that the diverging behavior is caused by parts of the excited state wave packet that re-enter the Franck–Condon region. Once part of the wave packet is in the Franck–Condon region, additional interference terms arise as the returning excited wave packet and the remaining ground state wave function can interfere if the laser still couples the bright excited state with the ground state. To verify whether this is actually the cause for the observed behavior, new sets of MCTDH simulations have been carried out where two identical t_p = 2 fs lasers separated by a time interval τ are employed. This way, one laser acts as a pump pulse and the other acts as a probe, detecting whether the returning wave packet causes interference terms. The resulting populations for different τ delay times are shown in Fig. 4(a). It can be seen that the probe laser just excites more S_0 population for small τ values. Upon reaching a time delay $\tau > 85$ fs, a strong dependence on τ is found, which first enhances the excitation induced by the probe pulse but results in a reduced excitation for delays of 89, 93, and 97 fs. From this, it can be concluded that after ~90 fs, a recurrence of the excited wave packet takes place and further coupling with the laser field yields a new interference term, drastically altering the observed overall excitation process.

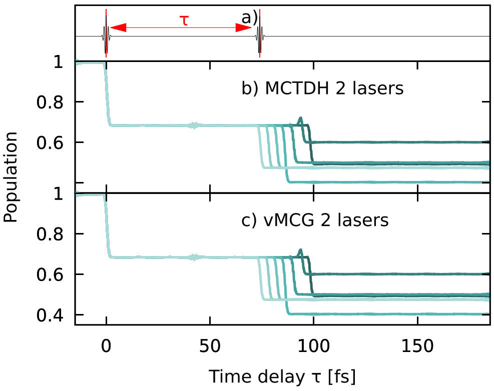

FIG. 4. The excitation process in SO_2 is investigated by two identical very short laser pulses (t_p = 2 fs) that act as pump pulses on the lowest excited state and are separated by a time delay τ. The time delay is measured between the center of the pulses, as indicated in panel (a) for the shortest τ. Panels (b) and (c) overlay multiple time-resolved S_0 populations coming from (b) MCTDH and (c) vMCG (using 50 GBFs) dynamics simulations using different τ (74, 78, 82, 86, 90, 94, and 98 fs).

As the lasers up to t_p = 50 fs are too short in time to be still active when the wave packet returns, the excitation follows the observed pattern. Only when going beyond this, a disturbance in the excitation pattern due to this effect is observed. To further support this argument, a complex absorbing potential (CAP) has been employed in the MCTDH calculations that destroys the excited state wave packet once it leaves the Franck–Condon region after initial excitation, thus hindering a possible return. Indeed, as shown in Fig. 3(b), the S_0 populations do not show this interference term anymore. Instead, the laser pulse induces a 55% S_0 population inversion.

Figure 3(c) demonstrates that vMCG dynamics is in extremely good agreement with MCTDH for laser pulses up to t_p = 50 fs. Therefore, for short to medium laser pulses, vMCG is able to capture the most important parts of the excitation process induced by explicit laser pulses. However, for longer laser pulses, vMCG deviates strongly from the MCTDH reference as the behavior due to the interference with the returning wave packet observed for the S_0 population of the t_p = 100 and t_p = 200 fs lasers is not reproduced.

Conducting the same pump–probe laser sequence dynamics as for MCTDH using two t_p = 2 fs pulses resulted in a perfect agreement between the vMCG and the MCTDH dynamics [see Fig. 4(b)]. This shows that vMCG is well suited to describe the additional interference in the pump–probe setup, especially considering that only 50 GBFs were necessary for agreement. However, in simulations employing long laser pulses with t_p = 100 and t_p = 200 fs, vMCG does not capture the interference that was observed in MCTDH. In these cases, the used GBFs are spread too thin, as the vMCG algorithm tries to describe the complete distributed excited state wave function at once—a much more difficult task than tracking the single excited state wave packet created in the pump–probe setup. Exploratory calculations employing larger numbers of GBFs indicated that the reversal of the population flow occurring for the S_0 population of the t_p = 200 fs dynamics needs more than 125 GBFs to be even visible. Unfortunately, calculations using this and larger number of GBFs could not be converged.

When comparing the MCTDH and vMCG dynamics to the FSSH dynamics using the ${}^{\mathrm{DIAG}}\mathrm{EDC}_{\nu}^{+}$ set of parameters [see Fig. 3(d)], a general underestimation of about 5%–10% in the amount of excited population is observed for laser lengths up to t_p = 50 fs. The reduced amount of excitation is mainly due to the employed decoherence correction. Different from other decoherence corrections such as AFSSH, the EDC acts instantaneously, meaning that in every time step of the simulations, the electronic coefficients of non-active states will be damped and the coefficient of the active state increased. During the excitation process, the applied external field will periodically and continuously increase the electronic coefficient of excited states and decrease the coefficient in the ground state, thus enabling the chance for the trajectory to perform a surface hop. The EDC therefore directly counteracts the influence of the laser field, resulting in a lower amount of excited population. Interestingly, applying the same amount of energy over a longer time did not decrease the performance of the EDC correction further. Similar to vMCG, the S_0 populations in FSSH do not show any significant irregularities when moving to the t_p = 100 fs and the t_p = 200 fs lasers and instead correspond closely to the populations observed in MCTDH when employing a CAP.

A screening for all combinations of surface hopping parameters considered in Sec. V A 1 has been conducted using the $t_p = 30$ fs laser pulse, where no additional interference due to the recurrence of the wave packet is observed. Note that the total calculated error with respect to the reference MCTDH dynamics is now split into an error in the S_0 population, ε_{S_0}, calculated according to Eq. (9), while the error in the excited states, ε^r, is calculated using renormalization following Eq. (10). ε^r is again split up into the contributions of singlets and triplet states. The total calculated error is then just the sum over these three contributions: $\varepsilon = \varepsilon_{S_0} + \varepsilon^r_{sing} + \varepsilon^r_{trip}$. All calculated ε values for all states, the S_0, the excited singlet state, and the excited triplet state, are presented in Fig. 5 and listed in Tables SIV–SVII. A very flat distribution of error values is observed for the total error ranging from 0.265 to 0.462, showing an increase in overall error by 75% for the worst set of parameters with respect to the best set.

First, the capability of the different parameters to describe the initial excitation is discussed. When investigating the influence of the representation on ε_{S_0}, the MCH picture is found to be better on average than the diagonal counterpart.

Regarding decoherence, the EDC performs best on average, giving very similar deviations from the MCTDH populations, irrespective of the chosen representation. This consistently good performance is rather surprising following the observations above as the EDC in general leads to an underestimation of the excited population due to its instantaneous nature. However, the ability to converge fast toward a trajectory that no longer contains considerable electronic S_0 population after the initial excitation is found to be beneficial here. This lowered population in the S_0 of an already excited trajectory reduces the chance of stimulated emission and therefore increases the overall agreement with the MCTDH reference. The use of AFSSH is found with a higher average error than the EDC. All sets of parameters that use AFSSH paired with the MCH representation result in a ε_{S_0} between 0.058 and 0.076 and therefore show the lowest ε_{S_0} values. However, when using AFSSH in combination with the diagonal representation, the errors essentially double to a range of 0.123–0.136, showing a strong sensitivity with the representation. Such differences are not observed in the more robust EDC, indicating that the diagonal representation is interfering with the AFSSH algorithm in SO_2.

Using no decoherence correction at all is associated with very bad agreement throughout all considered sets of parameters. This indicates that the correct decay of the ground state electronic

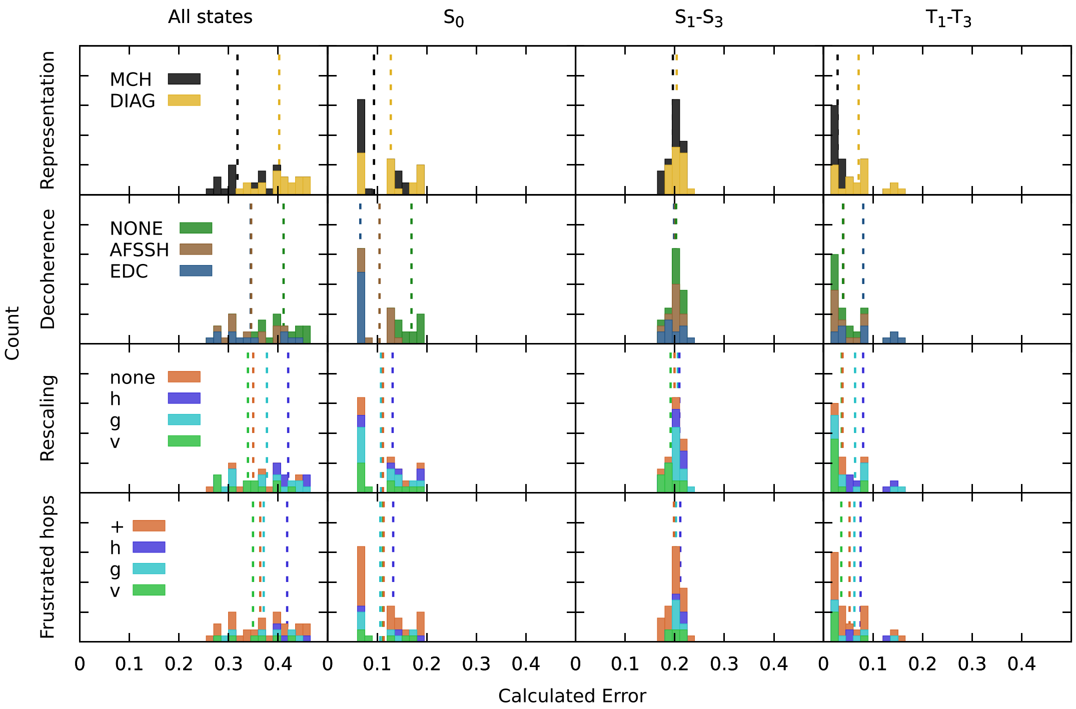

FIG. 5. Calculated ε values for each set of surface hopping parameters employed for the simulation of SO_2 represented as a stacked histogram, combining errors that fall into bins of size 0.015. The contribution of each surface hopping parameter toward the histogram is colored as indicated. Dashed lines represent the average error associated with the identical colored parameter for the given panel. Each row displays the contribution of all parameters associated with a specific setting, as specified. The left-hand side panel shows the combined error running over all considered states. The next panel shows ε_{S_0}. The remaining columns show the ε^r_{sing} and ε^r_{trip} values. Note that all excited state populations have been renormalized to 1 in every time step for MCTDH and each FSSH simulation [see Eq. (10)].

coefficient plays a crucial role once the trajectory is excited. The performance in the absence of a treatment for the inherent overcoherence is slightly increased in the MCH representation and worsened in the diagonal one.

The different parameters for rescaling the kinetic energy after a hop and treating frustrated hops yielded almost identical averages. Indeed, this behavior is expected as these options manipulate the excited state dynamics after the initial excitation has occurred and are therefore of limited importance to the excitation process itself.

We now analyze the dynamics in the excited states and see that a much more compact error distribution in error values is observed for the renormalized ε^r_{sing} as compared to the dynamics in the absence of a laser field. Almost all parameters give identical averages, with these averages also being smaller than those for the dynamics without the laser field. The lower average errors are mostly due to loss of the fine structure of the population curves in the $^1B_1$ and the $^1A_2$ states: This fast and strongly oscillating behavior of the excited state populations depicted in Fig. 1(a) was one of the major sources of disagreement between MCTDH and FSSH, with FSSH predicting more damped oscillations. Applying a long laser pulse completely changes the observed picture, as the starting point of the dynamics in the excited states is now distributed across the duration of the complete laser pulse, as shown in Fig. S1 of the supplementary material. The delayed excitation results in a smearing of the transfer between the $^1B_1$ and the $^1A_2$ states that now show a simple oscillating behavior without a fine structure. This behavior is easier to reproduce using FSSH, which also profits from the very forgiving nature of using populations to calculate the deviation from exact quantum dynamics. For the triplet states, all parameters that were found to increase description of triplet states in the simulations without explicit laser fields are also found to be the dominating factors in the presence of laser fields. Hence, the MCH representation gives significantly improved results over the diagonal representation for the triplet state populations too. The EDC is associated with higher errors in the triplet populations than using no decoherence correction or AFSSH. For rescaling the energies after a hopping event and the treatment of frustrated hops, the velocity vector is the most prominent option followed by the complete neglect of adapting the kinetic energies.

Altogether, we find that an appropriate choice of the decoherence correction together with a compatible representation is the driving factor to capture the excitation process correctly. The EDC emerged here as a rather robust variant, while AFSSH was found to perform better in the MCH basis. For the remaining dynamics, the MCH basis was found to improve agreement for the triplet populations with the MCTDH reference. Additionally, using the **h** and **g** vectors to rescale or reflect the velocity vector along after a real or frustrated hop was found to give larger deviations with respect to the reference.

There are multiple approaches to find the best set of surface hopping parameters in the presented case: either the best performing set of parameters for a given ε is taken or the parameter of each option that obtained the lowest average error is considered. In this work, the parameters yielding the lowest average errors have been taken for each option, as this represents a more robust error measure instead of cherry-picking a single combination that could well be the result of error compensation. Therefore, the following sets have been determined in the absence of a laser field: $^{\mathrm{MCH}}\mathrm{NONE}_v^{-v}$ (best average ε and ε_{trip}) and $^{\mathrm{DIAG}}\mathrm{EDC}_v^{-v}$ (best ε_{sing}). For dynamics initiated using a t_p = 30 fs laser, the combinations $^{\mathrm{MCH}}\mathrm{EDC}_v^{-v}$ (best ε), $^{\mathrm{MCH}}\mathrm{EDC}_g^{-g}$ (ε_{S_0}), and $^{\mathrm{MCH}}\mathrm{EDC}_v^{+}$ (ε^r_{sing}) were added, as the on-average best performing options resulted again in $^{\mathrm{MCH}}\mathrm{NONE}_v^{-v}$ for ε^r_{trip}. These sets were then used to simulate dynamics using different laser lengths for excitation varying in size from t_p = 2 to t_p = 50 fs and ε_{S_0} calculated with respect to the MCTDH dynamics. The resulting deviations from the reference dynamics are depicted in Fig. 6. Three different classes of surface hopping parameters can be clearly distinguished: (i) surface hopping sets using the MCH representation and the EDC clearly show the same trend for different t_p of the laser, starting with a very small error that increases for t_p = 10 and t_p = 17 fs before decreasing for lasers t_p = 30 and t_p = 50 fs long. Essentially, no differences between the different rescaling or reflection parameters can be discerned for these three combinations. (ii) Employing the diagonal representation initially results in a larger deviation from the MCTDH S_0 population for short laser lengths, which can be attributed to the different form the laser coupling takes in the diagonal representation. For longer laser lengths, this is evened out and no differences are observed between EDC in the diagonal and the MCH representation when looking at the S_0 populations. (iii) A completely different picture can be observed when no decoherence correction is used ($^{\mathrm{MCH}}NONE_v^{v}$). Here, the excitation due to very short laser pulses is well described, but as soon as the excitation events and subsequent dynamics start occurring at the same time scale, the need to treat overcoherence is apparent. Longer laser pulses lead to a larger deviation from the MCTDH S_0 population, resulting in very larger errors for this set of parameters.

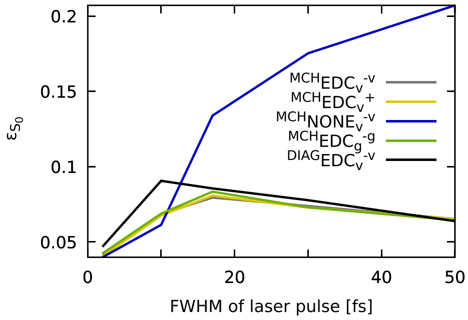

FIG. 6. Calculated error in the S_0 population for each set of FSSH parameters that resulted in the lowest average errors for at least one of the columns in Figs. 2 or 5 for different t_p of the laser pulse.

B. 2-Thiocytosine

The substituted nucleobase 2-thiocytosine represents a much more challenging system for dynamics due to the increased number of normal modes with respect to SO_2. *Ab initio* on-the-fly FSSH simulations and experimental results are available for 2-thiocytosine,[73] showing a significant triplet yield. Substituting the on-the-fly PES by the more rigid LVC Hamiltonian was found previously to result in a reduced transfer toward the triplet states after 500 fs, but to maintain all other essential features.[64] With this in mind, in order to test the effect of different FSSH settings, here, we consider simulation times of up to 400 fs.

1. 2-Thiocytosine dynamics in the absence of a laser field

Figure 7(a) shows FSSH dynamics including all normal modes in conjunction with the ${}^{\mathrm{DIAG}}\mathrm{EDC}_v^+$ set of parameters in the absence of a laser field. The ground state Wigner distribution of geometries has been excited into the bright diabatic S_2 state from where subsequent dynamics takes place. A strong coupling of this bright state with S_0 results in a fast oscillating transfer between these two states, recovering population in the S_0 state. At the same time, internal conversion to the diabatic S_1 and intersystem crossing to the triplet manifold is observed. After 400 fs, both the S_1 and the S_2 have similar populations, and a higher population is found in the diabatic T_1 state.

In order to obtain a reference dynamics to assess different FSSH parameters using an affordable MCTDH computation, the amount of normal modes was reduced using the so-called SHARC-gym.[74] In the SHARC-gym, systematic calculations to identify the most important normal modes are carried out as follows: For every vibrational normal mode, an independent FSSH simulation is conducted with all gradients and coupling elements associated with that mode set to zero. The so-obtained populations are then compared to the reference populations in Fig. 7(a) by calculating ε values according to Eq. (9). If the omission of a mode results in a large ε, the mode carries essential coupling terms for the overall dynamics and should be included in the reduced set (see the ε values associated with the neglect of specific normal modes in Sec. S2 A). Using this approach, it is possible to find the modes relevant for the deactivation dynamics without any selection bias that could derive if the selection would be conducted based on the strength of specific coupling elements—a common approach in low-dimensional systems carrying limited amounts of states.[75,76] Following the SHARC-gym, we selected the ten most important modes that can reproduce the 33-dimensional dynamics of 2-thiocytosine. This reduced ten-dimensional set will be now used for the remainder of the simulations. As shown in Fig. 7(b), the FSSH dynamics using this ten-dimensional Hamiltonian captures the overall behavior of the full-dimension very reasonably.

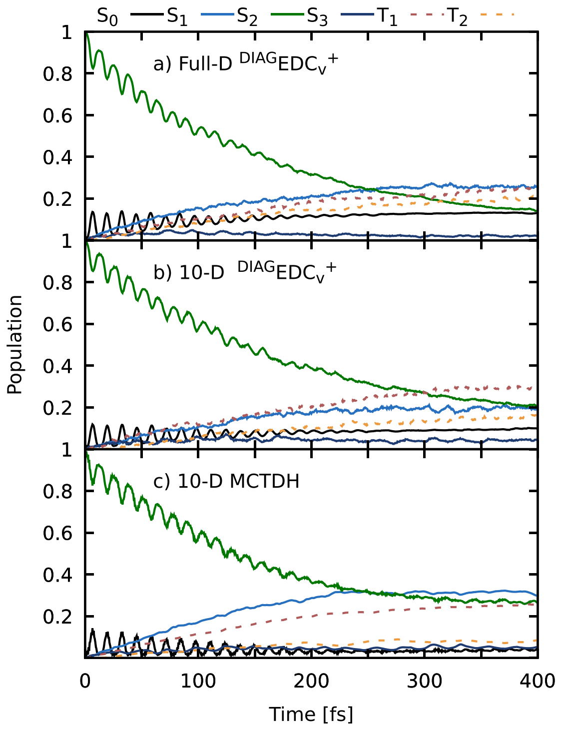

FIG. 7. (a) Diabatic populations of FSSH simulations on a full dimensional LVC model of 2-thiocytosine using the ${}^{\mathrm{DIAG}}\mathrm{EDC}_v^v$ set of parameters starting from the bright S_2. Triplet populations (dashed) are summed up over all components of the respective triplet state. (b) Diabatic populations obtained from ${}^{\mathrm{DIAG}}\mathrm{EDC}_v^v$ simulations on a reduced ten-dimensional model of 2-thiocytosine starting again from the S_2 state. (c) MCTDH dynamics on the ten-dimensional model system starting from the S_2 state.

With this reduced model at hand, MCTDH calculations have been converged yielding the populations presented in Fig. 7(c). Compared to the ${}^{\mathrm{DIAG}}\mathrm{EDC}_v^+$ presented set of parameters, the MCTDH simulations predict larger S_1 and smaller T_2 population. The amount of S_0 population is lower in MCTDH due to the inability of EDC to describe fast oscillations as it tries to end up in pure states. Overall, the agreement between both methods is nevertheless quite reasonable with an error $\varepsilon = 0.214$ for the ${}^{\mathrm{DIAG}}\mathrm{EDC}_v^+$ set.

Using the ten-dimensional 2-thiocytosine model, we obtain the distribution of ε values presented in Fig. 8 (see also Tables SXII–XIV). The errors are spread wide, ranging from 0.163 to 0.488, with the largest accumulation of parameter sets giving very good results. Similar to SO_2, the MCH picture gives a better description of the triplet populations, while most simulations using the diagonal picture perform worse. The EDC decoherence treatment performed well both for the singlet and the triplet populations. Using no decoherence correction resulted in somewhat surprisingly good results when compared to the AFSSH, which in turn gave larger ε values on average than the other treatments. When including the effect of rescaling of the kinetic energies after a hop, the driving factor in the current dynamics becomes apparent: rescaling along the **h** and the **g** vectors is associated with the largest errors, while neglecting the rescaling completely or rescaling along the velocity vector gives very good agreement with the MCTDH populations. Interestingly, there are two exceptions to this, as the ${}^{MCH}EDC_g^+$ and the ${}^{MCH}EDC_g^g$ sets of parameters are the best performing sets investigated. All but a single set of parameters using **v** gave better ε values than for any set using rescaling along **h**. Reflection of frustrated hops is found to be important; however, due to the pairing criterion of using the same vector for reflecting at a frustrated hop and to rescale along in the case of a hop, the errors are very similar to the errors observed for the corresponding rescaling option. This does not hold true for not reflecting hops at all, which was combined with all possible rescaling options. The associated average error for not reflecting frustrated hops at all is found at

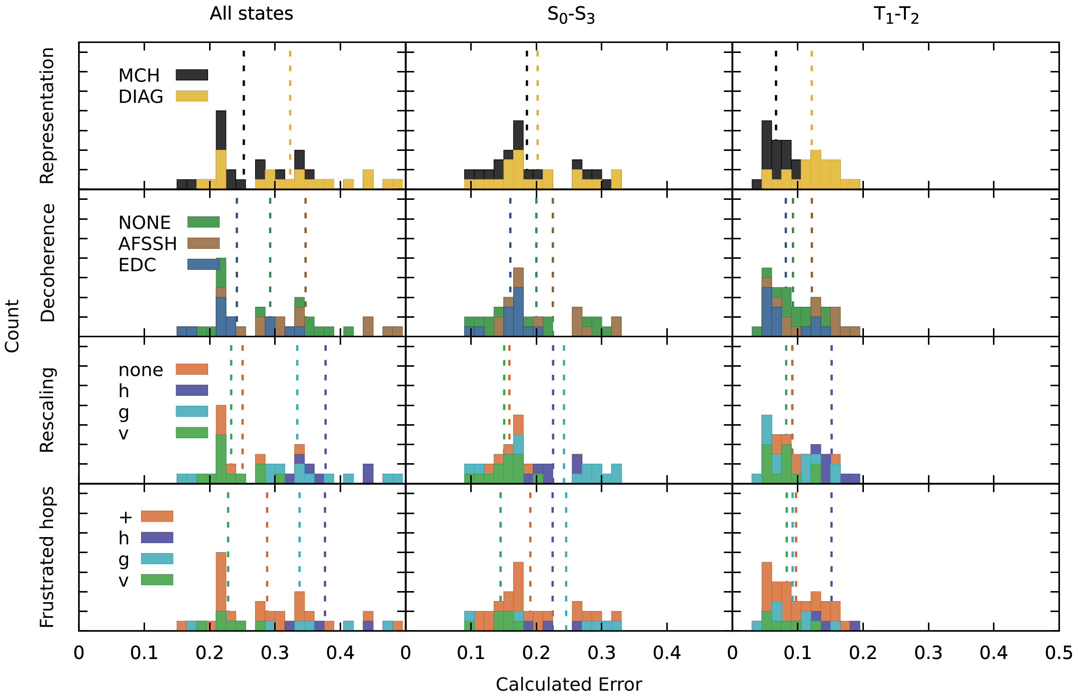

FIG. 8. The calculated error for the ten-dimensional 2-thiocytosine dynamics for each set of surface hopping parameters is collected in this picture as a stacked histogram combining errors that fall into bins of size 0.015. Then, the contribution of each surface hopping parameter toward the histogram is colored correspondingly. The dashed lines represent the average error associated with the identical colored parameter for the given panel. Each row displays the contribution of all parameters associated with a specific setting, labeled at the left-hand side. The left-hand side panel shows the combined error running over all considered states. This error is then split up into the middle and the left-hand side panels, which display the calculated error over all singlet and triplet states, respectively.

almost the same value as the average over all calculated ε values, indicating that this parameter has no influence here. The analysis of the sets resulting in larger ε values reveals that AFSSH dynamics in the diagonal representation results in too fast transfer from the S_2 to the $_1$ and increases the population of the T_1 state, thus giving a bad description. This effect is drastically enhanced when rescaling along **h** or **g**.

2. 2-thiocytosine dynamics in the presence of a laser field

Following the framework presented in Sec. V A 2, a set of seven lasers that differ in their t_p and their maximum amplitude have been applied to excite population from the ground state and initiate dynamics. First, the influence of different lengths of laser excitation has been investigated. Figure 9(a) presents the results obtained for MCTDH. Although the pulses are tuned to carry the same amount of overall energy, the amount of excited population increases with the pulse length. Accordingly, the longest pulse achieves almost ground state population inversion. The same trend is achieved by the FSSH dynamics using the $^{\mathrm{DIAG}}\mathrm{EDC}_v^+$ setup [see Fig. 9(b)] but in a much weaker extent. This is, in part, due to the EDC acting against the excitation process. The hampering effect of the EDC is more pronounced than in SO_2 because the strength of this decoherence correction is based on the kinetic energy of the system, which, on average, is much larger for 2-thiocytosine than SO_2 due to size.

Intriguingly, the MCTDH S_0 populations do not show any surprises for longer pulses—contrary to what was observed for SO_2 where the recurrence of the wave packet resulted in additional interferences. This is investigated in more detail in Fig. 9(c) where ten different model systems containing one to ten normal modes of 2-thiocytosine (sorted according to their importance for the overall dynamics, see Table SX for the explicit modes) are used to probe the interaction with the $t_p = 200$ fs laser pulse. With very few modes, almost no population remains in the excited state, as the recurrence of the wavepacket occurs very fast and further excitation is hampered and even reversed, similar to what occurred in SO_2. The more modes are added to the system, the more excited state pathways open up, increasing the time needed until the excited wave packet returns to the Franck–Condon region, reducing the transfer back to the S_0 population as the laser duration is shorter than the recurrence time. The increase in recoherence time shows that this effect is only affecting simulations of very small systems and it is almost undetectable for a ten-mode system with a rather long laser pulse of t_p of 200 fs.

The t_p = 30 fs pulse duration was selected to estimate the performance of the different FSSH parameter combinations on the ten mode 2-thiocytosine model. As shown in Fig. 10, a very broad distribution of total errors is obtained for the overall error (see Tables SXV–XVIII in the supplementary material for the complete lists). This is mostly due to the high deviation observed in the S_0 state population, yielding ε_{S_0} values larger than 0.2 for all sets.

The description of the S_0 population was found to be rather independent of the representation but strongly dependent on the presence of a decoherence correction, with better results when this is considered. Rescaling the momenta after a surface hop impacts the S_0 population, with not rescaling the energies resulting in bigger disagreement with MCTDH. The overall increase in deviation from the MCTDH S_0 population when compared to the deviations in SO_2 can partially be attributed to the use of the rather strong laser pulse that inverts 90% of the population in the MCTDH reference. Indeed, strong laser fields have been previously found to increase the deviation from quantum dynamics reference results.[58]

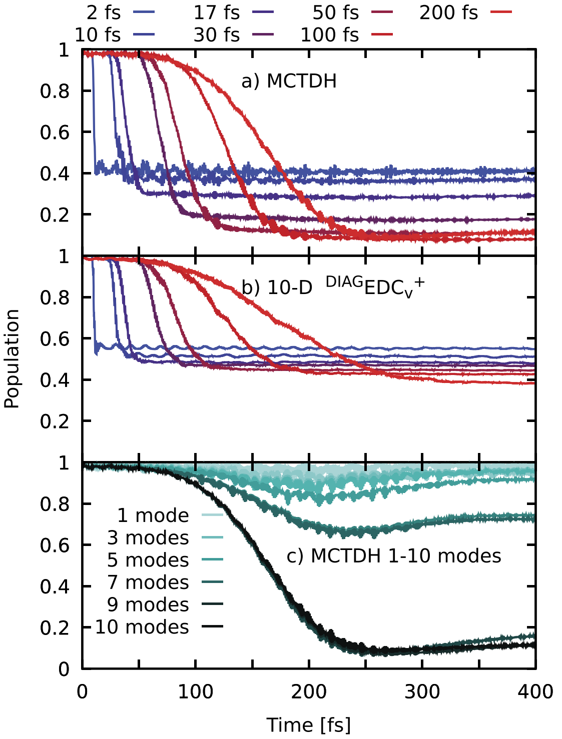

FIG. 9. [(a) and (b)] Time-resolved S_0 population of 2-thiocytosine (ten-dimensional model) using seven different laser pulse durations (as indicated) obtained with MCTDH (a) or FSSH with the parameter set ${}^{\mathrm{DIAG}}EDC_v^+$ (b). (c) Time evolution of the S_0 population using the t_p = 200 fs and a different number of normal modes (from 1 to 10).

In that paper, it was reported that the excitation process, in general, results in a net vibrational cooling of the swarm of excited trajectories with respect to the average kinetic energy of the ground state population, resulting in slower movement of the FSSH trajectories away from the region where the laser couples the bright and ground states. In the presence of a strong laser field, dwelling in the region of strong coupling increases the chance of inducing radiative emission to the ground state, effectively decreasing the amount of excited population. This poses an important dilemma for carrying out FSSH dynamics with laser pulses when generating initial conditions: On one hand, the stronger the pulse, the more trajectories will be excited, thereby decreasing the amount of unexcited trajectories that are now obsolete for describing excited state dynamics and thus represent the computation time essentially wasted. On the other hand, stronger lasers will lead to larger deviations from the exact dynamics due to the cooling effect and the increased interplay between different parts of the wave packet that are more strongly coupled.

For the excited state dynamics following excitation, ε^r_{sing} shows a rather narrow distribution. Surprisingly, a complete change in the observed order of importance for the various parameters can be detected with respect to the dynamics without any external field. Two effects are responsible for the presented errors: First, the influence due to the fast oscillating coupling element with the S_0 on the ε values is reduced as the S_0 component of this error is included in ε_{S_0} and therefore only taken into account via the S_2 state. Second, the fine structure is smoothed out, giving rise to simpler decay patterns, as shown in Fig. S3 in the supplementary material. Still, it comes as a big surprise to find that the performance of the EDC is reduced and that rescaling of the kinetic energy after a hop along **g** in the MCH representation gives by far the best renormalized singlet populations. The latter behavior is the opposite of what was observed in the absence of a laser field, i.e., this rescaling option was found with the largest average ε_{sing}. When including an explicit laser pulse, rescaling along **g** gives good agreement with MCTDH independent of the applied decoherence correction if the MCH representation is used. However, a strong dependence on the applied decoherence correction in the diagonal representation can be seen where ${}^{\mathrm{DIAG}}EDC_g^{-g}$ and ${}^{\mathrm{DIAG}}EDC_g^{+}$ are among the largest deviations from the MCTDH results for all sets observed.

The deviation in the populations of the triplet states follows the same trends found in the excited state dynamics without an external field, with a decrease in the importance of the chosen representation and an overall better performance of the AFSSH. Rescaling along the non-adiabatic coupling vector is still found to decrease agreement with the MCTDH reference.

Summarizing this section, modeling the excitation of S_0 population by an explicit laser pulse with t_p = 30 fs in the ten-dimensional 2-thiocytosine model system using FSSH results in deviations of about 30%. Differences due to the representation are negligible, while using a decoherence correction was found to be an important factor, similar to observations in SO_2. For the excited state dynamics following excitation, rescaling of the energies after a hop was found to be important, this time favoring rescaling along the gradient difference vector for the dynamics in the singlet manifold. Transfer of population toward the triplet states is found to be only slightly influenced by the decoherence treatment and the chosen representation.

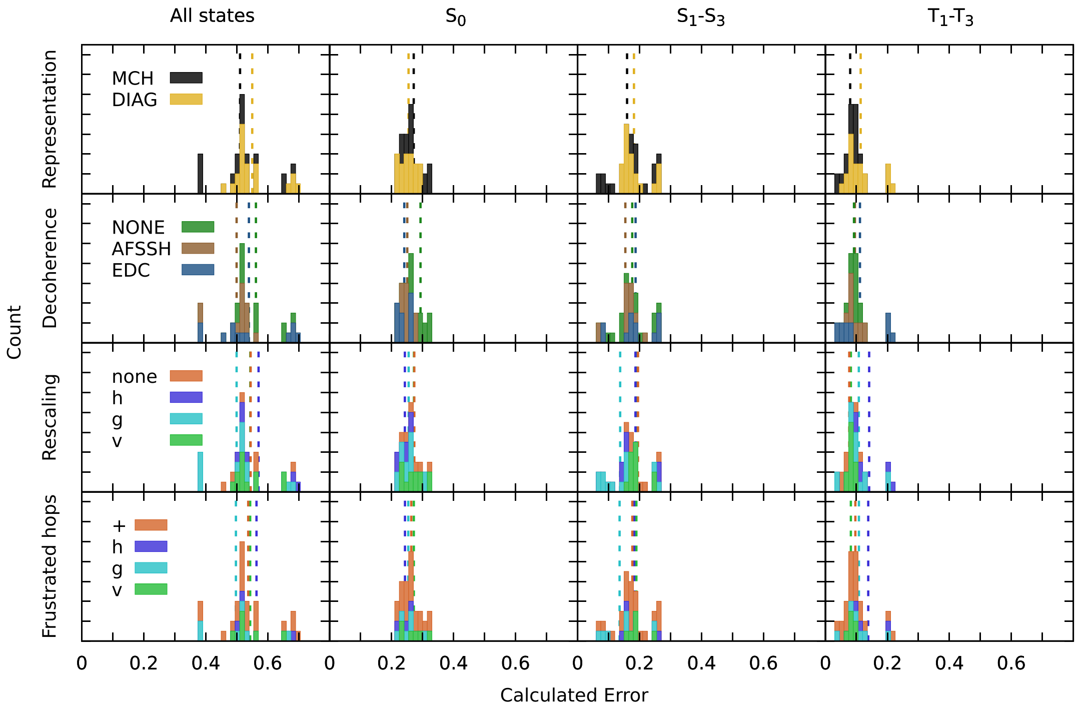

FIG. 10. Calculated error for the ten-dimensional 2-thiocytosine dynamics for each set of surface hopping parameters as a stacked histogram combining errors that fall into bins of size 0.015. The contribution of each surface hopping parameter toward the histogram is colored correspondingly. Dashed lines represent the average error associated with the identical colored parameter for the given panel. Each row displays the contribution of all parameters associated with a specific setting, labeled at the left-hand side. The left-hand side panel shows the combined error running over all considered states. The next panel shows ε_{S_0}. The remaining columns show the ε^r_{sing} and ε^r_{trip} values. Note that all excited state populations have been renormalized to 1 in every time step for MCTDH and each FSSH simulation [see Eq. (10)].

VI. CONCLUSIONS

In this work, we benchmark the performance of different parameters that are needed in FSSH against a MCTDH reference for two molecular systems: SO_2 and 2-thiocytosine using parametrized LVC potentials. We investigate the effect of such parameters on simulations that do not explicitly include a laser field and compare with dynamics initiated by laser pulses of different time durations.

Previous work[5,6,12,33,58] has reported the inability of FSSH to correctly describe the excitation process and the subsequent dynamics in the presence of explicit light–matter interactions and pointed out the dependence of the results on the chosen FSSH parameters. In this work, we quantitatively measure the deviation of FSSH from real wave packet dynamics, and by studying molecular systems with and without the influence of external fields, we discern between effects coming from the dynamics itself or from the laser interaction. Furthermore, the two chosen models, SO_2 and 2-thiocytosine, with three and up to ten normal modes, are beyond the commonly one-dimensional test systems employed to investigate the interaction with an external field. The consideration of both singlet and triplet states poses an additional difficulty for FSSH as both very weak delocalized coupling between singlets an triplets and the time-dependent coupling via an external field have to be treated correctly.

A set of four parameters with different options available in each of those have been tried and tested. The various employed options span from exact procedures (such as adapting the nuclear velocities after a hop along the non-adiabatic coupling vector) to extremely crude approximations (e.g., not adapting the energies at all at a hopping event). This incomplete variation in parameters does not aim at providing a single set of "best" performing options, of which the conducted comparison of a single electronic property is not capable of. Instead, it should illustrate how diverse the field of surface hopping parameters and users thereof is, and call for caution when choosing and combining surface hopping parameters.

We find that FSSH has difficulties in low-dimensional models if long laser pulses (FWHM > 100 fs) are present, where the excited state wave packet returns to the Franck–Condon region within the time scale of the applied laser pulse. MCTDH simulations in SO_2 indicate that the returning wave packet interacts with the active laser pulse, resulting in an additional interference, for laser pulses of at least t_p = 100 fs. FSSH is not capable of reproducing these interference terms, and vMCG can only capture this effect when going beyond 100 GBFs. Moving to larger model systems decreases the recurrence time until it is not observed with the longest ($t_p = 200$ fs) laser pulse in the ten-mode model of 2-thiocytosine, indicating that these effects will be absent in systems with more degrees of freedom.

In SO_2, no perfect set of parameters was found suitable to describe quantitatively all different transition processes triggered by an ultrafast ($t_p = 30$ fs) laser pulse or when the simulation starts directly from the bright state. The decoherence correction emerges as the most essential parameter to model the excitation process and therefore also the overall laser-induced dynamics in the presence of laser pulses longer than a few cycles. The MCH representation where both the coupling via a laser field and the spin–orbit coupling are treated as off-diagonal elements is found beneficial to describe adequately both the S_0 and the triplet populations. This is mainly due to a better performance of AFSSH in the MCH representation to describe the change in the S_0 population as compared to AFSSH in the fully diagonal representation. For the EDC, no such strong basis dependence was identified for the excitation process, but larger disagreements for the triplet states are observed. For the observed dynamics in the excited singlet states, most parameters were found with almost identical errors. When using a reasonable combination of FSSH parameters, similar deviations are obtained for the excitation process for different lengths of the laser pulse until the wave packet recurrence is observed. Finally, the importance of rescaling the kinetic energy after a hopping event (not influenced by the laser field) is evident in the excited state dynamics, with rescaling along both the non-adiabatic coupling vector and the gradient difference vector showing high deviations for the triplet state dynamics. The performance of rescaling along both the NAC and the gradient difference vectors to mimic the MCTDH dynamics suffers from a large amount of frustrated hops but would most probably be improved by including additional nuclear properties in the comparison. Overall, the best FSSH parameter sets are associated with ~20% deviation in the amount of excited S_0 population with respect to MCTDH, while the subsequent population evolution is described with a similar level of accuracy as without the laser pulse.

For 2-thiocytosine, larger differences in the amount of excited population are observed due to the strong laser applied, increasing the difference in excited population by 35% and more, almost irrespective of the chosen parameters. The use of a decoherence correction increases the overall agreement throughout the excitation process, similar to the observations in SO_2. In the subsequent dynamics, rescaling of the kinetic energy after a hop reveals itself as the most important factor to obtain lower errors with respect to the MCTDH populations. Interestingly, the gradient difference vector is found to mostly result in large deviations from the reference if no laser is present but becomes the best performing parameter in the dynamics including the $t_p = 30$ fs laser pulse.

In summary, this work shows the difficulties in choosing a universal set of parameters that guarantees quantitative agreement against quantum reference results, particularly in the presence of an electric field. However, and despite many difficulties, FSSH can qualitatively reproduce the dynamics ensuing after excitation using an exemplary laser pulse of FWHM = 30 fs on two different test systems with three and ten dimensions—an encouraging result that paves the way for the use of explicit laser pulses in FSSH simulations. Based on the observations made in this paper, a few caveats have been identified. The use of very short laser pulses is encouraged due to the small amount of coupled electronic-nuclear motion during the pulse duration, thereby reducing the laser field to an almost purely electronic effect where FSSH yields good results. Additionally, quantum interferences are drastically reduced when employing short pulses, especially for larger systems. The same holds true for the use of very strong laser pulses, which will enhance problems inherent to FSSH without any laser pulse. Additionally, it is advised to use a decoherence correction (from the many available) because it is demonstrated to be, in most cases, the dominating factor to increase the agreement with the MCTDH reference, especially when considering explicit excitation. Caution is also advised when it comes to choosing a vector to adjust the momenta after a non-laser induced hop, as this parameter strongly influences the presented dynamics.

SUPPLEMENTARY MATERIAL

See the supplementary material for examples of population evolution in the presence of laser fields, highlighting the renormalization conducted within Eq. (10); sorted lists containing all calculated ε values used in Figs. 2, 5, 8, and 10; all ε values calculated for SO_2 using vMCG with different numbers of basis functions (which are presented in the PDF file); input and operator files used to simulate all MCTDH and vMCG calculations in QUANTICS; and Molden files and LVC template files for SO_2 and 2-thiocytosine (full-dimensional and one- up to ten-dimensional) use in SHARC (which are presented in the ZIP file).

ACKNOWLEDGMENTS

The authors thank the University of Vienna for providing access to the Vienna Scientific Cluster where part of the presented simulations was computed. The authors also thank S. Mai and P. Marquetand for discussions on the various flavors of FSSH.

DATA AVAILABILITY

The data that support the findings of this study are available from the corresponding author upon reasonable request.

REFERENCES

[1] M. Maiuri, M. Garavelli, and G. Cerullo, “Ultrafast spectroscopy: State of the art and open challenges,” J. Am. Chem. Soc. **142**, 3 (2020).
[2] R. Mitrić, J. Petersen, and V. Bonačić-Koutecký, “Laser-field-induced surface-hopping method for the simulation and control of ultrafast photodynamics,” Phys. Rev. A **79**, 053416 (2009).
[3] P. Marquetand, M. Richter, J. González-Vázquez, I. Sola, and L. González, “Nonadiabatic *ab initio* molecular dynamics including spin–orbit coupling and laser fields,” Faraday Discuss. **153**, 261 (2011).
[4] J. J. Bajo, J. González-Vázquez, I. R. Sola, J. Santamaria, M. Richter, P. Marquetand, and L. González, “Mixed quantum-classical dynamics in the adiabatic representation to simulate molecules driven by strong laser pulses,” J. Phys. Chem. A **116**, 2800 (2012).
[5] T. Fiedlschuster, J. Handt, and R. Schmidt, “Floquet surface hopping: Laser-driven dissociation and ionization dynamics of H_2^+,” Phys. Rev. A **93**, 053409 (2016).

[6] B. Mignolet and B. F. E. Curchod, "Excited-state molecular dynamics triggered by light pulses—*Ab initio* multiple spawning vs trajectory surface hopping," J. Phys. Chem. A **123**, 3582 (2019).

[7] D. V. Makhov and D. V. Shalashilin, "Floquet Hamiltonian for incorporating electronic excitation by a laser pulse into simulations of non-adiabatic dynamics," Chem. Phys. **515**, 46 (2018).

[8] J. Suchan, D. Hollas, B. F. E. Curchod, and P. Slavíček, "On the importance of initial conditions for excited-state dynamics," Faraday Discuss. **212**, 307 (2018).

[9] T. J. Penfold, M. Pápai, K. B. Møller, and G. A. Worth, "Excited state dynamics initiated by an electromagnetic field within the variational multi-configurational Gaussian (vMCG) method," Comput. Theor. Chem. **1160**, 24 (2019).

[10] C. Sanz-Sanz and G. A. Worth, "Field modified spin–orbit potential curves of IBr. Preliminary dynamical results," Phys. Chem. Chem. Phys. **21**, 14429 (2019).

[11] M. Wohlgemuth and R. Mitrić, "Excitation energy transport in DNA modelled by multi-chromophoric field-induced surface hopping," Phys. Chem. Chem. Phys. **22**, 16536 (2020).

[12] Z. Zhou, H.-T. Chen, A. Nitzan, and J. E. Subotnik, "Nonadiabatic dynamics in a laser field: Using Floquet fewest switches surface hopping to calculate electronic populations for slow nuclear velocities," J. Chem. Theory Comput. **16**, 821 (2020).

[13] L. González, *Quantum Chemistry and Dynamics of Excited States* (John Wiley & Sons, Ltd., 2020).

[14] P. V. Parandekar and J. C. Tully, "Mixed quantum-classical equilibrium," J. Chem. Phys. **122**, 094102 (2005).

[15] M. Ben-Nun, J. Quenneville, and T. J. Martínez, "Ab initio multiple spawning: Photochemistry from first principles quantum molecular dynamics," J. Phys. Chem. A **104**, 5161 (2000).

[16] J. C. Tully, "Molecular dynamics with electronic transitions," J. Chem. Phys. **93**, 1061 (1990).

[17] J. E. Subotnik, A. Jain, B. Landry, A. Petit, W. Ouyang, and N. Bellonzi, "Understanding the surface hopping view of electronic transitions and decoherence," Annu. Rev. Phys. Chem. **67**, 387 (2016).

[18] M. H. Beck, A. Jäckle, G. A. Worth, and H.-D. Meyer, "The multiconfiguration time-dependent Hartree (MCTDH) method: A highly efficient algorithm for propagating wavepackets," Phys. Rep. **324**, 1 (2000).

[19] G. A. Worth, M. A. Robb, and I. Burghardt, "A novel algorithm for non-adiabatic direct dynamics using variational Gaussian wavepackets," Faraday Discuss. **127**, 307 (2004).

[20] B. Lasorne, M. A. Robb, and G. A. Worth, "Direct quantum dynamics using variational multi-configuration Gaussian wavepackets. Implementation details and test case," Phys. Chem. Chem. Phys. **9**, 3210 (2007).

[21] T. J. Martínez, M. Ben-Nun, and R. D. Levine, "Multi-electronic-state molecular dynamics: A wave function approach with applications," J. Phys. Chem. **100**, 7884 (1996).

[22] M. Ben-Nun and T. J. Martínez, "Nonadiabatic molecular dynamics: Validation of the multiple spawning method for a multidimensional problem," J. Chem. Phys. **108**, 7244 (1998).

[23] A. Abedi, T. Neepa, and E. K. U. Gross, "Exact factorization of the time-dependent electron-nuclear wave function," Phys. Rev. Lett. **105**, 123002 (2010).

[24] F. Agostini, A. Abedi, Y. Suzuki, S. K. Min, N. T. Maitra, and E. K. U. Gross, "The exact forces on classical nuclei in non-adiabatic charge transfer," J. Chem. Phys. **142**, 084303 (2015).

[25] F. Agostini, "An exact-factorization perspective on quantum-classical approaches to excited-state dynamics," Eur. Phys. J. B **91**, 143 (2018).

[26] C. C. Martens and J.-Y. Fang, "Semiclassical-limit molecular dynamics on multiple electronic surfaces," J. Chem. Phys. **106**, 4918 (1997).

[27] J. E. Subotnik, W. Ouyang, and B. R. Landry, "Can we derive Tully's surface-hopping algorithm from the semiclassical quantum Liouville equation? Almost, but only with decoherence," J. Chem. Phys. **139**, 214107 (2013).

[28] R. Kapral, "Surface hopping from the perspective of quantum–classical Liouville dynamics," Chem. Phys. **481**, 77 (2016).

[29] E. R. Bittner and P. J. Rossky, "Quantum decoherence in mixed quantum-classical systems: Nonadiabatic processes," J. Chem. Phys. **103**, 8130 (1995).

[30] B. J. Schwartz, E. R. Bittner, O. V. Prezhdo, and P. J. Rossky, "Quantum decoherence and the isotope effect in condensed phase nonadiabatic molecular dynamics simulations," J. Chem. Phys. **104**, 5942 (1996).

[31] F. Plasser, S. Mai, M. Fumanal, E. Gindensperger, C. Daniel, and L. González, "Strong influence of decoherence corrections and momentum rescaling in surface hopping dynamics of transition metal complexes," J. Chem. Theory Comput. **15**, 5031 (2019).

[32] M. Richter, P. Marquetand, J. González-Vázquez, I. Sola, and L. González, "SHARC: *Ab initio* molecular dynamics with surface hopping in the adiabatic representation including arbitrary couplings," J. Chem. Theory Comput. **7**, 1253 (2011).

[33] T. Fiedlschuster, J. Handt, E. K. U. Gross, and R. Schmidt, "Surface hopping in laser-driven molecular dynamics," Phys. Rev. A **95**, 063424 (2017).

[34] A. Bjerre and E. E. Nikitin, "Energy transfer in collisions of an excited sodium atom with a nitrogen molecule," Chem. Phys. Lett. **1**, 179 (1967).

[35] J. C. Tully and R. K. Preston, "Trajectory surface hopping approach to nonadiabatic molecular collisions: The reaction of H^+ with D_2," J. Chem. Phys. **55**, 562 (1971).

[36] L. Wang, A. Akimov, and O. V. Prezhdo, "Recent progress in surface hopping: 2011–2015," J. Phys. Chem. Lett. **7**, 2100 (2016).

[37] G. Granucci and M. Persico, "Critical appraisal of the fewest switches algorithm for surface hopping," J. Chem. Phys. **126**, 134114 (2007).

[38] R. Crespo-Otero and M. Barbatti, "Recent advances and perspectives on nonadiabatic mixed quantum–classical dynamics," Chem. Rev. **118**, 7026 (2018).

[39] S. Mai, P. Marquetand, and L. González, "A general method to describe intersystem crossing dynamics in trajectory surface hopping," Int. J. Quantum Chem. **115**, 1215 (2015).

[40] A. Abedi, F. Agostini, Y. Suzuki, and E. K. U. Gross, "Dynamical steps that bridge piecewise adiabatic shapes in the exact time-dependent potential energy surface," Phys. Rev. Lett. **110**, 263001 (2013).

[41] L. Wang, D. Trivedi, and O. V. Prezhdo, "Global flux surface hopping approach for mixed quantum-classical dynamics," J. Chem. Theory Comput. **10**, 3598 (2014).

[42] S. Mai, P. Marquetand, and L. González, "Nonadiabatic dynamics: The SHARC approach," Wiley Interdiscip. Rev.: Comput. Mol. Sci. **8**, e1370 (2018).

[43] H. Köppel, W. Domcke, and L. S. Cederbaum, "Multimode molecular dynamics beyond the Born-Oppenheimer approximation," in *Advances in Chemical Physics* (John Wiley & Sons, Ltd., 2007), p. 59.

[44] C. A. Mead and D. G. Truhlar, "Conditions for the definition of a strictly diabatic electronic basis for molecular systems," J. Chem. Phys. **77**, 6090 (1982).

[45] H.-T. Chen, Z. Zhou, and J. E. Subotnik, "On the proper derivation of the Floquet-based quantum classical Liouville equation and surface hopping describing a molecule or material subject to an external field," J. Chem. Phys. **153**, 044116 (2020).

[46] K. Drese and M. Holthaus, "Floquet theory for short laser pulses," Eur. Phys. J. D **5**, 119 (1999).

[47] M. V. Korolkov and B. Schmidt, "Quantum molecular dynamics driven by short and intense light pulses: Towards the limits of the Floquet picture," Comput. Phys. Commun. **161**, 1 (2004).

[48] L. M. Ibele and B. F. E. Curchod, "A molecular perspective on Tully models for nonadiabatic dynamics," Phys. Chem. Chem. Phys. **22**, 15183 (2020).

[49] J. E. Subotnik and N. Shenvi, "A new approach to decoherence and momentum rescaling in the surface hopping algorithm," J. Chem. Phys. **134**, 024105 (2011).

[50] A. Jain, E. Alguire, and J. E. Subotnik, "An efficient, augmented surface hopping algorithm that includes decoherence for use in large-scale simulations," J. Chem. Theory Comput. **12**, 5256 (2016).

[51] G. Granucci, M. Persico, and A. Zoccante, "Including quantum decoherence in surface hopping," J. Chem. Phys. **133**, 134111 (2010).

[52] C. Zhu, S. Nangia, A. W. Jasper, and D. G. Truhlar, "Coherent switching with decay of mixing: An improved treatment of electronic coherence for non-Born–Oppenheimer trajectories," J. Chem. Phys. **121**, 7658 (2004).

[53] M. S. Topaler, T. C. Allison, D. W. Schwenke, and D. G. Truhlar, "Test of trajectory surface hopping against accurate quantum dynamics for an electronically nonadiabatic chemical reaction," J. Phys. Chem. A **102**, 1666 (1998).

[54] M. D. Hack, A. W. Jasper, Y. L. Volobuev, D. W. Schwenke, and D. G. Truhlar, "Quantum mechanical and quasiclassical trajectory surface hopping studies of the electronically nonadiabatic predissociation of the Ã state of NaH_2," J. Phys. Chem. A **103**, 6309 (1999).

[55] J. R. Schmidt, P. V. Parandekar, and J. C. Tully, "Mixed quantum-classical equilibrium: Surface hopping," J. Chem. Phys. **129**, 044104 (2008).

[56] A. Carof, S. Giannini, and J. Blumberger, "Detailed balance, internal consistency, and energy conservation in fragment orbital-based surface hopping," J. Chem. Phys. **147**, 214113 (2017).

[57] G. Miao, N. Bellonzi, and J. Subotnik, "An extension of the fewest switches surface hopping algorithm to complex Hamiltonians and photophysics in magnetic fields: Berry curvature and 'magnetic' forces," J. Chem. Phys. **150**, 124101 (2019).

[58] J. J. Bajo, G. Granucci, and M. Persico, "Interplay of radiative and nonradiative transitions in surface hopping with radiation-molecule interactions," J. Chem. Phys. **140**, 044113 (2014).

[59] H.-D. Meyer, U. Manthe, and L. S. Cederbaum, "The multi-configurational time-dependent Hartree approach," Chem. Phys. Lett. **165**, 73 (1990).

[60] G. A. Worth, H.-D. Meyer, H. Köppel, L. S. Cederbaum, and I. Burghardt, "Using the MCTDH wavepacket propagation method to describe multimode non-adiabatic dynamics," Int. Rev. Phys. Chem. **27**, 569 (2008).

[61] G. A. Worth, M. A. Robb, and B. Lasorne, "Solving the time-dependent Schrödinger equation for nuclear motion in one step: Direct dynamics of non-adiabatic systems," Mol. Phys. **106**, 2077 (2008).

[62] B. R. Landry, M. J. Falk, and J. E. Subotnik, "Communication: The correct interpretation of surface hopping trajectories: How to calculate electronic properties," J. Chem. Phys. **139**, 211101 (2013).

[63] S. Mai, M. Richter, M. Heindl, M. F. S. J. Menger, A. Atkins, M. Ruckenbauer, F. Plasser, M. Oppel, P. Marquetand, and L. González, SHARC2.0: Surface Hopping Including Arbitrary Couplings—Program Package for Non-Adiabatic Dynamics, 2018, see sharc-md.org.

[64] F. Plasser, S. Gómez, M. F. S. J. Menger, S. Mai, and L. González, "Highly efficient surface hopping dynamics using a linear vibronic coupling model," Phys. Chem. Chem. Phys. **21**, 57 (2019).

[65] E. Wigner, "On the quantum correction for thermodynamic equilibrium," Phys. Rev. **40**, 749 (1932).

[66] G. Granucci, M. Persico, and A. Toniolo, "Direct semiclassical simulation of photochemical processes with semiempirical wave functions," J. Chem. Phys. **114**, 10608 (2001).

[67] G. A. Worth, K. Giri, G. W. Richings, M. H. Beck, A. Jäckle, and H.-D. Meyer, QUANTICS, a suite of programs for molecular QUANTum dynamICS simulations, Version 1.1, 2015.

[68] G. A. Worth and L. S. Cederbaum, "Beyond Born-Oppenheimer: Molecular dynamics through a conical intersection," Annu. Rev. Phys. Chem. **55**, 127 (2004).

[69] C. Lévêque, R. Taïeb, and H. Köppel, "Communication: Theoretical prediction of the importance of the $^3B_2$ state in the dynamics of sulfur dioxide," J. Chem. Phys. **140**, 091101 (2014).

[70] C. Lévêque, H. Köppel, and R. Taïeb, "Excited state dynamics in SO_2. III. An *ab initio* quantum study of single- and multi-photon ionization," J. Chem. Phys. **140**, 204303 (2014).

[71] S. Mai, P. Marquetand, and L. González, "Non-adiabatic and intersystem crossing dynamics in SO_2. II. The role of triplet states in the bound state dynamics studied by surface-hopping simulations," J. Chem. Phys. **140**, 204302 (2014).

[72] A. W. Jasper, S. N. Stechmann, and D. G. Truhlar, "Fewest-switches with time uncertainty: A modified trajectory surface-hopping algorithm with better accuracy for classically forbidden electronic transitions," J. Chem. Phys. **116**, 5424 (2002).

[73] S. Mai, M. Pollum, L. Martínez-Fernían dez, N. Dunn, P. Marquetand, I. Corral, C. Crespo-Hernández, and L. González, "The origin of efficient triplet state population in sulfur-substituted nucleobases," Nat. Commun. **7**, 13077 (2016).

[74] S. Gómez, M. Heindl, A. Szabadi, and L. González, "From surface hopping to quantum dynamics and back. Finding essential electronic and nuclear degrees of freedom and optimal surface hopping parameters," J. Phys. Chem. A **123**, 8321 (2019).

[75] B. Lasorne, F. Sicilia, M. J. Bearpark, M. A. Robb, G. A. Worth, and L. Blancafort, "Automatic generation of active coordinates for quantum dynamics calculations: Application to the dynamics of benzene photochemistry," J. Chem. Phys. **128**, 124307 (2008).

[76] G. Richings, C. Robertson, and S. Habershon, "Can we use on-the-fly quantum simulations to connect molecular structure and sunscreen action?," Faraday Discuss. **216**, 476 (2019).

APPENDIX A.3 A RU APPLICATION

APPENDIX A.3.1

Electrochemical and Photophysical Properties of Ruthenium(II) Complexes Equipped with Sulfurated Bipyridine Ligands

Shao-An Hua, Mauricio Cattaneo, Manuel Oelschlegel, Moritz Heindl, Lucius Schmid, Sebastian Dechert, Oliver S. Wenger, Inke Siewert, Leticia González, and Franc Meyer

Inorg. Chem., **59**, 4972-4984 (2020).
`https://doi.org/10.1021/acs.inorgchem.0c00220`

Contributions:

Shao-An Hua synthesized the photosensitizer, performed electrochemical measurements, and wrote the first draft of the manuscript.

Mauricio Cattaneo synthesized the photosensitizer, conducted preliminary characterizations and theoretical computations, contributed to the writing of the manuscript.

Manuel Oelschlegel optimized the synthesis of the photosensitizer.

Moritz Heindl performed the SH simulations, analyzed the results and contributed to the initial draft of the manuscript.

Lucius Schmid performed optical spectroscopic measurements.

Sebastian Dechert helped in the characterization of the sample.

Oliver S. Wenger conceived and supervised the project, analyzed the results and contributed to the writing of the manuscript.

Inke Siewert performed cyclo voltammetric measurements, analyzed the thermodynamic and kinetic properties.

Leticia González conceived and supervised the project, analyzed the results and contributed to the writing of the manuscript.

Franc Meyer conceived and supervised the project, analyzed the results and contributed to the writing of the manuscript.

Inorganic Chemistry

pubs.acs.org/IC

Article

Electrochemical and Photophysical Properties of Ruthenium(II) Complexes Equipped with Sulfurated Bipyridine Ligands

Shao-An Hua, Mauricio Cattaneo, Manuel Oelschlegel, Moritz Heindl, Lucius Schmid, Sebastian Dechert, Oliver S. Wenger, Inke Siewert,* Leticia González,* and Franc Meyer*

Cite This: *Inorg. Chem.* 2020, 59, 4972−4984

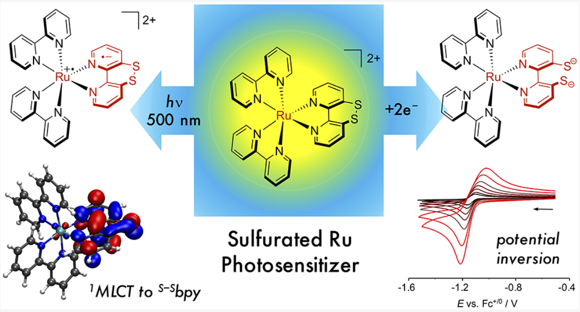

ABSTRACT: The development of new solar-to-fuel scenarios is of great importance, but the construction of molecular systems that convert sunlight into chemical energy represents a challenge. One specific issue is that the molecular systems have to be able to accumulate redox equivalents to mediate the photodriven transformation of relevant small molecules, which mostly involves the orchestrated transfer of multiple electrons and protons. Disulfide/dithiol interconversions are prominent $2e^-/2H^+$ couples and can play an important role for redox control and charge storage. With this background in mind, a new photosensitizer $[Ru(^{S-S}bpy)(bpy)_2]^{2+}$ ($\mathbf{1}^{2+}$) equipped with a disulfide functionalized bpy ligand ($^{S-S}$bpy, bpy = 2,2′-bipyridine) was synthesized and has been comprehensively studied, including structural characterization by X-ray diffraction. In-depth electrochemical studies show that the $^{S-S}$bpy ligand in $\mathbf{1}^{2+}$ can be reduced twice at moderate potentials (around −1.1 V vs $Fc^{+/0}$), and simulation of the cyclic voltammetry (CV) traces revealed potential inversion ($E_2 > E_1$) and allowed to derive kinetic parameters for the sequential electron-transfer processes. However, reduction at room temperature also triggers the ejection of one sulfur atom from $\mathbf{1}^{2+}$, leading to the formation of $[Ru(^{S}bpy)(bpy)_2]^{2+}$($\mathbf{2}^{2+}$). This chemical reaction can be suppressed by decreasing the temperature from 298 to 248 K. Compared to the archetypical photosensitizer $[Ru(bpy)_3]^{2+}$, $\mathbf{1}^{2+}$ features an additional low energy optical excitation in the MLCT region, originating from charge transfer from the metal center to the $^{S-S}$bpy ligand (aka MSCT) according to time-dependent density functional theory (TD-DFT) calculations. Analysis of the excited states of $\mathbf{1}^{2+}$ on the basis of ground-state Wigner sampling and using charge-transfer descriptors has shown that bpy modification with a peripheral disulfide moiety leads to an energy splitting between charge-transfer excitations to the $^{S-S}$bpy and the bpy ligands, offering the possibility of selective charge transfer from the metal to either type of ligands. Compound $\mathbf{1}^{2+}$ is photostable and shows an emission from a ^{3}MLCT state in deoxygenated acetonitrile with a lifetime of 109 ns. This work demonstrates a rationally designed system that enables future studies of photoinduced multielectron, multiproton PCET chemistry.

■ INTRODUCTION

The transformation of small molecules relevant for sustainable energy scenarios, specifically the generation of solar fuels, is a key challenge of current research addressing urgent energy storage needs. Light-driven fuel production requires the development of catalysts capable of mediating challenging transformations of rather inert molecules, which mostly involve the orchestration of complex multielectron, multiproton transfers to/from the substrate.[1] Furthermore, light-harvesting systems need to be integrated into this proton/electron-transfer scheme in order to achieve the light-to-chemical energy conversion.[2]

During the past few decades, photoinduced single electron transfer in donor−acceptor compounds has been thoroughly investigated. However, the above light-driven multielectron-transfer processes are still difficult to achieve. Therefore, recent years have seen considerable growth in interest toward photoinduced multielectron transfer and the light-driven charge accumulation.[3] Despite the major efforts relying on the usage of sacrificial reagents, currently few examples of fully integrated systems capable of photoinduced multielectron transfer have been introduced.[4] Among them, ruthenium(II) polypyridine-type complexes are often chosen as building blocks for the construction of covalently linked donor−photosensitizer−acceptor systems, because they exhibit favorable excited-state and redox properties. While synthetically the assembly of such metal-containing building blocks with

Received: January 21, 2020
Published: March 6, 2020

https://dx.doi.org/10.1021/acs.inorgchem.0c00220
Inorg. Chem. 2020, 59, 4972−4984

covalently linked ligands is feasible, the preparation of multimetallic complexes is particularly tedious. For simplicity, an alternative approach is the design of new polypridyl chelating ligands capable of storing multiple charges.

Previously, we reported a bipyridine analogue ligand equipped with a peripheral disulfide moiety ($^{S-S}$bpy, bpy = 2,2′ bipyridine, Figure 1), which exhibits two chemically reversible reduction processes.[5] In-depth electrochemical studies in combination with density functional theory (DFT) computations were conducted to unravel the sequence of redox events. In the presence of water, the protonation of free $^{S-S}$bpy facilitates the second reduction, which then occurs at a slightly lower potential than the first one; hence, protonation triggers potential inversion and switches the mechanism from *EEC* to *ECEC* (*E* = electrochemical step, *C* = chemical step). This is reminiscent of related aromatic disulfide molecules such as dibenzo[1,2]dithiins that are capable of promoting the uptake of multiple electrons through redox potential inversion.[4a,6] The dual functionality of the $^{S-S}$bpy ligand, i.e., the combination with its *N*,*N*′-chelate site and the backside disulfide/dithiol 2H$^+$/2e$^-$ switch, offers interesting prospects when decorating common 4d^6 and 5d^6 transition metal photoabsorbers with this new sulfurated bpy derivative. Inter alia, such molecular design could potentially benefit the storage of redox equivalents and enable photoinduced multielectron/proton-transfer reactions, which are of essential importance for solar fuel production.

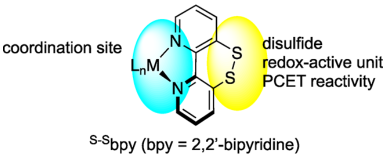

Figure 1. Dual-functionality of the $^{S-S}$bpy ligand.

Herein, we present first results in this direction, viz., the preparation and comprehensive characterization of a novel Ru^{II} complex equipped with one $^{S-S}$bpy ligand; a related complex with a modified bpy ligand featuring a single S atom (^{S}bpy) is also studied. Both complexes have been structurally authenticated and well characterized by electrochemistry, providing detailed understanding of their ground-state nature. The photophysical properties have also been investigated and interpreted with the help of time-dependent density functional theory (TD-DFT) calculations that allow for assignment of the optical transitions.

■ EXPERIMENTAL SECTION

General Considerations and Materials. All manipulations of air- and moisture-sensitive materials were carried out under an anaerobic and anhydrous atmosphere of dry argon using standard Schlenk techniques or in a N_2-filled MBraun glovebox. [Ru(bpy)$_2$Cl$_2$],[7] [Hdmf](OTf) (dmf is dimethylformamide; OTf$^-$ = $CF_3SO_3^-$),[8] $^{S-S}$bpy,[5] and ^{S}bpy[5] were prepared according to the reported literature procedures. All used chemicals were reagent grade. CH_3CN was freshly distilled for electrochemical measurements. Tetrakis(*n*-butyl)ammonium hexafluorophosphate ($^nBu_4NPF_6$) was dried and stored in the glovebox.

Instrumentation. IR spectra were measured with KBr pellets using a Digilab Excalibur Series FTS 3000 or Bruker Vertex 70 spectrometer. UV–vis spectra of solutions in quartz cuvettes were recorded with an Agilent Cary 60 spectrometer. Steady-state absorption and luminescence spectra were recorded using a Cary 5000 spectrophotometer from Varian and a Fluorolog-3-22 instrument from Horiba Jobin-Yvon, respectively. Transient absorption and emission studies were carried out with a LP920-KS apparatus from Edinburgh Instruments. Excitation at 430 and 450 nm was achieved by a Quantel Brilliant Nd:YAG laser equipped with an OPO from Opotek. Excitation at 532 nm was achieved by a frequency doubled Nd:YAG laser (Quantel Brilliant, pulse width ca. 10 ns). For detection of transient absorption spectra, an iCCD camera from Andor was used, whereas kinetic traces at a single wavelength were recorded using a photomultiplier tube. Cyclic voltammetry (CV) experiments were measured under an argon atmosphere with a Gamry Interface Reference 600 potentiostat equipped with a three electrode setup consisting of a 3 mm glassy carbon working electrode (WE), a platinum wire counter electrode (CE), and a Ag wire as pseudoreference electrode (RE). $^nBu_4NPF_6$ (0.2 M) in deoxygenated dry CH_3CN was used as the supporting electrolyte and was prepared in the glovebox. Ferrocene was used as an internal standard, and the data were referenced to the Fc$^{+/0}$ redox couple at the respective temperature. Corrections for the temperature-dependent potential shift of Fc are explained in the Supporting Information. *iR* compensation was applied by the positive feedback method, which is implemented in the Gamry software package. Controlled-potential coulometry (CPC) was performed in a glovebox under a nitrogen atmosphere with a Gamry Interface 1000B, using a Pt mesh (WE), a Pt wire (CE), and a Ag wire (RE) in a glass-fritted compartment cell. Data were analyzed by Gamry Framework software. (Spectro)-electrochemistry experiments were performed in a glovebox under a nitrogen atmosphere with an Interface 1000B potentiostat, Deuterium/Tungsten light source (BWTEK), Exemplar LS spectrometer (BWTEK), and quartz cuvettes. A platinum mesh was used as the working electrode, a platinum wire was used as the auxiliary electrode, and a Ag wire was used as the reference electrode. $^nBu_4NPF_6$ (0.2 M) in MeCN was used as supporting electrolyte. The potential was controlled by Gamry Framework software, and the data was analyzed by BWSpec software. NMR spectra were recorded on Avance DRX 500 (Bruker), Avance 500 Ultrashield (Bruker), Avance 300 (Bruker), and Avance III 300 (Bruker) instruments in $CDCl_3$ or CD_3CN, with residual protons as internal references. Mass spectrometry was performed with a Finnigan MAT 8200 (EI-MS) or a Bruker HTC Ultra (ESI-MS). Combustion analyses were performed by the Analytic Service at the Department of Chemistry of the University of Göttingen. X-ray diffraction data were collected on a STOE IPDS II with graphite monochromated Mo Kα radiation (λ = 0.71073 Å) by use of ω scans at −140 °C. Details of the X-ray crystallographic structure determinations are provided in the Supporting Information. CCDC 1979158 and 1979159 contain the supplementary crystallographic data for this paper. These data can be obtained free of charge from The Cambridge Crystallographic Data Centre via http://www.ccdc.cam.ac.uk/data_request/cif.

Synthesis. *[Ru($^{S-S}$bpy)(bpy)$_2$](PF$_6$)$_2$ (**1**(PF$_6$)$_2$).* $^{S-S}$bpy (218 mg, 1.00 mmol, 1.00 equiv) and [Ru(bpy)$_2$Cl$_2$] (520 mg, 1.00 mmol, 1.00 equiv) in MeOH (20 mL) were placed in a 50 mL round-bottom Schlenk flask. The mixture was degassed and heated at 60 °C in the dark overnight. After cooling to room temperature (RT), the dark violet suspension was filtered, and to the resulting deep red solution, 300 mg of KPF_6 was added and the mixture was stirred for 30 min. The solvent was removed under reduced pressure, and the solid was extracted with CH_2Cl_2 (100 mL). The crude product was further purified by column chromatography (Alox, with CH_3CN/ethyl acetate: 1/10 as eluent). The amount of solvent was reduced to around 10 mL, and hexane was added to the solution to precipitate the final product as red powder. This powder was subsequently washed with diethyl ether and dried under a vacuum (437 mg, 47%). Deep red crystals suitable for X-ray diffraction were obtained by the slow diffusion of diethyl ether into a solution of **1**(PF$_6$)$_2$ in CH_3CN/acetone. Anal. calc for $C_{36}H_{34}N_8F_{12}P_2O_2RuS_2$: % C 39.09, % H 2.41, % N 9.12, % S 6.96. Found: % C 39.32, % H 2.34, % N 9.04, % S 6.94. IR (KBr pellets): ν 3117 (w), 3084 (w), 1602 (m), 1559 (w), 1467 (m), 1446 (m), 1420 (m), 1409 (m), 1313 (w), 1292 (w), 1271 (w), 1243 (w), 1215 (w), 1203 (w), 1163 (w), 1124 (w), 1112 (w), 1068 (w), 1036 (w), 875 (m), 833 (s), 800 (s), 760 (s), 731 (s), 719 (s), 706 (m), 660 (m) cm^{-1}. ^{1}H NMR spectrum (500 MHz, CD_3CN): δ 8.50 (7^{bpy}, ddd, 2H, $J_{7bpy-8bpy}$ = 8.2 Hz, $J_{7bpy-9bpy}$ = 1.4 Hz, $J_{7bpy-10bpy}$ = 0.8 Hz), 8.49 (4^{bpy}, ddd, 2H, $J_{4bpy-3bpy}$ = 8.2 Hz, $J_{4bpy-2bpy}$ = 1.4 Hz, $J_{4bpy-1bpy}$ = 0.8 Hz), 8.10 (8^{bpy}, 2 × dd, 2H, $J_{8bpy-7bpy}$ = 8.2 Hz, $J_{8bpy-9bpy}$ = 1.4 Hz), 8.05 (3^{bpy}, 2 × dd, 2H, $J_{3bpy-4bpy}$ = 8.2 Hz, $J_{3bpy-2bpy}$ = 1.4 Hz), 7.89 (3, dd, 2H J_{3-2} = 8.1 Hz, J_{3-1} = 1.3 Hz), 7.83 (10^{bpy}, ddd, 2H, $J_{10bpy-9bpy}$ = 5.7 Hz, $J_{10bpy-8bpy}$ = 1.5 Hz, $J_{10bpy-7bpy}$ = 0.8 Hz), 7.65 (1^{bpy}, ddd, 2H, $J_{1bpy-2bpy}$ = 5.7 Hz, $J_{1bpy-3bpy}$ = 1.5 Hz, $J_{1bpy-4bpy}$ = 0.8 Hz), 7.62 (1, dd, 2H, J_{1-2} = 5.6 Hz, J_{1-3} = 1.3 Hz), 7.47 (9^{bpy}, 2 × dd, 2H, $J_{9bpy-10bpy}$ = 5.7 Hz, $J_{9bpy-8bpy}$ = 1.4 Hz), 7.39 (2^{bpy}, 2 × dd, 2H, $J_{2bpy-1bpy}$ = 5.7 Hz, $J_{2bpy-3bpy}$ = 1.4 Hz), 7.30 (2, dd, 2H, J_{2-3} = 8.1 Hz, J_{2-1} = 5.6 Hz). $^{13}C\{^1H\}$ NMR (500 MHz, CD_3CN): δ 157.80 (6^{bpy}), 157.76 (5^{bpy}), 155.58 (4), 152.95 (10^{bpy}), 152.66 (1^{bpy}), 151.96 (1), 139.14 (8^{bpy}), 139.10 (3^{bpy}), 137.52 (3), 135.75 (5), 129.11 (2), 128.72 (9^{bpy}), 128.68 (2^{bpy}), 125.37 (7^{bpy},4^{bpy}). ESI(+)-MS (CH_3CN, m/z): $[M]^{2+}$ 316.0 (100%), $[M + PF_6]^+$ 777.0 (50%). UV−vis (CH_3CN): λ_{max} (nm, ε [L mol^{-1} cm^{-1}]): 244 (26400), 286 (73900), 318 (19600), 398 (8000), 435 (11300), 492 (8500).

*[Ru(^{S}bpy)(bpy)$_2$](PF$_6$)$_2$ (**2**(PF$_6$)$_2$).* ^{S}bpy (93 mg, 0.50 mmol, 1.0 equiv) and $[Ru(bpy)_2Cl_2]$ (260 mg, 0.500 mmol, 1.00 equiv) in MeOH (15 mL) were placed in a 50 mL round-bottom Schlenk flask. The mixture was degassed and heated to 70 °C in the dark overnight. After cooling to RT, the dark violet suspension was filtered, and to the resulting deep orange solution, 300 mg of KPF_6 was added and the mixture was stirred for 30 min. The solvent was removed under reduced pressure, and the solid was extracted with CH_2Cl_2 (40 mL). The crude product was purified by column chromatography (Alox, with CH_3CN/ethyl acetate: 1/10 as eluent) to give the target compound (302 mg, 68%). Orange-red crystals suitable for X-ray diffraction were obtained by slow diffusion of diethyl ether into a solution of **2**$(PF_6)_2$ in CH_3CN. Anal. calc for $C_{30}H_{22}N_6F_{12}P_2RuS\cdot H_2O$: % C 39.70, % H 2.66, % N 9.26, % S 3.53. Found: % C 39.56, % H 2.73, % N 9.57, % S 3.10. IR (KBr pellets): ν 3115 (w), 3084 (w), 1604 (w), 1464 (m), 1448 (m), 1425 (m), 1405 (m), 1312 (w), 1271 (w), 1243 (w), 1226 (w), 1203 (w), 1161 (w), 1125 (w), 1108 (w), 1064 (w), 890 (m), 874 (m), 831 (s), 786 (s), 754 (s), 728 (s), 715 (s), 611 (m) cm^{-1}. ^{1}H NMR spectrum (500 MHz, CD_3CN): δ 8.54 (3, dd, 2H, J_{3-2} = 8.4 Hz, J_{3-1} = 0.8 Hz), 8.50 (7^{bpy}, ddd, 2H, $J_{7bpy-8bpy}$ = 8.1 Hz, $J_{7bpy-9bpy}$ = 1.4 Hz, $J_{7bpy-10bpy}$ = 0.8 Hz), 8.49 (4^{bpy}, ddd, 2H, $J_{4bpy-3bpy}$ = 8.1 Hz, $J_{4bpy-2bpy}$ = 1.4 Hz, $J_{4bpy-1bpy}$ = 0.8 Hz), 8.10 (8^{bpy}, 2 × dd, 2H, $J_{8bpy-7bpy}$ = 8.2 Hz, $J_{8bpy-9bpy}$ = 1.4 Hz), 8.05 (3^{bpy}, 2 × dd, 2H, $J_{3bpy-4bpy}$ = 8.2 Hz, $J_{3bpy-2bpy}$ = 1.4 Hz), 7.83 (10^{bpy}, ddd, 2H, $J_{10bpy-9bpy}$ = 5.7 Hz, $J_{10bpy-8bpy}$ = 1.5 Hz, $J_{10bpy-7bpy}$= 0.8 Hz), 7.65 (1^{bpy}, ddd, 2H, $J_{1bpy-2bpy}$ = 5.7 Hz, $J_{1bpy-3bpy}$ = 1.5 Hz, $J_{1bpy-4bpy}$ = 0.8 Hz), 7.72 (1, dd, 2H J_{1-2} = 5.3 Hz, J_{1-3} = 0.9 Hz), 7.57 (2, dd, 2H J_{2-3} = 8.4 Hz, J_{2-1} = 5.3 Hz), 7.47 (9^{bpy}, 2 × dd, 2H, $J_{9bpy-10bpy}$ = 5.7 Hz, $J_{9bpy-8bpy}$ = 1.4 Hz), 7.39 (2^{bpy}, 2 × dd, 2H, $J_{2bpy-1bpy}$ = 5.7 Hz, $J_{2bpy-3bpy}$ = 1.4 Hz). $^{13}C\{^1H\}$ NMR (500 MHz, CD_3CN): δ 158.95 (5^{bpy}), 158.19 (5^{bpy}), 154.34 (5), 153.72 (10^{bpy}), 153.65 (1^{bpy}), 150.25 (1), 138.82 (3^{bpy}), 138.80 (8^{bpy}), 135.16 (4), 134.14 (3), 128.63 (9^{bpy}), 128.23 (2^{bpy}), 126.60 (2), 125.07 (4^{bpy}), 125.03 (7^{bpy}). ESI(+)-MS (MeOH, m/z): $[M]^{2+}$ 300.0 (100%), $[M + PF_6]^+$ 745.1 (1%). UV−vis (CH_3CN): λ_{max} (nm, ε [L mol^{-1} cm^{-1}]): 234 (43400), 256 (30600), 286 (71000), 424 (12300), 448 (14800).

Density Functional Theory (DFT) Calculations. [Ru($^{S-S}$bpy)(bpy)$_2$]$^{2+}$ (**1**$^{2+}$) and [Ru(^{S}bpy)(bpy)$_2$]$^{2+}$ (**2**$^{2+}$) were optimized in CH_3CN using the B3LYP[9] hybrid functional combined with the 6-311G(d) basis set for nonmetal atoms and the LANL2DZ[10] effective core potential for the ruthenium center (B3LPY/6-311G(d)-LANL2DZ). Long-range interactions are taken into account with the Grimme[11] D3 dispersion correction. Scalar relativistic effects are included through the use of the second-order Douglas−Kroll−Hess[12] integrals. Solvent effects were accounted implicitly with the integral equation formalism polarized continuum model[13] (ε = 35.688). The electronic excited-state calculations were done employing linear response time-dependent DFT (TD-DFT)[14] at the B3LYP/6-311G(d)-LANL2DZ level of theory on the lowest-lying 20 electronic singlet states. The character of the most important (brightest) electronic excited states at the equilibrium geometry is illustrated using leading natural transition orbital[15] (NTO) pairs. All calculations have been carried out using the Gaussian09[16] suite of programs.

The calculation of the absorption spectra is done by convoluting pairs of excitation energies and oscillator strengths of a set of 200 geometries obtained from a ground-state Wigner sampling[17] to take into account nuclear motion. Gaussian functions with a fwhm of 0.15 eV were used in the convolution. The 4000 (20 × 200) resulting excited states were analyzed using charge-transfer descriptors[18] as implemented in the TheoDORE[19] program package. For this analysis, the complexes were divided into four fragments: the $^{S-S}$bpy or ^{S}bpy ligand, respectively (referred to as S), the Ru metal center (M), and each of the two bpy ligands (L). Accordingly, the excited states are classified according to the most important charge-transfer contribution from the "hole" (the fragment from which the electron is excited) to the "electron" (the fragment to which the electron is excited). If the hole and electron fragment is the same, it is a local excitation, denoted by MC or LC/SC if this fragment is the M or the L/S ligand. If the hole and electron fragments differ, it is a charge-transfer excitation and will be written as, e.g., MLCT/MSCT when the hole fragment is M and the electron fragment is one of the L or S ligands, etc. Within the considered four fragment scheme, there are ten different types of excitations (MC, LC, MLCT, LMCT, LLCT, SC, MSCT, SMCT, LSCT, and SLCT).

■ RESULTS AND DISCUSSION

Synthesis and Characterization of Ru^{II} Complexes. The ligand [1,2]dithiino[4,3-b:5,6-b′]bipyridine ($^{S-S}$bpy) was prepared via the previously reported multistep protocol, starting from 2-bromo-3-pyridinol.[5] The monosulfurated bipyridine, viz., the thiophene derivative ^{S}bpy,[20] is formed in substantial amounts as a side-product during the synthesis of $^{S-S}$bpy.[5] Both bpy derivatives can be readily coordinated to Ru^{II} (Scheme 1). The mononuclear complex [Ru($^{S-S}$bpy)(bpy)$_2$](PF$_6$)$_2$ (**1**(PF$_6$)$_2$) was synthesized by heating a solution of $[Ru(bpy)_2Cl_2]$ and $^{S-S}$bpy in MeOH to reflux overnight. Anion exchange gave the PF_6^- salt, which shows high solubility in polar organic solvents. After column chromatography, pure [Ru($^{S-S}$bpy)(bpy)$_2$](PF$_6$)$_2$ (**1**(PF$_6$)$_2$) was obtained in 47% yield. Using ^{S}bpy and applying the same synthetic procedure gave [Ru(^{S}bpy)(bpy)$_2$](PF$_6$)$_2$ (**2**(PF$_6$)$_2$) in 68% yield.

Scheme 1. Synthetic Routes for Mounting the $^{S-S}$bpy and ^{S}bpy Ligands on the {Ru(bpy)$_2$$^{2+}$} Fragment

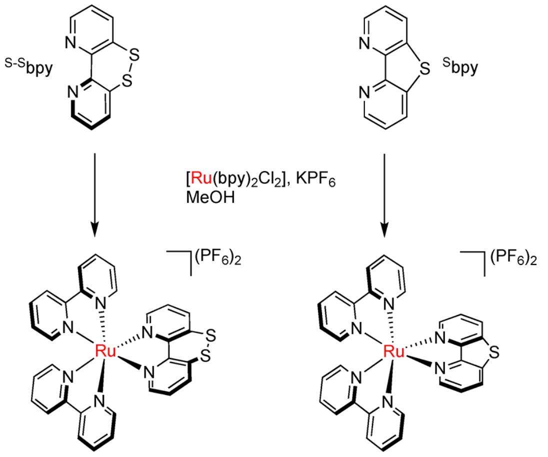

[Ru($^{S-S}$bpy)(bpy)$_2$]$^{2+}$ (**1**$^{2+}$) [Ru(^{S}bpy)(bpy)$_2$]$^{2+}$ (**2**$^{2+}$)

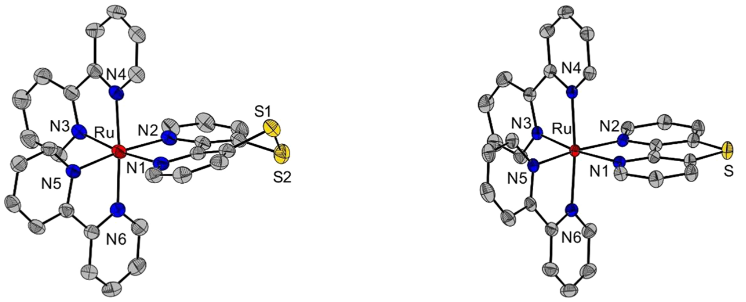

Figure 2. Molecular structures of the cations of **1**$^{2+}$ (left) and **2**$^{2+}$ (right) shown as 50% probability thermal ellipsoids. Hydrogens, solvent molecules, and PF$_6^-$ counterions are omitted for clarity.

Table 1. Selected Bond Lengths and Angles for 1^{2+} and 2^{2+a}

	[Ru($^{S-S}$bpy)(bpy)$_2$](PF$_6$)$_2$ (**1**$^{2+}$)			[Ru(^{S}bpy)(bpy)$_2$](PF$_6$)$_2$ (**2**$^{2+}$)	
ligand	bond	distance (Å)	ligand	bond	distance (Å)
$^{S-S}$bpy	Ru−N(1)	2.057(2)/*2.097*	^{S}bpy	Ru−N(1)	2.109(2)/*2.154*
	Ru−N(2)	2.058(2)/*2.097*		Ru−N(2)	2.115(2)/*2.152*
	S(1)−S(2)	2.048(1)/*2.106*			
bpy-1	Ru−N(3)	2.061(2)/*2.097*	bpy-1	Ru−N(3)	2.049(2)/*2.097*
	Ru−N(4)	2.074(2)/*2.103*		Ru−N(4)	2.068(2)/*2.083*
bpy-2	Ru−N(5)	2.045(2)/*2.096*	bpy-2	Ru−N(5)	2.045(2)/*2.083*
	Ru−N(6)	2.066(2)/*2.101*		Ru−N(6)	2.054(2)/*2.096*
	atoms	angle (deg)		atoms	angle (deg)
$^{S-S}$bpy	N(1)−Ru−N(2)	78.79(9)/*78.14*	^{S}bpy	N(1)−Ru−N(2)	81.87(7)/*81.07*
bpy-1	N(3)−Ru−N(4)	78.68(9)/*78.07*	bpy-1	N(3)−Ru−N(4)	78.80(7)/*78.37*
bpy-2	N(5)−Ru−N(6)	78.73(9)/*78.11*	bpy-2	N(5)−Ru−N(6)	78.72(7)/*78.36*
	planes	dihedral angle (deg)		planes	dihedral angle (deg)
$^{S-S}$bpy	N(1)−C−C−N(2)	12.28/*11.42*	^{S}bpy	N(1)−C−C−N(2)	0.37/*0.71*
	C−S(1)−S(2)−C	56.71/*54.11*			

^{a}Parameters for B3LYP optimized geometries are given in italics.

ESI(+)-MS spectra of CH$_3$CN solutions of the complexes show major peaks for ions [Ru($^{S-S}$bpy)(bpy)$_2$]$^{2+}$ and [Ru($^{S-S}$bpy)(bpy)$_2$(PF$_6$)]$^+$ in case of **1**(PF$_6$)$_2$, or for [Ru(^{S}bpy)(bpy)$_2$]$^{2+}$ and [Ru(^{S}bpy)(bpy)$_2$(PF$_6$)]$^+$ in case of **2**(PF$_6$)$_2$, respectively, with the expected isotopic distribution patterns (Figures S1 and S2). ^{1}H and ^{13}C NMR spectra of both complexes reflect C_2 symmetry in solution with eight proton signals for the bpy ligands and three proton signals for the $^{S-S}$bpy and ^{S}bpy ligand moieties, respectively. NMR spectra and full spectral assignments are provided in Figures S3−S10.

Single crystals of **1**(PF$_6$)$_2$ and **2**(PF$_6$)$_2$ were obtained by slow diffusion of diethyl ether into CH$_3$CN/acetone or CH$_3$CN solutions of the complexes, respectively. Molecular structures of the cations are depicted in Figure 2, and selected atom distances and bond angles are listed in Table 1. Both complexes exhibit a distorted octahedral geometry, which is a typical feature for Ru^{II} complexes ligated by three ligands that form 5-membered chelate rings. In **1**$^{2+}$, bidentate *N*,*N*′ coordination of $^{S-S}$bpy results in N1−C−C−N2 and C−S1−S2−C torsion angles of 12.28° and 56.71°, respectively, as well as a S−S bond length of 2.048 Å. For **2**$^{2+}$ with a single S atom bridge, the two pyridine rings of the ^{S}bpy moiety are essentially coplanar, as evidenced by a very small N1−C−C−N2 angle of 0.37°. Furthermore, the overall ligand planarity induced by the planar thiophene fragment slightly opens the *N*,*N*′ bite angle, which is reflected by a N1−Ru−N2 angle of 81.87° in **2**$^{2+}$, in comparison with the N1−Ru−N2 angle of 78.9° in $^{S-S}$bpy ligated **1**$^{2+}$. Ru−N distances are in the typical range,[21] namely, 2.055−2.070 Å for **1**$^{2+}$ and 2.045−2.074 Å for **2**$^{2+}$.

UV−vis Absorption, Luminescence, and Transient Absorption Spectroscopy. The UV−vis absorption spectrum of **2**$^{2+}$ in CH$_3$CN solution displays the characteristic bands reminiscent of those of [Ru(bpy)$_3$]$^{2+}$,[22] comprising an intense ligand $\pi-\pi^*$ absorption at 287 nm alongside with broad and less intense MLCT bands at 424 and 448 nm, (Figure 3a and Table 2). In contrast, the MLCT absorption signature of **1**$^{2+}$ is distinctly different and shows three maxima instead of two, with all these absorptions having smaller extinction coefficients. The first two maxima located at 398 and 435 nm are slightly hypsochromically shifted by approximately 20 nm compared to **2**$^{2+}$, but a distinct low-energy band is observed at around 500 nm. These findings are suggestive of a separated, low-lying MLCT state due to the introduction of the $^{S-S}$bpy ligand. The assignment of these charge-transfer absorptions will be discussed in detail in the computational part (vide infra).

Solutions of **1**$^{2+}$ or **2**$^{2+}$ in deaerated CH$_3$CN are emissive when excited at 430 or 400 nm, respectively, as shown in Figure 3a. For **1**$^{2+}$, varying the excitation wavelength from 400 to 532 nm results in the same broad, featureless emission band with maximum intensity at 730 nm (Figure S12), indicative of a typical Kasha behavior. Time-resolved luminescence decay curves recorded at 730 nm in deaerated CH$_3$CN after excitation of **1**$^{2+}$ at 430 and 532 nm result in identical traces, with a lifetime of 109 ns (Figure 3b,c). A measurement in

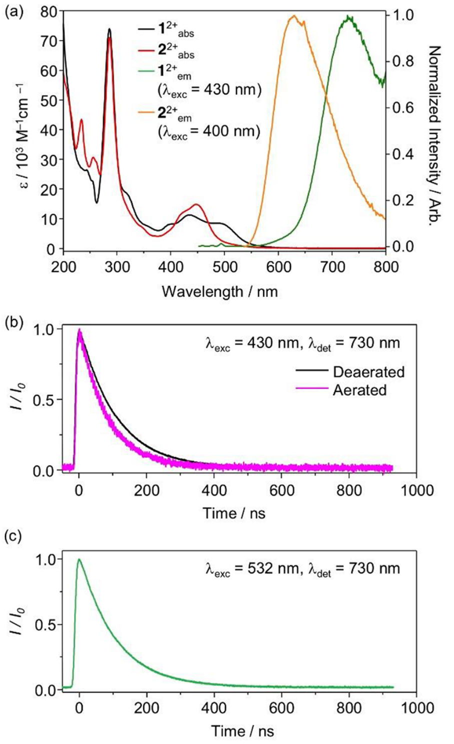

Figure 3. (a) Room temperature absorption and emission spectra of 10^{-5} M solutions of $\mathbf{1}^{2+}$ and $\mathbf{2}^{2+}$ in CH_3CN. (b) Luminescence decay curves of the solution of $\mathbf{1}^{2+}$ recorded at 730 nm after excitation at 430 nm with laser pulses of ~10 ns duration. Measurements were performed in both deaerated and aerated CH_3CN. (c) Luminescence decay curve of the solution of $\mathbf{1}^{2+}$ recorded at 730 nm after excitation at 532 nm.

Table 2. Spectroscopic Properties of the Complexes in CH_3CN at 293 K

	λ_{abs}/nm (ε/10^{-3} M^{-1} cm^{-1})	λ_{em} /nm	τ/ ns[a]	ϕ_{em} /%
$\mathbf{1}^{2+}$	286 (74)	730	109	0.55
	398 (8.2)			
	435 (11)			
	492 (8.5)			
$\mathbf{2}^{2+}$	286 (71)	630	871	0.062
	424 (12)			
	448 (15)			
$[Ru(bpy)_3]^{2+}$ [b]	286 (80)	620	831	9.5
	424 (10)			
	450 (12)			

[a] In deaerated CH_3CN. [b] From ref 23.

aerated CH_3CN shows a shorter lifetime of τ = 84 ns due to quenching by O_2, suggesting that the emission originates from a ^{3}MLCT state. The luminescence quantum yields are ϕ = 0.55% and 0.36% for excitation at 430 and 500 nm, respectively; both values are lower than for $[Ru(bpy)_3]^{2+}$ by an order of magnitude (Table 2). This finding might be associated with the remarkable red shift of the emission band. UV−vis spectra of the solutions of $\mathbf{1}^{2+}$ recorded after the kinetic measurements are identical to the original ones, indicating that $\mathbf{1}^{2+}$ is photostable (Figure S13). In contrast, $\mathbf{2}^{2+}$ shows only a very weak emission with a maximum around 630 nm (Figure 3a). A biexponential decay was observed for its luminescence (Figure S14), indicating that the luminescence may originate from two different excited states or from two different compounds or conformers. The first component is instrumentally limited (<10 ns), while the second component is associated with a lifetime of ca. 800 ns. To test the photostability of $\mathbf{2}^{2+}$, irradiation experiments were conducted and both UV−vis spectra and luminescence decay curves were recorded at different times after illumination of a CH_3CN solution of $\mathbf{2}^{2+}$ with a 455 nm LED (Figure S15). In the UV−vis spectra, a clear change with increasing irradiation time is obvious. Interestingly, after 10 min irradiation, the resulting MLCT bands look very similar to those of known $[Ru(bpy)_2(CH_3CN)_2]^{2+}$;[24] an overlay of the UV−vis spectra (Figure S16) confirms that $[Ru(bpy)_2(CH_3CN)_2]^{2+}$ and free ^{S}bpy (identified by an intense absorption at 230 nm) are formed. These findings strongly suggest ^{S}bpy ligand dissociation from the metal center after excitation of $\mathbf{2}^{2+}$. To further corroborate the photoinduced ligand dissociation, two solutions containing $\mathbf{2}^{2+}$ in CD_3CN were treated with heat or light, respectively, and ^{1}H NMR spectra were recorded (Figure S17). No change was found after heating of $\mathbf{2}^{2+}$ at 70 °C overnight, indicating that $\mathbf{2}^{2+}$ is thermostable. In contrast, irradiation with a 440 nm LED over a period of 1 h leads to the appearance of ^{1}H NMR signals of $[Ru(bpy)_2(CH_3CN)_2]^{2+}$ and free ^{S}bpy. We attribute this to the bite angle enlargement of the $\{N,N'\}$-bidentate metal coordination site and, hence, to the reduced ligand field strength of ^{S}bpy in which the two pyridines are linked via a single S atom. This facilitates the thermally activated ^{3}MLCT−^{3}LF (LF = ligand field state) conversion and prompts the photoreaction (photosolvation).[25] In the luminescence decay curves, the long-lived (ca. 800 ns) component, which is attributed to the luminescence of $\mathbf{2}^{2+}$, disappears over time (Figure S15b and Table S1). Consequently, the instrumentally limited signal is attributed to the degradation product $[Ru(bpy)_2(CH_3CN)_2]^{2+}$. The quantum yield of $\mathbf{2}^{2+}$ is extremely low (0.062%).

To explore the decay characteristics of the emissive excited states of $\mathbf{1}^{2+}$ and to confirm their MLCT nature, transient UV−vis absorption spectroscopy was carried out. Figure 4 shows the transient absorption spectra averaged over a period of 200 ns immediately after excitation at 430 and 532 nm, respectively, with laser pulses of ca. 10 ns duration. A ground-state bleach is observed at 400 to 500 nm, in accordance with the lowest-energy ^{1}MLCT absorption bands in Figure 3a. In addition, excited-state absorption bands at 310 and 370 nm are observed, similar to the absorption bands observed for ^{3}MLCT-excited $[Ru(bpy)_3]^{2+}$. These signals arise from the π−π* transitions on the transiently reduced bpy ligand.[26] Switching the excitation wavelength from 532 to 430 nm gives an identical transient absorption spectrum. The MLCT bleach at 500 nm and the transient absorption signal at 370 nm both exhibit the same decay as the MLCT luminescence at 730 nm, confirming that signals from the same excited states are monitored by emission and transient absorption spectroscopy. The MLCT lifetime (τ) extractable from the transient absorption data is analogous to that obtained from emission data, and the absorption is also quenched by O_2, as shown in the bottom of Figure 4, in line with the findings in Figure 3b for emission. In the case of $\mathbf{2}^{2+}$, because of its photoinstability only low quality transient

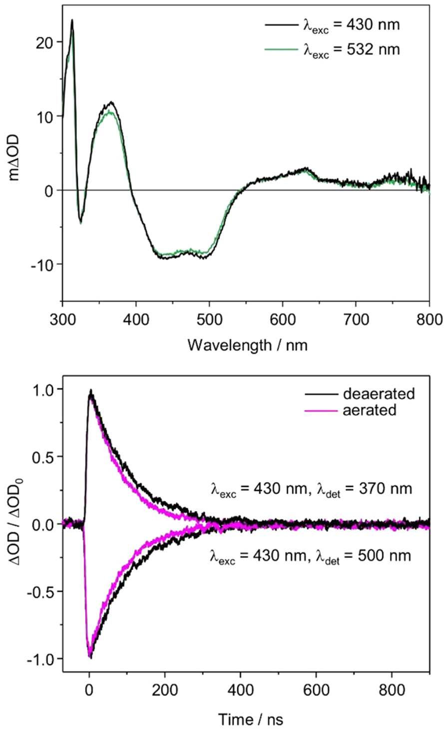

Figure 4. Top: transient absorption spectra measured after excitation of 10^{-5} M solutions of $\mathbf{1}^{2+}$ in deaerated CH_3CN at 430 (black) and 532 nm (green) with laser pulses of ~10 ns duration. The signals were time integrated over 200 ns immediately after excitation. Bottom: transient absorption decays recorded from deaerated and aerated CH_3CN solutions of $\mathbf{1}^{2+}$ at 370 nm and recoveries of the MLCT bleaches at 500 nm.

absorption spectra could be obtained (Figure S18); nevertheless, the bleach at 450 nm and a new signal at 390 nm are still observed.

Electrochemistry. To evaluate how the peripheral sulfuration of one bpy ligand impacts the electronic properties of the Ru^{II} complexes, detailed electrochemical studies on $\mathbf{1}^{2+}$ and $\mathbf{2}^{2+}$ were performed. A glassy carbon working electrode was used, and all data were referenced versus the internal standard $Fc^{+/0}$. The cyclic voltammetry (CV) data of $\mathbf{1}^{2+}$ and $\mathbf{2}^{2+}$ were recorded at 298 K in dry CH_3CN containing 0.2 M $^nBu_4NPF_6$. Both complexes show a reversible redox couple at $E^{1/2}$ = +0.96 ($\mathbf{1}^{2+}$) and +0.93 V ($\mathbf{2}^{2+}$), which is assigned to the Ru$^{II/III}$ oxidation (Table 3 and Figure S20) and is very similar to the value for parent $[Ru(bpy)_3]^{2+}$,[21] indicating that the peripheral sulfuration exerts only a marginal effect on the central metal ion.

The CV data of $\mathbf{2}^{2+}$ show reversible redox couples at $E^{1/2}$ = −1.70, − 1.89, and −2.13 V (Figure 5 and Table 3). The peak potentials do not shift with increasing scan rate, and the peak-to-peak separation is close to the Nernstian value for a reversible redox process (Figure S21 shows scan rate dependent data). The potentials are almost identical to those of $[Ru(bpy)_3]^{2+}$, indicative of consecutive ligand centered reductions.[21] This suggests that ^{S}bpy serves as a one electron acceptor, and the introduction of one sulfur atom does not significantly alter the electronic nature of the bpy ligand.

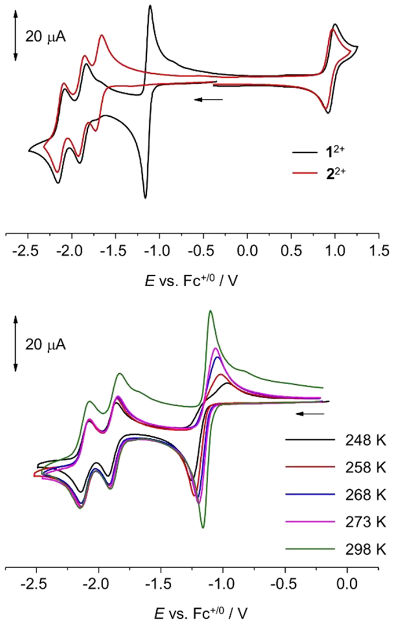

Figure 5. Top: CV data of $\mathbf{1}^{2+}$ and $\mathbf{2}^{2+}$ at RT. Bottom: temperature-dependent CV data of $\mathbf{1}^{2+}$; CH_3CN, 0.2 M $^nBu_4NPF_6$, ν = 0.1 V s^{-1}.

In stark contrast, the first reduction peak for $\mathbf{1}^{2+}$ shows a remarkable anodic shift to E_{pc} = −1.16 V (ν = 0.1 V s^{-1}), whereas the formal potentials of the second and third reduction events are very similar to the corresponding ones in $\mathbf{2}^{2+}$ and parent $[Ru(bpy)_3]^{2+}$. This suggests a $^{S-S}$bpy-centered reduction in the first process and bipyridine-centered reductions in the latter ones. The large current of the first reduction wave in the forward scan indicates that the process is actually a $2e^-$ event, as was also observed for the free $^{S-S}$bpy ligand.[5] Indeed, estimation of the number of transferred electrons according to the Randles−Sevcik equation leads to ~1.6 electrons for the first reduction process (Figure S22). This indicates that reduction of $\mathbf{1}^{2+}$ yields $\mathbf{1}$ in which two adjacent thiolates are present. The peak potentials of the cathodic and anodic events for $\mathbf{1}^{2+}$ around −1.1 V largely shift with increasing scan rate, and the large peak separation of the anodic and cathodic waves indicate that it is not a Nernstian $2e^-$ event (Figure S23, Table S2). Similar ruthenium and osmium complexes with RO^- functionalities instead of RS^-, i.e., [2,2′-bipyridine]-3,3′-bis(olate) instead of [2,2′-bipyridine]-3,3′-bis(thiolate), have been shown to be prone for protonation,[27] and thus, we investigated whether the $2e^-$ reduction is coupled to proton transfer, e.g., due to traces of water. UV−vis-spectroelectrochemical (UV−vis-SEC) reduction of $\mathbf{1}^{2+}$ at −35 °C leads to a new species with a pronounced absorption at 350 nm and visible bands at 440 and 500 nm (Figure S31). The redox process is fully reversible as the original UV−vis spectra are recovered after reoxidation. The same experiment at −35 °C in the presence of 1 equiv of [Hdmf](OTf) leads to a reduced species with distinctly different absorption properties, namely, the species exhibits two bands at 440 and 470 nm and lacks the band at 350 nm (Figure S32). The process is also fully reversible as reoxidation establishes $\mathbf{1}^{2+}$. This suggests that reduction in the former experiment is not coupled to a proton transfer, as protonation is typically associated with a blue shift of the MLCT bands in

Table 3. Half Peak Potentials ($E^{1/2}$) and Peak Potentials (E_p) at 0.1 Vs^{-1} for 1^{2+}, 2^{2+}, and $[Ru(bpy)_3]^{2+}$ in Acetonitrile at 298 K[a]

	ligand reduction and Ru oxidation					
	$E_{pc,1}$	$E_{pa,1}$	$E_1^{1/2}$	$E_2^{1/2}$	$E_3^{1/2}$	$E_4^{1/2}$
$1^{2+}{}_{298\ K}$	−1.16	−1.10		−1.87 (74)	−2.11 (80)	+0.96 (76)
$2^{2+}{}_{298\ K}$			−1.70 (69)	−1.89 (71)	−2.13 (73)	+0.93 (73)
$[Ru(bpy)_3]^{2+}$ [b]			−1.66	−1.86	−2.11	+0.94

[a] Values in V vs $Fc^{+/0}$. Peak separation in mV is given in parentheses. [b] From ref 21.

the visible region and of the IL (intra ligand) band at 350 nm in **1** since bpy(SH)(S^-) is a weaker CT acceptor than bpy$(S^-)_2$.[28] Chemical reduction with 2 equiv of cobaltocene[29] leads to the same species as electrochemical reduction, and the addition of two equivalents of the strong base 1,8-diazabicyclo[5.4.0]undec-7-en (pK_a = 24.34 in CH_3CN)[30] does not lead to any changes in the UV−vis spectra, whereas addition of 1 equiv of [Hdmf](OTf) results in the same species as in the electrochemical experiment in the presence of protons (Figure S19). These experiments suggest that reduction in anhydrous CH_3CN in the absence of added proton source is not coupled to proton transfer and that a neutral species **1** with a dianionic bpy$(S^-)_2$ ligand is obtained after two-electron reduction in CH_3CN (Scheme 2).

Scheme 2. $2e^-$ Reduction of Disulfide Complex 1^{2+} to Give Dithiolate Complex 1 and Subsequent Conversion to 2^{2+}[a]

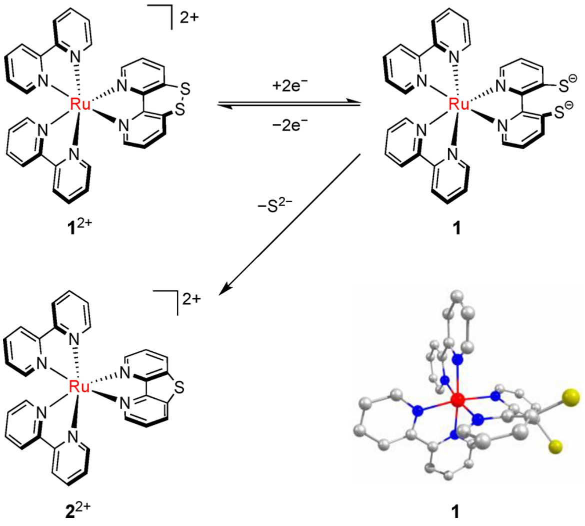

[a] The DFT optimized structure of **1** is shown in the lower right (red, Ru; blue, N; yellow, S; grey, C; see SI for details).

In the CV trace of 1^{2+}, after initial reduction, a small oxidation peak appears in the reverse scan at −1.70 V at slow scan rates, e.g., < 0.1 V s^{-1}. The peak potential matches the one for the anodic feature in the reverse scan after the first reduction of 2^{2+}, which suggests that 1^{2+} transforms into 2^{2+} under reductive conditions (Scheme 2). Indeed, coulometry at an applied potential of −1.25 V leads to full conversion of 1^{2+} into 2^{2+} (Figure S24). Such facile elimination of one sulfur atom from a disulfide moiety was previously observed for diaromatic disulfide compounds, where the decomposition of the disulfide bridge is triggered by heating.[6b] Our previous study of free $^{S-S}$bpy revealed that S−S bond breaking and rotation around the central C−C bond of the bipyridine unit occurs after the second reduction step.[5] However, as the $^{S-S}$bpy ligand coordinates to the metal ion, rotation of the two pyridine units upon injecting the electrons is restricted in 1^{2+}. Thus, the accumulation of negative charges in close proximity in combination with the nucleophilic character of thiolates might induce the elimination of a sulfide ion. The CV feature attributed to 2^{2+} vanishes upon increasing the scan rates (ν > 0.5 V s^{-1}, see Figure S23), indicating that the chemical reaction rate constant for sulfide extrusion is on the order of 0.05 s^{-1}.

In order to slow down the transformation of the $^{S-S}$bpy into the ^{S}bpy ligand upon reduction of 1^{2+}, CV data were recorded at lower temperatures (Figure S26). Below 273 K, no decomposition was observed on the time scale of the experiment at 0.1 V s^{-1}. However, the oxidative features of the initial $2e^-$ reduction process change significantly with decreasing temperature, most strikingly in the reverse scan. As temperature decreases, the cathodic peak potential shifts to more negative potentials, while the anodic peak broadens and shifts to higher potentials; thus, the peak-to-peak separation increases (Figure 5, bottom). These findings can be attributed to slower electron-transfer rates at lower temperatures. Therefore, simulation of the CV data was pursued to extract thermodynamic and kinetic information.

The four reduction processes of 1^{2+} were simulated utilizing CV data over a large scan rate range from 0.1 to 10 V s^{-1}, applying a Butler−Volmer model.[31] Representative experimental data and fits are presented in Figure 6. Further figures showing the other scan rates at various temperatures can be found in the Supporting Information (Figure S28).

Good simulations were achieved using reasonable values for the various parameters over the full sweep rate range (Table 4). The large cathodic current and the rather broad reverse peak of the first feature, reflected by the i_{pc} over i_{pa} ratio, indicates an α value above 0.5; α for E_1 and E_2 were set to 0.7. The steep slope of the first process indicates potential inversion, meaning that the initial reduction facilitates the subsequent reduction process.[32] Indeed, on the basis of the simulations, the potential of the second reduction process is always less negative than the potential of the first process, irrespective of the temperature (Table 4). In free $^{S-S}$bpy, the second reduction appeared at lower potentials than the first one (cf. E_1 = −1.20 V and E_2 = −1.38 V).[5] Given that $^{S-S}$bpy is bound to a positively charged metal ion in 1^{2+}, the formal potential of the initial redox process is slightly higher than in free $^{S-S}$bpy. However, the geometric constraints after reduction of 1^{2+} are much larger in comparison to free $^{S-S}$bpy as the two pyridine units cannot rotate freely around the central C−C axis. Nevertheless, such a redox-triggered structural variation could facilitate the potential compression, as was reported for some *N*-aryl expanded pyridinium electrophores.[33]

Redox potentials may change with varying temperatures.[34] Since ΔG equals $-n{\cdot}F{\cdot}E$, the change in the redox potential can

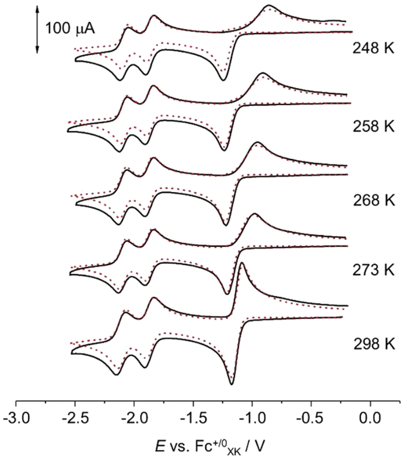

Figure 6. Experimental (black lines) and simulated (red dashed lines) CV data of $\mathbf{1}^{2+}$ in CH_3CN at various temperatures, representative scan rate of 1 V s^{-1}, $[\mathbf{1}^{2+}]$ = 0.98 mM, 0.2 M $^{n}Bu_4NPF_6$; parameters: see Table 4.

be related to change in entropy and enthalpy (n = number of electrons, F = Faraday constant). These changes can be calculated from the slope $\partial E/\partial T$ as ΔS equals $-(\partial G/\partial T)_p$ and ΔH equals $nF(T(\partial E/\partial T)_p - E)$.[35] However, since we determined E'^0 versus the formal redox couple of ferrocene at the respective temperature, the experimentally observed potential shifts include the temperature dependence of the $Fc^{+/0}$ couple, too. Thus, we corrected the potentials accordingly from temperature-dependent CV measurements of ferrocene (see the Supporting Information).[36] A decrease of temperature has virtually no influence on the redox potential of the reversible reduction processes E_3 and E_4 of $\mathbf{1}^{2+}$. The potentials E_4 remain constant within a standard deviation of ±3 mV and the ones of E_3 within about ±7 mV standard deviation. The same is observed for E_1 and E_2, although the standard deviation is slightly larger for E_1, namely, ±10 mV, and ±6 mV for E_2. However, none of the potentials follows a clear trend, which indicates that the changes in entropy and enthalpy upon reduction are likely small (Figure S29).

Subsequently, we had a closer look at the kinetics of the reductive electron-transfer processes. Electron-transfer rates for the first and the second reduction process, E_1 and E_2, strongly depend on the temperature. At 248 K, the processes are both quasi-reversible, i.e., $k_{s,1} = 4 \times 10^{-4}$ cm s^{-1} and $k_{s,2} = 1.5 \times 10^{-3}$ cm s^{-1}, whereas at 298 K both processes are reversible, i.e., $k_{s,1}$ = 0.02 cm s^{-1} and $k_{s,2}$ = 0.07 cm s^{-1} (Table 4). From the Arrhenius plot of E_1 and E_2, i.e., $\ln(k_s)$ vs $1/T$, the activation energy and the pre-exponential factor A are estimated (Figure 7).[37] The plot reveals very similar activation

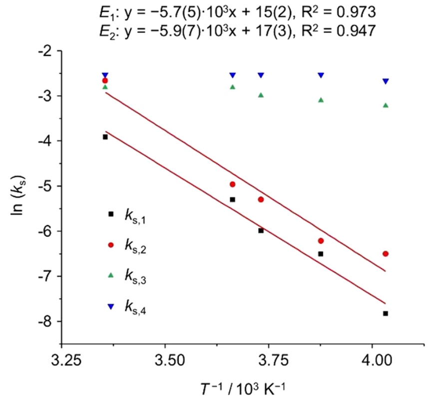

Figure 7. Arrhenius plot for the four sequential electron-transfer rates of $\mathbf{1}^{2+}$ in the temperature range from −25 to +25 °C. The red lines represent the linear fits.

Table 4. Thermodynamic and Kinetic Parameters Obtained from the Simulations of the CV Data for $\mathbf{1}^{2+}$ at Various Temperatures.[a]

T (K)		E_1	E_2	E_3	E_4
248	E'^0 vs $Fc^{+/0}{}_{248\ K}$ (V)	−1.120	−1.065	−1.865	−2.080
	E'^0 vs $Fc^{+/0}{}_{RT}$ (V)	−1.140	−1.085	−1.885	−2.100
	k_s (cm s^{-1})	4×10^{-4}	1.5×10^{-3}	0.04	0.07
	α	0.7	0.7	0.5	0.5
258	$E'^{0'0}$ vs $Fc^{+/0}{}_{258\ K}$ (V)	−1.140	−1.080	−1.865	−2.085
	E'^0 vs $Fc^{+/0}{}_{RT}$ (V)	−1.160	−1.100	−1.885	−2.105
	k_s (cm s^{-1})	0.0015	0.002	0.045	0.08
	α	0.7	0.7	0.5	0.5
268	E'^0 vs $Fc^{+/0}{}_{268\ K}$ (V)	−1.145	−1.075	−1.870	−2.095
	E'^0 vs $Fc^{+/0}{}_{RT}$ (V)	−1.160	−1.090	−1.885	−2.110
	k_s (cm s^{-1})	0.0025	0.005	0.05	0.08
	α	0.7	0.7	0.5	0.5
273	E'^0 vs $Fc^{+/0}{}_{273\ K}$ (V)	−1.155	−1.080	−1.870	−2.095
	E'^0 vs $Fc^{+/0}{}_{RT}$ (V)	−1.165	−1.090	−1.880	−2.105
	k_s (cm s^{-1})	0.005	0.007	0.06	0.08
	α	0.7	0.7	0.5	0.5
298	E'^0 vs $Fc^{+/0}{}_{298\ K}$ (V)	−1.145	−1.100	−1.865	−2.105
	k_s (cm s^{-1})	0.02	0.07	0.06	0.08
	α	0.7	0.7	0.5	0.5

[a] E vs. $Fc^{+/0}{}_{XK}$ denotes the formal redox potential versus the potential of $Fc^{+/0}$ at the respective temperature X, and E vs. $Fc^{+/0}{}_{RT}$ versus the potential of $Fc^{+/0}$ at 298 K. The values of E were set with an accuracy of ±5 mV.

energies for both reduction processes, namely, 47 and 49 kcal mol^{-1} for E_1 and E_2, respectively (Table 5). The pre-exponential factors A for $\mathbf{1}^{2+}$ are about 2 orders of magnitude larger than expected for outer sphere adiabatic electron-transfer reactions according to Marcus−Hush theory.[38] This suggests a contribution of the inner sphere reorganization energy to A; that is, tilting of the ligand as well as elongation of the S−S bond and finally bond rupture, since a bond rupture coupled to the electron-transfer processes leads to higher frequency factors. Indeed, the DFT optimized structure of **1** (Scheme 2) reveals an increase of the C−S1−S2−C torsion angle from 56.71° to 79.62° upon two-electron reduction of $\mathbf{1}^{2+}$, concomitant with lengthening of the S···S distance to 3.56 Å (2.05 Å in $\mathbf{1}^{2+}$). The pre-exponential factors are similar, which points to a rather smooth tilting of the ligand and S···S bond elongation over the two reduction processes. The electron-transfer rate of the third reduction process, E_3, indicates a reversible process over the entire temperature range; though, it depends slightly on the temperature (Figure S30). However, these small changes are within the error margins, and linearization of the data leads to low correlation and large errors for the slope and the intercept. The electron-transfer rate of the fourth reduction process, E_4, which is related to one of the bipyridine ligands, is essentially independent of temperature. The transfer rate of 0.08 cm s^{-1} is characteristic for a reversible process.

Table 5. Activation Energies and Pre-exponential Factors for the Electron-Transfer Processes of $\mathbf{1}^{2+}$ According to the Arrhenius Equation.[38]

	E_a/kJ mol^{-1}	A/cm s^{-1}
E_1	47 (4)	3.9 (0.3) × 10^6
E_2	49 (6)	1.9 (0.3) × 10^7

DFT Calculations of Electronic Excitations. The optical absorption properties of $\mathbf{1}^{2+}$ and $\mathbf{2}^{2+}$ have been further characterized with the help of DFT/TD-DFT computations. As a validation of the computational method, we rely on the reasonably good agreement (RMSD = 0.263 Å) of the optimized geometries of both complexes with respect to X-ray diffraction data (see relevant geometrical parameters in Table 1). Note however, a slight but systematic elongation of the Ru−N bonds by 0.03−0.05 Å in the calculated structures of both complexes. Additionally, the optimized geometries reveal that the two pyridine rings of the parent bpy ligands are perfectly coplanar, whereas they are slightly tilted toward each other in the crystallographically determined structures. Notably, the calculated disulfide S−S bond length in $\mathbf{1}^{2+}$ is 2.106 Å, about 0.05 Å longer than that in the crystal structure, while the calculated torsion angle C−S1−S2−C is well reproduced. The Cartesian coordinates of the DFT optimized structures of $\mathbf{1}^{2+}$ and $\mathbf{2}^{2+}$ are given in the Supporting Information.

The electronic excited states calculated at the optimized geometries of $\mathbf{1}^{2+}$ and $\mathbf{2}^{2+}$ are listed in Table 6. For $\mathbf{1}^{2+}$, there are two states with large oscillator strengths, S_3 and S_9, at 2.64 eV (470 nm) and 3.04 eV (408 nm), respectively. Interestingly, these excited states are representative of two blocks of excitations localized at different ligands; while S_3 is primarily an excitation from the Ru center toward the $^{S-S}$bpy ligand (MSCT), S_9 is composed of two MLCT contributions originating from charge transfer from the Ru center to both bpy ligands (shown as NTOs in Figure 8). Such electronic structure offers an interesting opportunity for steering the direction of electron transfer at low or high excitation energies, either to the disulfide bridged $^{S-S}$bpy or toward one (or both) of the unsubstituted bpy ligands, respectively. Charge transfer from any of the ligands toward the metal is found to be unlikely.

Table 6. Calculated Excited States of $\mathbf{1}^{2+}$ and $\mathbf{2}^{2+}$

	$\mathbf{1}^{2+}$		
	ΔE (eV)	$f_{osc.}$ (a.u.)	character
S_1	2.31	0.001	MSCT
S_2	2.50	0.002	MSCT
S_3	2.64	0.103	MSCT
S_4	2.64	0.011	SC
S_5	2.72	0.004	MLCT
S_6	2.72	0.001	MLCT
S_7	2.93	0.008	MLCT
S_8	2.97	0.005	MLCT
S_9	3.04	0.125	MLCT
S_{10}	3.20	0.033	MLCT
	$\mathbf{2}^{2+}$		
	ΔE (eV)	$f_{osc.}$ (a.u.)	character
S_1	2.69	0.000	MSCT
S_2	2.72	0.002	MLCT
S_3	2.73	0.001	MLCT
S_4	2.88	0.003	MLCT
S_5	2.89	0.035	MLCT
S_6	2.90	0.006	MLCT/MSCT
S_7	2.98	0.104	MSCT/MLCT
S_8	3.03	0.134	MLCT
S_9	3.22	0.002	MLCT
S_{10}	3.54	0.001	MC

A more realistic description of the lowest-energy band of both absorption spectra is obtained by including nuclear vibrational motion via a harmonic Wigner ensemble of 200 geometries. As shown in Figure 9a,b, the calculated spectra are in excellent agreement with the experimental ones. Both spectra have been decomposed into contributions from the different types of excitations. The experimental absorption spectrum of $\mathbf{1}^{2+}$ shows a peak at 435 nm with a low-energy shoulder below 500 nm. The decomposition of the spectrum reveals that the high-energy peak is dominated by charge-transfer processes toward the bpy ligands (MLCT), while the low-energy shoulder mainly originates from charge transfer toward the $^{S-S}$bpy (denoted MSCT), with only minor contributions from MLCT processes. These results reinforce the interpretation based on the optimized geometry that the ability to stabilize the electron at the $^{S-S}$bpy ligand results in a red shift of the corresponding states, leading to the observed shoulder in the experimental absorption spectrum. The energetic separation of excitations toward the $^{S-S}$bpy or bpy ligands (MSCT and MLCT) holds upon including vibrational sampling. When comparing the position of the calculated absorption maxima with the excitation energies of the two states with large oscillator strengths at the optimized geometry, a red shift of about 20 nm is observed. In passing, we note that the low-energy MSCT shoulder at 500 nm is only present due to the solvent, as calculations in the gas phase (not shown) place the contribution of the MSCT states blue-shifted to 460

https://dx.doi.org/10.1021/acs.inorgchem.0c00220
Inorg. Chem. 2020, 59, 4972−4984

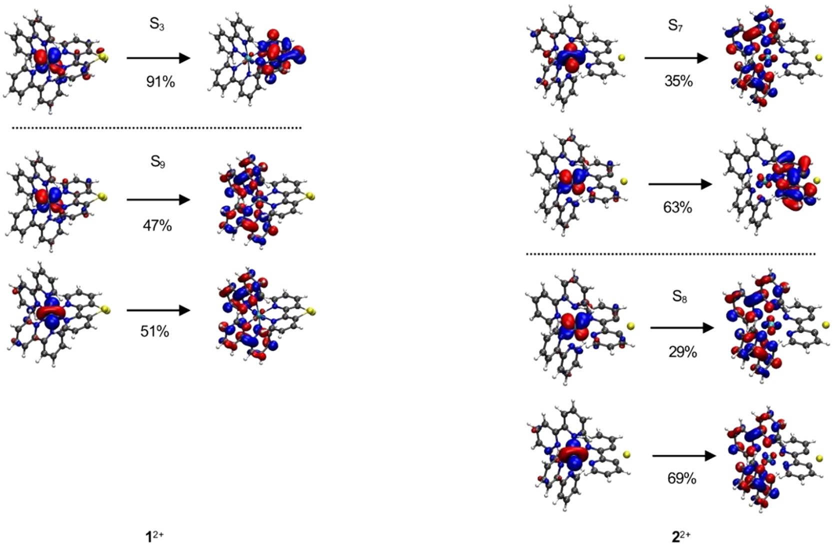

Figure 8. NTOs of the two states with large oscillator strengths S_3 and S_9 of $\mathbf{1}^{2+}$ and S_7 and S_8 of $\mathbf{2}^{2+}$. The contribution of the transition to the excited state is given below the corresponding arrow.

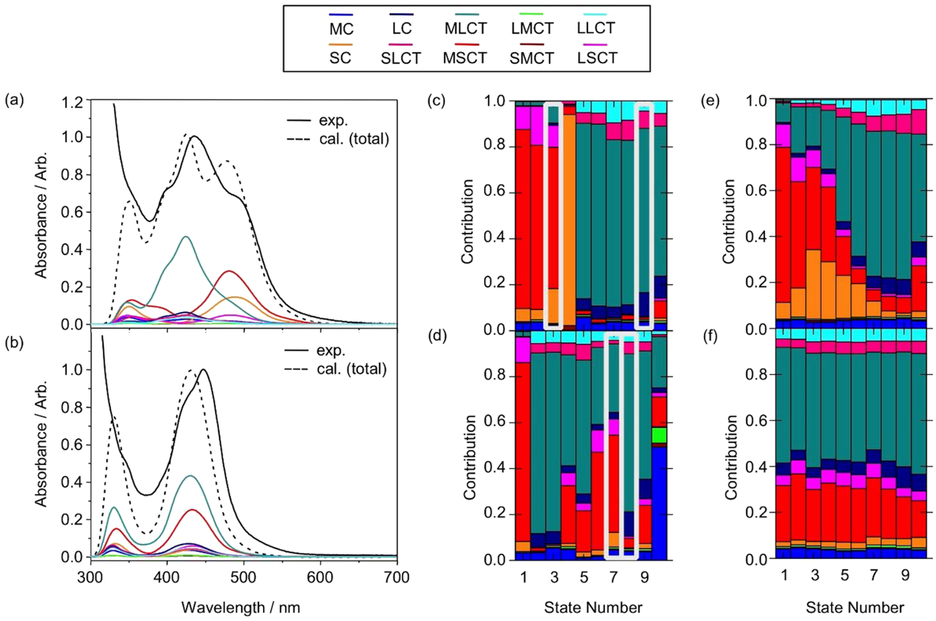

Figure 9. Calculated absorption spectra of $\mathbf{1}^{2+}$ (a) and $\mathbf{2}^{2+}$ (b) based on a harmonic Wigner ensemble. The spectra are decomposed into the different contributions to the absorbing states. Panels (c) and (d) show bar histograms of the different character contribution of each electronic singlet state at the optimized geometry based on charge-transfer numbers (see also Table 6). Gray boxes indicate states with large oscillator strengths. Panels (e) and (f) show the averaged charge-transfer character obtained from the Wigner ensemble. Color codes for the different types of excitations are given in the top part of the figure.

nm, strongly overlapping with the MLCT band, which is unshifted.

The experimental spectrum of $\mathbf{2}^{2+}$ exhibits two maxima in close proximity within the MLCT region. The calculated absorption maximum is slightly blue-shifted with respect to the experimental absorption peak. Decomposition of the spectrum indicates that excitations from the Ru center toward all three ligands contribute equally to the absorption. Similar to $\mathbf{1}^{2+}$, a red shift of the absorption maxima with respect to the excitation energies of the bright states is observed.

The character of the first low-lying ten excited states of $\mathbf{1}^{2+}$ (panels c and e) and $\mathbf{2}^{2+}$ (panels d and f) at the optimized geometry and within the average ensemble including nuclear motion, respectively, is shown in Figure 9. The separation between the low-lying excitations located at the $^{S-S}$bpy ligand from the other MLCT states that follow at higher energies is evident at the optimized geometry of $\mathbf{1}^{2+}$ (panel c), while no clear separation is visible for $\mathbf{2}^{2+}$ (panel d). The inclusion of nuclear motion (panels e and f) entails mixing of MSCT and MLCT characters, highlighting the importance of the vibrational zero-point energy. However, one can appreciate a dominance of the MSCT band at lower energies and MLCT at high energies in $\mathbf{1}^{2+}$ (panel e), while MSCT and MLCT completely overlap in $\mathbf{2}^{2+}$ (panel f).

■ CONCLUSION

In summary, we have presented here a new $[\mathrm{Ru(bpy)_3}]^{2+}$-type photosensitizer $\mathbf{1}^{2+}$ equipped with a disulfide bridge at the backside of one bipyridine ligand. An important feature is that the $^{\mathrm{S-S}}$bpy ligand can serve as a two-electron acceptor associated with the disulfide/ditholate redox pair. From thorough electrochemical characterization of $\mathbf{1}^{2+}$ in combination with simulation of the CV traces, it can be concluded that the $^{\mathrm{S-S}}$bpy ligand is reduced first and at much less negative potentials than the parent bpy ligands, and that it undergoes a two-electron reduction with potential inversion; the electron transfer is kinetically controlled. The activation energies for both reduction processes are almost identical, indicating a smooth transition for the uptake of two electrons. Furthermore, the reduction of $^{\mathrm{S-S}}$bpy at room temperature triggers ligand decomposition by S-extrusion, resulting in the rapid formation of $\mathbf{2}^{2+}$. This transformation can be suppressed on the CV time scale by lowering the temperature. Comparing the UV−vis spectra of $\mathbf{1}^{2+}$, $\mathbf{2}^{2+}$, and $[\mathrm{Ru(bpy)_3}]^{2+}$ reveals that $\mathbf{1}^{2+}$ features an additional low-energy absorption in the MLCT region at around 500 nm. TD-DFT calculations show that the presence of the disulfide substituent in $\mathbf{1}^{2+}$ leads to a stabilization of charge-transfer excitations toward the $^{\mathrm{S-S}}$bpy ligand (MSCT). The splitting in energy between the absorption maxima of excitations toward the $^{\mathrm{S-S}}$bpy and the bpy ligands is about 2700 $\mathrm{cm^{-1}}$, offering the possibility of selectively exciting charge transfer into either of the two types of ligands. This could trigger different excited-state dynamics and opens up the road for targeted electron transfer. Such energy splitting between the different excitations is absent in $\mathbf{2}^{2+}$ where excitations toward the $^{\mathrm{S}}$bpy and bpy ligands are almost iso-energetic. While this distinct behavior starts to be apparent from the NTOs of the specific states of $\mathbf{1}^{2+}$ and $\mathbf{2}^{2+}$ calculated at the optimized geometry, the inclusion of vibrational nuclear motion clearly pinpoints the onset and end of the respective MSCT and MLCT bands, which in $\mathbf{1}^{2+}$ are energetically separated and in $\mathbf{2}^{2+}$ overlap. The MLCT luminescence of $\mathbf{1}^{2+}$ is phosphorescent in nature, with a lifetime of 109 ns. In contrast, $\mathbf{2}^{2+}$ is not photostable and irradiation of $\mathbf{2}^{2+}$ leads to dissociation of the $^{\mathrm{S}}$bpy ligand.

It should be noted here that the design principle of $\mathbf{1}^{2+}$ offers interesting prospects. First, this new $[\mathrm{Ru(bpy)_3}]^{2+}$ derivative $\mathbf{1}^{2+}$ is able to accommodate two electrons on the sulfurated bpy-type chelate ligand of the photosensitizer. After photoexcitation, this complex could potentially mediate two-electron two-proton conversions involving the peripheral disulfide/dithiol switch, which might enable novel excited-state PCET chemistry and light-driven multielectron transformations. Second, the peripheral disulfide/dithiol functionality of $^{\mathrm{S-S}}$bpy can be exploited for anchoring the $[\mathrm{Ru(bpy)_3}]^{2+}$ photosensitizers onto, e.g., gold surfaces, or for directly attaching it to catalytically active metal complexes. Work in both directions is ongoing in our laboratories.

■ ASSOCIATED CONTENT

Supporting Information

The Supporting Information is available free of charge at https://pubs.acs.org/doi/10.1021/acs.inorgchem.0c00220.

Figures of ESI-MS spectra, NMR spectra, IR spectra, UV−vis absorption and normalized photoluminescence spectra, luminescence decay curves, transient absorption spectra, CV data, redox couple plots, diffusion coefficients, temperature dependency, and optimized structures, tables of excited-state luminescence lifetimes, peak potentials, redox potentials, measured and calculated diffusion coefficients, and X-ray crystallographic data, and discussions of UV−vis experiments, Randles−Sevcik equation, temperature-dependent CV data, simulation of the CV data, X-ray crystallography, DFT calculations, and Cartesian coordinates (PDF)

Accession Codes

CCDC 1979158−1979159 contain the supplementary crystallographic data for this paper. These data can be obtained free of charge via www.ccdc.cam.ac.uk/data_request/cif, or by emailing data_request@ccdc.cam.ac.uk, or by contacting The Cambridge Crystallographic Data Centre, 12 Union Road, Cambridge CB2 1EZ, UK; fax: +44 1223 336033.

■ AUTHOR INFORMATION

Corresponding Authors

Inke Siewert − *University of Göttingen, Institute of Inorganic Chemistry, D-37077 Göttingen, Germany;* orcid.org/0000-0003-3121-3917; Email: inke.siewert@chemie.uni-goettingen.de

Leticia González − *Institute of Theoretical Chemistry, Faculty of Chemistry, University of Vienna, A-1090 Vienna, Austria;* orcid.org/0000-0001-5112-794X; Email: leticia.gonzalez@univie.ac.at

Franc Meyer − *University of Göttingen, Institute of Inorganic Chemistry, D-37077 Göttingen, Germany;* orcid.org/0000-0002-8613-7862; Email: franc.meyer@chemie.uni-goettingen.de

Authors

Shao-An Hua − *University of Göttingen, Institute of Inorganic Chemistry, D-37077 Göttingen, Germany*

Mauricio Cattaneo − *University of Göttingen, Institute of Inorganic Chemistry, D-37077 Göttingen, Germany*

Manuel Oelschlegel − *University of Göttingen, Institute of Inorganic Chemistry, D-37077 Göttingen, Germany*

Moritz Heindl − *Institute of Theoretical Chemistry, Faculty of Chemistry, University of Vienna, A-1090 Vienna, Austria*

Lucius Schmid − *Department of Chemistry, University of Basel, CH-4056 Basel, Switzerland*

Sebastian Dechert − *University of Göttingen, Institute of Inorganic Chemistry, D-37077 Göttingen, Germany*

Oliver S. Wenger − *Department of Chemistry, University of Basel, CH-4056 Basel, Switzerland;* orcid.org/0000-0002-0739-0553

Complete contact information is available at: https://pubs.acs.org/10.1021/acs.inorgchem.0c00220

Author Contributions

The manuscript was written through contributions of all authors.

Funding

F.M. and L.G. are grateful to the DFG for financial support of this work (projects Me1313/15-1 and Go1059/8-1 within the SPP 2102 "Light-Controlled Reactivity of Metal Complexes"). Initially this project was supported by the Alexander von Humboldt Foundation (postdoctoral fellowship for M.C.). O.S.W. acknowledges funding from the Swiss National Science Foundation through grant number 200021_178760.

Notes

The authors declare no competing financial interest.

ACKNOWLEDGMENTS

L.G. is grateful to the Göttingen Academy of Sciences for awarding a Gauss Professorship that allowed for an extended research stay in Göttingen. M.C. is member of the Research Career (CONICET, Argentina). L.G. also thanks the Vienna Scientific Cluster for allocation of computer time.

REFERENCES

(1) (a) Hammes-Schiffer, S. Theory of Proton-Coupled Electron Transfer in Energy Conversion Processes. *Acc. Chem. Res.* **2009**, *42*, 1881−1889. (b) Warren, J. J.; Tronic, T. A.; Mayer, J. M. Thermochemistry of Proton-Coupled Electron Transfer Reagents and Its Implications. *Chem. Rev.* **2010**, *110*, 6961−7001.

(2) (a) Gagliardi, C. J.; Westlake, B. C.; Kent, C. A.; Paul, J. J.; Papanikolas, J. M.; Meyer, T. J. Integrating Proton Coupled Electron Transfer (PCET) and Excited States. *Coord. Chem. Rev.* **2010**, *254*, 2459−2471. (b) Hammes-Schiffer, S. Proton-Coupled Electron Transfer: Moving Together and Charging Forward. *J. Am. Chem. Soc.* **2015**, *137*, 8860−8871. (c) Lennox, J. C.; Kurtz, D. A.; Huang, T.; Dempsey, J. L. Excited-State Proton-Coupled Electron Transfer: Different Avenues for Promoting Proton/Electron Movement with Solar Photons. *ACS Energy Lett.* **2017**, *2*, 1246−1256. (d) Pannwitz, A.; Wenger, O. S. Proton-coupled Multi-Electron Transfer and Its Relevance for Artificial Photo Synthesis and Photoredox Catalysis. *Chem. Commun.* **2019**, *55*, 4004−4014. (e) Wenger, O. S. Proton-Coupled Electron Transfer with Photoexcited Metal Complexes. *Acc. Chem. Res.* **2013**, *46*, 1517−1526. (f) Wenger, O. S. Proton-Coupled Electron Transfer with Photoexcited Ruthenium (II), Rhenium (I), and Iridium (III) Complexes. *Coord. Chem. Rev.* **2015**, *282*, 150−158.

(3) (a) Pellegrin, Y.; Odobel, F. Molecular Devices Featuring Sequential Photoinduced Charge Separations for the Storage of Multiple Redox Equivalents. *Coord. Chem. Rev.* **2011**, *255*, 2578−2593. (b) Hammarstrom, L. Accumulative Charge Separation for Solar Fuels Production: Coupling Light-Induced Single Electron Transfer to Multielectron Catalysis. *Acc. Chem. Res.* **2015**, *48*, 840−850. (c) Konduri, R.; Ye, H.; MacDonnell, F. M.; Serroni, S.; Campagna, S.; Rajeshwar, K. Ruthenium Photocatalysts Capable of Reversibly Storing up to Four Electrons in a Single Acceptor Ligand: A Step Closer to Artificial Photosynthesis. *Angew. Chem., Int. Ed.* **2002**, *41*, 3185−3187. (d) Konduri, R.; de Tacconi, N. R.; Rajeshwar, K.; MacDonnell, F. M. Multielectron Photoreduction of a Bridged Ruthenium Dimer,[(phen)$_2$Ru(tatpp) Ru(phen)$_2$][PF$_6$]$_4$: Aqueous Reactivity and Chemical and Spectroelectrochemical Identification of the Photoproducts. *J. Am. Chem. Soc.* **2004**, *126*, 11621−11629. (e) Chiorboli, C.; Fracasso, S.; Scandola, F.; Campagna, S.; Serroni, S.; Konduri, R.; MacDonnell, F. M. Primary Charge Separation in Photoinduced Multielectron Storage Systems. A Dinuclear Ruthenium (ii) Species Featuring a Charge-Separated State with a Lifetime of 1.3 μs. *Chem. Commun.* **2003**, 1658−1659.

(4) (a) Nomrowski, J.; Wenger, O. S. Exploiting Potential Inversion for Photoinduced Multielectron Transfer and Accumulation of Redox Equivalents in a Molecular Heptad. *J. Am. Chem. Soc.* **2018**, *140*, 5343−5346. (b) Kuss-Petermann, M.; Orazietti, M.; Neuburger, M.; Hamm, P.; Wenger, O. S. Intramolecular Light-Driven Accumulation of Reduction Equivalents by Proton-Coupled Electron Transfer. *J. Am. Chem. Soc.* **2017**, *139*, 5225−5232. (c) Mendes Marinho, S.; Ha-Thi, M. H.; Pham, V. T.; Quaranta, A.; Pino, T.; Lefumeux, C.; Chamaille, T.; Leibl, W.; Aukauloo, A. Time-Resolved Interception of Multiple-Charge Accumulation in a Sensitizer-Acceptor Dyad. *Angew. Chem., Int. Ed.* **2017**, *56*, 15936−15940. (d) Karlsson, S.; Boixel, J.; Pellegrin, Y.; Blart, E.; Becker, H. C.; Odobel, F.; Hammarstrom, L. Accumulative Charge Separation Inspired by Photosynthesis. *J. Am. Chem. Soc.* **2010**, *132*, 17977−17979. (e) O'Neil, M. P.; Niemczyk, M. P.; Svec, W. A.; Gosztola, D.; Gaines, G. L.; Wasielewski, M. R. Picosecond Optical Switching based on Biphotonic Excitation of an Electron Donor-Acceptor-Donor Molecule. *Science* **1992**, *257*, 63−65. (f) Orazietti, M.; Kuss-Petermann, M.; Hamm, P.; Wenger, O. S. Light-Driven Electron Accumulation in a Molecular Pentad. *Angew. Chem., Int. Ed.* **2016**, *55*, 9407−9410.

(5) Cattaneo, M.; Schiewer, C. E.; Schober, A.; Dechert, S.; Siewert, I.; Meyer, F. 2,2′-Bipyridine Equipped with a Disulfide/Dithiol Switch for Coupled Two-Electron and Two-Proton Transfer. *Chem. - Eur. J.* **2018**, *24*, 4864−4870.

(6) (a) Hall, G. B.; Kottani, R.; Felton, G. A.; Yamamoto, T.; Evans, D. H.; Glass, R. S.; Lichtenberger, D. L. Intramolecular Electron Transfer in Bipyridinium Disulfides. *J. Am. Chem. Soc.* **2014**, *136*, 4012−4018. (b) Benniston, A. C.; Hagon, J.; He, X.; Yang, S.; Harrington, R. W. Spring Open Two-Plus-Two Electron Storage in a Disulfide-Strapped Methyl Viologen Derivative. *Org. Lett.* **2012**, *14*, 506−509. (c) Benniston, A. C.; Allen, B. D.; Harriman, A.; Llarena, I.; Rostron, J. P.; Stewart, B. Accessing Molecular Memoryvia a Disulfide Switch. *New J. Chem.* **2009**, *33*, 417−427. (d) Nomrowski, J.; Guo, X.; Wenger, O. S. Charge Accumulation and Multi-Electron Photoredox Chemistry with a Sensitizer-Catalyst-Sensitizer Triad. *Chem. - Eur. J.* **2018**, *24*, 14084−14087.

(7) Al-Rawashdeh, N. A.; Chatterjee, S.; Krause, J. A.; Connick, W. B. Ruthenium Bis-Diimine Complexes with a Chelating Thioether Ligand: Delineating 1,10-Phenanthrolinyl and 2,2′-Bipyridyl Ligand Substituent Effects. *Inorg. Chem.* **2014**, *53*, 294−307.

(8) Favier, I.; Duñach, E. New Protic Salts of Aprotic Polar Solvents. *Tetrahedron Lett.* **2004**, *45*, 3393−3395.

(9) (a) Becke, A. Density-Functional Thermochemistry: The Role of Extract Exchange. *J. Chem. Phys.* **1993**, *98*, 5648−5652. (b) Lee, C.; Yang, W.; Parr, R. G. Development of the Colle-Salvetti Correlation-Energy Formula into a Functional of the Electron Density. *Phys. Rev. B: Condens. Matter Mater. Phys.* **1988**, *37*, 785.

(10) Hay, P. J.; Wadt, W. R. Ab Initio Effective Core Potentials for Molecular Calculations. Potentials for the Transition Metal StomsSc to Hg. *J. Chem. Phys.* **1985**, *82*, 270−283.

(11) Grimme, S.; Antony, J.; Ehrlich, S.; Krieg, H. A Consistent and Accurate Ab Initio Parametrization of Density Functional Dispersion Correction (DFT-D) for the 94 Elements H-Pu. *J. Chem. Phys.* **2010**, *132*, 154104.

(12) Hess, B. A. Relativistic Electronic-Structure Calculations Employing a Two-Component No-Pair Formalism with External-Field Projection Operators. *Phys. Rev. A: At., Mol., Opt. Phys.* **1986**, *33*, 3742.

(13) Cances, E.; Mennucci, B.; Tomasi, J. A New Integral Equation Formalism for the Polarizable Continuum Model: Theoretical Background and Applications to Isotropic and Anisotropic Dielectrics. *J. Chem. Phys.* **1997**, *107*, 3032−3041.

(14) (a) Casida, M. E.; Jamorski, C.; Casida, K. C.; Salahub, D. R. Molecular Excitation Energies to High-Lying Bound States from Time-Dependent Density-Functional Response Theory: Characterization and Correction of the Time-Dependent Local Density Approximation Ionization Threshold. *J. Chem. Phys.* **1998**, *108*, 4439−4449. (b) Runge, E.; Gross, E. K. Density-Functional Theory for Time-Dependent Systems. *Phys. Rev. Lett.* **1984**, *52*, 997.

(15) Martin, R. L. Natural Transition Orbitals. *J. Chem. Phys.* **2003**, *118*, 4775−4777.

(16) Frisch, M. J.; Trucks, G.; Schlegel, H.; Scuseria, G.; Robb, M.; Cheeseman, J.; Scalmani, G.; Barone, V.; Mennucci, B.; Petersson, G. et al. *Gaussian 09 Revision D.01*; Gaussian. Inc.: Wallingford, CT, 2009.

(17) Crespo-Otero, R.; Barbatti, M. Spectrum Simulation and Decomposition with Nuclear Ensemble: Formal Derivation and Application to Benzene, Furan and 2-Phenylfuran. *Theor. Chem. Acc.* **2012**, *131*, 1237.

(18) Mai, S.; Plasser, F.; Dorn, J.; Fumanal, M.; Daniel, C.; Gonzalez, L. Quantitative Wave Function Analysis for Excited States of Transition Metal Complexes. *Coord. Chem. Rev.* **2018**, *361*, 74−97.

(19) Plasser, F. Theo DORE: APackage for Theoretical Density, Orbital Relaxation, and Exciton Analysis. Available at http://theodore-qc.sourceforge.net/.

(20) Klemm, L.; McCoy, D.; Klopfenstein, C. Condensed Thiophenes from Sulfur Bridging. II. Catalyzed Reaction of Azabiaryls with Hydrogen Sulfide. *J. Heterocycl. Chem.* **1971**, *8*, 383−389.

(21) Heuer, W. B.; Xia, H. L.; Ward, W.; Zhou, Z.; Pearson, W. H.; Siegler, M. A.; NarducciSarjeant, A. A.; Abrahamsson, M.; Meyer, G. J. New Dicarboxylic Acid BipyridineLigand for Ruthenium PolypyridylSensitization of TiO_2. *Inorg. Chem.* **2012**, *51*, 3981−3988.

(22) Leigh, V.; Ghattas, W.; Lalrempuia, R.; Muller-Bunz, H.; Pryce, M. T.; Albrecht, M. Synthesis, Photo-, and Electrochemistry of Ruthenium Bis(bipyridine) Complexes Comprising a N-heterocyclic carbene Ligand. *Inorg. Chem.* **2013**, *52*, 5395−5402.

(23) (a) Ashford, D. L.; Glasson, C. R.; Norris, M. R.; Concepcion, J. J.; Keinan, S.; Brennaman, M. K.; Templeton, J. L.; Meyer, T. J. Controlling Ground and Excited State Properties Through Ligand Changes in Ruthenium Polypyridyl complexes. *Inorg. Chem.* **2014**, *53*, 5637−5646. (b) Suzuki, K.; Kobayashi, A.; Kaneko, S.; Takehira, K.; Yoshihara, T.; Ishida, H.; Shiina, Y.; Oishi, S.; Tobita, S. Reevaluation of Absolute Luminescence Quantum Yields of Standard Solutions Using a Spectrometer with an Integrating Sphere and a Back-Thinned CCD Detector. *Phys. Chem. Chem. Phys.* **2009**, *11*, 9850−9860.

(24) (a) Rapp, T. L.; Phillips, S. R.; Dmochowski, I. J. Kinetics and Photochemistry of Ruthenium Bisbipyridine Diacetonitrile Complexes: An Interdisciplinary Inorganic and Physical Chemistry Laboratory Exercise. *J. Chem. Educ.* **2016**, *93*, 2101−2105. (b) Yoshikawa, N.; Kimura, H.; Yamabe, S.; Kanehisa, N.; Inoue, T.; Takashima, H. Emission Property and DFT Calculation for the ^{3}MLCT Luminescence of $Ru(bpy)_2(L)^{2+}$Complex. *J. Mol. Struct.* **2016**, *1117*, 49−56.

(25) Henderson, L. J., Jr; Fronczek, F. R.; Cherry, W. R. Selective Perturbation of Ligand Field Excited States in Polypyridine Ruthenium(II) Complexes. *J. Am. Chem. Soc.* **1984**, *106*, 5876−5879.

(26) Yoshimura, A.; Hoffman, M. Z.; Sun, H. An Evaluation of the Excited State Absorption Spectrum of $Ru(bpy)_3{}^{2+}$ in Aqueous and Acetonitrile Solutions. *J. Photochem. Photobiol., A* **1993**, *70*, 29−33.

(27) (a) Thompson, A. M. W. C.; Jeffery, J. C.; Liard, D. J.; Ward, M. D. Mono-and Di-Nuclear Ruthenium (II) Complexes of the Ambidentate Ligand 3,3′-Dihydroxy-2,2′-bipyridine: Spectroscopic, Electrochemical and Mixed-Valence Properties. *J. Chem. Soc., Dalton Trans.* **1996**, 879−884. (b) Ghosh, P.; Ray, R.; Das, A.; Lahiri, G. K. Revelation of Varying Coordination Modes and Noninnocence of Deprotonated 2,2′-Bipyridine-3,3′-diol in $\{Os(bpy)_2\}$ Frameworks. *Inorg. Chem.* **2014**, *53*, 10695−10707.

(28) Kunkely, H.; Vogler, A. Optical Properties of (3,3′-Dihydroxy-2,2′-bipyridine)Tricarbonyl-Rhenium (I) Chloride. Absorption and Emission Spectra. *Inorg. Chim. Acta* **2003**, *343*, 357−360.

(29) Connelly, N. G.; Geiger, W. E. Chemical Redox Agents for Organometallic Chemistry. *Chem. Rev.* **1996**, *96*, 877−910.

(30) Kaljurand, I.; Kütt, A.; Sooväli, L.; Rodima, T.; Mäemets, V.; Leito, I.; Koppel, I. A. Extension of the Self-Consistent Spectrophotometric Basicity Scale in Acetonitrile to a Full Span of 28 pK_aUnits: Unification of Different Basicity Scales. *J. Org. Chem.* **2005**, *70*, 1019−1028.

(31) Henstridge, M. C.; Laborda, E.; Rees, N. V.; Compton, R. G. Marcus−Hush−Chidsey Theory of Electron Transfer Applied to Voltammetry: A Review. *Electrochim. Acta* **2012**, *84*, 12−20.

(32) (a) Evans, D. H.; Hu, K. Inverted Potentials in Two-Electron Processes in Organic Electrochemistry. *J. Chem. Soc., Faraday Trans.* **1996**, *92*, 3983−3990. (b) Hammerich, O. In *Organic Electrochemistry*, 5th ed.; Revised and Expanded; Speiser, B., Eds.; CRC Press: LLC, 2015.

(33) (a) Lachmanová, S.; Dupeyre, G.; Tarábek, J.; Ochsenbein, P.; Perruchot, C.; Ciofini, I.; Hromadová, M.; Pospísil, L.; Lainé, P. P. Kinetics of Multielectron Transfers and Redox-Induced Structural Changes in N-Aryl-Expanded Pyridiniums: Establishing Their Unusual, Versatile Electrophoric Activity. *J. Am. Chem. Soc.* **2015**, *137*, 11349−11364. (b) Fortage, J.; Peltier, C.; Perruchot, C.; Takemoto, Y.; Teki, Y.; Bedioui, F.; Marvaud, V.; Dupeyre, G.; Pospíšil, L.; Adamo, C.; Hromadová, M.; Ciofini, I.; Lainé, P. P. Single-Step versus Stepwise Two-Electron Reduction of Polyarylpyridiniums: Insights from the Steric Switching of Redox Potential Compression. *J. Am. Chem. Soc.* **2012**, *134*, 2691−2705.

(34) Schulzke, C. Temperature Dependent Electrochemistry-AVersatile Tool for Investigations of Biology Related Topics. *Dalton Trans.* **2009**, 6683−6691.

(35) Bard, A. J.; Faulkner, L. R. *Electrochemical methods: Fundamentals and Applications*; Wiley: New York, 2001; Vol. *2*.

(36) Tsierkezos, N. G. Cyclic Voltammetric Studies of Ferrocene in Nonaqueous Solvents in the Temperature Range from 248.15 to 298.15 K. *J. Solution Chem.* **2007**, *36*, 289−302.

(37) Bard, A. J.; Faulkner, L. R. *Electrochemical methods: Fundamentals and Applications*; Wiley: New York, 2001; p 87.

(38) (a) Costentin, C.; Robert, M.; Savéant, J.-M. Reorganization Energies and Pre-exponential Factors in the One-Electron Electrochemical and Homogeneous Oxidation of Phenols Coupled with an Intramolecular Amine-Driven Proton Transfer. *Phys. Chem. Chem. Phys.* **2010**, *12*, 13061−13069. (b) He, Z. D.; Chen, Y. X.; Santos, E.; Schmickler, W. The Pre-exponential Factor in Electrochemistry. *Angew. Chem., Int. Ed.* **2018**, *57*, 7948−7956.

appendix a.3.2

Excited-State Dynamics of $[\mathrm{Ru}(^{S-S}\mathrm{bpy})(\mathrm{bpy})_2]^{2+}$ to Form Long-Lived Localized Triplet States

Moritz Heindl, Jiang Hongyan, Shao-An Hua, Manuel Oelschlegel, Franc Meyer, Dirk Schwarzer, and Leticia González

Inorg. Chem., **60**, 1672-1682 (2021).
`https://doi.org/10.1021/acs.inorgchem.0c03163`

Contributions:

Moritz Heindl performed the surface hopping simulations, analyzed the results and wrote the initial draft of the manuscript.

Jiang Hongyan performed time-dependent measurements, analyzed the results, contributed to the writing of the manuscript.

Shao-An Hua synthesized the photosensitizer, contributed to the writing of the manuscript.

Manuel Oelschlegel optimized the synthesis of the photosensitizer.

Franc Meyer conceived and supervised the project and contributed to the writing of the manuscript.

Dirk Schwarzer conceived and supervised the project, analyzed the results and contributed to the writing of the manuscript.

Leticia González conceived and supervised the project, analyzed the results and contributed to the writing of the manuscript.

Inorganic Chemistry

pubs.acs.org/IC

Article

Excited-State Dynamics of $[Ru(^{S-S}bpy)(bpy)_2]^{2+}$ to Form Long-Lived Localized Triplet States

Moritz Heindl, Jiang Hongyan, Shao-An Hua, Manuel Oelschlegel, Franc Meyer, Dirk Schwarzer, and Leticia González*

Cite This: *Inorg. Chem.* 2021, 60, 1672−1682

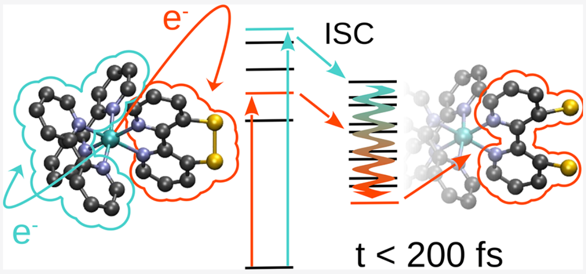

ABSTRACT: The novel photosensitizer $[Ru(^{S-S}bpy)(bpy)_2]^{2+}$ harbors two distinct sets of excited states in the UV/Vis region of the absorption spectrum located on either bpy or $^{S-S}$bpy ligands. Here, we address the question of whether following excitation into these two types of states could lead to the formation of different long-lived excited states from where energy transfer to a reactive species could occur. Femtosecond transient absorption spectroscopy identifies the formation of the final state within 80 fs for both excitation wavelengths. The recorded spectra hint at very similar dynamics following excitation toward either the parent or sulfur-decorated bpy ligands, indicating ultrafast interconversion into a unique excited-state species regardless of the initial state. Non-adiabatic surface hopping dynamics simulations show that ultrafast spin−orbit-mediated mixing of the states within less than 50 fs strongly increases the localization of the excited electron at the $^{S-S}$bpy ligand. Extensive structural relaxation within this sulfurated ligand is possible, via S−S bond cleavage that results in triplet state energies that are lower than those in the analogue $[Ru(bpy)_3]^{2+}$. This structural relaxation upon localization of the charge on $^{S-S}$bpy is found to be the reason for the formation of a single long-lived species independent of the excitation wavelength.

1. INTRODUCTION

Natural photocatalytic systems include a light-harvesting complex, where absorption occurs, covalently linked to a site of catalytic activity. Energy transfer from the absorptive to the reactive site is achieved *via* a multitude of proton-coupled electron transfers that form a complicated network of single- and multi-step subreactions themselves.[1−4] The efficiency of these energy and electron transfers is increased in biological photosynthesis by a supramolecular arrangement, which connects the light-harvesting unit to the catalytic site *via* a cascade of electron transporters operating near the thermodynamical optimum.[5,6] Selectivity in this directional transfer is of utmost importance as other pathways could lead to the formation of reactive oxygen species and other harmful products. One challenge in building artificial photocatalytic systems is to identify suitable photosensitizers that not only efficiently harness the photon energy but also transfer it conveniently to the actual catalytic entity or act themselves as catalysts.

A prototypical photosensitizer that has seen decades of experimental and theoretical investigations[7−15] and advancements in the form of modifications is $[Ru(bpy)_3]^{2+}$ (bpy = 2,2′-bipyridine). The prominence of this and other ruthenium complexes featuring polypyridine ligands is credited to their visible-light absorption in the blue end, allowing for selective absorption via the complex in the presence of most organic compounds and solvents, as well as photostability and capability to be directly attached to an acceptor functionality. Recently, the bpy ligand itself has been found to exhibit both π-donating and π-accepting features in iron complexes.[16] The low-energy photon absorption leads to excitation of a singlet state of metal-to-ligand charge-transfer (^{1}MLCT) character, oxidizing the ruthenium center and reducing the ligands whereto the electrons are excited. From this initial ^{1}MLCT excited state, ultrafast intersystem crossing into the triplet manifold is observed in less than 50 fs[17−19] followed by a descent into the lowest ^{3}MLCT state from which phosphorescence is observed or an electron could be transferred to another species. Population of the same ^{3}MLCT state has been observed independent of the excitation wavelength resulting in a stable hot precursor for energy or electron transfer to other reagents.[20] The phosphorescence decays in hundreds of nanoseconds,[21] providing ample time for interaction with other species whereto the energy or electron is transferred.

Received: October 26, 2020
Published: January 12, 2021

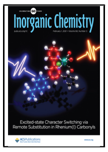

https://dx.doi.org/10.1021/acs.inorgchem.0c03163
Inorg. Chem. 2021, 60, 1672−1682

Rooted in $[Ru(bpy)_3]^{2+}$, other ruthenium complexes capable of harboring multiple charges at once without loss of stability[22−25] have been investigated. Recently, we synthesized and characterized $[Ru(^{S-S}bpy)(bpy)_2](PF_6)_2$, a complex containing two bipyridine ligands and a modified bipyridine ligand decorated by a bridging disulfide moiety ($^{S-S}$bpy; Figure 1).[21,26] Other ruthenium complexes with constrained bipyridyl-type ligands, *viz.*, with 3,3′-methylene or -ethylene bridged bipyridine, have been investigated decades ago, but time-resolved studies of their ultrafast excited-state dynamics are lacking so far.[27−30] In contrast to those previous systems with a peripheral aliphatic bridge, the present $[Ru(^{S-S}bpy)(bpy)_2]^{2+}$ has a disulfide linkage in the constrained bpy ligand, which represents a redox-active switch imparting distinct electronic structure modulations of the $[Ru(bpy)_3]^{2+}$-type complex. In-depth electrochemical studies showed that $^{S-S}$bpy can reversibly accommodate two electrons at moderate potentials (−1.1 V vs $Fc^{+/0}$), making it appealing to mediate novel excited-state proton-coupled multielectron-transfer reactions.[21] Furthermore, it was theoretically predicted[21] that solvation in acetonitrile shifts the excited states located at the $^{S-S}$bpy ligand to lower energies that allows for selective charge transfer from the metal to either the bpy or $^{S-S}$bpy ligand. From these two different excitations to the bpy or $^{S-S}$bpy ligands, two different relaxation pathways are then conceivable, which might result in the formation of two triplet states from which energy or an electron could be transferred. The question arises whether a small change in excitation energy might be able to induce these different deactivation pathways creating different long-lived triplet states. In this paper, we address this question by investigating the early excited-state dynamics of $[Ru(^{S-S}bpy)(bpy)_2]^{2+}$ both experimentally and theoretically. Specifically, we are interested to see whether $[Ru(^{S-S}bpy)(bpy)_2]^{2+}$ shows the ability to form different final triplet excited states upon excitation to different excitation bands or whether despite the availability of two different ligands, only one triplet state is populated, and if so from where the energy would be subsequently transferred. To this aim, time-resolved transient absorption spectra at different wavelengths were collected and then interpreted with the help of non-adiabatic dynamics simulations.

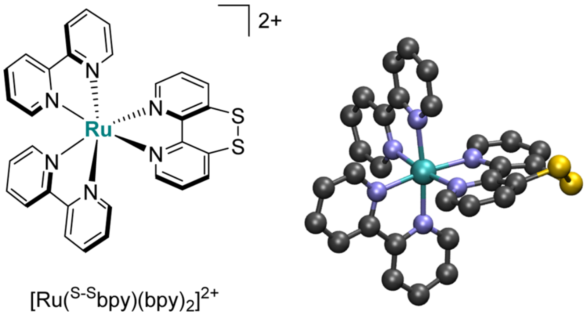

Figure 1. Schematic and three-dimensional representation of $[Ru(^{S-S}bpy)(bpy)_2]^{2+}$.

2. METHODOLOGY

2.1. Femtosecond Transient Absorption Spectroscopy. $[Ru(^{S-S}bpy)(bpy)_2](PF_6)_2$ has been synthesized as described earlier.[21] Femtosecond transient absorption spectroscopy was carried out on a setup similar to the one described in ref 31. The 35-fs laser output centered at 800 nm (Solstice Ace, Spectra physics) was split into two pulses. One pulse served as input for an optical parametric amplifier (TOPAS Prime+, Spectra Physics) and a subsequent frequency mixer (NirUVis, Spectra Physics), generating pump pulses at 430 and 520 nm. The other pulse (∼3 μJ) passed a translational stage (max 1.1 ns delay) and was focused into a 4 mm CaF_2 crystal for white light continuum generation. The generated white light was further split into two pulses of equal energies. One of them was overlapped with the pump pulse and served as the probe beam, and the other pulse served as the reference beam. The sample was sealed in a quartz cuvette (2 mm in optical path length) equipped with a magnetic stirrer for refreshing the solution between laser shots. The plane of polarization of pump and probe pulses was set to 54.7° (magic angle). Energies of pump pulses were typically 0.5−1 μJ to avoid multiphoton excitation. Probe and reference spectra were measured using two spectrometers equipped with 256 element linear image sensors.

2.2. Non-adiabatic Excited-State Dynamics. The propagation of nuclei and electronic state populations has been performed in the framework of surface hopping[31] using the SHARC method,[32,33] which can include non-adiabatic and spin−orbit couplings (SOCs) on the same footing.[34] Electronic properties for every time-step of a trajectory have been obtained from a parameterized linear vibronic coupling (LVC)[35−37] model that included 21 singlet states and the lowest lying 20 triplet electronic states, calculated as described below. All simulations are based on a set of 10,000 initial conditions created from a ground-state Wigner sampling.[38] Two sets of simulations have been done, exciting into the two parts of the low-energy absorption peak, featuring different charge-transfer character, assuming instantaneous δ-pulse excitation. One excitation window (EW) allows populating exclusively excited states falling inside the high-energy side (2.85−3.05 eV, EW-I) and another into the low-energy (2.4−2.6 eV, EW-II) side of the peak. The choice of the initially populated states and initial conditions inside each EW is based upon a stochastic selection process rooted in the relative oscillator strength within the corresponding EW. This process resulted in 5125 and 3838 excited initial conditions for EW-I and EW-II, respectively. All so-obtained initial conditions are propagated for 250 fs using nuclear time-steps of 0.5 fs in a fully diagonal basis for propagation.[34] Propagation of the electronic wave function is interpolated using 0.002 fs time-steps. The overcoherence problem inherent to surface hopping trajectories is tackled by applying the energy-based decoherence correction by Granucci and Persico[39] with the suggested value of 0.1 E_h for the C parameter. Nuclear velocities are rescaled after every hopping event to conserve the total energy of the ensemble by enforcing energy conservation inside each trajectory. All simulations have been conducted using the SHARC program suite.[40] The obtained trajectories and the corresponding state populations are analyzed employing a spin-pure adiabatic set of states when the lowest triplet state populations are discussed, and a diabatic representation based on the reference states in the LVC model when the charge-transfer character of the wave function is presented. In both cases, a mixed quantum-classical transformation of the obtained populations has been conducted.[41]

2.3. Parameterized Potential Energy Surfaces. The excited-state dynamics of $[Ru(^{S-S}bpy)(bpy)_2]^{2+}$ has been

https://dx.doi.org/10.1021/acs.inorgchem.0c03163
Inorg. Chem. 2021, 60, 1672−1682

simulated on parameterized potential energy surfaces (PESs) obtained from a LVC[35−37] model up to the first order. The LVC model describes the PES along every vibrational normal mode in the proximity of a chosen reference point—which in this case is the optimized ground-state geometry—via the diabatic Hamiltonian $\boldsymbol{V}$, written as

$$\boldsymbol{V} = V_0\mathbf{1} + \boldsymbol{W}$$

Here, $\mathbf{1}$ is the unit matrix, $\boldsymbol{W}$ is the matrix that contains all interstate (κ) and intrastate (λ) couplings, and V_0 is the ground-state potential. It is obtained as

$$V_0 = \sum_i \frac{\hbar\omega_i}{2} Q_i^{\,2}$$

with ω_i and Q_i being the calculated frequency and mass-weighted normal mode coordinate of mode i, respectively. To obtain the κ and λ values, for every one of the 177 vibrational normal modes present in the complex, two molecular structures were generated. These structures correspond to the optimized structure ±0.05 times the corresponding normal mode in mass-weighted coordinates. On these structures, the κ values are obtained as numerical gradients, while the λ values are approximated via a change in the state-to-state overlap of wave functions. Overlaps have been truncated at 99.9% of the norm. SOCs between the singlet and triplet states have been approximated using the program PySOC,[42] which is based on MolSOC.[43] An estimation for the effective charge of ruthenium[44] was added to the existing code to allow the evaluation of the SOC elements. The SOC elements between triplet states have been disregarded as the triplet−triplet interactions are governed by the respective non-adiabatic coupling elements with only small contributions from the respective triplet−triplet SOCs. Both, SOCs and transition dipole moments, are taken from the optimized geometry and no linear scaling parameters have been determined for these properties.

2.4. Quantum Chemical Calculations. The electronic excited states of the absorption spectrum and the parametrization of the LVC model of $[\mathrm{Ru}(^{\mathrm{S-S}}\mathrm{bpy})(\mathrm{bpy})_2]^{2+}$ have been calculated employing time-dependent density functional theory (TD-DFT)[45,46] employing the B3LYP[47,48] functional with the D3 dispersion correction.[49] The LANL2DZ[50] basis set was used at the ruthenium center, while the 6-311G(d)[51] basis set was employed for all other atoms (B3LYP/6-311G(d)-LANL2DZ). The geometries were optimized at the same level of theory (see Section S1 of the Supporting Information). The inclusion of relativistic effects in all the calculations is taken into account via Douglas−Kroll−Hess integrals.[52] Solvation of the complex in acetonitrile was mimicked by the integral equation formalism polarized continuum model[53] using the default set of parameters for this solvent in Gaussian09.[54] This level of theory is the same as that employed previously,[21] which was able to successfully reproduce the experimental electronic absorption spectrum of the complex. The latter is theoretically simulated using *ab initio* calculations of 21 singlet excited states on a set of 200 geometries obtained from a zero-point energy Wigner sampling.[38,55] Every excited state is convoluted with a Gaussian function with a full width at half maximum (FWHM) of 0.1 eV to move from discrete absorption toward a continuous one. For the parametrization of the LVC template, 21 singlet and 20 triplet states have been calculated using the same computational setup.

The wave functions of the resulting 4200 electronic states are characterized in terms of charge-transfer numbers[56] using the TheoDORE[57] program package. For this purpose, $[\mathrm{Ru}(^{\mathrm{S-S}}\mathrm{bpy})(\mathrm{bpy})_2]^{2+}$ is fragmented into the central ruthenium atom (M), two bipyridine ligands (L), and the bipyridine ligand that is functionalized by a S−S bridge (S). Depending on where the electron is excited from (hole) and to (electron), the following classification scheme for every excited state can be devised: If both the hole and the electron are located at Ru, a metal-centered state (MC) is obtained. A charge-transfer (CT) state is characterized by a difference in the hole and electron fragments. In this work, the hole fragment is noted in front of the electron fragment; hence, an excitation of a metal-based electron to the sulfur-substituted ligand is called an MSCT state. In this framework, a set of 10 different labels is available to investigate the excited-state dynamics: MC, SC, LC, MSCT, MLCT, SMCT, LMCT, SLCT, LSCT, and LLCT. Contributions toward and from the two bpy ligands are added up for simplicity, see Section S2 for more details.

3. EXPERIMENTAL RESULTS

Pump−probe UV−vis absorption spectroscopy was carried out to investigate the excited-state dynamics of $[\mathrm{Ru}(^{\mathrm{S-S}}\mathrm{bpy})(\mathrm{bpy})_2](\mathrm{PF}_6)_2$. Figure 2 shows the transient difference spectra measured in acetonitrile solution. Different pump wavelengths of 430 and 520 nm were used to preferentially excite the complex either to the parent bpy ligands' charge-transfer states (MLCT states) or to the metal-to-ligand charge-transfer states that are predominantly associated with the sulfur-decorated $^{\mathrm{S-S}}$bpy ligand (MSCT states), respectively. The spectra show ground-state bleaches between 400 and 550 nm superimposed by excited-state absorption resulting in a positive peak at 370 nm and a plateau at >570 nm. The excited-state absorption around 370 nm is assigned to spin-allowed π−π^* transitions in the transient bpy radical anion. The ground-state bleach in the

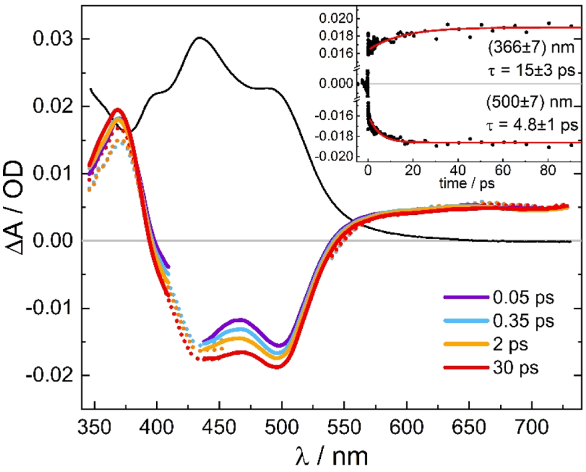

Figure 2. Pump pulse-induced difference spectra of $[\mathrm{Ru}(^{\mathrm{S-S}}\mathrm{bpy})(\mathrm{bpy})_2](\mathrm{PF}_6)_2$ (1.2×10^{-4} M in acetonitrile) at pump−probe delays, as indicated (solid colored lines: $\lambda_{\mathrm{pump}} = 430$ nm, dotted lines: $\lambda_{\mathrm{pump}} = 520$ nm, black line: scaled linear absorption spectrum). The insert shows time traces at (366 ± 7) and (500 ± 7) nm with exponential fits giving time constants of (15 ± 3) and (4.8 ± 1) ps, respectively.

https://dx.doi.org/10.1021/acs.inorgchem.0c03163
Inorg. Chem. 2021, 60, 1672−1682

lower energy region can be assigned to the vanishing ^{1}MLCT transition in the excited state of the complex.[20] All the transients in Figure 2 show striking similarities to those measured recently with ns time resolution and which were unequivocally assigned to the triplet excited state of $[\mathrm{Ru}(^{\mathrm{S-S}}\mathrm{bpy})(\mathrm{bpy})_2]^{2+}$ with a lifetime of 109 ns.[21] It is therefore not possible to experimentally differentiate the excited-state absorptions associated with the parent bpy and the sulfurated $^{\mathrm{S-S}}$bpy ligand. Furthermore, no dependence on the pump wavelength is observed within the pump−probe delay range (0.05−100 ps) of these measurements.

Within the time resolution of our experiment, the data do not show any evidence of a precursor state, which means that the triplet state is formed in <80 fs. Afterwards, the spectra exhibit slight amplitude changes on a tens of picosecond timescale, as illustrated in the inset of Figure 2. At the peak of the $\pi-\pi^*$ transitions of the transient bpy radical anion band (370 nm), there is a minor increase in absorption, whereas in the bleach region (400−500 nm), a drop is observed. After that, no further spectral changes appear up to 1 ns, indicating the formation of a long-lived excited state. The minor amplitude modulations seen in Figure 2 have further been analyzed by estimating the spectral evolution of the triplet state ($A_\mathrm{T}(t)$) from the sum of the transient spectra ($\Delta A(t)$) and the linear absorption spectrum (A_GS), $A_\mathrm{T}(t) = \Delta A(t) + a{\cdot}A_\mathrm{GS}$. The scaling factor a was chosen such that the drop in absorption seen in the transients at 500−550 nm arising from the ground state bleach just disappeared. The resultant spectra shown in Figure 3 are initially broadened with enhanced absorption at the red wing and less absorption in the center of the $\pi-\pi^*$ band, which subsequently contract to the relaxed spectrum of the triplet state. This behavior along with the observed relaxation time of about 10 ps is a clear indication of a vibrationally hot electronic state. From the pump photon energy (430 nm) and the onset of phosphorescence spectrum (650 nm),[21] an excess vibrational energy of 7900 cm^{-1} in the triplet state directly after excitation and intersystem crossing is estimated giving rise to hot bands and subsequent vibrational cooling. Similar behavior was observed for related complexes such as $[\mathrm{Os}(\mathrm{bpy})_3]^{2+}$[58] and $[\mathrm{Ru}(\mathrm{bpy})_3]^{2+}$.[59]

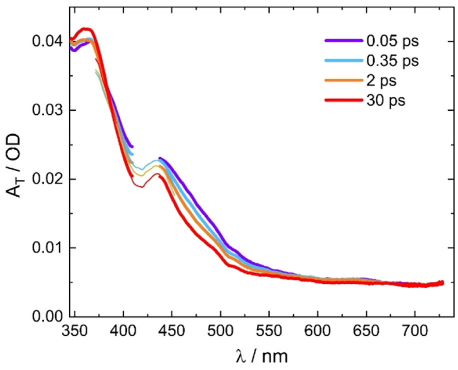

Figure 3. Time-dependent spectra of the triplet state of $[\mathrm{Ru}(^{\mathrm{S-S}}\mathrm{bpy})(\mathrm{bpy})_2](\mathrm{PF}_6)_2$ derived from the transients of Figure 2 by adding the scaled ground-state absorption spectrum (thick lines: λ_pump = 430 nm, thin lines: λ_pump = 520 nm).

Since the relaxation processes leading toward the long-lived triplet state are obviously very fast and no experimental evidence of a precursor state or different deactivation pathways could be obtained via pump−probe spectroscopy with the present setup, we turned to computations to shed light on the excited-state dynamics of the complex.

4. COMPUTATIONAL RESULTS

4.1. Absorption Spectrum and Model Potentials. The TD-DFT calculated electronic absorption spectrum of $[\mathrm{Ru}(^{\mathrm{S-S}}\mathrm{bpy})(\mathrm{bpy})_2]^{2+}$ in acetonitrile, decomposed in terms of different types of excitations, is shown in Figure 4a.

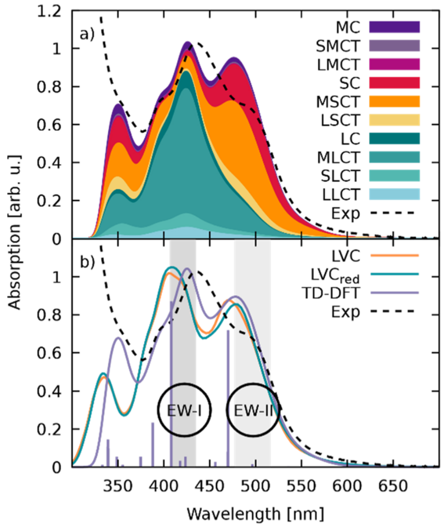

Figure 4. (a) Experimental[21] (dashed, black) and TD-DFT calculated (solid, black) absorption spectra of $[\mathrm{Ru}(^{\mathrm{S-S}}\mathrm{bpy})(\mathrm{bpy})_2]^{2+}$ in acetonitrile decomposed into different types of excitations. The scheme for labeling the types of excitation denotes the ruthenium atom as M, the $^{\mathrm{S-S}}$bpy ligand as S, and each bpy ligand as L. From this, excitations within each fragment are written as MC, SC, and LC, while the electron transfer between fragments is denoted XYCT, where X represents the fragment from which the electron is excited and Y the fragment to which it is excited. (b) Absorption spectra calculated with the full-parametrized LVC template (LVC), the reduced LVC template (LVC$_\mathrm{red}$), the ab initio TD-DFT absorption spectrum (TD-DFT), and the experimental one (exp). The electronically excited states at the optimized equilibrium geometry are indicated by bars at the corresponding energy with the relative height given by a normalized oscillator strength. EWs I and II used in the dynamics simulations are highlighted in gray.

Two distinct features of the CT character-dominated spectrum can be observed: (i) predominant excitations to the sulfur-decorated $^{\mathrm{S-S}}$bpy ligand (MSCT states) at lower energies around 500 nm and (ii) excitations to the parent bpy ligands (MLCT states) dominating at high energies around 420 nm with almost no (<10%) contribution of CT toward the $^{\mathrm{S-S}}$bpy ligand.[21] As shown in Figure 4b, the bright states obtained from the optimized geometry (lavender sticks) are found at higher energies than the respective experimental absorption maxima. This indicates vibronic intensity borrowing when moving away from the optimized structure, resulting in a transfer of oscillator strength toward lower lying electronic states in the ensemble of structures.

The dynamics ensuing after excitation toward the bpy and $^{\mathrm{S-S}}$bpy ligands is calculated using an LVC template, which approximates the real PES. In order to estimate the quality of the employed LVC Hamiltonian, we rely on two verifications. The first involves using the TD-DFT absorption spectrum (Figure 4a) as a quality check. Figure 4b shows (orange line) an absorption spectrum calculated with the LVC template from a set of 1000 geometries. The LVC spectrum shows a slightly blue-shifted onset of the first absorption band and a small shift of 0.12 eV for the main absorption peak around 420 nm, as compared with the TD-DFT one. However, the agreement of the two spectra can be considered very satisfactory considering the crude approximations present in the LVC model. The small deviations are due to the fact that the transition dipole moments in the LVC model are taken from the optimized geometry alone. Therefore, changes in the transition dipole moment only occur via mixing of the excited states with no explicit geometry dependence of these properties when using the LVC template. This results in absorption peaks centered on the absorption energy of the corresponding states.

The second validation of the LVC template refers to its ability to describe the subsequent excited-state dynamics adequately, for example, by testing how well the LVC model potential is able to locate a point likely to be encountered within the dynamics, for instance, the T_1 minimum structure. The optimized T_1 geometry at the B3LYP/6-311G(d)-LANL2DZ level of theory is very similar to the S_0 geometry, except for the drastically elongated S—S bond in the T_1 structure (2.57 Å, an increase of 0.46 Å). When performing a T_1 optimization using the LVC template, an S—S bond of only 2.43 Å is observed. This is little surprising as a harmonic model is expected to be capable of describing adequately the region close to the reference point but deteriorates at larger distances. With the reference being the S_0 geometry, leaving the Frank—Condon (FC) region and simulating the S—S bond elongation to this extent goes beyond the capabilities of this LVC setup. Besides the S—S bond being too short, the LVC optimization of the T_1 minimum leads to non-planar bpy ligands with the two pyridine rings twisted against each other, in disagreement with the TD-DFT results where the two bpy ligands are found to be planar to support extended π-conjugation. This indicates that some artificial energy lowering occurs in the LVC optimization due to coupling of a low-frequency bpy-twisting mode with a large λ value. This is reflected in a very low energy of the LVC T_1 (0.87 eV) when compared to the ab initio T_1 (1.41 eV) with respect to the ground-state energy at the S_0 optimized geometry.

The disagreement between the LVC-optimized T_1 minimum energy structure and the B3LYP/6-311G(d)-LANL2DZ-optimized structure is due to the inability of the LVC model to correctly describe large-scale displacements in the molecule. This stems from the harmonic approximation used for calculating the basic shape of the PES of the molecule and the inclusion of only linear coupling terms in the definition of the Hamiltonian. Hence, this model is not suited to describe anharmonic motion such as rotation and can lead to computational artifacts if strong movement along such specific normal mode occurs. In order to identify problematic normal modes, 60 different T_1 optimizations have been conducted where 60 different numbers of normal modes have been removed from the template file. The reduction is done by removing all κ and λ values related to the lowest x vibrational normal modes, with x ranging from 0 to 59. The so-obtained T_1 geometries have been then analyzed with regard to the S—S bond length, the adiabatic energy gap, and the root-mean-square deviation (RMSD) of the full structure as compared to those of the *ab initio* one. Figure 5 (see also Figure S2) collects values from which multiple trends are apparent: (i) The more the low-frequency modes are neglected, the smaller the obtained S—S bond length is, converging almost to the initial ground state S—S bond length of 2.11 Å as more and more modes that involve the sulfur atoms are removed. Unfortunately, none of the optimized T_1 geometries shows an S—S bond length longer than 2.43 Å, pointing to a general shortcoming of the LVC model to describe large amplitude motion. (ii) The adiabatic S_0—T_1 energy gap displays the opposite trend: the energy difference increases with decreasing number of considered modes. It starts out at 0.87 eV and increases up to 1.93 eV upon removal of 60 normal modes, showing its strong sensitivity. Finally, (iii) the RMSD value decreases rapidly and is almost converged at 0.09 Å after omitting the lowest 16 vibrational modes.

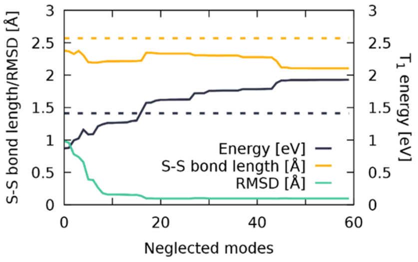

Figure 5. S—S bond length (Å, yellow), T_1 energy (eV, dark blue), and the RMSD (Å, teal) of the LVC-optimized T_1 geometry as a function of the number of neglected normal modes. Values for the full-dimensional geometry optimization at the B3LYP/6-311G(d)-LANL2DZ level of theory are shown in dashed lines.

The previous results evidence that including all the normal modes into the LVC template will yield unreasonable results once the dynamics simulation approaches structures close to the T_1 minimum energy structure, as both the RMSD values and T_1 energy of the *ab initio* optimization are not reproducible with the LVC model. As a remedy, specific normal modes that were found to have the largest impact on the observed deviations from the desired properties have been removed from the simulations. Accordingly, a "reduced-LVC" model was created, where 16 vibrational modes (v_1—v_{10}, v_{16}, v_{17}, v_{20}, v_{23}, v_{26}, and v_{28}, see Table S1) from a total of 177 have been removed. The absorption spectrum calculated with this reduced LVC model is shown for comparison in Figure 4b (green line). As it can be seen, the impact of these 16 normal modes in the absorption spectrum is negligible, so this reduced template is now used to simulate the excited-state dynamics of $[Ru^{(S-S}bpy)(bpy)_2]^{2+}$ in acetonitrile.

Initial excited-state simulations revealed that including the diabatic T_{17} state forms a low-lying triplet minimum, which is not reproducible with TD-DFT. Given the unphysical presence of this state and its ability to warp the excited-state dynamics, we excluded this state from the diabatic LVC Hamiltonian, resulting in a final template with 161 modes, 21 singlet and 19 triplet states; this is denoted LVC_{red}. The influence of the T_{17} state is thoroughly discussed in Section S3.2 of the Supporting Information.

4.2. Non-adiabatic Dynamics.

Two separate sets of excited-state dynamics simulations have been carried out to initially excite into the MLCT- or MSCT-dominated regions of the low-energy absorption band, recall Figure 4b. First, the results for excitation into the MLCT region of the EW-I band (2.85−3.05 eV) will be discussed. After excitation into low-energy singlet states (S_4−S_{11} are initially populated), ultrafast intersystem crossing to the triplet manifold is observed. Figure 6a shows the time evolution over 250 fs of all the singlet and triplet states grouped together for simplicity. To fit the retained populations, a kinetic model was employed that features a fast and a slow reacting singlet component, termed hot and cold singlets for the remainder, and the manifold of all triplet states combined. Population can be transferred between the two singlet components via k^{IC}, and ISC can occur from both of these. This results in two different ISC crossing rates to the triplet manifold, $k^{\mathrm{ISC,fast}}$ and $k^{\mathrm{ISC,slow}}$, one from the hot- and one from the cold-singlet component. Using this model, a perfect fit of the observed populations was possible, resulting in a $k^{\mathrm{ISC,fast}}$ of 46 fs, indicating an initial ultrafast transfer via spin mixing, followed by a transfer with a time constant, $k^{\mathrm{ISC,slow}}$, of 337 fs. Transfer from the hot-singlet component to the cold one occurred with k^{IC} = 72 fs. This fast transfer via $k^{\mathrm{ISC,fast}}$ toward the triplet states is not surprising as the initially excited states are embedded in a multitude of energetically close triplet states with strong SOCs, as seen in other Ru complexes.[19] The transfer to the triplet states is present from the very first time step, indicating that this is an electronically driven ISC process, which does not depend strongly on structural changes, similar to recent observations in a $\mathrm{Re^I}$ metal complex.[60] In this $\mathrm{Re^I}$ complex, this electronic, ultrafast ISC is related to the excitation, in that case, simulated with a δ-pulse that excites pure singlet states, from which the system undergoes almost instantaneous spin-mixing due to substantial SOC. Such electronic spin-mixing can be verified by carrying out a separate simulation that employs the same set of initial conditions but with frozen nuclear coordinates where all momenta in all time steps are set to zero. In doing so, any structural relaxation beyond the original zero-point energy sampling of the wavepacket is omitted, allowing the separation of ISC induced by nuclear motion from the electronic coupling of states in the initial distribution of geometries. The resulting plot of the diabatic populations of this frozen dynamics for $[\mathrm{Ru}(^{\mathrm{S-S}}\mathrm{bpy})(\mathrm{bpy})_2]^{2+}$ in acetonitrile is shown in Figure 6b. Employing an identical fitting scheme, $k^{\mathrm{ISC,fast}}$ amounts to 49 fs, while the slow component $k^{\mathrm{ISC,slow}}$ is now at −3189 fs. Hence, preventing the nuclei to move results in an almost identical fast ISC component (46 vs 49 fs) but completely stops any delayed ISC. The fast ISC component is therefore attributed to electronic spin-mixing, while the slow ISC is clearly driven by nuclear relaxation, as in the $\mathrm{Re^I}$ complex.[60]

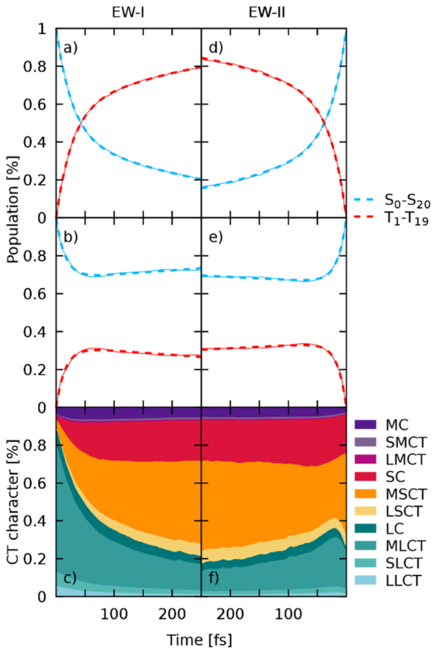

Figure 6. Excited-state dynamics simulations of $[\mathrm{Ru}(^{\mathrm{S-S}}\mathrm{bpy})(\mathrm{bpy})_2]^{2+}$ for both EWs. Note the inverted time axis for the right-hand side plots. Results for simulations starting in EW-I and EW-II are shown on the left- and right-hand side, respectively. (a,d) Sum of singlet and triplet populations for excitation in EW-I and EW-II, respectively. Thin lines represent the sum of all trajectories and thick dashed lines represent fits of populations. (b,e) Sum of singlet and triplet populations for frozen nuclear dynamics after excitation in EW-I and EW-II, respectively. (c,f) Evolution of charge-transfer character along the simulations for the non-frozen dynamics shown in (a,d), respectively.

Following the initial crossing into the triplet manifold, a rapid cascading down the ladder of states occurs. At the end of the simulation, 47% of the population ends up in the lowest triplet state. From there, the population could either decay to the initial ground state via emission of a photon or via a conical intersection with the ground state PES. The process of phosphorescence is not modeled in the present dynamics, which is not supposed to have any influence on the current simulations, considering the simulated time scale of only 250 fs, while luminescence was experimentally observed with a lifetime of 109 ns. On the basis of this longevity, an accessible crossing to the singlet ground state is unlikely.

The investigation of the nature of the wave function throughout the dynamics is straightforward as the LVC template is diabatic by construction. Therefore, the wave function at each point of dynamics is already expressed in terms of states at the optimized geometry. With this information, the wave function of the ensemble of all trajectories can be understood in terms of CT characters and is plotted in Figure 6c. Initially, the character of the complete wave function represents the partitioning of oscillator strengths in the initial EW-I (see Figure 4) and is predominantly of MLCT character with very small contributions of excited states located at the central metal atom or the $^{\mathrm{S-S}}$bpy ligand. This prevalence of MLCT changes almost instantaneously with the onset of dynamics, where transfer toward excited states where the electron is located at the $^{\mathrm{S-S}}$bpy ligand increases. The time scale of the observed decay in bpy-directed excitations (MLCT, SLCT, and LLCT) coincides with the ISC crossing rate, indicating that spin-mixing with triplet states of strong SC and MSCT character is responsible for the speed of this transfer. During the total 250 fs, a continuous increase in MSCT character is observed. The final composition of the wave function amounts to about 44% MSCT, 21% SC, 13% MLCT, and 6% MC. The T_1 state is populated with 47% of the total population at the end of the simulation. It has to be noted that a small number of trajectories (∼1%) were found in the lowest state. Since the coupling between S_0 and all other singlet states is zero per construction and only SOCs are included that couple to this lowest state, these transitions to S_0 will be considered erroneous.

https://dx.doi.org/10.1021/acs.inorgchem.0c03163
Inorg. Chem. 2021, 60, 1672−1682

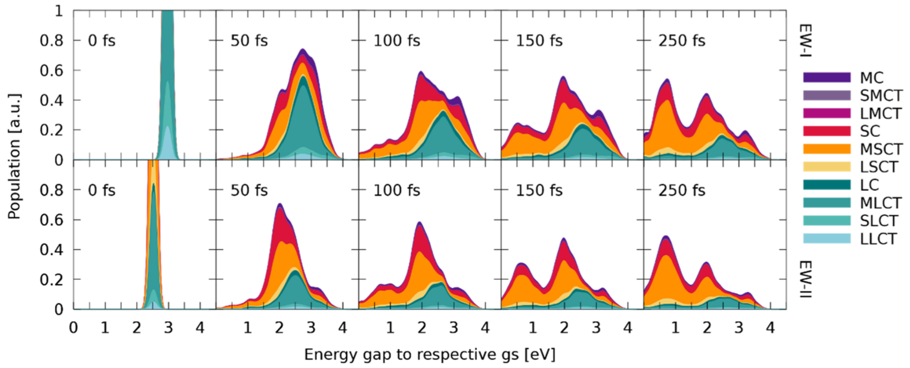

Figure 7. Evolution of the excited-state wavepacket for different time-steps throughout the dynamics starting from EWs I (top) and II (bottom). Each panel contains information about the active state at the given time-step for each trajectory to provide an overview of the distribution of energy gaps for each time frame. The CT character of every trajectory is plotted against the energy gap to the S_0 state at the corresponding geometry. For this, the character of the diabatic quantum population of a trajectory is transformed into the corresponding CT characters and then depicted at the energy gap of the currently active state to the S_0 energy of this trajectory at this state. All these values are then convoluted to yield the shown wavepackets.

The results obtained upon excitation to the low-energy band of the absorption spectrum (EW-II) are presented in Figure 6d−f. In this energy range, the lowest seven excited-singlet states are initially populated. From them, ultrafast decay from the hot singlet population is observed with fitted time constants of $k^{\mathrm{ISC,fast}}$ = 43 fs and k^{IC} = 74 fs, almost identical to the ones obtained for EW-I. Larger differences in time constants are found for $k^{\mathrm{ISC,slow}}$, which amount to 256 fs for the low-energy excitation. The similarity in the crossing rates for the fast part highlights the fact that this initial ISC is driven by state-mixing alone without any need for approaching crossing points between the singlet and triplet energy surfaces. It is therefore independent of the excitation wavelength as even at this lower energy range, an abundance of triplet states is close to the initially excited singlet states. For simulations in EW-II, a high accumulation of population is found in the adiabatic T_1 (57%) state at the end of the dynamics. The analysis of CT character of the wave function reveals that most of the initial population starts in MSCT (41%) or SC (19%) states. However, after few fs, there is transfer from MSCT to MLCT and LC states, followed by a decrease in MLCT and an increase in SC states. After 100 fs, only the MSCT character increases at the expense of states located at the bare bpy ligands. Thus, almost identical ending points in the CT picture are reached after 250 fs for simulations in EW-I and EW-II, and it can be concluded that dynamics starting from both EWs converge toward identical final states. To verify whether this could be a mere coincidence, the energy with respect to the lowest state of every trajectory is plotted with its current CT character for both EWs against time. The few snapshots shown at selected times in Figure 7 illustrate that the nuclear wavepackets disperse soon and strive toward lower potential energy gaps while descending the ladder of states, which is expected. Two facts can be deduced from the presented figure. First, it is evident that a lower potential energy gap is directly connected to an increase in MSCT and SC character. This emphasizes the importance of the $^{\mathrm{S-S}}$bpy ligand, which accommodates these low-lying states, and therefore, favors this fast decrease in potential energy by S−S bond elongation. Second, both the dynamics starting in EW I and II show almost identical final distributions both in energy and the corresponding CT character. Despite the initial localization of the excited electron on a specific fragment, the excitation evolves toward the $^{\mathrm{S-S}}$bpy ligand in the dynamics due to the corresponding lowering of energy, which seems to dominate all other deactivation pathways restricted to the pure bpy ligands. Therefore, it can be concluded that the same deactivation pathways are triggered for both excitation wavelengths.

The importance of states located at the $^{\mathrm{S-S}}$bpy ligand for the excited-state dynamics has surfaced at multiple parts throughout this discussion. In an attempt to further investigate the influence of the sulfur bond on the excited-state dynamics, a geometric analysis of all trajectories has been conducted. For this, pairs of S−S bond lengths and energy gaps of the currently active state to the lowest singlet state have been collected along each trajectory across both ensembles of EWs. These time-resolved data points have been convoluted both in space and energy by Gaussian functions to give Figure 8, employing FWHM values of 0.025 Å and 0.1 eV, respectively. An animated collection across the complete dynamics can be found in the Supporting Information. Figure 8 shows the distribution of energies and bond lengths at the initial state of simulations. Both EWs are clearly visible, and the S−S bond lengths correspond to the Wigner-sampled S−S bond lengths of the ground-state geometry. From this initially small distribution in both energy and space, broadening in populated energy gaps and bond lengths is observed in the first steps of dynamics. Already after 50 fs, a slight elongation of the S−S bond is evident for the trajectories that underwent energy gap lowering and are now found in the region of energy gaps between 1.5 and 2.5 eV. The corresponding plot of the character of the wave function indicates that population of this low energy gap region between 1.5 and 2.5 eV is predominantly linked to SC and MSCT states, which facilitate S−S bond elongation. At 100 fs, this minimum is even more pronounced, with most of the wavepacket being located in this region of bond lengths and energies. This energy lowering is directly correlated to destabilization of the singlet ground state that lowers the energy gap, while the active state is stabilized or hopping to lower states takes place. When going beyond 100 fs, quantitative population of T_1 accompanied by further sulfur bond elongation is observed, as more and more trajectories populate the energy region between 0.2 and 1 eV. In this region, the wave function comprised almost exclusively of

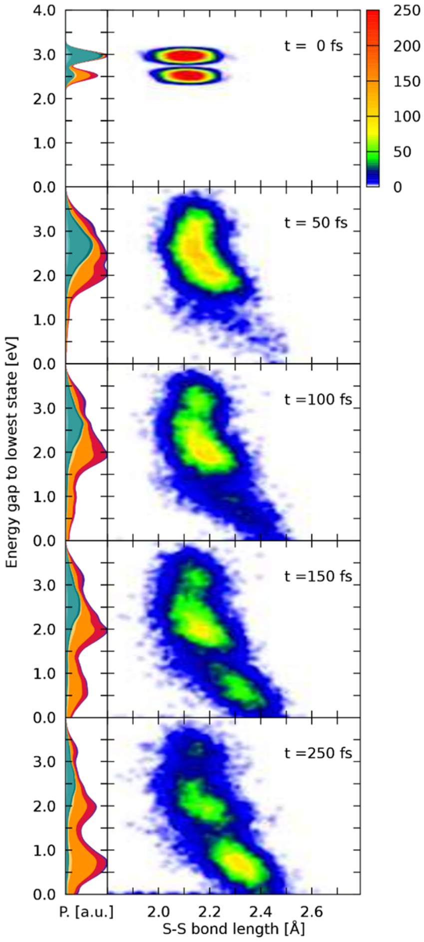

Figure 8. Left-hand side panels show the distribution of the wave function character against the energy gap between the classical active state and the lowest singlet state, similar to Figure 7, with the difference being that trajectories from both EWs are combined. The nuclear density is normalized in every time-step. On the right-hand side, a convoluted scatter plot of the S−S bond length with the corresponding energy gaps to the lowest state is given.

states that locate the excited electron on the sulfur-decorated bpy ligand. At the final time-step of the simulation, most of the trajectories are found in this T_1 minimum from where the population depletes via radiative emission, as has been shown in the experiment.[21] Plotting the energy gaps with respect to the S−S bond length shows that three hot spots are populated throughout the dynamics. First, there is a high energy population at moderate S−S bond lengths indicating trajectories in higher lying states where the sulfur bond is of no consequence. The electronic character at these states is a mixture of all considered types of excitations and features the highest amount of MC character. From these high-lying states, stabilization can occur either via occupation of predominantly MLCT or MSCT states centered around energy gaps of 2.5 and 2.0 eV, respectively. It can be seen that population of the MSCT states is associated with a slightly increased bond length. Trajectories can be trapped for a short amount of time in these two quasi-minima before ending up in a state that further promotes elongation of the S−S bond upon which energy gaps are decreased and the T_1 minimum is reached. We note that in the first 150 fs of the dynamics, coherent motion of the S−S bond length is observable due to the initial population of non-equilibrium states that all seem to favor bond elongation compared to the ground-state bond length[61] (Figure S4). The presence of $^{S-S}$bpy modification results in the stabilization of charge on the corresponding ligand due to a dynamical energy-lowering of the associated states as the S−S bond is lengthened. This additional dynamical stabilization of the excited electron is not observed in some modifications to the $[Ru(bpy)_3]^{2+}$ complex where selective metal-to-modified ligand excitation is possible.[62,63] Similarly to the $^{S-S}$bpy ligand, selective excitation is possible here due to lowering of the absorption energy of bright states that are characterized by charge transfer to the modified ligand. The additional dynamical stabilization within the $^{S-S}$bpy ligand is assumed to decrease the reversibility of the localization process on this ligand, resulting in a stronger trapping of the electron on the $^{S-S}$bpy ligand in comparison to more rigid modifications of the bpy ligand. The availability for both further relaxing and rather rigid ligands that can be selectively excited enables the synthesis of tailored complexes and opens up the avenue to a set of interesting questions regarding competitive pathways if both types of ligands are present.

5. SUMMARY

A time-resolved investigation of the nuclear and electronic dynamics of $[Ru(^{S-S}bpy)(bpy)_2]^{2+}$ in acetonitrile following excitations with green (520 nm) to blue (430 nm) light has been conducted. Two different sets of excited states are initially populated via absorption, each reminiscent of transferring an electron from the ruthenium center to one of the two types of ligands present: the parent bpy ligands or the modified $^{S-S}$bpy ligand, which are experimentally accessible at 430 and 520 nm, respectively. From these diverging sets of initially populated states, formation of a unique localized long-lived triplet state is observed from where radiative decay can occur.

After formal oxidation of the metal atom and reduction of the respective ligands via metal-to-ligand charge transfer, ultrafast time-resolved UV/Vis pump−probe spectroscopy reveals an excitation wavelength-independent behavior of the observed complex, where the absence of precursor states unequivocally identifies the formation of the lowest energy state within less than 80 fs. Excess vibrational energy in the T_1 state is transferred to the solvent on a 10 ps timescale.

A direct insight into the molecular dynamics occurring in the early times is obtained with surface-hopping trajectory simulations, using a TD-DFT-fitted LVC model. The general validity of this LVC model to describe the ensuing dynamics was verified using the absorption spectrum as a reference. Furthermore, it was found that 16 vibrational modes and one triplet state had to be removed from the LVC Hamiltonian to allow the correct formation of the minimum energy structure of the lowest triplet state. The non-adiabatic dynamics was then performed with a Hamiltonian containing 78 states and 161 vibrational degrees of freedom, where a total of 8983 trajectories were propagated during 250 fs each to unravel the mechanisms of ultrafast formation of the emissive state.

The non-adiabatic dynamics show that ultrafast intersystem crossing into the triplet manifold occurs on two time scales, a fast intersystem crossing component $k^{\mathrm{ISC,fast}}$ and a slow one $k^{\mathrm{ISC,slow}}$. Simulations starting in an energy range of 2.85−3.05 eV delivered $k^{\mathrm{ISC,fast}}$ = 46 fs and $k^{\mathrm{ISC,slow}}$ = 337 fs. Similar time constants have been obtained for the low-energy excitation (2.4 to 2.6 eV) with $k^{\mathrm{ISC,fast}} = 43$ fs and $k^{\mathrm{ISC,slow}} = 256$ fs. The fast ISC component persists if the dynamics are repeated while keeping all nuclei in every trajectory frozen, proving it to be due to electronic spin-mixing that does not rely on any structural rearrangement beyond the zero-point energy sampling of the ground-state geometry. Contrarily, the slow component completely vanishes in the absence of structural relaxation. At the end of the 250-fs simulation time, half of the population is found in the lowest triplet state for both excitation wavelengths. When looking at the electronic wave functions of the two ensembles of structures, the character of the total wave function changes toward increased contribution of MSCT states during the dynamics, regardless of the initial population of states. Therefore, during the very first few fs, the excited electron gets more localized on the sulfur-decorated ligand, forming a $[\mathrm{Ru^{III}}(^{\mathrm{S-S}}\mathrm{bpy}^{\bullet-})(\mathrm{bpy})_2]^{2+}$ species, where an electron has been excited from the central metal to the $^{\mathrm{S-S}}$bpy ligand. This early dominance of MSCT states is due to their lower energy in comparison to the MLCT counterparts. Another reason that drives the prevalence of MSCT states during the dynamics is the energetic stabilization of some MSCT states upon elongating—and essentially breaking—the attached S−S bond resulting in a further energetic separation between MSCT and other MLCT states where parent bpy ligands are involved. During the dynamics, a decrease in the S_0−T_1 energy gap was found to directly correlate with an increase of the S−S bond length.

Both experimental observations and theoretical predictions reveal an ultrafast ISC coupled with the formation of an excited triplet state minimum from where emission has been observed with a timescale of 109 ns.[21] While the formation of this state is independent of the excitation wavelength in the visible region of the spectrum, the final state is solely located on one ligand ($^{\mathrm{S-S}}$bpy), opening up the possibility of directed energy transfer to another reactive species. Furthermore, the excited-state geometric evolution, *viz.*, the elongation/rupture of the S−S bond, is reminiscent of the ground-state changes of the $^{\mathrm{S-S}}$bpy ligand upon reduction, and thus, renders this photosensitizer a promising candidate for investigation on excited-state proton-coupled multielectron-transfer reactivity via the peripheral disulfide/dithiol switch.

■ ASSOCIATED CONTENT

Supporting Information

The Supporting Information is available free of charge at https://pubs.acs.org/doi/10.1021/acs.inorgchem.0c03163.

Optimized geometry and Cartesian coordinates of optimized S_0 and T_1 minima; labeling of the charge-transfer states used for the classification of electronic states; and reduction of the employed LVC Hamiltonian; mode reduction; S−S bond lengths; and T_{17} state; exemplary input file for the gaussian calculations (PDF)

Full and reduced LVC templates and the corresponding frequency files in Molden format to set up initial conditions (ZIP)

■ AUTHOR INFORMATION

Corresponding Author

Leticia González − *Institute of Theoretical Chemistry, Faculty of Chemistry and Vienna Research Platform on Accelerating Photoreaction Discovery, University of Vienna, A-1090 Vienna, Austria*; orcid.org/0000-0001-5112-794X; Email: leticia.gonzalez@univie.ac.at

Authors

Moritz Heindl − *Institute of Theoretical Chemistry, Faculty of Chemistry, University of Vienna, A-1090 Vienna, Austria*
Jiang Hongyan − *Department of Dynamics at Surfaces, Max-Planck-Institute for Biophysical Chemistry, D-37077 Göttingen, Germany*
Shao-An Hua − *Institute of Inorganic Chemistry, University of Göttingen, D-37077 Göttingen, Germany*
Manuel Oelschlegel − *Institute of Inorganic Chemistry, University of Göttingen, D-37077 Göttingen, Germany*
Franc Meyer − *Institute of Inorganic Chemistry, University of Göttingen, D-37077 Göttingen, Germany*; orcid.org/0000-0002-8613-7862
Dirk Schwarzer − *Department of Dynamics at Surfaces, Max-Planck-Institute for Biophysical Chemistry, D-37077 Göttingen, Germany*; orcid.org/0000-0003-3838-2211

Complete contact information is available at: https://pubs.acs.org/10.1021/acs.inorgchem.0c03163

Author Contributions

All authors have given approval to the final version of the manuscript.

Funding

L.G., D.S., and F.M. are grateful to the Deutsche Forschungsgemeinschaft (DFG) for financial support of this work (projects Go1059/8-1, SCHW 661/4-1, and Me1313/15-1 within the SPP 2102 "Light-Controlled Reactivity of Metal Complexes").

Notes

The authors declare no competing financial interest.

■ ACKNOWLEDGMENTS

L.G. is grateful to the Göttingen Academy of Sciences for awarding a Gauss Professorship that allowed for an extended research stay in Göttingen. The Vienna Scientific Cluster is gratefully acknowledged for generous computational resources.

■ REFERENCES

(1) Gagliardi, C. J.; Westlake, B. C.; Kent, C. A.; Paul, J. J.; Papanikolas, J. M.; Meyer, T. J. J. Integrating Proton Coupled Electron Transfer (PCET) and Excited States. *Coord. Chem. Rev.* **2010**, *254*, 2459−2471.

(2) Wenger, O. S. Proton-Coupled Electron Transfer with Photoexcited Metal Complexes. *Acc. Chem. Res.* **2013**, *46*, 1517−1526.

(3) Pannwitz, A.; Wenger, O. S. Proton-Coupled Multi-Electron Transfer and Its Relevance for Artificial Photosynthesis and Photoredox Catalysis. *Chem. Commun.* **2019**, *55*, 4004−4014.

(4) Hammes-Schiffer, S. Theory of Proton-Coupled Electron Transfer in Energy Conversion Processes. *Acc. Chem. Res.* **2009**, *42*, 1881−1889.

(5) Roach, T.; Krieger-Liszkay, A. Regulation of Photosynthetic Electron Transport and Photoinhibition. *Curr. Protein Pept. Sci.* **2014**, *15*, 351−362.

(6) Wherland, S.; Pecht, I. Controlling Time Scales for Electron Transfer through Proteins. *Perspect. Sci.* **2015**, *6*, 94−105.

(7) Crosby, G. A. Spectroscopic Investigations of Excited States of Transition-Metal Complexes. *Acc. Chem. Res.* **1975**, *8*, 231−238.

(8) Thompson, D. W.; Ito, A.; Meyer, T. J. $[\mathrm{Ru(bpy)_3}]^{2+*}$ and Other Remarkable Metal-to-Ligand Charge Transfer (MLCT) Excited States. *Pure Appl. Chem.* **2013**, *85*, 1257−1305.

(9) Müller, P.; Brettel, K. $[\mathrm{Ru(bpy)_3}]^{2+}$ as a Reference in Transient Absorption Spectroscopy: Differential Absorption Coefficients for Formation of the Long-Lived ^{3}MLCT Excited State. *Photochem. Photobiol. Sci.* **2012**, *11*, 632−636.

(10) Bock, C. R.; Connor, J. A.; Gutierrez, A. R.; Meyer, T. J.; Whitten, D. G.; Sullivan, B. P.; Nagle, J. K. Estimation of Excited-State Redox Potentials by Electron-Transfer Quenching. Application of Electron-Transfer Theory to Excited-State Redox Processes. *J. Am. Chem. Soc.* **1979**, *101*, 4815−4824.

(11) Ito, A.; Meyer, T. J. The Golden Rule. Application for Fun and Profit in Electron Transfer, Energy Transfer, and Excited-State Decay. *Phys. Chem. Chem. Phys.* **2012**, *14*, 13731−13745.

(12) Kober, E. M.; Meyer, T. J. Concerning the Absorption Spectra of the Ions $\mathrm{M(bpy)_3}^{2+}$ (M = Fe, Ru, Os; bpy = 2,2'-bipyridine). *Inorg. Chem.* **1982**, *21*, 3967−3977.

(13) Soupart, A.; Dixon, I. M.; Alary, F.; Heully, J.-L. DFT Rationalization of the Room-Temperature Luminescence Properties of $\mathrm{Ru(bpy)_3}^{2+}$and $\mathrm{Ru(tpy)_2}^{2+}$: ^{3}MLCT−^{3}MC Minimum Energy Path from NEB Calculations and Emission Spectra from VRES Calculations. *Theor. Chem. Acc.* **2018**, *137*, 37.

(14) Prier, C. K.; Rankic, D. A.; MacMillan, D. W. C. Visible Light Photoredox Catalysis with Transition Metal Complexes: Applications in Organic Synthesis. *Chem. Rev.* **2013**, *113*, 5322−5363.

(15) Kober, E. M.; Meyer, T. J. An Electronic Structural Model for the Emitting MLCT Excited States of $\mathrm{Ru(bpy)_3}^{2+}$ and $\mathrm{Os(bpy)_3}^{2+}$. *Inorg. Chem.* **1984**, *23*, 3877−3886.

(16) Ashley, D. C.; Jakubikova, E. Tuning the Redox Potentials and Ligand Field Strength of Fe(II) Polypyridines: The Dual π-Donor and π-Acceptor Character of Bipyridine. *Inorg. Chem.* **2018**, *57*, 9907−9917.

(17) Damrauer, N. H.; Cerullo, G.; Yeh, A.; Boussie, T. R.; Shank, C. V.; McCusker, J. K. Femtosecond Dynamics of Excited-State Evolution in $[\mathrm{Ru(bpy)_3}]^{2+}$. *Science* **1997**, *275*, 54−57.

(18) Bräm, O.; Messina, F.; El-Zohry, A. M.; Cannizzo, A.; Chergui, M. Polychromatic Femtosecond Fluorescence Studies of Metal−Polypyridine Complexes in Solution. *Chem. Phys.* **2012**, *393*, 51−57.

(19) Atkins, A. J.; González, L. Trajectory Surface-Hopping Dynamics Including Intersystem Crossing in $[\mathrm{Ru(bpy)_3}]^{2+}$. *J. Phys. Chem. Lett.* **2017**, *8*, 3840−3845.

(20) Arias-Rotondo, D. M.; McCusker, J. K. The Photophysics of Photoredox Catalysis: A Roadmap for Catalyst Design. *Chem. Soc. Rev.* **2016**, *45*, 5803−5820.

(21) Hua, S.-A.; Cattaneo, M.; Oelschlegel, M.; Heindl, M.; Schmid, L.; Dechert, S.; Wenger, O. S.; Siewert, I.; González, L.; Meyer, F. Electrochemical and Photophysical Properties of Ruthenium(II) Complexes Equipped with Sulfurated Bipyridine Ligands. *Inorg. Chem.* **2020**, *59*, 4972−4984.

(22) Whittemore, T. J.; White, T. A.; Turro, C. New Ligand Design Provides Delocalization and Promotes Strong Absorption throughout the Visible Region in a Ru(II) Complex. *J. Am. Chem. Soc.* **2018**, *140*, 229−234.

(23) Rau, S.; Walther, D.; Vos, J. G. Inspired by Nature: Light Driven Organometallic Catalysis by Heterooligonuclear Ru(II) Complexes. *Dalton Trans.* **2007**, 915−919.

(24) Kinoshita, T.; Nonomura, K.; Joong Jeon, N.; Giordano, F.; Abate, A.; Uchida, S.; Kubo, T.; Seok, S. I.; Nazeeruddin, M. K.; Hagfeldt, A.; Grätzel, M.; Segawa, H. Spectral Splitting Photovoltaics Using Perovskite and Wideband Dye-Sensitized Solar Cells. *Nat. Commun.* **2015**, *6*, 1−8.

(25) Hagfeldt, A.; Grätzel, M. Molecular Photovoltaics. *Acc. Chem. Res.* **2000**, *33*, 269−277.

(26) Cattaneo, M.; Schiewer, C. E.; Schober, A.; Dechert, S.; Siewert, I.; Meyer, F. 2,2′-Bipyridine Equipped with a Disulfide/Dithiol Switch for Coupled Two-Electron and Two-Proton Transfer. *Chem.—Eur. J.* **2018**, *24*, 4864−4870.

(27) Taffarel, E.; Chirayil, S.; Kim, W. Y.; Thummel, R. P.; Schmehl, R. H. Coexistence of Ligand Localized and MLCT Excited States in a 2-(2′-Pyridyl)Benzo[g]Quinoline Complex of Ruthenium(II). *Inorg. Chem.* **1996**, *35*, 2127−2131.

(28) Henderson, L. J.; Cherry, W. R. Dynamics of Ligand Field Excited States in Polypyridine Ruthenium(II) Complexes. *Chem. Phys. Lett.* **1985**, *114*, 553−556.

(29) Henderson, L. J.; Fronczek, F. R.; Cherry, W. R. Selective Perturbation of Ligand Field Excited States in Polypyridine Ruthenium(II) Complexes. *J. Am. Chem. Soc.* **1984**, *106*, 5876−5879.

(30) Thummel, R. P.; Lefoulon, F.; Korp, J. D. Polyaza Cavity-Shaped Molecules. 12. Ruthenium(II) Complexes of 3,3'-Annelated 2,2'-Bipyridine: Synthesis, Properties, and Structure. *Inorg. Chem.* **1987**, *26*, 2370−2376.

(31) Tully, J. C. Molecular Dynamics with Electronic Transitions. *J. Chem. Phys.* **1990**, *93*, 1061−1071.

(32) Richter, M.; Marquetand, P.; González-Vázquez, J.; Sola, I.; González, L. SHARC: Ab Initio Molecular Dynamics with Surface Hopping in the Adiabatic Representation Including Arbitrary Couplings. *J. Chem. Theory Comput.* **2011**, *7*, 1253−1258.

(33) Mai, S.; Marquetand, P.; González, L. Nonadiabatic Dynamics: The SHARC Approach. *Wiley Interdiscip. Rev.: Comput. Mol. Sci.* **2018**, *8*, No. e1370.

(34) Mai, S.; Marquetand, P.; González, L. A General Method to Describe Intersystem Crossing Dynamics in Trajectory Surface Hopping. *Int. J. Quantum Chem.* **2015**, *115*, 1215−1231.

(35) Köppel, H.; Domcke, W.; Cederbaum, L. S. Multimode Molecular Dynamics Beyond the Born-Oppenheimer Approximation. *Advances in Chemical Physics*; John Wiley & Sons, Ltd., 2007; pp 59−246.

(36) Worth, G. A.; Cederbaum, L. S. Beyond Born-Oppenheimer: Molecular Dynamics Through a Conical Intersection. *Annu. Rev. Phys. Chem.* **2004**, *55*, 127−158.

(37) Plasser, F.; Gómez, S.; Menger, M. F. S. J.; Mai, S.; González, L. Highly Efficient Surface Hopping Dynamics Using a Linear Vibronic Coupling Model. *Phys. Chem. Chem. Phys.* **2018**, *21*, 57−69.

(38) Wigner, E. On the Quantum Correction For Thermodynamic Equilibrium. *Phys. Rev.* **1932**, *40*, 749−759.

(39) Granucci, G.; Persico, M. Critical Appraisal of the Fewest Switches Algorithm for Surface Hopping. *J. Chem. Phys.* **2007**, *126*, 134114.

(40) Mai, S.; Richter, M.; Heindl, M.; Menger, M. F. S. J.; Atkins, A.; Ruckenbauer, M.; Plasser, F.; Ibele, L. M.; Kropf, S.; Oppel, M.; Marquetand, P.; González, L. SHARC2.1: Surface Hopping Including Arbitrary Couplings—Program Package for Non-adiabatic Dynamics, http://Sharc-Md.Org (2019).

(41) Landry, B. R.; Falk, M. J.; Subotnik, J. E. Communication: The Correct Interpretation of Surface Hopping Trajectories: How to Calculate Electronic Properties. *J. Chem. Phys.* **2013**, *139*, 211101.

(42) Gao, X.; Bai, S.; Fazzi, D.; Niehaus, T.; Barbatti, M.; Thiel, W. Evaluation of Spin-Orbit Couplings with Linear-Response Time-Dependent Density Functional Methods. *J. Chem. Theory Comput.* **2017**, *13*, 515−524.

(43) Chiodo, S. G.; Leopoldini, M. MolSOC: A Spin−Orbit Coupling Code. *Comput. Phys. Commun.* **2014**, *185*, 676−683.

(44) Koseki, S.; Schmidt, M. W.; Gordon, M. S. Effective Nuclear Charges for the First- through Third-Row Transition Metal Elements in Spin−Orbit Calculations. *J. Phys. Chem. A* **1998**, *102*, 10430−10435.

(45) Runge, E.; Gross, E. K. U. Density-Functional Theory for Time-Dependent Systems. *Phys. Rev. Lett.* **1984**, *52*, 997−1000.

(46) Casida, M. E.; Jamorski, C.; Casida, K. C.; Salahub, D. R. Molecular Excitation Energies to High-Lying Bound States from Time-Dependent Density-Functional Response Theory: Characterization and Correction of the Time-Dependent Local Density Approximation Ionization Threshold. *J. Chem. Phys.* **1998**, *108*, 4439−4449.

(47) Becke, A. D. Density-functional Thermochemistry. III. The Role of Exact Exchange. *J. Chem. Phys.* **1993**, *98*, 5648−5652.

(48) Lee, C.; Yang, W.; Parr, R. G. Development of the Colle-Salvetti Correlation-Energy Formula into a Functional of the Electron Density. *Phys. Rev. B* **1988**, *37*, 785−789.

(49) Grimme, S.; Antony, J.; Ehrlich, S.; Krieg, H. A Consistent and Accurate Ab Initio Parametrization of Density Functional Dispersion Correction (DFT-D) for the 94 Elements H-Pu. *J. Chem. Phys.* **2010**, *132*, 154104.

(50) Hay, P. J.; Wadt, W. R. Ab Initio Effective Core Potentials for Molecular Calculations. Potentials for K to Au Including the Outermost Core Orbitals. *J. Chem. Phys.* **1985**, *82*, 299−310.

(51) Krishnan, R.; Binkley, J. S.; Seeger, R.; Pople, J. A. Self-consistent Molecular Orbital Methods. XX. A Basis Set for Correlated Wave Functions. *J. Chem. Phys.* **1980**, *72*, 650−654.

(52) Hess, B. A. Relativistic Electronic-Structure Calculations Employing a Two-Component No-Pair Formalism with External-Field Projection Operators. *Phys. Rev. A* **1986**, *33*, 3742−3748.

(53) Cancès, E.; Mennucci, B.; Tomasi, J. A New Integral Equation Formalism for the Polarizable Continuum Model: Theoretical Background and Applications to Isotropic and Anisotropic Dielectrics. *J. Chem. Phys.* **1997**, *107*, 3032−3041.

(54) Frisch, M. J.; Trucks, G. W.; Cheeseman, J. R.; Scalmani, G.; Caricato, M.; Hratchian, H. P.; Li, X.; Barone, V.; Bloino, J.; Zheng, G.; Vreven, T.; Montgomery, J. A.; Petersson, G. A.; Scuseria, G. E.; Schlegel, H. B.; Nakatsuji, H.; Izmaylov, A. F.; Martin, R. L.; Sonnenberg, J. L.; Peralta, J. E.; Heyd, J. J.; Brothers, E.; Ogliaro, F.; Bearpark, M.; Robb, M. A.; Menucci, B.; Kudin, K. N.; Staroverov, V. N.; Kobayashi, R.; Normand, J.; Rendell, A.; Gomperts, R.; Zakrzewski, V. G.; Hada, M.; Ehara, M.; Toyota, K.; Fukuda, R.; Hasegawa, J.; Ishida, M.; Nakajima, T.; Honda, Y.; Kitao, O.; Nakai, H. A. *Gaussian09*, 1. 2197; Gaussian Inc.: Wallingford CT, 2009.

(55) Crespo-Otero, R.; Barbatti, M. Spectrum Simulation and Decomposition with Nuclear Ensemble: Formal Derivation and Application to Benzene, Furan and 2-Phenylfuran. *Theor. Chem. Acc.* **2012**, *131*, 1237.

(56) Mai, S.; Plasser, F.; Dorn, J.; Fumanal, M.; Daniel, C.; González, L. Quantitative Wave Function Analysis for Excited States of Transition Metal Complexes. *Coord. Chem. Rev.* **2018**, *361*, 74−97.

(57) Plasser, F. TheoDORE: A Package for Theoretical Density Orbital Relaxation and Exciton Analysis. Available at Http://Theodore-Qc.Sourceforge.Net/ (accessed January 09, 2021).

(58) Shaw, G. B.; Styers-Barnett, D. J.; Gannon, E. Z.; Granger, J. C.; Papanikolas, J. M. Interligand Electron Transfer Dynamics in $[Os(Bpy)_3]^{2+}$: Exploring the Excited State Potential Surfaces with Femtosecond Spectroscopy. *J. Phys. Chem. A* **2004**, *108*, 4998−5006.

(59) Wallin, S.; Davidsson, J.; Modin, J.; Hammarström, L. Femtosecond Transient Absorption Anisotropy Study on $[Ru(Bpy)_3]^{2+}$ and $[Ru(Bpy)(Py)_4]^{2+}$. Ultrafast Interligand Randomization of the MLCT State. *J. Phys. Chem. A* **2005**, *109*, 4697−4704.

(60) Mai, S.; González, L. Unconventional Two-Step Spin Relaxation Dynamics of $[Re(CO)_3(Im)(Phen)]^+$ in Aqueous Solution. *Chem. Sci.* **2019**, *10*, 10405−10411.

(61) Mai, S.; González, L. Identification of Important Normal Modes in Nonadiabatic Dynamics Simulations by Coherence, Correlation, and Frequency Analyses. *J. Chem. Phys.* **2019**, *151*, 244115.

(62) McCusker, C. E.; McCusker, J. K. Synthesis and Spectroscopic Characterization of CN-Substituted Bipyridyl Complexes of Ru(II). *Inorg. Chem.* **2011**, *50*, 1656−1669.

(63) Brown, A. M.; McCusker, C. E.; Carey, M. C.; Blanco-Rodríguez, A. M.; Towrie, M.; Clark, I. P.; Vlček, A.; McCusker, J. K. Vibrational Relaxation and Redistribution Dynamics in Ruthenium(II) Polypyridyl-Based Charge-Transfer Excited States: A Combined Ultrafast Electronic and Infrared Absorption Study. *J. Phys. Chem. A* **2018**, *122*, 7941−7953.

APPENDIX A.3.3

Taming S-S Bonds with Laser Fields. Nonadiabatic Surface-Hopping Simulations in a Ruthenium Complex

MORITZ HEINDL AND LETICIA GONZÁLEZ

submitted to J. Phys. Chem. Lett., , XXX-XXX (2021).
- - -

Contributions:

MORITZ HEINDL performed the surface hopping simulations, analyzed the results and wrote the initial draft of the manuscript.

LETICIA GONZÁLEZ conceived and supervised the project and contributed to the writing of the manuscript.

Taming S–S Bonds with Laser Fields. Nonadiabatic Surface-Hopping Simulations in a Ruthenium Complex

Moritz Heindl and Leticia González*

Institute of Theoretical Chemistry, Faculty of Chemistry, University of Vienna,
Währingerstr. 17, 1090 Vienna, Austria

E-mail: leticia.gonzalez@univie.ac.at

Abstract

Laser control of chemical reactions is a challenging field of research. In particular, the theoretical description of coupled electronic and nuclear motion in the presence of laser fields is not a trivial task and simulations are mostly restricted to small systems or molecules in reduced dimensionality. Here, we demonstrate how the excited state dynamics of $[\mathrm{Ru}(^{\mathrm{S--S}}\mathrm{bpy})(\mathrm{bpy})_2]^{2+}$ can be controlled using explicit laser fields in the context of fewest switches surface-hopping. In particular, the transient properties along the excited state dynamics leading to population of the T_1 minimum energy structure are exploited to define simple laser fields capable of slowing and even completely stopping the onset of S–S bond dissociation. The use of a linear vibronic coupling model to parameterize the potential energy surfaces showcases the strength of the surface hopping methodology to study systems including explicit laser fields in full dimensionality and with a large amount of close-lying electronic excited states.

Graphical TOC Entry

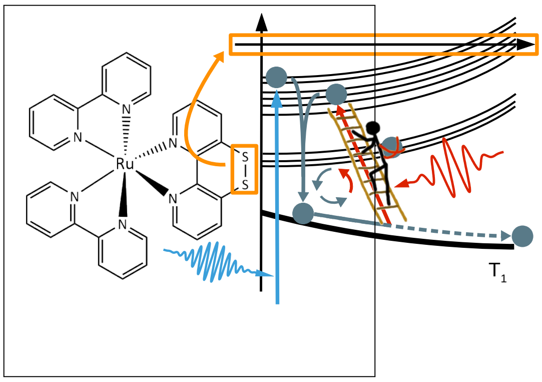

Keywords

Laser Fields, Excited State Dynamics, Transition Metal Complexes, Surface Hopping

Laser fields can be used to monitor but also to modify ultrafast dynamical processes on a molecular level. Experimental progress in laser spectroscopy allows for increasing resolution to unravel the flow of excited molecular wave packets.[1] In parallel, dynamical simulations provide atomistic insight into the potential energy surfaces (PESs) visited by the wave packets.[2] However, only few of these simulations include explicit laser fields to excite the system and thus reconcile experimental and theoretical observations.[3–13]

The observed excited state dynamics can be altered using additional pulses tailored to yield outcomes differing from the unperturbed dynamics.[14–16] Here, a classification into weak- and strong-field effects is useful, where weak-field pulses induce transitions between states but do not change the shape of the respective PESs and strong-field pulses influence the dynamics by introducing time-dependence PESs. The large number of successful simulations reported in the literature (see e.g. Refs. 17–26) highlights their versatility. In general, two main avenues can be distinguished to design computationally control pulses.[16] One is based on exploiting knowledge about the underlying PES and designing laser pulses with a particular reaction pathway. The other uses automated control theories in the form of optimal or local control theory. In optimal control theory, a desired product state or property is maximized over the course of the complete dynamics, relying on a multitude of runs, resulting in an iteratively adapting pulse.[16,19,27] In contrast, local control theory tries to maximize the chosen state or property in each time step, requiring only a single simulation to yield a locally optimized pulse shape.[17,18,28,29] The downside of these forms of control is the non-analytical shape of the resulting fine-tuned pulses, oftentimes hindering physical interpretation of the excited state mechanisms at work and complicating experimental realization of these pulses.

Previous theoretical work using explicit laser control pulses was mostly done on small systems or relying on few selected degrees of freedom as well as with limiting participating states –as the sheer number of states and possible relaxation pathways in large systems complicates the excited state dynamics considerably. In the present Letter, we use nonadiabatic dynamics simulations in full dimensionality to manipulate the excited state dynamics of

$[\mathrm{Ru}(^{\mathrm{S--S}}\mathrm{bpy})(\mathrm{bpy})_2]^{2+}$ (bpy=2,2'-bipyridine). This transition metal complex is a prototype of experimentally relevant metal-based photosensitizers, with sufficient complexity so that many competing processes take place and control is not straightforward. The peripheral disulfide bridge induces the appearance of metal-to-ligand charge-transfer states localized on the $^{\mathrm{S--S}}$bpy ligand (henceforth labelled MSCT) at energies lower than those pertaining the standard MLCT states localized on the bpy ligands.[30,31] However, selective excitation of the MLCT or MSCT states in the UV range, leads to a decay into the lowest T_1 state in less than 200 fs, regardless of the initially populated states[32] (see Figure 1a). This unselective deactivation is due to the high density of states that form a ladder along which efficient funneling into the T_1 state occurs. The T_1 state, with the excited electron located at the $^{\mathrm{S-S}}$bpy ligand, relaxes by weakening the S–S bond and eventually undergoes sulfide extrusion giving a monosulfurated decomposition product.[31] Such unwanted reaction ruins the promising applications of this complex for excited-state proton-coupled multielectron transfer reactivity via the peripheral disulfide/dithiol switch. The present work is thus an ambitious attempt to avoid S–S dissociation by altering the natural dynamics of a transition metal complex that posses a extensive number of nuclear and near-degenerate electronic degrees of freedom.

The simulation and control of the excited state dynamics of $[\mathrm{Ru}(^{\mathrm{S--S}}\mathrm{bpy})(\mathrm{bpy})_2]^{2+}$ is performed using trajectory surface-hopping dynamics simulations with the SHARC (surface-hopping including arbitrary couplings) package.[33–35] SHARC is an extension of Tully surface-hopping,[36] where not only nonadiabatic couplings are considered, but also spin-orbit couplings and dipole couplings –the latter enabling explicit interaction with laser fields.[37,38] The trajectories are based on a set of 4000 initial conditions created from a ground-state Wigner sampling.[39] The PES of the molecule are obtained from a linear vibronic coupling model (LVC),[40,41] that includes 21/19 singlet/triplet electronic states and 161 vibrational normal modes with parameters described elsewhere.[32] As an LVC model cannot describe dissociation, this is hinted by monitoring the initial stretching of the S–S bond. The transition dipole moments that account for the interaction with external laser fields are calculated with

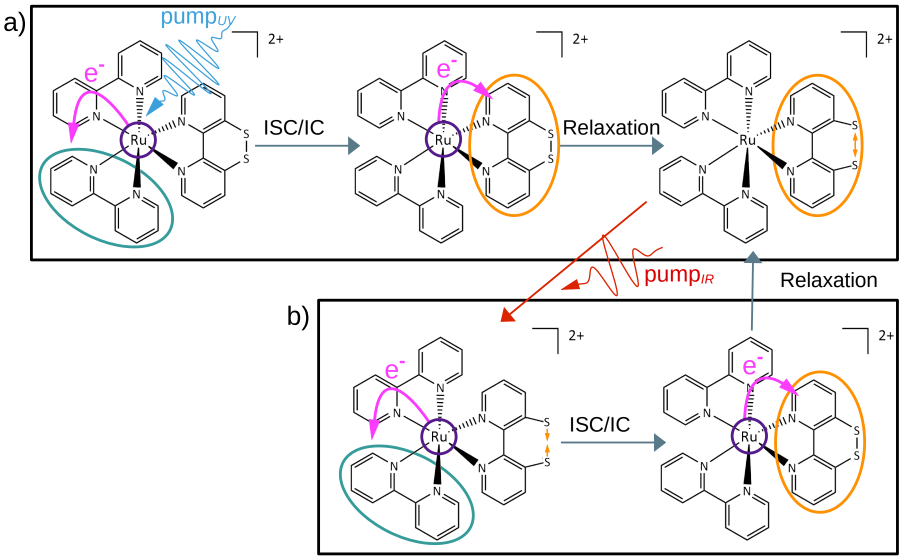

Figure 1: a) Schematic representation of the natural excited state dynamics of $[\mathrm{Ru}(^{\mathrm{S{-}-S}}\mathrm{bpy})(\mathrm{bpy})_2]^{2+}$. After irradiation with a UV laser pump pulse at 2.95 eV, mostly MLCT states at the bpy ligands are excited (in petrol green). Within few hundred fs, subsequent intersystem crossing (ISC) and internal conversion (IC) lead to the population of states where the excited electron is located at the $^{\mathrm{S-S}}$bpy ligand (in orange). From there, the T_1 state is reached and the S–S bond length weakens. (b) By adding a subsequent IR laser control pump field (or sequence of those), S–S weakening can be preventing transferring population from the MSCT back to the MLCT states.

the pySOC suite.[42] Further computational details are in Section S1 of the ESI.

Before undertaking the challenge to modify the excited state dynamics of the complex, it is necessary to investigate the natural response of the molecule using an excitation pump pulse explicitly. To this aim, we employ a pulse with an energy of 2.95 eV, resonant with the main absorption peak of mainly MLCT character;[32] henceforth, labelled as pump$_{UV}$ pulse (Figure S1 and Table S1). We take a Gaussian envelope function with full width half maximum (FWHM) of 50 fs, corresponding to a peak intensity of 75 GW/cm^2 ($1.46{\cdot}10^{-3}$ a.u. maximum amplitude of the electric field). This pump$_{UV}$ pulse is able to invert 41% of the population (see Figure 2a) from a set of 4000 trajectories initialized in the electronic singlet ground state. Further details on the laser pulse are provided in Section S2. The resulting time-dependent populations are shown in Figure 2a. They are classified according to their electronic character as follows. $[\mathrm{Ru}(^{\mathrm{S--S}}\mathrm{bpy})(\mathrm{bpy})_2]^{2+}$ is split into 4 fragments, the central metal atom (M), the two bpy ligands (L and L) and $^{\mathrm{S-S}}$bpy (S). If both, electron and hole in the excitation are located on the same fragment, the state is a centered state (that is, metal-centered MC, ligand-centered LC or SC) while if electron and hole are located on different fragments, the states have charge-transfer (CT) character (i.e. MLCT, MSCT, LMCT, SMCT, LSCT, SLCT, LLCT). This analysis is done from the transition density matrices using TheoDORE.[43]

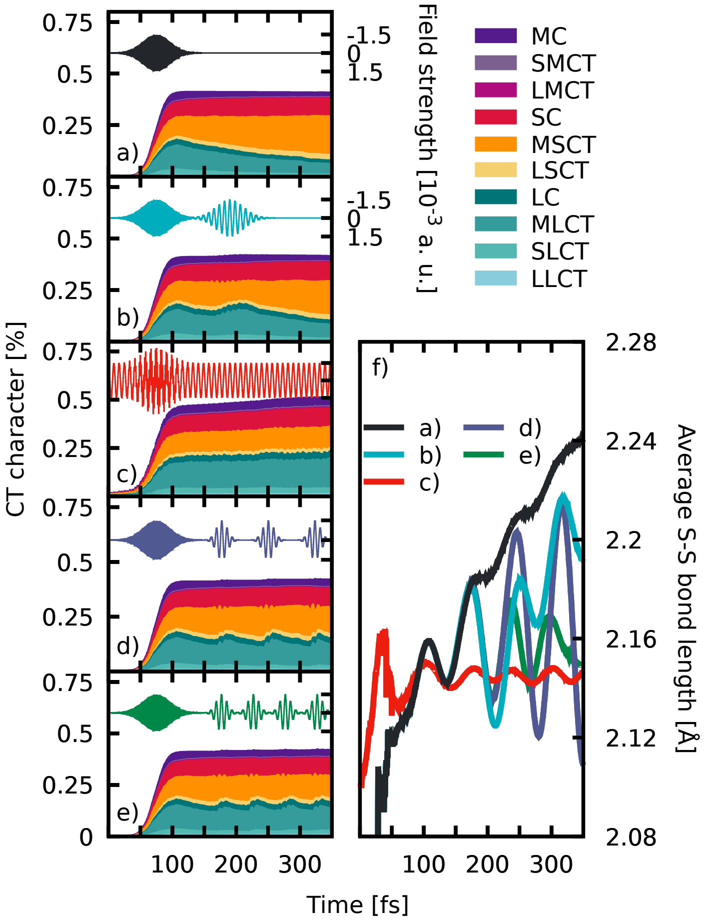

Figure 2: a-e) Time-dependent populations classified according to their charge-transfer character influenced by pulse sequences depicted. f) Time-evolution of the average S–S bond length for all excited trajectories simulated using the pulse sequences depicted in a)-e).

According to their electronic character, the pump$_{UV}$ pulse excites a mixture of MLCT, MSCT, and SC states (Figure 2a). However, after ca 100 fs there is a clear decline of the MLCT contribution in favor of MSCT states. This declines agrees with the decrease previously found in the simulations of Ref. 32 that instead of a pump pulse used an instantaneous excitation (i.e. placing all the trajectories at t=0 fs directly in the electronic excited states, reminiscent of the reflection principle in wave packet dynamics[44]). Both sets of dynamics are yet different at initial times: upon instantaneous excitation,[32] the initial distribution of CT states is dominated by MLCT states, which then undergo ultrafast transfer into MSCT states; using a finite pulse, there is an almost equal mixture of MSCT+SC and MLCT states at the peak of the pulse. The latter is due to the delayed excitation implicit within the finite pump pulse, where any excited trajectory will already start the ultrafast relaxation towards MSCT states while other trajectories are only excited later, resulting in a mixture of populations at the peak of the pulse.

Population of the T_1 is associated with an increase in the equilibrium S–S bond length, which in the employed LVC model goes from 2.11 Å in the S_0 to 2.34 Å in the T_1. Note that the latter value is underestimated with respect to TD-DFT reference calculations,[32] due to the harmonic character of the LVC potentials. In any case, the elongation of the average S–S bond length for all excited trajectories (Figure 2f) can be taken as a clear indication of S-S dissociation leading to eventual sulfide extrusion.[31] The observed S–S bond stretching is not linear but goes in steps. The initial peak can be explained by two concurrent effects: On the one hand, a coherent increase in the S–S bond length for the excited state trajectories is visible as trajectories are promoted out of the S–S equilibrium bond length in the S_0 state. On the other hand, the use of a Gaussian shaped pump pulse, imprints a Gaussian shape in the evolution of the properties of the excited wave packet (Section S3). Indeed, the first maximum of the S–S bond length average located at 104.5 fs has exactly the width of the intensity of the laser pulse (Figure S2) and arises 29.5 fs after the maximum of the pump pulse. Therefore, excited trajectories take on average 30 fs to increase the S–S bond length from the initial length. Subsequent maxima are roughly 75 fs apart, corresponding to the time needed for a single oscillation of the disulfide bond. Those subsequent maxima undergo a visible broadening at later times due to an increase in population of the T_1 state and relaxation to the respective minimum structure featuring the weakened S–S bond. The weakened disulfide bond in turn increases the time needed for a single oscillation, resulting in a broadening in time for reaching the S–S bond length maxima as more and more trajectories fall out of sync.

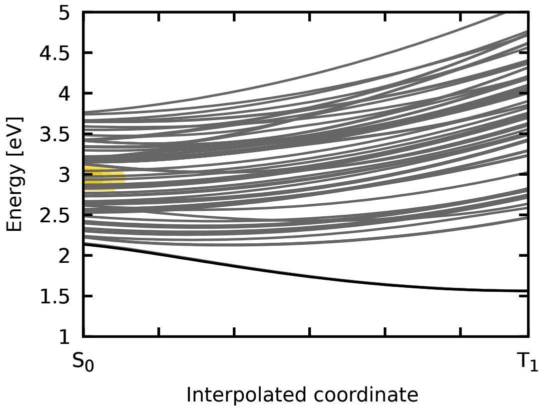

Figure 3: Potential energy plot for all considered states along the interpolation of internal coordinates from the S_0 to the T_1 minimum energy geometry. The T_1 state is highlighted in black and the region where the pump pulse will promote strongest is marked in yellow.

Looking at the PESs that connect the S_0 with the T_1 minimum structures (Figure 3), one can see that all states but T_1 are destabilized when approaching the T_1 minimum. Thus, once the T_1 state is populated, relaxation is barrierless and almost ballistic. The high density of states surrounding the initially excited states opens up a multitude of different branching pathways, all eventually leading to the T_1 state, where the excited electron is located at the $^{S-S}$bpy ligand. To modify this ultrafast decay towards states that involve the $^{S-S}$bpy ligand and ultimately lead to an S–S bond length elongation, a suitable target needs to be defined. Keeping in mind that the T_1 state is of MSCT+SC character and knowing that MLCT states are found at energies higher than their MSCT counterparts, we set our control goal to increase the population of states located at the plain bpy ligands through the dynamics.

Due to the high number of states, different onset times, and possible relaxation routes, no suitable laser pulse can be derived from a mere inspection of the PESs in Figure 3. Instead, and borrowing from local control theory,[45] we define the time-dependent target quantity $p_L(E_{\beta\alpha}, t)$

$$p_L(E_{\beta\alpha}, t) = |\mu_{\beta\alpha}| \cdot \mathrm{MLCT}_\alpha^2, \tag{1}$$

where β is the active excited state in the current trajectory and α is another excited state with a particular percentage of MLCT character (MLCT_α). The transition dipole element between α and β ($\mu_{\beta\alpha}$) is proportional to the ease of a transition between both states and $E_{\beta\alpha}$ is the energy difference between the active state and state α and therefore reminiscent of the frequency needed for resonance between β and α. This time-dependent measure can be evaluated for each state and each time step for all trajectories to obtain a map that showcases which laser pulses are likely to excite population to the MLCT band.

To further increase selectivity between MLCT and MSCT or SC states, we expand the quantity $p_L(E_{\beta\alpha}, t)$ to $p(E_{\beta\alpha}, t)$, defined as:

$$p(E_{\beta\alpha}, t) = |\mu_{\beta\alpha}| \cdot (\mathrm{MLCT}_\alpha^2 - \mathrm{MSCT}_\alpha^2 - \mathrm{SC}_\alpha^2) \tag{2}$$

where MSCT_α and SC_α are the contributions of MSCT and SC character of the excited state α. We collected $p(E_{\beta\alpha}, t)$ values for 1000 trajectories propagated during 250 fs, starting in the S_0, and using the pump pulse described above. The resulting $p(E_{\beta\alpha}, t)$ values have been convoluted in energy with Gaussian functions of 0.3 eV FWHM, yielding Figure 4.

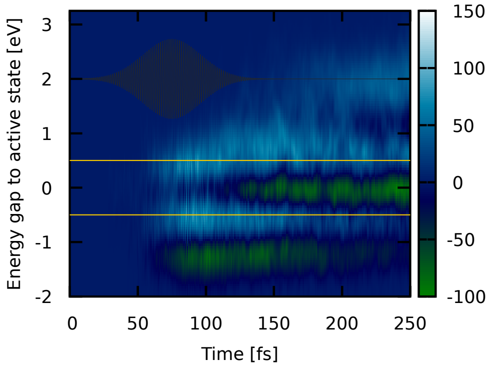

Figure 4: Values of $p(E_{\beta\alpha}, t)$ initiated by the pump$_{UV}$ pulse, reminiscent of the density of trajectories that could transiently be excited from the current active state to either MLCT states (positive $p(E_{\beta\alpha}, t)$ values shown in light blue to white) or MSCT+SC states (negative $p(E_{\beta\alpha}, t)$ values shown in green). The y-axis is the energy needed for a resonant transition with the active state. The pump pulse is depicted in black and a viable laser frequency to excite MLCT states is indicated with horizontal lines in gold.

We see that around $t = 75$ fs, MLCT bands (light blue) that could be transiently excited build around 0.5 eV above and below the currently active state (see gold lines). MSCT+SC states (in green) instead are found at lower energy differences (1.2 eV below the active states), corroborating their overall stabilization with respect the MLCT states. Throughout the dynamics, the energetic position of these MLCT and MSCT+SC bands stay constant, only fading out slowly towards the end of the dynamics as they represent lower energy states accessible from rather high energy states; these higher energy states get less and less populated the longer the dynamics continues due to non-adiabatic relaxation to lower energy states. An additional MSCT+SC band appears at the same energy as the active states (0 eV in Figure 4) because it gets more and more populated, with other MSCT+SC states in close vicinity. Finally, we can see that a MLCT band raises around 200 fs at ca 2 eV. This additional band represents trajectories that are very close to the T$_1$ minimum energy geometry from where the MLCT band is far away in energy.

The analysis of Figure 4 hints to a two-laser-pulse scenario to change the excited state dynamics of [Ru($^{S--S}$bpy)(bpy)$_2$]$^{2+}$: a first pulse with frequency of 2 eV could be used to excite trajectories close to the T_1 minimum geometry back to MLCT states, from where the S–S bond would contract. A second pulse could act at a much lower frequency (0.5 eV) and target trajectories in the process of descending down the ladder of states towards the low-lying MSCT+SC states. However, a 2 eV pulse would also act as an additional pump pulse inverting S_0 population, further complicating the ensuing dynamics. Therefore, the 2 eV pulse was discarded and only the infrared (IR) 0.5 eV pulse will be used besides the original pump$_{UV}$ pulse. We note that surface hopping cannot account for vibrationally excited states that could potentially be excited by an IR pulse within the electronic ground state, so these are excluded.

Accordingly, the following two-pulse setup is envisioned: the pump$_{UV}$ pulse used previously to excite population from the S_0, followed by a 0.5 eV pulse (labelled pump$_{IR}$), with again a FWHM 50 fs Gaussian envelope and a maximum intensity of 75 GW/cm^2 (corresponding to $1.46 \cdot 10^{-3}$ a.u. maximum amplitude of the electric field). The schematic influence of the expected dynamics when applying the pump$_{IR}$ to control the dynamics of Ru($^{S--S}$bpy)(bpy)$_2$]$^{2+}$ is shown in Figure 1b. The delay time (τ) between UV and IR pulses is defined as

$$\tau = t_{0,IR} - t_{0,UV} \tag{3}$$

where $t_{0,IR/UV}$ are the centers of IR and UV pulses, respectively. This delay is set to 115 fs (Section S3, Figure S3) to guarantee a distinct separation between the initial UV pump and the IR pulse. We note that because the transition dipole moments of [Ru($^{S--S}$bpy)(bpy)$_2$]$^{2+}$ are very large and they are paired with an intense laser field, the resulting dynamics will be a combination of weak- and strong-field effects. The evolution of the states triggered by the pump$_{UV}$-pump$_{IR}$ pulse sequence is shown in Figure 2b. During the duration of the pump$_{IR}$ pulse, an increase of MLCT character is visible accompanied by a decrease of MSCT character, resulting in a distribution of MLCT to MSCT+SC characters similar to the distribution at the end of the pump$_{UV}$ pulse. Accordingly, the average S–S bond length of excited trajectories (Figure 2f), undergoes a strong reduction during the time the pump$_{IR}$

pulse is on. Both observations indicate a successful population of MLCT states during the pump_{IR} pulse, that in turn leads to a hardening of the S–S bond. However, as the pump_{IR} pulse ends, repopulation of MSCT states is observed paired with an increase in the average S–S bond length.

As a next attempt to stop the decay towards the T_1 state completely, the pump_{IR} pulse was substituted with a continuous wave of frequency 0.5 eV providing a permanent drain from MSCT to MLCT. This continuous wave overlaps with the pump_{UV} pulse, so that it excites few trajectories at earlier times than the pulse(s) of Figures 2a and 2b, as it can seen in Figure 2c. After the pump_{UV} pulse ends, more and more trajectories are excited with 51% population inversion at $t = 350$ fs. As intended, the decay of the MLCT character is completely blocked and the ratio of CT states remains constant after the maximum of the initial pump_{UV} pulse. Furthermore, the S–S bond length (Figure 2f) oscillates around a value of 2.145 Å – only slightly elongated with respect to the equilibrium value (2.11 Å). Thus, this permanent IR continuous wave traps the excited population effectively in a mixture of states where the electron is located at any of the three ligands without relaxing to the T_1 minimum structure.

Finally, we investigate whether the continuous wave can be efficiently replaced by a train of short pump_{IR} pulses –allowing for a more targeted modulation of the excited state dynamics–, where each single IR pulse would promote population of MLCT states accompanied by a reduction of the S–S bond. To position the pump pulses, we use the oscillations of the S–S bond length, so that the pump pulses are placed at the respective maxima. We use three pump_{IR} pulses with a FWHM of 20 fs, separated from each other by 73 fs with the first acting with a τ of 102 fs between the pump_{UV} pulse and the first IR pulse. The resulting dynamics are shown in Figure 2d. As it can be seen the MLCT character increases during the duration of all three laser pulses at the expense of MSCT contribution and the S–S bonds decreases strongly for each pulse hitting the complex. However, concomitant to each decrease of the S–S bond length there is a stronger increase, leading to even stronger coherent oscillations after each pulse. This unwanted behaviour can be rationalized by two accumulating effects. One relates to the timing of the pump$_{IR}$ pulses, which acting at the maximum of the S–S bond length for most trajectories, promotes the system to populate MLCT states but the accompanying hardening of the bond results in a gain of kinetic energy along the S–S bond vibration –resembling a swing on a playground where a extra force is applied when the maximum height is reached. The second is that the strong pump$_{IR}$ pulses can increase the synchronization between more and more trajectories as the PESs shift with the time-dependent slow oscillations of the pulse. As a result, this train of IR pulses is not useful to prevent S–S dissociation.

An alternative is to set the centers of the IR pulses asynchronous to the S–S bond oscillations to obtain the opposite of the swing-effect described above. To this aim, another train of pump$_{IR}$ pulses is simulated, starting from the same first IR pulse with all subsequent laser pulses acting with a τ of only 50 fs. This way, the first pump$_{IR}$ pulse initiates the swing, which is then damped by the next pulse acting before a full oscillation of the S–S bond can be completed, effectively removing kinetic energy from the vibration. The time-resolved population is depicted in Figure 2e. A larger proportion of MLCT states and a decrease of the average S–S bond length is achieved, when compared to the previous pulse sequence. The asynchronous timing of the pulses with respect to the S–S bond oscillations results in an effective shortening of the average S–S bond length compared to the uncontrolled dynamics, giving an average bond length that oscillates around a value of 2.16 Å.

In conclusion, in this Letter we show how the excited state dynamics of $[\mathrm{Ru}(^{\mathrm{S--S}}\mathrm{bpy})(\mathrm{bpy})_2]^{2+}$, a derivative of the well-known photosensitizer $[\mathrm{Ru(bpy)_3}]^{2+}$, can be modified using laser pulses in the context of surface hopping trajectory simulations. We showed that a simple IR pulse is capable of transiently exciting population away from the pathway to the T_1 minimum energy structure, which is characterized by a weakening of the S–S bond that finally leads to dissociation. However, after the pulse ends, the natural course of the dynamics turns on, steering back towards the T_1 minimum and thus leading to S–S bond stretching. By replacing the infrared pulse by a continuous wave of the same frequency, we demonstrated that the distribution of populated states and the S–S bond length can be frozen almost at the ground state equilibrium value preventing dissociation. Similar effects can be achieved by using a train of pulses, where depending on the interval between two pulses, the oscillations of the S–S bond can be better synchronized or be kept at a strongly reduced level close to the modifications achieved using a continuous wave. By ultimately avoiding sulfide extrusion, such compound could be subsequently reduced exploiting the $2e/2H^+$ nature of the disulfide/dithiol interconversion and find application in solar fuel generation.

This example suggests that control of excited state dynamics in large molecular systems can be successfully modelled in full dimensionality and can hopefully inspire laser control experiments. The presented approach could be extended to other transition metal complexes, where manipulating the different electronic states can be useful to break or hold a particular bond or push electron transfer in a particular direction.

Acknowledgement

The authors thank the University of Vienna for continuous support and the Vienna Scientific Cluster for generous allocation of computational resources.

Supporting Information Available

Further computational details, definition of the laser fields used, additional simulations and analysis of the S–S bond length through the dynamics, as well as time delays among the pulses.

References

(1) Maiuri, M.; Garavelli, M.; Cerullo, G. Ultrafast Spectroscopy: State of the Art and Open Challenges. *J. Am. Chem. Soc.* **2020**, *142*, 3.

(2) Henriksen, N. E.; Hansen, F. Y. *Theories of Molecular Reaction Dynamics 2nd Edition*; Oxford University Press.

(3) Mitrić, R.; Petersen, J.; Bonačić-Koutecký, V. Laser-Field-Induced Surface-Hopping Method for the Simulation and Control of Ultrafast Photodynamics. *Phys. Rev. A* **2009**, *79*, 053416.

(4) Marquetand, P.; Richter, M.; González-Vázquez, J.; Sola, I.; González, L. Nonadiabatic ab initio Molecular Dynamics Including Spin–Orbit Coupling and Laser Fields. *Faraday Discuss.* **2011**, *153*, 261.

(5) Bajo, J. J.; Granucci, G.; Persico, M. Interplay of Radiative and Nonradiative Transitions in Surface Hopping with Radiation-Molecule Interactions. *J. Chem. Phys.* **2014**, *140*, 044113.

(6) Fiedlschuster, T.; Handt, J.; Schmidt, R. Floquet Surface Hopping: Laser-Driven Dissociation and Ionization Dynamics of H_2^+. *Phys. Rev. A* **2016**, *93*, 053409.

(7) Makhov, D. V.; Shalashilin, D. V. Floquet Hamiltonian for Incorporating Electronic Excitation by a Laser Pulse into Simulations of Non-adiabatic Dynamics. *Chem. Phys.* **2018**, *515*, 46.

(8) Penfold, T. J.; Pápai, M.; Møller, K. B.; Worth, G. A. Excited State Dynamics Initiated by an Electromagnetic Field within the Variational Multi-Configurational Gaussian (vMCG) Method. *Comput. Theor. Chem.* **2019**, *1160*, 24.

(9) Röder, A.; Petersen, J.; Issler, K.; Fischer, I.; Mitrić, R.; Poisson, L. Exploring the Excited-State Dynamics of Hydrocarbon Radicals, Biradicals, and Carbenes Using

Time-Resolved Photoelectron Spectroscopy and Field-Induced Surface Hopping Simulations. *J. Phys. Chem. A* **2019**, 10643.

(10) Sanz-Sanz, C.; Worth, G. A. Field Modified Spin–Orbit Potential Curves of IBr. Preliminary Dynamical Results. *Phys. Chem. Chem. Phys.* **2019**, *21*, 14429.

(11) Zhou, Z.; Chen, H.-T.; Nitzan, A.; Subotnik, J. E. Nonadiabatic Dynamics in a Laser Field: Using Floquet Fewest Switches Surface Hopping To Calculate Electronic Populations for Slow Nuclear Velocities. *J. Chem. Theory Comput.* **2020**, *16*, 821.

(12) Schirò, M.; Eich, F. G.; Agostini, F. Quantum–classical nonadiabatic dynamics of Floquet driven systems. *J. Chem. Phys.* **2021**, *154*, 114101.

(13) Heindl, M.; González, L. Validating Fewest-Switches Surface Hopping in the Presence of Laser Fields. *J. Chem. Phys.* **2021**, *154*, 144102.

(14) González, L. In *Lasers in Chemistry: Probing and Influencing Matter: Vol 2*; M., L., Ed.; Wiley-Vch, 2008.

(15) Henriksen, N. E. Laser control of chemical reactions. *Chem. Soc. Rev.* **2002**, *31*, 37–42.

(16) Worth, G. A.; Richings, G. W. Optimal Control by Computer. *Annu. Rep. Prog. Chem., Sect. C: Phys. Chem.* **2013**, *109*, 113–139, Publisher: The Royal Society of Chemistry.

(17) Malinovsky, V. S.; Meier, C.; Tannor, D. J. Optical Paralysis in Electronically Congested Systems: Application to Large-Amplitude Vibrational Motion of Ground State Na_2. *Chem. Phys.* **1997**, *221*, 67.

(18) Marquetand, P.; Engel, V. Local Control Theory Applied to Molecular Photoassociation. *J. Chem. Phys.* **2007**, *127*, 084115.

(19) Hoff, P. v. d.; Thallmair, S.; Kowalewski, M.; Siemering, R.; Vivie-Riedle, R. d. Optimal Control Theory – Closing the Gap Between Theory and Experiment. *Phys. Chem. Chem. Phys.* **2012**, *14*, 14460.

(20) Geißler, D.; Marquetand, P.; González-Vázquez, J.; González, L.; Rozgonyi, T.; Weinacht, T. Control of Nuclear Dynamics with Strong Ultrashort Laser Pulses. *J. Phys. Chem. A* **2012**, *116*, 11434–11440.

(21) Petersen, J.; Mitrić, R. Electronic Coherence Within the Semiclassical Field-Induced Surface Hopping Method: Strong Field Quantum Control in K_2. *Phys. Chem. Chem. Phys.* **2012**, *14*, 8299.

(22) Arasaki, Y.; Takatsuka, K. Pulse-Train Photoelectron Spectroscopy of Electronic and Nuclear Dynamics in Molecules. *ChemPhysChem* **2013**, *14*, 1387.

(23) Waldl, M.; Oppel, M.; González, L. Controlling the Excited-State Dynamics of Nuclear Spin Isomers Using the Dynamic Stark Effect. *J. Phys. Chem. A* **2016**, *120*, 4907–4914.

(24) Ganesa Subramanian, M. K.; Santra, R.; Welsch, R. Infrared-laser-pulse-enhanced Ultrafast Fragmentation of N_2^{2+} Following Auger Decay: Mixed Quantum-Classical Simulations. *Phys. Rev. A* **2018**, *98*, 063421.

(25) Tóth, A.; Csehi, A.; Halász, G. J.; Vibók, A. Control of Photodissociation with the Dynamic Stark Effect Induced by THz Pulses. *Phys. Rev. Research* **2020**, *2*, 013338.

(26) Valentini, A.; Wildenberg, S. v. d.; Remacle, F. Selective Bond Formation Triggered by Short Optical Pulses: Quantum Dynamics of a Four-Center Ring Closure. *Phys. Chem. Chem. Phys.* **2020**, *22*, 22302.

(27) Tannor, D. J.; Rice, S. A. Control of selectivity of chemical reaction via control of wave packet evolution. *J. Chem. Phys.* **1985**, *83*, 5013–5018.

(28) Curchod, B. F. E.; Penfold, T. J.; Rothlisberger, U.; Tavernelli, I. Local Control Theory in Trajectory-Based Nonadiabatic Dynamics. *Phys. Rev. A* **2011**, *84*, 042507.

(29) Curchod, B. F. E.; Penfold, T. J.; Rothlisberger, U.; Tavernelli, I. Local Control Theory

in Trajectory Surface Hopping Dynamics Applied to the Excited-State Proton Transfer of 4-Hydroxyacridine. *ChemPhysChem* **2015**, *16*, 2127.

(30) Cattaneo, M.; Schiewer, C. E.; Schober, A.; Dechert, S.; Siewert, I.; Meyer, F. 2,2'-Bipyridine Equipped with a Disulfide/Dithiol Switch for Coupled Two-Electron and Two-Proton Transfer. *Chem. Eur. J.* **2018**, *24*, 4864.

(31) Hua, S.-A.; Cattaneo, M.; Oelschlegel, M.; Heindl, M.; Schmid, L.; Dechert, S.; Wenger, O. S.; Siewert, I.; González, L.; Meyer, F. Electrochemical and Photophysical Properties of Ruthenium(II) Complexes Equipped with Sulfurated Bipyridine Ligands. *Inorg. Chem.* **2020**, *59*, 4972.

(32) Heindl, M.; Hongyan, J.; Hua, S.-A.; Oelschlegel, M.; Meyer, F.; Schwarzer, D.; González, L. Excited-State Dynamics of $[\mathrm{Ru}(^{\mathrm{S-S}}\mathrm{bpy})(\mathrm{bpy})_2]^{2+}$ to Form Long-Lived Localized Triplet States. *Inorg. Chem.* **2021**, *60*, 1672.

(33) Richter, M.; Marquetand, P.; González-Vázquez, J.; Sola, I.; González, L. SHARC: ab Initio Molecular Dynamics with Surface Hopping in the Adiabatic Representation Including Arbitrary Couplings. *J. Chem. Theory Comput.* **2011**, *7*, 1253.

(34) Mai, S.; Marquetand, P.; González, L. Nonadiabatic dynamics: The SHARC approach. *WIREs Comput. Mol. Sci.* **2018**, *8*, e1370.

(35) Mai, S.; Richter, M.; Heindl, M.; Menger, M. F. S. J.; Atkins, A.; Ruckenbauer, M.; Plasser, F.; Ibele, L. M.; Kropf, S.; Oppel, M. et al. SHARC2.1: Surface Hopping Including Arbitrary Couplings — Program Package for Non-Adiabatic Dynamics. sharc-md.org, 2019.

(36) Tully, J. C. Molecular Dynamics with Electronic Transitions. *J. Chem. Phys.* **1990**, *93*, 1061.

(37) Marquetand, P.; Richter, M.; González-Vázquez, J.; Sola, I.; González, L. Nonadiabatic ab initio molecular dynamics including spin–orbit coupling and laser fields. *Faraday Discuss.* **2011**, *153*, 261.

(38) Bajo, J. J.; González-Vázquez, J.; Sola, I. R.; Santamaria, J.; Richter, M.; Marquetand, P.; González, L. Mixed Quantum-Classical Dynamics in the Adiabatic Representation To Simulate Molecules Driven by Strong Laser Pulses. *J. Phys. Chem. A* **2012**, *116*, 2800–2807.

(39) Wigner, E. On the Quantum Correction for Thermodynamic Equilibrium. *Phys. Rev.* **1932**, *40*, 749.

(40) Köppel, H.; Domcke, W.; Cederbaum, L. S. In *Advances in Chemical Physics Vol. 57*; Prigogine, I., Rice, S. A., Eds.; John Wiley & Sons, 1984; pp 59–246.

(41) Plasser, F.; Gómez, S.; Menger, M. F. S. J.; Mai, S.; González, L. Highly efficient surface hopping dynamics using a linear vibronic coupling model. *Phys. Chem. Chem. Phys.* **2019**, *21*, 57–69.

(42) Gao, X.; Bai, S.; Fazzi, D.; Niehaus, T.; Barbatti, M.; Thiel, W. Evaluation of Spin-Orbit Couplings with Linear-Response Time-Dependent Density Functional Methods. *J. Chem. Theory Comput.* **2017**, *13*, 515.

(43) Plasser, F. TheoDORE: A Toolbox for a Detailed and Automated Analysis of Electronic Excited State Computations. *J. Chem. Phys.* **2020**, *152*, 084108.

(44) Schinke, R. The rotational reflection principle in the direct photodissociation of triatomic molecules. Close-coupling and classical calculations. *J. Chem. Phys.* **1986**, *85*, 5049–5060.

(45) J. Tannor, D.; Kosloff, R.; Bartana, A. Laser cooling of internal degrees of freedom of molecules by dynamically trapped states. *Faraday Discuss.* **1999**, *113*, 365–383.

Supporting Information: Taming S–S Bonds with Laser Fields. Nonadiabatic Surface-Hopping Simulations in a Ruthenium Complex

Moritz Heindl, Leticia González
Institute of Theoretical Chemistry, Faculty of Chemistry, University of Vienna,
Währingerstr. 17, 1090 Vienna, Austria

December 22, 2021

Contents

S1 Further computational details

All the nonadiabatic dynamics simulations have been carried out using the program package SHARC 2.1.[1] The nuclear and electronic propagation was performed in a completely diagonal basis where both the off-diagonal coupling terms of the transition dipole moments with the external field and the spin-orbit couplings are projected onto the diagonal of the Hamiltonian, forming a set of spin-mixed states.[2, 3] In the context of laser fields, such a procedure is known as the instantaneous adiabatic representation or instantaneous Born-Oppenheimer representation.[4] Such a basis has been found to be beneficial compared to keeping the laser interactions as off-diagonal elements in the presence of strong external fields[5] but has also been shown to give nonphysical results in other cases where a Floquet basis was found to be superior.[6, 4, 7] A time step of 0.25 fs has been employed for the nuclear propagation while the electronic wave function was propagated using time steps of 0.01 fs in a locally diabatic basis.[8] The simulations carried out to find suitable wave lengths for control of the excited state dynamics have been run for 250 fs, while all other simulations were run for 350 fs.

Decoherence of the electronic wave function on different states has been considered with the energy-based criterion acting in every time step using a decoherence parameter of 0.1 Hartree.[9, 10] Commonly, the kinetic energy of surface hopping trajectories is adapted at a hopping event to counteract the change in the potential energy experienced at the hop, hence, conserving the total energy of each trajectory.[11, 12] In the presence of laser fields, this is complicated by the fact that energy uptake or dissipation in the form of photon absorption or stimulated emission is possible, resulting in changes to the total energy. To differentiate between both types of hops (light-induced and not light-induced), a number of possibilities exist, [2, 13] but none of them were found suited to deal with the here investigated transition metal complex in the diagonal representation and the sets of pulses employed. Additionally, modifying the kinetic energy along the non-adiabatic coupling vector –which is considered the best direction to rescale the kinetic energy along[14, 15, 12]– is complicated in the presence of states of different multiplicities, and this is not remedied by the use of a set of mixed states.[16] Therefore, it has been decided that the kinetic energy at a transition between states is not adapted, even if in the literature such decision showed deviations in comparison with quantum simulations.[17, 18, 12] In order to estimate how much the current dynamics is affected by this choice, a comparison is shown below in Section S6.

S2 The laser pulses

The interaction of the molecule with laser fields is treated within the semi-classical dipole approximation, where the field is classical and the electrons are quantum mechanical objects. A uniform field within each time step is assumed. The multipole expansion of the interaction of the field with the molecule is truncated to linear terms, i.e. to the interaction with the transition dipole moments of the system. Interactions due to the overall charge of the molecule are neglected as these would be identical for all considered states because the number of electrons does not change within the simulations. Accordingly, the simulated interaction ($\hat{V}_{ext}$) takes the form of

$$\hat{V}_{ext} = -\hat{\mu}(\mathbf{R}) \cdot \epsilon(t) \tag{1}$$

with $\hat{\mu}(\mathbf{R})$ being the dipole matrix and $\epsilon(t)$ the time-dependent field. The field can be written as a sum of N_L laser pulses as follows

$$\epsilon(t) = \sum_{i}^{N_L} \mathbf{p}_i \cdot \epsilon_i^0 \cdot \cos(\omega_i(t - t_{0,i}) + \eta) \exp\left[-4 \cdot \ln 2 \left(\frac{t - t_{0,i}}{FWHM_i}\right)^2\right]. \tag{2}$$

Here $\mathbf{p}_i$ is the polarization vector of laser pulse i with a maximum amplitude of ϵ_i^0 and frequency ω_i. The phase factor η is set to zero. The envelope function is a simple Gaussian function centered at $t_{0,i}$. For all simulations, a linearly polarized field along the x direction was used, as the molecule showed the largest transition dipole moments along this axis (which in a laboratory fixed molecule, it points from the central metal atom towards the disulfide bridge of $^{\text{S}-\text{S}}$bpy). The estimation of the $p(E_{\beta\alpha}, t)$ values to determine suitable control pulses also include transition dipole moments along x. In order to verify that the observed dynamics is not an artifact of the assumed alignment of the simulated ruthenium complex, the influence of changing the polarization from x direction to a random polarization is discussed in Section S5.

All laser fields used in the main manuscript are depicted in Figure S1 with laser parameters collected in Table S1.

	ϵ_i^0 [GW/cm^2]	ω [eV]	$t_{0,i}$ [fs]	$FWHM_i$ [fs]
a)	75	2.95	75.0	50.0
b)	75	0.50	190.0	50.0
c)	75	0.50	0.00	∞
d)	75	0.50	177.5/250.5/323.5	20.0
e)	75	0.50	177.5/227.5/277.5/327.5	20.0

Table S1: Laser parameters of the lasers employed in panels a-e of Fig S1.

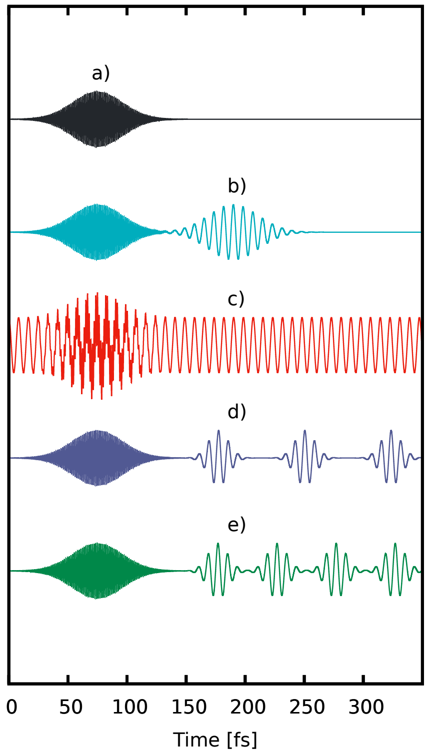

Figure S1: Laser fields used in the main manuscript. Parameters listed in Table S1 .

S3 Coherent increase in the S–S bond length

Excitation of $[\mathrm{Ru}(^{\mathrm{S--S}}\mathrm{bpy})(\mathrm{bpy})_2]^{2+}$ with the pump$_{UV}$ pulse triggers coherent oscillations in the average of the S–S bond length, see Figure S2. The average S–S bond length increases until reaching a first maximum located 29 fs after the maximum of the pump pulse. Following this first maximum, the average S–S bond length oscillates to lower values before entering a stepwise and recurring increase in average as more and more trajectories decay towards the T_1 minimum energy structure, where the S–S bond drastically weakens.

When investigating this oscillatory behavior, we found that the first oscillation of the average bond length almost exactly coincides with the shape of the applied intensity I ($I \propto \epsilon(t)^2$). As mentioned in the main text, a two-fold mechanism is at work here: I) First, the amount of excited trajectories changes during the length of the pump pulse. Each excited trajectory initiates its dynamics at a different point in time, resulting in different absolute time scales at which the T_1 minimum is reached. The more trajectories get excited in a single time step, the stronger the influence of these coherently excited trajectories on the average S–S bond length, resulting in an intensity shaped oscillation. II) Second, the S–S bond length moves coherently in the initially excited states. The interested reader can go to Figure S5c where no explicit laser pulse is used to excite the trajectories but instead the trajectories are directly projected in the electronic excited states at time zero. In this case, a very similar pattern of rising average S–S bond length is observed, albeit the oscillations are sharper than when using an explicit UV laser pulse.

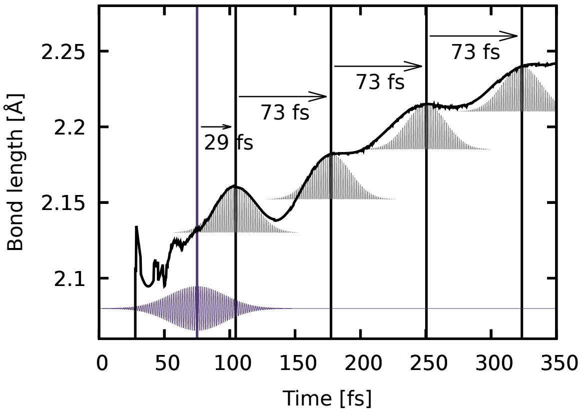

Figure S2: Average S–S bond length (black) after a pump$_{UV}$ excitation. The laser field $\epsilon(t)$ is plotted in purple. The grey shapes fitted into the maxima along the S–S bond average correspond to the (scaled) intensity ($\epsilon(t)^2$) of the pump pulse, which was manually moved to be centered at the respective maxima.

Overall, we can conclude that the oscillations are due to differences in the equilibrium point of the ground and the excited states, while the broadening of the observed oscillation is due to the employed pulse. The oscillation has a recurrence time of ca 73 fs, close to experimentally determined disulfide bridge bond vibrations (between 65-77 fs).[19] At later times, the oscillations flatten out as trajectories follow different relaxation pathways, resulting in slightly shorter or longer bond oscillations, until more trajectories show longer bond oscillations as the S–S bond weakens.

S4 Time delay analysis

To see how sensitive the excited state dynamics is to the position of the broad FWHM=50 fs pump$_{IR}$ pulse, the effect of several time delays (τ) have been investigated using 4000 trajectories. Besides τ of 115 fs, presented in the main manuscript, we have simulated τ=95 and 135 fs. As shown in Figure S3, the S–S bond length is different, with a smaller dip for τ = 95 fs compared to τ = 115 fs. For a τ = 135 fs the dynamics is similar as for τ =115, indicating that with the employed broad pulse featuring a FWHM of 50 fs, the exact position of the IR pulse is not important to see a reduction in the average of the S–S bond length.

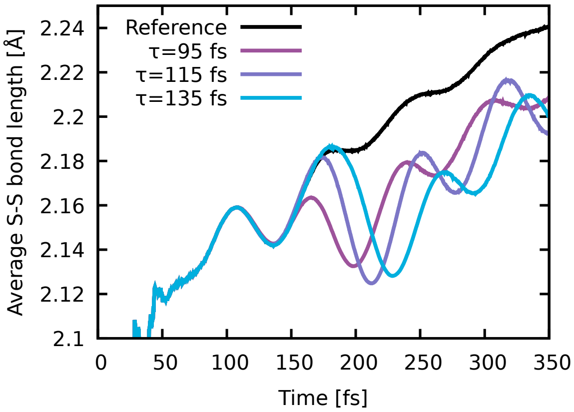

Figure S3: Average S–S bond length for different time delays (τ) between the pump$_{UV}$ and the pump$_{IR}$ pulses (FWHM=50 fs). The reference uses only pump$_{UV}$.

S5 Random laser polarisation

All simulations presented up to now have been conducted using linearly polarized electric fields in the x-direction, because it corresponds to the direction of the largest transition dipole moment, and and thus the initial excitation is maximum along this direction. In order to estimate the effect of the polarization, two computational approaches can be conceived. One is to randomly assign the spatial orientation of each molecule while the electric field acts along x. Another is to keep the orientation of the molecule and randomly adapt the polarization vector of the electric field. We chose the latter approach as it is simpler to implement, especially since each rotated molecule would need to be rotated back into the reference system of normal modes employed in the LVC model.

Using a random polarization for the electric field, two new simulations are set up (Figure S4c and S4d) and compared to those of the main manuscript in Figure 2a and 2b (shown again in Figure S4a and S4b). 4000 trajectories are set up in all cases, each having a completely randomized polarization vector for the complete field (i.e. in a two-pulse setup, both pulses share the same polarization vector) and normalized to still yield a maximum of 75 GW/cm^{-2} intensity. For the case of only pump$_{UV}$, less population is excited with randomly polarized light (26 % compared to 41 %), corroborating that the largest transition dipole moment is located along the x direction. The character of the states populated in both cases (Figure

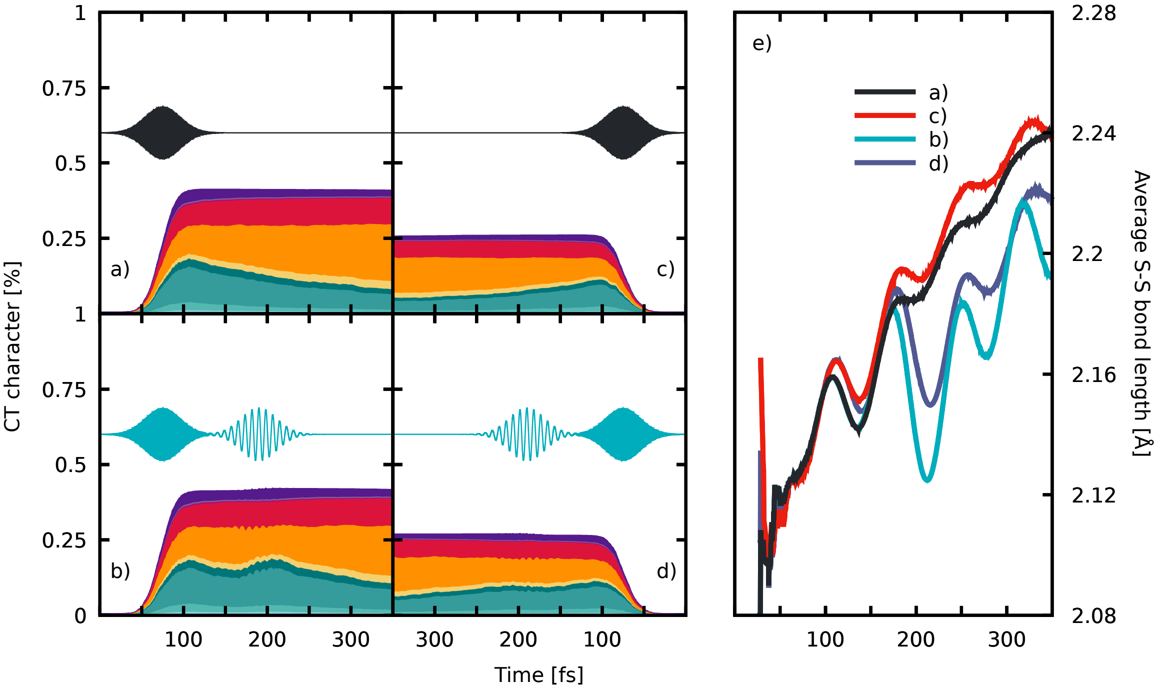

Figure S4: a) Time-resolved population after, (a) a pump$_{UV}$ pulse x-polarized, (b) a pump$_{UV}$-pump$_{IR}$ sequence x-polarized, (c) a pump$_{UV}$ pulse randomly polarized, and d) a pump$_{UV}$-pump$_{IR}$ sequence randomly polarized. e) Corresponding time-evolution of the S–S bond length. All laser pulses have a FWHM=50 fs.

S4a and c, for polarized along x or randomly) are very similar. In the S–S bond length for (Figure S4e), a slightly larger average is found for a randomly orientated electric field but overall the dynamics is very similar.

In the case of the pump$_{UV}$-pump$_{IR}$ sequence we also see a reduction in the amount of excited trajectories using randomized polarization vectors. However, the IR pulse results in a smaller increase of MLCT character than for a similar pulse along x. The average S–S bond length of excited trajectories is also less influenced by the control IR pulse but yields qualitatively similar results. Overall, we can conclude that the choice of the x direction for the electric field only enhance a stronger interaction with the ruthenium complex but dynamics is not affected. In an experiment, where the molecules are randomly oriented, only a smaller amount of those would be excited but the dynamics is expected to be qualitatively the same.

S6 Influence of adapting kinetic energy on a hop

In the main manuscript, the kinetic energy of a surface hopping trajectory was preserved during a hopping event. Therefore, the total energy in a trajectory is not conserved but instead increases for hops to higher lying surfaces and decreases for switches to lower energy surfaces. This methodology has been found[11, 20, 12] to give detrimental results for hops induced via non-adiabatic couplings as the presence of frustrated hops and the instantaneous adjustment of the kinetic energy is said to be important to mimic quantum behavior with the non-adiabatic coupling vector being the best choice for the direction of the velocity adjustment. However, when surface-hopping dynamics includes explicit laser fields, the overall energy conservation does not strictly apply, as hops caused by interaction with the electric field represent absorption or stimulated emission of a photon, associated with an allowed change in total energy. The presence of low-energy laser fields coupled with the propagation in a field-dependent basis invalidates using criteria to differentiate field- and non-adiabatic-induced. Hence, here the hops were not adjusted for energy.

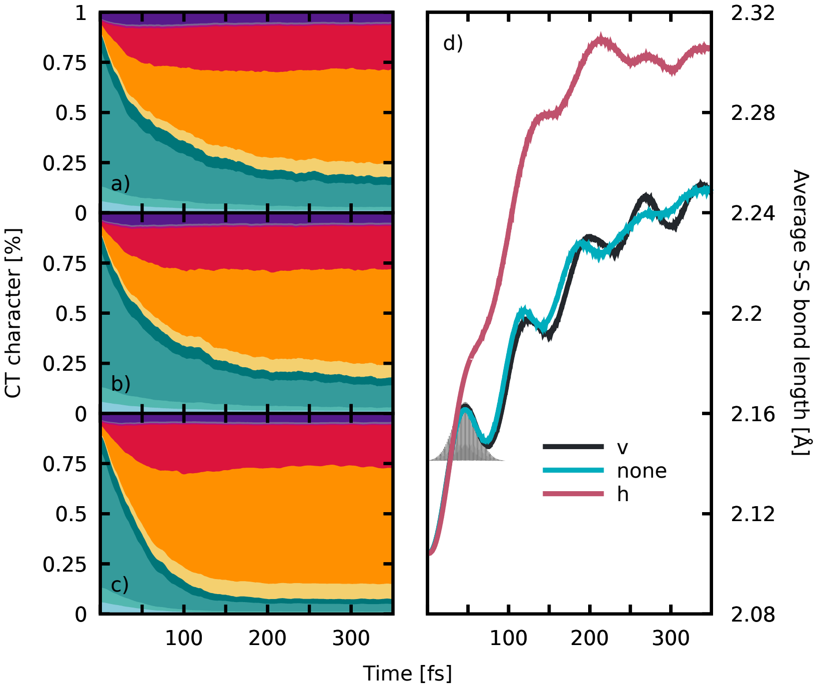

Figure S5: a-c) Time-resolved populations after trajectories are started directly in the electronic excited states. The difference between the sets is that the velocity vector (v) is rescaled at a hopping event to conserve the total energy in a) while b) does not show conservation of energy at a transition between surfaces (none) and c) uses the non-adiabatic coupling vector (h) to adjust the kinetic energy. d) Time evolution of the S–S bond length. The intensity of the pump pulse that was used for dynamics including electric fields is fitted as best as possible to the first maximum of the S–S bond length (see Section S3 for the corresponding discussion).

Still, we found interesting to investigate how large is the influence of adapting or not the kinetic energy, for which two sets of trajectories have been simulated starting in the excited states, differing only in their treatment of velocity adjustment. Accordingly, we prepared two sets of 1000 trajectories, which for convenience, are stochastically selected based on the relative oscillator strength in the energy range of 2.85 to 3.05 eV and projected onto the corresponding excited states (i.e. no explicit laser pump pulse is used). One set of trajectories is rescaled along the velocity vector (v) at a hop, another set is not rescaled at all (none) and a final set uses the non-adiabatic coupling vectors (h) between the involved states to adjust the kinetic energy along. The resulting time-resolved populations are presented in Figure S5a-c. Interestingly, tiny deviations can be observed for the first two sets of dynamics. Only when using the non-adiabatic coupling vector to rescale, distinct and larger increase in MSCT states is observed, indicating that population of low-lying triplet states increases faster in this protocol. Also when looking at the S–S bond length (Figure S5d), deviations between both the first two protocols are negligible and occur only at later times. Not rescaling the velocities results in a stronger broadening of the oscillations of the S–S bond length compared to the adjustment along the full velocity vector. However, when using the non-adiabatic coupling vectors for energy conservation, a very steep increase in S–S bond length is observed, reaching a maximum value of around 2.31 Å after 200 fs from where on it stays almost constant. This value is very close to the equilibrium bond distance found at the T_1 minimum structure of the employed LVC model (2.34 Å), hinting that almost all trajectories are in the T_1 minimum after 200 fs. The differences between the dynamics and both the dynamics without energy adjustment and adjustment along the full velocity vector are twofold: when using the non-adiabatic coupling vectors, on the one side, the kinetic energy along specific bonds is increased when descending down the multitude of states, potentially increasing the kinetic energy along the S–S bond. On the other side, as the active state tries to switch to states with higher potential energy, frustrated hops are encountered when the kinetic energy along the non-adiabatic coupling vector is insufficient. This happened a total of 7231 times when using the non-adiabatic coupling vector and 0 times in the case of the full velocity vector which always contained enough energy (more than 7 eV in most cases) to accommodate the respective energy change. Therefore, on average 7 hops to higher-lying states have been frustrated per trajectory, barricading access to states that potentially feature larger MLCT character as they are generally located at higher energy and restricting the space of active states to lower energy states of predominantly MSCT character. We note that the non-adiabatic coupling vector has been commonly deemed the best and most physically sound choice for rescaling direction.[11, 17, 18, 12]

In summary, we find that the differences between not rescaling or rescaling along the full velocity vector are very small. Overall, the energetic closeness of the excited states in this transition metal complex results in a large number of hops with small energy gaps. When distributing this small amount of energy using the full velocity vector, very small changes to the momenta of each single atom are observed. Therefore, rescaling along the full velocity vector conserves the total energy, but gives very similar results to not rescaling the kinetic energy at all. Adjusting the kinetic energy along the non-adiabatic coupling vector is found to change the speed upon which the S–S bond elongates as well the speed of the deactivation mechanics and would be the preferred treatment for hops that are not induced by an external field. Unfortunately, it is not possible to properly distinguish between field-induced hops and hops due to non-adiabatic couplings and spin-orbit couplings. Therefore, in order to not interfere with field-induced hops the simplest choice of not conserving the total energy was chosen for all encountered hops.

References

[1] Sebastian Mai, Martin Richter, Moritz Heindl, Maximilian F. S. J. Menger, Andrew Atkins, Matthias Ruckenbauer, Felix Plasser, Lea Maria Ibele, Simon Kropf, Markus Oppel, Philipp Marquetand, and Leticia González. Sharc2.1: Surface hopping including arbitrary couplings — program package for non-adiabatic dynamics. sharc-md.org, 2019.

[2] Martin Richter, Philipp Marquetand, Jesús González-Vázquez, Ignacio Sola, and Leticia González. SHARC: ab Initio Molecular Dynamics with Surface Hopping in the Adiabatic Representation Including Arbitrary Couplings. *J. Chem. Theory Comput.*, 7(5):1253, May 2011.

[3] Sebastian Mai, Philipp Marquetand, and Leticia González. A general method to describe intersystem crossing dynamics in trajectory surface hopping. *Int. J. Quantum Chem.*, 115(18):1215–1231, September 2015.

[4] T. Fiedlschuster, J. Handt, E. K. U. Gross, and R. Schmidt. Surface hopping in laser-driven molecular dynamics. *Phys. Rev. A*, 95(6):063424, June 2017.

[5] Juan José Bajo, Jesús González-Vázquez, Ignacio R. Sola, Jesus Santamaria, Martin Richter, Philipp Marquetand, and Leticia González. Mixed Quantum-Classical Dynamics in the Adiabatic Representation To Simulate Molecules Driven by Strong Laser Pulses. *J. Phys. Chem. A*, 116(11):2800–2807, March 2012.

[6] Tobias Fiedlschuster, Jan Handt, and Rüdiger Schmidt. Floquet surface hopping: Laser-driven dissociation and ionization dynamics of h_2^+. *Phys. Rev. A*, 93(5):053409, May 2016.

[7] Zeyu Zhou, Hsing-Ta Chen, Abraham Nitzan, and Joseph Eli Subotnik. Nonadiabatic Dynamics in a Laser Field: Using Floquet Fewest Switches Surface Hopping To Calculate Electronic Populations for Slow Nuclear Velocities. *J. Chem. Theory Comput.*, 16(2):821, February 2020.

[8] G. Granucci, M. Persico, and A. Toniolo. Direct semiclassical simulation of photochemical processes with semiempirical wave functions. *J. Chem. Phys.*, 114(24):10608, June 2001.

[9] Giovanni Granucci and Maurizio Persico. Critical appraisal of the fewest switches algorithm for surface hopping. *J. Chem. Phys.*, 126(13):134114, April 2007.

[10] Giovanni Granucci, Maurizio Persico, and Alberto Zoccante. Including quantum decoherence in surface hopping. *J. Chem. Phys.*, 133(13):134111, October 2010.

[11] John C. Tully. Molecular dynamics with electronic transitions. *J. Chem. Phys.*, 93(2):1061, 1990.

[12] Mario Barbatti. Velocity adjustment in surface hopping: Ethylene as a case study of the maximum error caused by direction choice. *J. Chem. Theory Comp.*, 17(5):3010, 2021.

[13] Juan José Bajo, Giovanni Granucci, and Maurizio Persico. Interplay of radiative and nonradiative transitions in surface hopping with radiation-molecule interactions. *J. Chem. Phys.*, 140(4):044113, January 2014.

[14] Maria S. Topaler, Thomas C. Allison, David W. Schwenke, and Donald G. Truhlar. Test of trajectory surface hopping against accurate quantum dynamics for an electronically nonadiabatic chemical reaction. *J. Phys. Chem. A*, 102(10):1666, 1998.

[15] Michael D. Hack, Ahren W. Jasper, Yuri L. Volobuev, David W. Schwenke, and Donald G. Truhlar. Quantum mechanical and quasiclassical trajectory surface hopping studies of the electronically nonadiabatic predissociation of the $\tilde{\mathrm{A}}$ state of $\mathrm{NaH_2}$. *J. Phys. Chem. A*, 103(32):6309, 1999.

[16] Moritz Heindl and Leticia González. Validating fewest-switches surface hopping in the presence of laser fields. *J. Chem. Phys.*, 154(14):144102, 2021.

[17] Felix Plasser, Sebastian Mai, Maria Fumanal, Etienne Gindensperger, Chantal Daniel, and Leticia González. Strong Influence of Decoherence Corrections and Momentum Rescaling in Surface Hopping Dynamics of Transition Metal Complexes. *J. Chem. Theory Comput.*, 15(9):5031, September 2019.

[18] Lea M. Ibele and Basile F. E. Curchod. A molecular perspective on Tully models for nonadiabatic dynamics. *Phys. Chem. Chem. Phys.*, 22(27):15183, July 2020.

[19] Boris A. Trofimov, Lidiya M. Sinegovskaya, and Nina K. Gusarova. Vibrations of the s–s bond in elemental sulfur and organic polysulfides: a structural guide. *J Sulfur Chem*, 30(5):518, 2009.

[20] Federica Agostini, Ali Abedi, Yasumitsu Suzuki, Seung Kyu Min, Neepa T. Maitra, and E. K. U. Gross. The exact forces on classical nuclei in non-adiabatic charge transfer. *J. Chem. Phys.*, 142(8):084303, 2015.

BIBLIOGRAPHY

[1] J. D'Orazio, S. Jarrett, A. Amaro-Ortiz, S. T: UV radiation and the skin, *Int J. Mol. Sci.*, **14**, 12222 (2013).

[2] P. Nayak, S. Mahesh, H. Snaith, D. Cahen: Photovoltaic solar cell technologies: analysing the state of the art, *Nat. Rev. Mater.*, **4**, 269 (2019).

[3] P. Agostinis, K. Berg, K. A. Cengel, T. H. Foster, A. W. Girotti, S. O. Gollnick, S. M. Hahn, M. R. Hamblin, A. Juzeniene, D. Kessel, M. Korbelik, J. Moan, P. Mroz, D. Nowis, J. Piette, B. C. Wilson, J. Golab: Photodynamic therapy of cancer: An update, *CA: A Cancer Journal for Clinicians*, **61**, 250 (2011).

[4] A. H. Zewail: Femtochemistry: Atomic-scale dynamics of the chemical bond, *J. Phys. Chem. A*, **104**, 5660 (2000).

[5] M. Maiuri, M. Garavelli, G. Cerullo: Ultrafast spectroscopy: State of the art and open challenges, *J. Am. Chem. Soc.*, **142**, 3 (2020).

[6] E. Schrödinger: An undulatory theory of the mechanics of atoms and molecules, *Phys. Rev.*, **28**, 1049 (1926).

[7] L. González, R. Lindh (editors): *Quantum Chemistry and Dynamics of Excited States*, John Wiley & Sons, Ltd (2020).

[8] M. Beck, A. Jäckle, G. Worth, H.-D. Meyer: The multiconfiguration time-dependent Hartree (MCTDH) method: A highly efficient algorithm for propagating wavepackets, *Phys. Rep.*, **324**, 1 (2000).

[9] H.-D. Meyer, U. Manthe, L. S. Cederbaum: The multi-configurational time-depenendet Hartree approach, *Chem. Phys. Lett.*, **165**, 73 (1990).

[10] G. A. Worth, G. Welch, M. J. Paterson: Wavepacket dynamics study of Cr(CO)$_5$ after formation by photodissociation: relaxation through an (E$\bigoplus$A)$\bigotimes$e Jahn–Teller conical intersection, *Mol. Phys.*, **104**, 1095 (2006).

[11] M. Pápai, G. Vankó, T. Rozgonyi, T. J. Penfold: High-efficiency iron photosensitizer explained with quantum wavepacket dynamics, *J. Phys. Chem. Lett.*, **7**, 2009 (2016).

[12] M. Fumanal, E. Gindensperger, C. Daniel: Ligand substitution and conformational effects on the ultrafast luminescent decay of [Re(CO)$_3$(phen)(L)]$^+$ (l = imidazole, pyridine): non-adiabatic quantum dynamics, *Phys. Chem. Chem. Phys.*, **20**, 1134 (2018).

[13] C. Sanz-Sanz, G. A. Worth: Field modified spin–orbit potential curves of IBr. Preliminary dynamical results, *Phys. Chem. Chem. Phys.*, **21**, 14429 (2019).

[14] I. Burghardt, H.-D. Meyer, L. S. Cederbaum: Approaches to the approximate treatment of complex molecular systems by the multiconfiguration time-dependent hartree method, *J. Chem. Phys.*, **111**, 2927 (1999).

[15] G. A. Worth, I. Burghardt: Full quantum mechanical molecular dynamics using gaussian wavepackets, *Chem. Phys. Lett.*, **368**, 502 (2003).

[16] H. Wang, M. Thoss: Multilayer formulation of the multiconfiguration time-dependent hartree theory, *J. Chem. Phys.*, **119**, 1289 (2003).

[17] J. Schulze, M. F. Shibl, M. J. Al-Marri, O. Kühn: Multi-layer multi-configuration time-dependent hartree (ML-MCTDH) approach to the correlated exciton-vibrational dynamics in the FMO complex, *J. Chem. Phys.*, **144**, 185101 (2016).

[18] H. Köppel, W. Domcke, L. S. Cederbaum: Multimode molecular dynamics beyond the Born-Oppenheimer approximation, in I. Prigogine, S. A. Rice (editors), *Adv. Chem. Phys. Vol. 57*, 59, John Wiley & Sons (1984).

[19] G. A. Worth, L. S. Cederbaum: BEYOND BORN-OPPENHEIMER: Molecular Dynamics Through a Conical Intersection, *Annu. Rev. Phys. Chem.*, **55**, 127 (2004).

[20] G. Richings, I. Polyak, K. Spinlove, G. Worth, I. Burghardt, B. Lasorne: Quantum dynamics simulations using Gaussian wavepackets: the vMCG method, *Int. Rev. Phys. Chem.*, **34**, 269 (2015).

[21] G. W. Richings, S. Habershon: Mctdh on-the-fly: Efficient grid-based quantum dynamics without pre-computed potential energy surfaces, *J. Chem. Phys.*, **148**, 134116 (2018).

[22] J. C. Tully: Molecular dynamics with electronic transitions, *J. Chem. Phys.*, **93**, 1061 (1990).

[23] M. Barbatti: Nonadiabatic dynamics with trajectory surface hopping method, *WIREs Comput Mol Sci*, **1**, 620 (2011).

[24] J. E. Subotnik, W. Ouyang, B. R. Landry: Can we derive Tully's surface-hopping algorithm from the semiclassical quantum Liouville equation? Almost, but only with decoherence, *J. Chem. Phys.*, **139**, 214107 (2013).

[25] R. Kapral: Surface hopping from the perspective of quantum–classical Liouville dynamics, *Chem. Phys.*, **481**, 77 (2016).

[26] F. Agostini, A. Abedi, Y. Suzuki, S. K. Min, N. T. Maitra, E. K. U. Gross: The exact forces on classical nuclei in non-adiabatic charge transfer, *J. Chem. Phys.*, **142**, 084303 (2015).

[27] M. Barbatti: Velocity adjustment in surface hopping: Ethylene as a case study of the maximum error caused by direction choice, *J. Chem. Theory Comp.*, **17**, 3010 (2021).

[28] F. Plasser, S. Mai, M. Fumanal, E. Gindensperger, C. Daniel, L. González: Strong influence of decoherence corrections and momentum rescaling in surface hopping dynamics of transition metal complexes, *J. Chem. Theory Comput.*, **15**, 5031 (2019).

[29] E. Heller, J.-O. oswig, G. Seifert: Exploring the effects of quantum decoherence on the excited-state dynamics of molecular systems, *Theor. Chem. Acc.*, **140** (2021).

[30] G. Granucci, M. Persico: Critical appraisal of the fewest switches algorithm for surface hopping, *J. Chem. Phys.*, **126**, 134114 (2007).

[31] G. Granucci, M. Persico, A. Zoccante: Including quantum decoherence in surface hopping, *J. Chem. Phys.*, **133**, 134111 (2010).

[32] L. M. Ibele, B. F. E. Curchod: A molecular perspective on Tully models for nonadiabatic dynamics, *Phys. Chem. Chem. Phys.*, **22**, 15183 (2020).

[33] J. E. Subotnik: Fewest-switches surface hopping and decoherence in multiple dimensions, *J. Phys. Chem. A*, **115**, 12083 (2011).

[34] M. S. Topaler, T. C. Allison, D. W. Schwenke, D. G. Truhlar: Test of trajectory surface hopping against accurate quantum dynamics for an electronically nonadiabatic chemical reaction, *J. Phys. Chem. A*, **102**, 1666 (1998).

[35] M. D. Hack, A. W. Jasper, Y. L. Volobuev, D. W. Schwenke, D. G. Truhlar: Quantum mechanical and quasiclassical trajectory surface hopping studies of the electronically nonadiabatic predissociation of the Ã state of NaH_2, *J. Phys. Chem. A*, **103**, 6309 (1999).

[36] J. Stark: Beobachtungen über den effekt des elektrischen feldes auf spektrallinien. I. Quereffekt, *Ann. Phys.*, **348**, 965 (1914).

[37] B. J. Sussman, D. Townsend, M. Y. Ivanov, A. Stolow: Dynamic Stark Control of Photochemical Processes, *Science*, **314**, 278 (2006).

[38] D. J. Tannor, S. A. Rice: Control of selectivity of chemical reaction via control of wave packet evolution, *J. Chem. Phys.*, **83**, 5013 (1985).

[39] P. Brumer, M. Shapiro: Control of unimolecular reactions using coherent light, *Chem. Phys. Lett.*, **126**, 541 (1986).

[40] A. P. Peirce, M. A. Dahleh, H. Rabitz: Optimal control of quantum-mechanical systems: Existence, numerical approximation, and applications, *Phys. Rev. A*, **37**, 4950 (1988).

[41] D. J. Tannor, R. Kosloff, A. Bartana: Laser cooling of internal degrees of freedom of molecules by dynamically trapped states, *Faraday Discuss.*, **113**, 365 (1999).

[42] V. S. Malinovsky, C. Meier, D. J. Tannor: Optical paralysis in electronically congested systems: Application to large-amplitude vibrational motion of ground state Na_2, *Chem. Phys.*, **221**, 67 (1997).

[43] P. Marquetand, V. Engel: Local control theory applied to molecular photoassociation, *J. Chem. Phys.*, **127**, 084115 (2007).

[44] R. Mitrić, J. Petersen, V. Bonačić-Koutecký: Laser-field-induced surface-hopping method for the simulation and control of ultrafast photodynamics, *Phys. Rev. A*, **79**, 053416 (2009).

[45] I. Tavernelli, B. F. E. Curchod, U. Rothlisberger: Mixed quantum-classical dynamics with time-dependent external fields: A time-dependent density-functional-theory approach, *Phys. Rev. A*, **81**, 052508 (2010).

[46] T. J. Penfold, G. A. Worth, C. Meier: Local control of multidimensional dynamics, *Phys. Chem. Chem. Phys.*, **12**, 15616 (2010).

[47] B. F. E. Curchod, T. J. Penfold, U. Rothlisberger, I. Tavernelli: Local control theory in trajectory-based nonadiabatic dynamics, *Phys. Rev. A*, **84**, 042507 (2011).

[48] P. Marquetand, M. Richter, J. González-Vázquez, I. Sola, L. González: Nonadiabatic ab initio molecular dynamics including spin–orbit coupling and laser fields, *Faraday Discuss.*, **153**, 261 (2011).

[49] J. J. Bajo, G. Granucci, M. Persico: Interplay of radiative and nonradiative transitions in surface hopping with radiation-molecule interactions, *J. Chem. Phys.*, **140**, 044113 (2014).

[50] T. Fiedlschuster, J. Handt, R. Schmidt: Floquet surface hopping: Laser-driven dissociation and ionization dynamics of H_2^+, *Phys. Rev. A*, **93**, 053409 (2016).

[51] D. V. Makhov, D. V. Shalashilin: Floquet Hamiltonian for incorporating electronic excitation by a laser pulse into simulations of non-adiabatic dynamics, *Chem. Phys.*, **515**, 46 (2018).

[52] T. J. Penfold, M. Pápai, K. B. Møller, G. A. Worth: Excited state dynamics initiated by an electromagnetic field within the variational multi-configurational Gaussian (vMCG) method, *Comput. Theor. Chem.*, **1160**, 24 (2019).

[53] B. Mignolet, B. F. E. Curchod: Excited-state molecular dynamics triggered by light pulses—ab initio multiple spawning vs trajectory surface hopping, *J. Phys. Chem. A* (2019).

[54] A. Röder, J. Petersen, K. Issler, I. Fischer, R. Mitrić, L. Poisson: Exploring the excited-state dynamics of hydrocarbon radicals, biradicals, and carbenes using time-resolved photoelectron spectroscopy and field-induced surface hopping simulations, *J. Phys. Chem. A*, 10643 (2019).

[55] Z. Zhou, H.-T. Chen, A. Nitzan, J. E. Subotnik: Nonadiabatic dynamics in a laser field: Using Floquet fewest switches surface hopping to calculate electronic populations for slow nuclear velocities, *J. Chem. Theory Comput.*, **16**, 821 (2020).

[56] M. Schirò, F. G. Eich, F. Agostini: Quantum–classical nonadiabatic dynamics of floquet driven systems, *J. Chem. Phys.*, **154**, 114101 (2021).

[57] M. Richter, P. Marquetand, J. González-Vázquez, I. Sola, L. González: SHARC: ab Initio Molecular Dynamics with Surface Hopping in the Adiabatic Representation Including Arbitrary Couplings, *J. Chem. Theory Comput.*, **7**, 1253 (2011).

[58] J. J. Bajo, J. González-Vázquez, I. R. Sola, J. Santamaria, M. Richter, P. Marquetand, L. González: Mixed quantum-classical dynamics in the adiabatic representation to simulate molecules driven by strong laser pulses, *J. Phys. Chem. A*, **116**, 2800 (2012).

[59] T. Fiedlschuster, J. Handt, E. K. U. Gross, R. Schmidt: Surface hopping in laser-driven molecular dynamics, *Phys. Rev. A*, **95**, 063424 (2017).

[60] M. Born: Zur quantenmechanik der stoßvorgänge, *Z. Physik*, **37**, 863–867 (1926).

[61] D. J. Tannor: *Introduction to Quantum Mechanics: A Time-Dependent Perspective*, University Science Books (2006).

[62] M. Born, R. Oppenheimer: Zur quantentheorie der molekeln, *Ann. Phys.*, **389**, 457 (1927).

[63] D. R. Hartree: The wave mechanics of an atom with a non-coulomb central field part I. Theory and methods, *Math. Proc. Cambridge*, **24** (1928).

[64] J. C. Slater: The theory of complex spectra, *Phys. Rev.*, **34**, 1293 (1929).

[65] F. Jensen: *Introduction to Computational Chemistry*, John Wiley & Sons, Inc. (2006).

[66] B. O. Roos, P. R. Taylor, P. E. M. Siegbahn: A complete active space SCF method (CASSCF) using a density matrix formulated super-CI approach, *Chem. Phys.*, **48**, 157 (1980).

[67] C. J. Stein, M. Reiher: Automated selection of active orbital spaces, *Chem. Theory Comput.*, **12**, 1760 (2016).

[68] C. J. Cramer: *Essentials of Computational Chemistry: Theories and Models.*, John Wiley & Sons, Inc. (2004).

[69] P. Hohenberg, W. Kohn: Inhomogeneous electron gas, *Phys. Rev.*, **136**, B864 (1964).

[70] W. Kohn, L. J. Sham: Self-consistent equations including exchange and correlation effects, *Phys. Rev.*, **140**, A1133 (1965).

[71] M. Huix-Rotllant, N. Ferré, M. Barbatti: *Time-Dependent Density Functional Theory*, chapter 2, 13–46, John Wiley & Sons, Ltd (2020).

[72] E. Runge, E. K. U. Gross: Density-functional theory for time-dependent systems, *Phys. Rev. Lett.*, **52**, 997 (1984).

[73] K. Yabana, G. F. Bertsch: Time-dependent local-density approximation in real time, *Phys. Rev. B*, **54**, 4484 (1996).

[74] M. Marques, E. Gross: Time-dependent density functional theory, *Annu. Rev. Phys. Chem.*, **55**, 427 (2004).

[75] M. Casida, M. Huix-Rotllant: Progress in time-dependent density-functional theory, *Annu. Rev. Phys. Chem.*, **63**, 287 (2012).

[76] S. Hirata, M. Head-Gordon: Time-dependent density functional theory within the Tamm–Dancoff approximation, *Chem. Phys. Lett.*, **314**, 291 (1999).

[77] J. P. Zobel, M. Heindl, F. Plasser, S. Mai, L. González: Surface hopping dynamics on vibronic coupling models, *Acc. Chem. Res.*, **54**, 3760 (2021).

[78] S. Thompson, J. Eng, T. J. Penfold: The intersystem crossing of a cyclic (alkyl)(amino) carbene gold (I) complex, *J. Chem. Phys.*, **149**, 014304 (2018).

[79] M. Fumanal, C. Daniel, E. Gindensperger: Excited-state dynamics of $[Mn(im)(CO)_3(phen)]^+$: PhotoCORM, catalyst, luminescent probe?, *J. Chem. Phys.*, **154**, 154102 (2021).

[80] C. M. Marian: Spin–orbit coupling and intersystem crossing in molecules, *WIREs Comput. Mol. Sci.*, **2**, 187 (2012).

[81] P. A. M. Dirac, R. H. Fowler: The quantum theory of the electron, *Proc. R. Soc. London Ser. A*, **117**, 610 (1928).

[82] T. J. Penfold, E. Gindensperger, C. Daniel, C. M. Marian: Spin-vibronic mechanism for intersystem crossing, *Chem. Rev.*, **118**, 6975 (2018).

[83] D. Parker, R. Minns, T. Penfold, G. Worth, H. Fielding: Ultrafast dynamics of the S_1 excited state of benzene, *Chem. Phys. Lett.*, **469**, 43 (2009).

[84] S. Mai, P. Marquetand, L. González: Non-adiabatic and intersystem crossing dynamics in SO_2. II. The role of triplet states in the bound state dynamics studied by surface-hopping simulations, *J. Chem. Phys.*, **140**, 204302 (2014).

[85] B. A. Hess, C. M. Marian, U. Wahlgren, O. Gropen: A mean-field spin-orbit method applicable to correlated wavefunctions, *Chem. Phys. Lett.*, **251**, 365 (1996).

[86] S. Reiter, D. Keefer, R. de Vivie-Riedle: *Exact Quantum Dynamics (Wave Packets) in Reduced Dimensionality*, chapter 11, 355–381, John Wiley & Sons, Ltd (2020).

[87] A. Hofmann, R. de Vivie-Riedle: Quantum dynamics of photoexcited cyclohexadiene introducing reactive coordinates, *J. Chem. Phys.*, **112**, 5054 (2000).

[88] B. Lasorne, F. Sicilia, M. J. Bearpark, M. A. Robb, G. A. Worth, L. Blancafort: Automatic generation of active coordinates for quantum dynamics calculations: Application to the dynamics of benzene photochemistry, *J. Chem. Phys.*, **128**, 124307 (2008).

[89] G. Capano, T. J. Penfold, M. Chergui, I. Tavernelli: Photophysics of a copper phenanthroline elucidated by trajectory and wavepacket-based quantum dynamics: a synergetic approach, *Phys. Chem. Chem. Phys.*, **19**, 19590 (2017).

[90] S. Gómez, M. Heindl, A. Szabadi, L. González: From surface hopping to quantum dynamics and back. finding essential electronic and nuclear degrees of freedom and optimal surface hopping parameters, *J. Phys. Chem. A*, **123**, 8321 (2019).

[91] M. Bonfanti, G. A. Worth, I. Burghardt: *Multi-Configuration Time-Dependent Hartree Methods: From Quantum to Semiclassical and Quantum-Classical*, chapter 12, 383–411, John Wiley & Sons, Ltd (2020).

[92] A. Bjerre, E. E. Nikitin: Energy transfer in collisions of an excited sodium atom with a nitrogen molecule, *Chem. Phys. Lett.*, **1**, 179 (1967).

[93] J. C. Tully, R. K. Preston: Trajectory Surface Hopping Approach to Nonadiabatic Molecular Collisions: The Reaction of H^+ with D_2, *J. Chem. Phys.*, **55**, 562 (1971).

[94] S. Mai, P. Marquetand, L. González: *Surface Hopping Molecular Dynamics*, chapter 16, 499–530, John Wiley & Sons, Ltd (2020).

[95] L. Verlet: Computer "experiments" on classical fluids. I. Thermodynamical properties of Lennard-Jones molecules, *Phys. Rev.*, **159**, 98 (1967).

[96] L. Verlet: Computer "experiments" on classical fluids. II. Equilibrium correlation functions, *Phys. Rev.*, **165**, 201 (1968).

[97] J. E. Subotnik, N. Shenvi: A new approach to decoherence and momentum rescaling in the surface hopping algorithm, *J. Chem. Phys.*, **134**, 024105 (2011).

[98] F. Brieuc, Y. Bronstein, H. Dammak, P. Depondt, F. Finocchi, M. Hayoun: Zero-point energy leakage in quantum thermal bath molecular dynamics simulations, *J. Chem. Theory Comput.*, **12**, 5688 (2016).

[99] P. Pechukas: Time-dependent semiclassical scattering theory. II. Atomic collisions, *Phys. Rev.*, **181**, 174 (1969).

[100] J. R. Schmidt, P. V. Parandekar, J. C. Tully: Mixed quantum-classical equilibrium: Surface hopping, *J. Chem. Phys.*, **129**, 044104 (2008).

[101] A. Carof, S. Giannini, J. Blumberger: Detailed balance, internal consistency, and energy conservation in fragment orbital-based surface hopping, *J. Chem. Phys.*, **147**, 214113 (2017).

[102] S. Hammes-Schiffer, J. C. Tully: Proton transfer in solution: Molecular dynamics with quantum transitions, *J. Chem. Phys.*, **101**, 4657 (1994).

[103] A. W. Jasper, M. D. Hack, D. G. Truhlar: The treatment of classically forbidden electronic transitions in semiclassical trajectory surface hopping calculations, *J. Chem. Phys.*, **115**, 1804 (2001).

[104] A. W. Jasper, S. N. Stechmann, D. G. Truhlar: Fewest-switches with time uncertainty: A modified trajectory surface-hopping algorithm with better accuracy for classically forbidden electronic transitions, *J. Chem. Phys.*, **116**, 5424 (2002).

[105] A. W. Jasper, D. G. Truhlar: Improved treatment of momentum at classically forbidden electronic transitions in trajectory surface hopping calculations, *Chem. Phys. Lett.*, **369**, 60 (2003).

[106] G. Granucci, M. Persico, A. Toniolo: Direct semiclassical simulation of photochemical processes with semiempirical wave functions, *J. Chem. Phys.*, **114**, 10608 (2001).

[107] B. F. E. Curchod, F. Agostini: On the dynamics through a conical intersection, *J. Phys. Chem. Lett.*, **8**, 831 (2017).

[108] B. J. Schwartz, E. R. Bittner, O. V. Prezhdo, P. J. Rossky: Quantum decoherence and the isotope effect in condensed phase nonadiabatic molecular dynamics simulations, *J. Chem. Phys.*, **104**, 5942 (1996).

[109] O. V. Prezhdo, P. J. Rossky: Evaluation of quantum transition rates from quantum-classical molecular dynamics simulations, *J. Chem. Phys.*, **107**, 5863 (1997).

[110] H. M. Jaeger, S. Fischer, O. V. Prezhdo: Decoherence-induced surface hopping, *J. Chem. Phys.*, **137**, 22A545 (2012).

[111] J. Xu, L. Wang: Branching corrected surface hopping: Resetting wavefunction coefficients based on judgement of wave packet reflection, *J. Chem. Phys.*, **150**, 164101 (2019).

[112] M. Heindl, L. González: Validating fewest-switches surface hopping in the presence of laser fields, *J. Chem. Phys.*, **154**, 144102 (2021).

[113] S. Mai, P. Marquetand, L. González: A general method to describe intersystem crossing dynamics in trajectory surface hopping, *Int. J. Quantum Chem.*, **115**, 1215 (2015).

[114] D. A. Blank, S. W. North, Y. T. Lee: The ultraviolet photodissociation dynamics of pyrrole, *Chem. Phys.*, **187**, 35 (1994).

[115] J. Wei, A. Kuczmann, J. Riedel, F. Renth, F. Temps: Photofragment velocity map imaging of H atom elimination in the first excited state of pyrrole, *Phys. Chem. Chem. Phys.*, **5**, 315 (2003).

[116] B. Cronin, M. G. D. Nix, R. H. Qadiri, M. N. R. Ashfold: High resolution photofragment translational spectroscopy studies of the near ultraviolet photolysis of pyrrole, *Phys. Chem. Chem. Phys.*, **6**, 5031 (2004).

[117] H. Lippert, H.-H. Ritze, I.-V. Hertel, W. Radloff: Femtosecond time-resolved hydrogen-atom elimination from photoexcited pyrrole molecules, *ChemPhysChem*, **5**, 1423 (2004).

[118] M. Staniforth, J. D. Young, D. R. Cole, T. N. V. Karsili, M. N. R. Ashfold, V. G. Stavros: Ultrafast excited-state dynamics of 2,4-dimethylpyrrole, *J. Phys. Chem. A*, **118**, 10909 (2014).

[119] G. Wu, S. P. Neville, O. Schalk, T. Sekikawa, M. N. R. Ashfold, G. A. Worth, A. Stolow: Excited state non-adiabatic dynamics of pyrrole: A time-resolved photoelectron spectroscopy and quantum dynamics study, *J. Chem. Phys.*, **142**, 074302 (2015).

[120] T. Geng, O. Schalk, S. P. Neville, T. Hansson, R. D. Thomas: Dynamics in higher lying excited states: Valence to Rydberg transitions in the relaxation paths of pyrrole and methylated derivatives, *J. Chem. Phys.*, **146**, 144307 (2017).

[121] O. M. Kirkby, M. A. Parkes, S. P. Neville, G. A. Worth, H. H. Fielding: Non-radiative relaxation dynamics of pyrrole following excitation in the range 249.5–200nm, *Chem. Phys. Lett.*, **683**, 179 (2017).

[122] B. O. Roos, P.-Å. Malmqvist, V. Molina, L. Serrano-Andrés, M. Merchán: Theoretical characterization of the lowest-energy absorption band of pyrrole, *J. Chem. Phys.*, **116**, 7526 (2002).

[123] V. Vallet, Z. Lan, S. Mahapatra, A. L. Sobolewski, W. Domcke: Time-dependent quantum wave-packet description of the $1\pi\sigma^*$ photochemistry of pyrrole, *Faraday Discuss.*, **127**, 283 (2004).

[124] V. Vallet, Z. Lan, S. Mahapatra, A. L. Sobolewski, W. Domcke: Photochemistry of pyrrole: Time-dependent quantum wave-packet description of the dynamics at the $\pi_1\sigma^*$-S_0 conical intersections, *J. Chem. Phys.*, **123**, 144307 (2005).

[125] M. Barbatti, M. Vazdar, A. J. A. Aquino, M. Eckert-Maksić, H. Lischka: The nonadiabatic deactivation paths of pyrrole, *J. Chem. Phys.*, **125**, 164323 (2006).

[126] M. Vazdar, M. Eckert-Maksić, M. Barbatti, H. Lischka: Excited-state non-adiabatic dynamics simulations of pyrrole, *Mol. Phys.*, **107**, 845 (2009).

[127] B. Sellner, M. Barbatti, H. Lischka: Dynamics starting at a conical intersection: Application to the photochemistry of pyrrole, *J. Chem. Phys.*, **131**, 024312 (2009).

[128] M. Barbatti, J. Pittner, M. Pederzoli, U. Werner, R. Mitrić, V. Bonačić-Koutecký, H. Lischka: Non-adiabatic dynamics of pyrrole: Dependence of deactivation mechanisms on the excitation energy, *Chem. Phys.*, **375**, 26 (2010).

[129] S. P. Neville, G. A. Worth: A reinterpretation of the electronic spectrum of pyrrole: A quantum dynamics study, *J. Chem. Phys.*, **140**, 034317 (2014).

[130] M. Sapunar, A. Ponzi, S. Chaiwongwattana, M. Mališ, A. Prlj, P. Decleva, N. Došlić: Timescales of N–H bond dissociation in pyrrole: a nonadiabatic dynamics study, *Phys. Chem. Chem. Phys.*, **17**, 19012 (2015).

[131] D. V. Makhov, K. Saita, T. J. Martinez, D. V. Shalashilin: Ab initio multiple cloning simulations of pyrrole photodissociation: TKER spectra and velocity map imaging, *Phys. Chem. Chem. Phys.*, **17**, 3316 (2015).

[132] K. R. Nandipati, Z. Lan, H. Singh, S. Mahapatra: An alternative laser driven photodissociation mechanism of pyrrole via $^1\pi\sigma^*/S_0$ conical intersection, *J. Chem. Phys.*, **146**, 214304 (2017).

[133] D. Picconi, S. Y. Grebenshchikov: Photodissociation dynamics in the first absorption band of pyrrole. II. Photofragment distributions for the $^1A_2(\pi\sigma^*)\leftarrow \tilde{X}^1A_1(\pi\pi)$ transition, *J. Chem. Phys.*, **148**, 104104 (2018).

[134] A. Ponzi, M. Sapunar, N. Došlić, P. Decleva: Photoionization of pyrrole from the B_2 state: a computational study on the effects of Rydberg–valence mixing, *Theor. Chem. Acc.*, **139** (2020).

[135] A. L. Sobolewski, W. Domcke: Conical intersections induced by repulsive $^1\pi\sigma^*$ states in planar organic molecules: malonaldehyde, pyrrole and chlorobenzene as photochemical model systems, *Chem. Phys.*, **259**, 181 (2000).

[136] G. M. Roberts, C. A. Williams, H. Yu, A. S. Chatterley, J. D. Young, S. Ullrich, V. G. Stavros: Probing ultrafast dynamics in photoexcited pyrrole: timescales for $^1\pi\sigma^*$ mediated H-atom elimination, *Faraday Discuss.*, **163**, 95 (2013).

[137] A. Dreuw, M. Wormit: The algebraic diagrammatic construction scheme for the polarization propagator for the calculation of excited states, *WIREs Comput. Mol. Sci.*, **5**, 82 (2015).

[138] T. Shiozaki, W. Győrffy, P. Celani, H.-J. Werner: Communication: Extended multi-state complete active space second-order perturbation theory: Energy and nuclear gradients, *J. Chem. Phys*, **135**, 081106 (2011).

[139] J. W. Park, T. Shiozaki: Analytical derivative coupling for multistate CASPT2 theory, *J. Chem. Theory Comput.*, **13**, 2561 (2017).

[140] B. Vlaisavljevich, T. Shiozaki: Nuclear energy gradients for internally contracted complete active space second-order perturbation theory: multistate extensions, *J. Chem. Theory Comput.*, **12**, 3781 (2016).

[141] K. Kaufmann, W. Baumeister, M. Jungen: Universal Gaussian basis sets for an optimum representation of Rydberg and continuum wavefunctions, *J. Phys. B*, **22**, 2223 (1989).

[142] T. Shiozaki: BAGEL: Brilliantly Advanced General Electronic-structure Library, *WIREs Comput. Mol. Sci.*, **8**, e1331 (2018).

[143] S. Mai, M. Richter, M. Heindl, M. F. S. J. Menger, A. Atkins, M. Ruckenbauer, F. Plasser, L. M. Ibele, S. Kropf, M. Oppel, P. Marquetand, L. González: Sharc2.1: Surface hopping including arbitrary couplings — program package for non-adiabatic dynamics, sharc-md.org (2019).

[144] E. Wigner: On the quantum correction for thermodynamic equilibrium, *Phys. Rev.*, **40**, 749 (1932).

[145] M. Barbatti: Simulation of excitation by sunlight in mixed quantum-classical dynamics, *J. Chem. Theory Comput.*, **16**, 4849 (2020).

[146] F. Plasser, S. Gómez, M. F. S. J. Menger, S. Mai, L. González: Highly efficient surface hopping dynamics using a linear vibronic coupling model, *Phys. Chem. Chem. Phys.*, **21**, 57 (2019).

[147] M. J. Paterson, P. A. Hunt, M. A. Robb, O. Takahashi: Non-adiabatic direct dynamics study of chromium hexacarbonyl photodissociation, *J. Phys. Chem. A*, **106**, 10494 (2002).

[148] I. Tavernelli, B. F. Curchod, U. Rothlisberger: Nonadiabatic molecular dynamics with solvent effects: A LR-TDDFT QM/MM study of ruthenium (II) tris (bipyridine) in water, *Chem. Phys.*, **391**, 101 (2011).

[149] A. J. Atkins, L. González: Trajectory surface-hopping dynamics including intersystem crossing in $[Ru(bpy)_3]^{2+}$, *J. Phys. Chem. Lett.*, **8**, 3840 (2017).

[150] Y.-G. Fang, L.-Y. Peng, X.-Y. Liu, W.-H. Fang, G. Cui: QM/MM nonadiabatic dynamics simulation on ultrafast excited-state relaxation in osmium(II) compounds in solution, *Comput. Theor. Chem.*, **1155**, 90 (2019).

[151] F. Talotta, M. Boggio-Pasqua, L. González: Early relaxation dynamics in the photoswitchable complex trans-$[RuCl(NO)(py)_4]^{2+}$, *Chem. Eur. J.*, **26**, 11522 (2020).

[152] P. Heim, S. Mai, B. Thaler, S. Cesnik, D. Avagliano, D. Bella-Velidou, W. E. Ernst, L. González, M. Koch: Revealing ultrafast population transfer between nearly degenerate electronic states, *J. Phys. Chem. Lett.*, **11**, 1443 (2020).

[153] S. Mai, M. F. S. J. Menger, M. Marazzi, D. L. Stolba, A. Monari, L. González: Competing ultrafast photoinduced electron transfer and intersystem crossing of $[Re(CO)_3(Dmp)(his124)(trp122)]^{+}$ in pseudomonas aeruginosa azurin: A nonadiabatic dynamics study, *Theor. Chem. Acc.*, **139** (2020).

[154] J. P. Zobel, O. S. Bokareva, P. Zimmer, C. Wölper, M. Bauer, L. González: Intersystem crossing and triplet dynamics in an iron(II) N-heterocyclic carbene photosensitizer, *Inorg. Chem.*, **59**, 14666 (2020).

[155] J. P. Zobel, T. Knoll, L. González: Ultrafast and long-time excited state kinetics of an nir-emissive vanadium(III) complex II. elucidating triplet-to-singlet excited-state dynamics, *Chem. Sci.*, **12**, 10791 (2021).

[156] P. Tavadze, G. Avendaño Franco, P. Ren, X. Wen, Y. Li, J. P. Lewis: A machine-driven hunt for global reaction coordinates of azobenzene photoisomerization, *J. Am. Chem. Soc.*, **140**, 285 (2018).

[157] I. L. Zheldakov, M. N. Ryazantsev, A. N. Tarnovsky: Wavepacket motion via a conical intersection in the photochemistry of aqueous transition-metal dianions, *J. Phys. Chem. Lett.*, **2**, 1540 (2011).

[158] I. P. Pozdnyakov, E. M. Glebov, S. G. Matveeva, V. F. Plyusnin, A. A. Mel´nikov, S. V. Chekalin: Primary photophysical and photochemical processes upon UV excitation of $PtBr_6^{2-}$ and $PtCl_6^{2-}$ complexes in water and methanol, *Russ. Chem. Bull.*, **64**, 1784 (2015).

[159] P. J. Stephens, F. J. Devlin, C. F. Chabalowski, M. J. Frisch: Ab initio calculation of vibrational absorption and circular dichroism spectra using density functional force fields, *J. Phys. Chem.*, **98**, 11623 (1994).

[160] E. J. Baerends, T. Ziegler, A. J. Atkins, J. Autschbach, D. Bashford, O. Baseggio, A. Bérces, F. M. Bickelhaupt, C. Bo, P. M. Boerritger, L. Cavallo, C. Daul, D. P. Chong, D. V. Chulhai, L. Deng, R. M. Dickson, J. M. Dieterich, D. E. Ellis, M. van Faassen, A. Ghysels, A. Giammona, S. J. A. van Gisbergen, A. Goez, A. W. Götz, S. Gusarov, F. E. Harris, P. van den Hoek, Z. Hu, C. R. Jacob, H. Jacobsen, L. Jensen, L. Joubert, J. W. Kaminski, G. van Kessel, C. König, F. Kootstra, A. Kovalenko, M. Krykunov, E. van Lenthe, D. A. McCormack, A. Michalak, M. Mitoraj, S. M. Morton, J. Neugebauer, V. P. Nicu, L. Noodleman, V. P. Osinga, S. Patchkovskii, M. Pavanello, C. A. Peeples, P. H. T. Philipsen, D. Post, C. C. Pye, H. Ramanantoanina, P. Ramos, W. Ravenek, J. I. Rodríguez, P. Ros, R. Rüger, P. R. T. Schipper, D. Schlüns, H. van Schoot, G. Schreckenbach, J. S. Seldenthuis, M. Seth, J. G. Snijders, M. Solà, S. M., M. Swart, D. Swerhone, G. te Velde, V. Tognetti, P. Vernooijs, L. Versluis, L. Visscher, O. Visser, F. Wang, T. A. Wesolowski, E. M. van Wezenbeek, G. Wiesenekker, S. K. Wolff, T. K. Woo, A. L. Yakovlev: ADF2017, SCM, Theoretical Chemistry, Vrije Universiteit, Amsterdam, The Netherlands, https://www.scm.com.

[161] P. Marquetand, M. Richter, J. González-Vázquez, I. Sola, L. González: Nonadiabatic ab initio molecular dynamics including spin–orbit coupling and laser fields, *Faraday Discuss.*, **153**, 261 (2011).

[162] C. Lévêque, H. Köppel, R. Taïeb: Excited state dynamics in SO_2. III. an ab initio quantum study of single- and multi-photon ionization, *J. Chem. Phys.*, **140**, 204303 (2014).

[163] C. Lévêque, R. Taïeb, H. Köppel: Communication: Theoretical prediction of the importance of the $^3B_2$ state in the dynamics of sulfur dioxide, *J. Chem. Phys.*, **140**, 091101 (2014).

[164] S. Mai, M. Pollum, L. Martínez-Ferníandez, N. Dunn, P. Marquetand, I. Corral, C. Crespo-Hernández, L. González: The origin of efficient triplet state population in sulfur-substituted nucleobases, *Nat. Commun.*, **7**, 13077 (2016).

[165] B. R. Landry, M. J. Falk, J. E. Subotnik: Communication: The correct interpretation of surface hopping trajectories: How to calculate electronic properties, *J. Chem. Phys.*, **139**, 211101 (2013).

[166] M. Cattaneo, C. E. Schiewer, A. Schober, S. Dechert, I. Siewert, F. Meyer: 2,2'-bipyridine equipped with a disulfide/dithiol switch for coupled two-electron and two-proton transfer, *Chem. Eur. J.*, **24**, 4864 (2018).

[167] G. A. Crosby: Spectroscopic investigations of excited states of transition-metal complexes, *Acc. Chem. Res.*, **8**, 231 (1975).

[168] K. Kalyanasundaram: Photophysics, photochemistry and solar energy conversion with tris(bipyridyl)ruthenium(II) and its analogues, *Coord. Chem. Rev.*, **46**, 159 (1982).

[169] E. M. Kober, T. J. Meyer: Concerning the absorption spectra of the ions $m(bpy)_3^{2+}$ (m = fe, ru, os; bpy = 2,2'-bipyridine), *Inorg. Chem.*, **21**, 3967 (1982).

[170] E. M. Kober, T. J. Meyer: An electronic structural model for the emitting MLCT excited states of Ru(bpy)$_3^{2+}$ and Os(bpy)$_3^{2+}$, *Inorg. Chem.*, **23**, 3877 (1984).

[171] P. Müller, K. Brettel: [ru(bpy)$_3$]$^{2+}$ as a reference in transient absorption spectroscopy: Differential absorption coefficients for formation of the long-lived ^{3}MLCT excited state, *Photochem. Photobiol. Sci.*, **11**, 632 (2012).

[172] D. W. Thompson, A. Ito, T. J. Meyer: [ru(bpy)$_3$]$^{2+*}$ and other remarkable metal-to-ligand charge transfer (MLCT) excited states:, *Pure Appl. Chem.*, **85**, 1257 (2013).

[173] F. Neese, F. Wennmohs, U. Becker, C. Riplinger: The orca quantum chemistry program package, *J. Chem. Phys.*, **152**, 224108 (2020).

[174] M. J. Frisch, G. W. Trucks, H. B. Schlegel, G. E. Scuseria, M. A. Robb, J. R. Cheeseman, G. Scalmani, V. Barone, B. Mennucci, G. A. Petersson, H. Nakatsuji, M. Caricato, X. Li, H. P. Hratchian, A. F. Izmaylov, J. Bloino, G. Zheng, J. L. Sonnenberg, M. Hada, M. Ehara, K. Toyota, R. Fukuda, J. Hasegawa, M. Ishida, T. Nakajima, Y. Honda, O. Kitao, H. Nakai, T. Vreven, J. A. Montgomery, J. E. Peralta, F. Ogliaro, M. Bearpark, J. J. Heyd, E. Brothers, K. N. Kudin, V. N. Staroverov, R. Kobayashi, J. Normand, K. Raghavachari, A. Rendell, J. C. Burant, S. S. Iyengar, J. Tomasi, M. Cossi, N. Rega, J. M. Millam, M. Klene, J. E. Knox, J. B. Cross, V. Bakken, C. Adamo, J. Jaramillo, R. Gomperts, R. E. Stratmann, O. Yazyev, A. J. Austin, R. Cammi, C. Pomelli, J. W. Ochterski, R. L. Martin, K. Morokuma, V. G. Zakrzewski, G. A. Voth, P. Salvador, J. J. Dannenberg, S. Dapprich, A. D. Daniels, Ö. Farkas, J. B. Foresman, J. V. Ortiz, J. Cioslowski, D. J. Fox: Gaussian 09 Revision A.2 (2009).

[175] M. Pápai, T. Rozgonyi, T. J. Penfold, M. M. Nielsen, K. B. Møller: Simulation of ultrafast excited-state dynamics and elastic x-ray scattering by quantum wavepacket dynamics, *J. Chem. Phys.*, **151**, 104307 (2019).

[176] M. Fumanal, E. Gindensperger, C. Daniel: Ultrafast excited-state decays in [Re(CO)$_3$(n,n)(l)]$^{n+}$: Nonadiabatic quantum dynamics, *J. Chem. Theory Comput.*, **13**, 1293 (2017).

[177] A. J. Atkins, F. Talotta, L. Freitag, M. Boggio-Pasqua, L. González: Assessing excited state energy gaps with time-dependent density functional theory on Ru(II) complexes, *J. Chem. Theory Comput.*, **13**, 4123 (2017).

[178] A. Cannizzo, F. van Mourik, W. Gawelda, G. Zgrablic, C. Bressler, M. Chergui: Broadband femtosecond fluorescence spectroscopy of [Ru(bpy)$_3$]$^{2+}$, *Angew. Chem. Int. Ed.*, **45**, 3174 (2006).

[179] O. Bräm, F. Messina, A. M. El-Zohry, A. Cannizzo, M. Chergui: Polychromatic femtosecond fluorescence studies of metal–polypyridine complexes in solution, *Chem. Phys.*, **393**, 51 (2012).

[180] B. A. Trofimov, L. M. Sinegovskaya, N. K. Gusarova: Vibrations of the s–s bond in elemental sulfur and organic polysulfides: a structural guide, *J Sulfur Chem*, **30**, 518 (2009).

[181] G. A. Worth, G. W. Richings: Optimal control by computer, *Annu. Rep. Prog. Chem., Sect. C: Phys. Chem.*, **109**, 113 (2013).

[182] P. v. d. Hoff, S. Thallmair, M. Kowalewski, R. Siemering, R. d. Vivie-Riedle: Optimal control theory – closing the gap between theory and experiment, *Phys. Chem. Chem. Phys.*, **14**, 14460 (2012).

[183] J. Petersen, R. Mitrić: Electronic coherence within the semiclassical field-induced surface hopping method: Strong field quantum control in K$_2$, *Phys. Chem. Chem. Phys.*, **14**, 8299 (2012).

[184] Y. Arasaki, K. Takatsuka: Pulse-train photoelectron spectroscopy of electronic and nuclear dynamics in molecules, *ChemPhysChem*, **14**, 1387 (2013).

[185] M. K. Ganesa Subramanian, R. Santra, R. Welsch: Infrared-laser-pulse-enhanced ultrafast fragmentation of N_2^{2+} following Auger decay: Mixed quantum-classical simulations, *Phys. Rev. A*, **98**, 063421 (2018).

[186] A. Tóth, A. Csehi, G. J. Halász, A. Vibók: Control of photodissociation with the dynamic Stark effect induced by THz pulses, *Phys. Rev. Research*, **2**, 013338 (2020).

[187] A. Valentini, S. v. d. Wildenberg, F. Remacle: Selective bond formation triggered by short optical pulses: Quantum dynamics of a four-center ring closure, *Phys. Chem. Chem. Phys.*, **22**, 22302 (2020).

[188] B. F. E. Curchod, T. J. Penfold, U. Rothlisberger, I. Tavernelli: Local control theory in trajectory surface hopping dynamics applied to the excited-state proton transfer of 4-hydroxyacridine, *ChemPhysChem*, **16**, 2127 (2015).